NEAR-WELLBORE PROCESSES IN NATURALLY FRACTURED OR WEAKLY CONSOLIDATED FORMATIONS

A Thesis
Presented to
The Academic Faculty

by

Yixuan Sun

In Partial Fulfillment
of the Requirements for the Degree
Doctor of Philosophy in the
School of Civil and Environmental Engineering

Georgia Institute of Technology
May 2017

NEAR-WELLBORE PROCESSES IN NATURALLY FRACTURED OR WEAKLY CONSOLIDATED FORMATIONS

Approved by:

Haiying Huang, Advisor
School of Civil and Environmental Engineering
Georgia Institute of Technology

Leonid Germanovich
School of Civil and Environmental Engineering
Georgia Institute of Technology

Ghassan AlRegib
School of Electrical and Computer Engineering
Georgia Institute of Technology

Paul W. Mayne
School of Civil and Environmental Engineering
Georgia Institute of Technology

J. David Frost
School of Civil and Environmental Engineering
Georgia Institute of Technology

Date Approved: March 30th, 2017

To my family

ACKNOWLEDGEMENTS

This dissertation would not become a reality without the infinite encouragement and support of my advisor, Dr. Haiying Huang. I would like to thank her for sharing important lessons on research, teaching, career, and life. Her unique perspective into science and research has set up a good example for me to follow in my future career.

I also want to thank my thesis committee. Dr. Ghassan AlRegib allowed me to reach outside of my field and brought important aspects of seismic interpretation into my research. Dr. Frost had shown genuine interest in my development and success at Georgia Tech. Every conversation I had with him was inspiring. Dr. Leonid Germanovich provided me with valuable suggestions and comments for my research, and his lectures introduce me to the beauty of mathematics and mechanics. I also would like to thank Dr. Paul Mayne for being supportive with my scholarship application, teaching me the knowledge that is very useful during my job interview, and sharing great music.

I should also acknowledge the faculty that did not serve on my thesis committee but with whom I also interacted, including Dr. Arson, Dr. Burns, Dr. Dai, Dr. Fedele, Dr. Muhanna, and Dr. Santamarina; and Civil and Environmental Engineering staff: Jenny Eaton, Carol Maddox. Daniela Estrada and Andy Udell.

I greatly appreciate the assistance and encouragement from past and present students of Dr. Huang's research group. In particular, I want to acknowledge Yifei Ma, Longde Jin, Ming Liu, Fengshou Zhang, Joy Zhang, Wan Cheng, Brian Emrich. I also would like to express my appreciation to all Geosystems Engineering fellows who make my journey at Georgia Tech so unforgettable and pleasant. I am very grateful to my friends, Jia He, Lu Xu, Yilin Liu, Qiulei Huang, Zhuo Li for their support and great friendship.

I would like to thank my parents, parents-in-law, aunts, uncle, grandparents and cousins in China for their continuous encouragement and support. I cannot fail to thank my husband, Naijia Xiao, for his patience and resourcefulness.

Partial financial support from the National Science Foundation through grant NSF/CMMI-1055882 and the Sand Control Client Advisory Board of Schlumberger is gratefully acknowledged.

TABLE OF CONTENTS

LIST OF TABLES

LIST OF FIGURES

SUMMARY

Drilling and completion in naturally fractured or weakly consolidated formations could be challenging. While drilling through naturally fractured reservoirs, severe lost circulation is a major contributor to the nonproductive time. It may also cause significant issues in subsequent well completion and reservoir production. Quantitative prediction of the drilling mud loss in a natural fracture is therefore critical for selecting prevention and remedial strategies to control lost circulation. Meanwhile, better understanding of how weakly consolidated formations respond to fluid injection is of fundamental importance to many engineering applications such as hydraulic fracturing, water flooding and drill cuttings reinjection. To be able to predict where the injected fluid goes and what kind of opening geometry is created in the subsurface is essential to the design and optimization of these engineering applications.

Theoretical models are formulated in this work to determine the drilling mud loss in a natural fracture intersected by a wellbore. We first consider the transient response for two particular cases when the natural fracture is either parallel or perpendicular to the vertical wellbore axis. We adopt the constant height and the radial fracture geometry models. Complex rheology of the drilling mud and natural fracture deformability are both accounted for in these models. Next the ultimate drilling mud loss from an inclined wellbore intersected by an arbitrarily oriented natural fracture is modeled. The drilling mud invasion profile can be predicted based on the yield stress and the geometrical configurations of the wellbore and the natural fracture. The solution, validated by published experimental data, can also be used to estimate natural fracture permeability based on mud loss data in the field. The theoretical models developed for predicting the mud loss can be applied directly in the field practices not only for drilling, but also for grouting in jointed rock mass.

A numerical strategy based on Discrete Element Method (DEM) is proposed to model the injection process of a high viscosity fluid into an unconsolidated or weakly consolidated

formation. Novelty of this numerical study is in the modeling methodology for the fluid-grain interface. Fluid front advances only when the gap between two neighboring particles exceeds a threshold value, a criterion which could be considered as similar to taking into account of the effect of surface tension. Constant rate of fluid injection is modeled and parametric analysis is conducted on the critical opening size, the confining stress, the initial borehole size, the injection flow rate, the friction angle and the stress anisotropy. Numerical results on the borehole breakdown pressure are then compared with those from the bifurcation analysis for the cohesionless case and elasto-plasticity solutions for the cohesive case. Evidences from the displacement field of particles suggest a process zone exists near the fracture tip. The DEM analysis of the injection process allows us to gain valuable insights into the fluid-grain displacement process in nearly unconsolidated media and could serve as guides for future development of fracture growth criteria at the continuum scale.

CHAPTER I

INTRODUCTION

1.1 Motivations and Research Objectives

Oil and gas reservoirs could be naturally fractured or weakly consolidated. Drilling and completion of wells in both types of formations require knowledge of the near-wellbore processes to address the challenges.

While drilling through naturally fractured reservoirs, severe lost circulation is a major contributor to the nonproductive time. It may also cause significant issues in subsequent well completion and reservoir production. Quantitative prediction of the drilling mud loss in a natural fracture is therefore critical for selecting prevention and remedial strategies to control lost circulation. Rheological measurement of a drilling mud is often limited to the relatively low shear rate range. Shear thinning following a power law is usually assumed for the entire shear rate range. Nevertheless, it is not uncommon that, due to the multiphase nature, the steady-state drilling mud rheology is shear thinning in the low shear rate range, but exhibits Newtonian or even shear thickening behaviors in the high shear rate range. While extensive literature exists for theoretical mud loss models, effect of the high shear rate rheology on drilling mud loss in a natural fracture has not been examined. Also, limited studies were published for the case when an arbitrarily oriented natural fracture intersects an inclined wellbore. Modeling an arbitrarily orientated fracture is a much more complicated task than modeling a horizontal or vertical fracture, since the mud invasion can no longer be simplified into one-dimensional mathematically.

Meanwhile, better understanding of how weakly consolidated formations respond to fluid injection is of fundamental importance to many engineering applications such as hydraulic fracturing, water flooding and drill cuttings reinjection. To be able to predict where the injected fluid goes and what kind of opening geometry is created in the subsurface is essential to the design and optimization of these engineering applications. While the mechanisms are

relatively well understood in competent rocks, fundamental questions such as whether the failure resulted from fluid pressurization would be in shear or in tensile, and if a fracture develops, what is the criterion for fracture growth, remain poorly understood for nearly unconsolidated formations. The highly nonlinear constitutive behaviors and the strong hydro-mechanical coupling have rendered the problem a great challenge.

In this work, we intend to address the following questions.

1. How the mud loss behaviors are affected by the rheological parameters, in particular, when both the yield stress and high shear rate rheology are taken into account?

2. How to determine the ultimate mud loss volume and the mud invasion profile?

3. How to numerically model the fluid injection process, in particular, a fluid of high viscosity, being injected into nearly unconsolidated formation?

4. How to characterize the failure mechanism and predict the breakdown pressure?

1.2 Research Outlines and Thesis Structures

Both theoretical and numerical analyses are performed in this work. The theoretical analysis focuses on invasion of drilling mud into a natural fracture. We first consider transient mud loss behavior for two cases when the wellbore axis is nearly perpendicular or parallel to the natural fracture, for which we adopted a radial geometry model and a constant height model. We assume that the drilling mud is incompressible and can be described by a piecewise rheological model, characterized by a yield stress and power laws for both the low shear rate and the high shear rate rheology, respectively. The natural fracture could either be closed or has a small opening initially. Fluid flow inside the fracture is coupled with the mechanical deformation of the permeable reservoir. The mathematical formulation is solved using an explicit moving mesh algorithm. Effects of the rheological parameters, the overbalance pressure, the fracture initial width, and the leak off coefficient on the transient mud loss behaviors are then analyzed. The ultimate invasion profile of the drilling mud in an inclined natural fracture is analyzed by considering limit equilibrium, which is the worst case scenario. The solution is validated by published experimental data and used to estimate the fracture permeability based on mud loss data in the field.

Numerical modeling is performed for the injection process in an unconsolidated or weakly consolidated formation using the Discrete Element Method (DEM) code *PFC2D*®. Novelty of this numerical study is in the modeling methodology for the fluid-grain interface. Fluid front advances only when the gap between two neighboring particles exceeds a threshold value, a criterion which could be considered as similar to taking into account of the effect of surface tension. The numerical test is performed with assemblies under both isotropic and anisotropic stress fields. Constant rate of injection is modeled and parametric analysis on the critical opening size, the confining stress, the initial borehole size, the injection flow rate, the friction angle and the stress anisotropy is performed. Numerical results on the breakdown of the cavity are then compared with those from the bifurcation analysis for the cohesionless case as well as elasto-plasticity solutions for the cohesive case.

The thesis is organized as follows.

Chapter 1 **Introduction** outlines the motivations and objectives of this study.

Chapter 2 **Theoretical Analysis of Drilling Mud Invasion into a Natural Fracture - a Radial Geometry Model** analyzes effects of the rheological parameters and the leakoff coefficient on the mud loss behaviors when the wellbore axis is nearly perpendicular to the natural fracture. A radial fracture model is adopted for mud invasion from a vertical wellbore into a horizontal fracture. The fluid behavior is described by a piecewise rheological model, characterized by a yield stress and power laws for both the low shear rate and the high shear rate rheology, respectively. The problem formulated is solved numerically using an explicit moving mesh algorithm. Variation of the mud loss volume and mud loss rate with time can both be predicted.

Chapter 3 **Theoretical Analysis of Drilling Mud Invasion into a Natural Fracture - a Constant Height Model** analyzes effects of the rheological parameters and the leakoff coefficient on the mud loss behaviors when the wellbore axis is parallel to the natural fracture. The piecewise fluid rheology model is incorporated into a PKN fracture model.

Chapter 4 **Limit Equilibrium Analysis of Drilling Mud Loss into an Inclined Natural Fracture** predicts the ultimate invasion profile of the drilling mud in an inclined natural fracture based on a limit equilibrium solution. The solution is validated by published

experimental data and can be used to estimate the fracture permeability based on mud loss data in the field.

Chapter 5 **DEM Modeling of Fluid Injection into a Nearly Unconsolidated Medium Subjected to Isotropic Stress** proposes a numerical strategy to model fluid injection into an unconsolidated or weakly consolidated medium using the DEM code *PFC2D®*. Growth mechanisms of the localized features resulted from fluid injection and the associated failure mechanisms in the granular medium are examined. Parametric analysis on the effects of the critical opening size, the confining stress, the borehole size, the injection flow rate and the friction angle on the failure mechanism is performed.

Chapter 6 **Theoretical Analysis of the Breakdown Pressure** compares the numerical results on the breakdown of the cavity with those from the bifurcation analysis for the cohesionless case as well as elasto-plasticity solutions.

Chapter 7 **DEM Modeling of Fluid Injection into an Unconsolidated Medium Subjected to Anisotropic Stress** investigates numerically the fluid injection process into the weak formation under anisotropic stress field. The effect of the stress anisotropy on the growth of the localized features is analyzed.

Chapter 8 **Conclusions and Future Work** summarizes the main findings obtained from this thesis and gives some suggestions for the future work.

CHAPTER II

THEORETICAL ANALYSIS OF DRILLING MUD INVASION INTO A NATURAL FRACTURE - A RADIAL GEOMETRY MODEL

2.1 Introduction

Naturally fractured reservoirs are prone to severe circulation loss. Circulation loss is a common contributor to the nonproductive time in drilling, it may also cause significant issues in subsequent well completion and reservoir production. Therefore, quantitative prediction of the drilling mud loss is crucial for selecting prevention and remedial strategies to control lost circulation. On the other hand, in practice, real-time monitoring of the mud loss in overbalance drilling has often been employed as a diagnostic tool of formation characterization for the *in-situ* fracture permeability [25, 27, 7].

To improve the interpretation of mud loss data, various theoretical models for mud invasion in a single isolated fracture have been developed in the literature. Theoretical treatments are generally limited to either radial or constant height fracture geometry models, where the problems can be mathematically simplied into one-dimensional. These models all extend from the simplest cases of one-dimensional linear or radial steady-state flow of a Newtonian fluid through a slot of constant width, where there is no leakoff from the fracture to the rigid rock matrix and the overpressure, i.e., the pressure above the reservoir pressure at the borehole, is constant. Basic elements in the theoretical models therefore include: the fracture orientation and geometry, the fracture deformation law, mud rheology, the leakoff behavior, whether the fracture walls are smooth or rough, whether the fracture length is finite or infinite, and whether the flow along the fracture is transient or steady state. From the point of view of mud loss control, we generally assume that the initial natural fracture width is known and solve for the total mud loss volume as a function of time. However, for the application of formation characterization, mud loss volume is known and we need to solve for the fracture aperture, which determines the fracture permeability.

Liétard *et al.* [65, 64] incorporated non-Newtonian Bingham rheology for radial steady-state flow into a non-deformable fracture. Mud loss therefore stops when the driving force resulted from the overbalance pressure cannot overcome the resistance from the yield stress of the fluid. The ultimate mud invasion radius is expressed analytically as a function of the fracture width, fluid yield stress and the overpressure based on limit equilibrium. The model was improved by Huang *et al.* [44] by directly relating the mud loss volume to the fracture width, which becomes more convenient to use in practice. It should be noted that in Liétard *et al.* [65, 64] and Huang *et al.* [44], their predictions of the ultimate mud loss volume is in fact incorrect because the expression for the local pressure drop in the limit of zero shear rate is wrong. We will discuss about this issue in Chapter IV. Lavrov and Tronvoll [61] included local linear elastic deformation for the fracture walls. The fluid is assumed to be Newtonian, flowing in one-dimension inside a fracture of finite length. An explicit finite difference scheme is employed to numerically solve the mud loss rate as a function of time. The sudden pressure increase from the initial reservoir pressure to the borehole pressure and the fracture inclination are both taken into account. Their work followed considered power law rheology in [62] and exponential deformation law and bi-viscous fluid rheology in [63]. Herschel–Bulkley rheology and local linear deformation for the fracture are taken into account in Majidi *et al.* [71, 72, 69]. Sanfillippo *et al.* [90] accounted for the fracture inclination by assuming that the mud invasion profile is elliptical and can be translated to an equivalent circular profile. A diffusion equation for radial flow is then solved numerically to determine the hydraulic aperture of the fracture.

Lost circulation in a natural fracture is driven by the pressure drop between the wellbore and the reservoir. For a complex fluid with yield stress, when the pressure gradient falls below a threshold, the mud invasion ceases and the fracture may be considered sealed. If we assume the overpressure is constant during mud invasion, the pressure gradient near the wellbore is the largest at the onset of the drilling mud invasion and decreases as the mud flows further into the fracture. The high shear rate fluid rheology is expected to govern the fluid flow behaviors at the early time. In other words, as far as fluid rheology is concerned, the yield stress takes effect at late time, while the high shear rate rheology could play a

critical role in controlling the rate of the mud loss at the early time.

Laboratory measurement of the high shear rate rheology ($\dot{\gamma} > 1000$ 1/s) is rather difficult to obtain due to issues such as wall slip and flow instability in the rheometers. Rheological measurement of a drilling mud is often limited to the relatively low shear rate range. Shear thinning following a power law is usually assumed for the entire shear rate range. Nevertheless, it is not uncommon that, due to the multiphase nature, the steady-state drilling mud rheology is shear thinning in the low shear rate range, but exhibits Newtonian or even shear thickening behaviors in the high shear rate range (see Fig. 1) [39, 86]. Effect of the high shear rate rheology on drilling mud loss in a natural fracture has not been examined previously in the literature. The most complex rheology in the aforementioned theoretical models is the Herschel–Bulkley model,

$$\tau = \tau_0 + k\dot{\gamma}^n \tag{1}$$

where τ and $\dot{\gamma}$ are the shear stress and shear rate; τ_0 is the yield stress; and n and k are the power law index and the flow consistency index. The rheology is usually termed shear thinning if $n < 1$ and shear thickening if $n > 1$.

The objective of Chapters II and III is therefore to investigate how the mud loss behaviors are affected by complex rheolgoy, in particular, when the high shear rate rheology differs from the low shear rate rheology. We assume that the drilling mud rheology can be described by a piecewise rheological model, characterized by a yield stress and power laws for both the low shear rate and the high shear rate rheology, respectively. Two particular cases, where the wellbore axis is either perpendidular or parallel to the natural fracture are modeled. When the wellbore axis is perpendicular to the fracture plane, we assume that mud flow is radial. When the wellbore axis is parallel to the fracture plane, the Perkins-Kern-Nordgen (PKN) geometry model [84, 80], commonly used for hydraulic fracturing modeling, is adopted in this work. Other elements in the general framework for hydraulic fracturing modeling, e.g, Carter's leakoff model, are also integrated in this study. The radial flow model is presented in Chapter II and the constant height PKN model is presented in Chapter III.

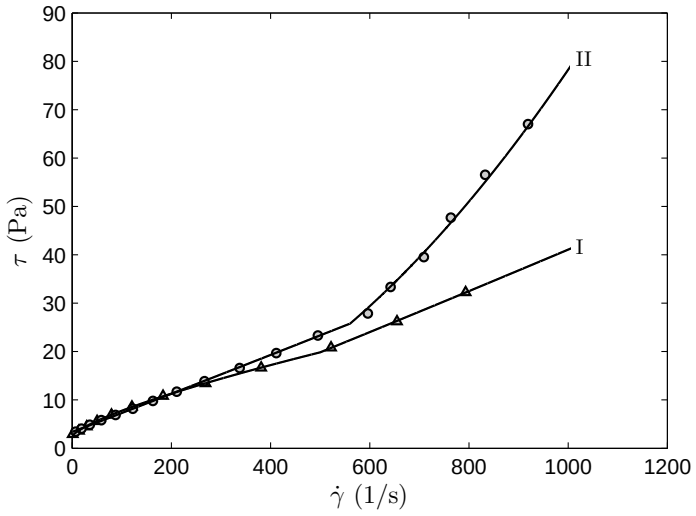

Figure 1: Flow curves (shear stress vs. shear strain rate) of drilling muds; the dots in flow curves I and II are re-plotted from the steady-state data from Ragouilliaux *et al.* [86] (decreasing stress ramp) and Herzhaft *et al.* [39], respectively; the solid lines are fitting curves.

2.2 Mathematical Formulation

Schematic of a fracture of radius r_f intersected by a wellbore of radius r_{in} is shown in Fig. 2. A cylindrical coordinate system is adopted with the origin being located at the wellbore axis. The problem so defined is axisymmetric. Compared with the mud invasion radius, the fracture width is much smaller. Fluid flow inside the fracture can therefore be treated as one-dimensional and lubrication theory applies. Field variables such as the net overpressure, p, and the fracture width, w, therefore vary along the radial direction only. The net pressure p is the overpressure above the initial reservoir pressure that drives the drilling mud to flow inside the natural fracture. The fluid is assumed to be single-phase and incompressible. The fluid flow equation can be obtained after combining the rheological equation with the equation for balance of momentum (equilibrium equation) and the geometrical equation. Other governing equations include the fracture deformation law and local fluid mass conservation equation. We seek to determine the fracture width $w\,(r,t)$ as a function of the position r and time t.

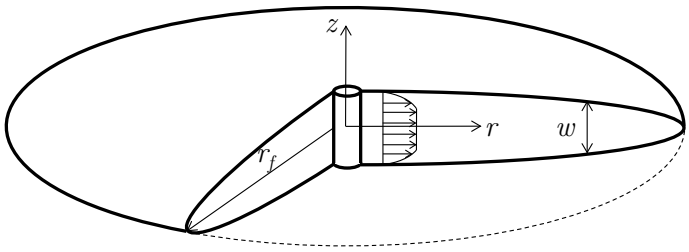

Figure 2: A fracture of radius r_f; at a given position, the fracture width is denoted as w.

2.2.1 Rheological Model

We assume that rheology of the drilling mud can be described by the following equation,

$$\tau = \begin{cases} \tau_0 + K_1 \dot{\gamma}^{n_1} & 0 < |\dot{\gamma}| \leq \dot{\gamma}_c \\ K_2 \dot{\gamma}^{n_2} & |\dot{\gamma}| > \dot{\gamma}_c \end{cases} \tag{2}$$

where K_1 and K_2 are the consistency parameters, and n_1 and n_2 are the power law indices. Symbol $\dot{\gamma}_c$ denotes a critical shear strain rate that characterizes the transition from the low shear rheology to the high shear rheology. Given the yield stress τ_0 and the critical shear stress τ_c at the critical shear strain rate $\dot{\gamma}_c$, the consistency parameters K_1 and K_2 can be determined from

$$K_1 = \frac{\tau_c - \tau_0}{\dot{\gamma}_c^{n_1}}, \qquad K_2 = \frac{\tau_c}{\dot{\gamma}_c^{n_2}} \tag{3}$$

The rheological behavior is generally termed shear thinning if $n < 1$ ($n = n_1$ or n_2) and shear thickening if $n > 1$. The model reduces to the Herschel–Bulkley model if $\dot{\gamma}_c \to \infty$.

The rheological parameters used to fit the flow curves in Fig. 1 are given in Table 1. At the high shear rate, flow curve I suggests that the drilling mud behaves as a Newtonian fluid ($n_2 = 1.0$), while flow curve II indicates that there is strong shear thickening ($n_2 = 1.9$).

Table 1: Rheological parameters of the drilling muds I and II.

	n_1	n_2	τ_0 (Pa)	τ_c (Pa)	$\dot{\gamma}_c$ (1/s)
I	0.7	1	3	20	500
II	1.0	1.9	3	25	560

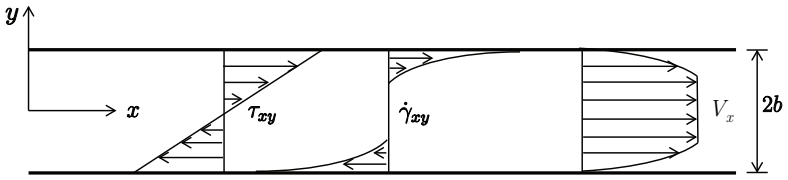

Figure 3: Schematic of a fracture of width $w = 2b$ showing profiles of shear stress, shear strain rate and velocity (not to scale).

2.2.2 Fluid Flow Equation

With the assumption of one dimensional lubrication flow, the equation of balance of momentum can be expressed as,

$$\frac{\partial \sigma_{xx}}{\partial x} + \frac{\partial \tau_{xy}}{\partial y} = 0 \tag{4}$$

$$\sigma_{xx} = -p \tag{5}$$

Here the sign convention of tension positive is adopted.

Consider locally the fracture aperture is $w = 2b$. Substituting Eq. (5) into Eq. (4) and integrating Eq. (4) with respect to y yield the shear stress distribution over cross section,

$$\tau_{xy} = \tau_w s, \quad \tau_w = \bar{p} b \tag{6}$$

where τ_w is the wall shear stress; s is the scaled coordinates, defined as $s = y/b$ $(-1 \leq s \leq 1)$ in the fracture width direction; and $\bar{p} = |dp/dx|$ is the magnitude of the pressure gradient along the flow direction. It should be noted that shear stress τ_{xy} across the fracture aperture is always continuous and linearly distributed, independent of the rheological properties of the fluid. Existence of the yield stress means that the fluid flow occurs only if the shear stress at the walls, τ_w, exceeds the yield stress τ_0 (or $\bar{p} > \tau_0/b$). Under flow condition, a plug flow zone moving at a constant speed is expected to appear around the centerline $(y = 0)$. Meanwhile, the piecewise rheological behavior expressed in Eq. 2 suggests that only when the wall shear stress is above the critical shear stress (i.e., $\tau_w > \tau_c$ or $\bar{p} > \tau_c/b$), the high shear rate rheology takes effect. Otherwise, the fluid flow behavior is governed by the yield stress and the low shear rate rheology only.

Three types of distinct flow regions are expected to appear across the width direction. Denote s_1 and s_2 as the scaled positions for the interfaces that separate the plug flow

zone, the low shear rate governed zone and the high shear rate governed zone. The scaled positions, s_1 and s_2, can be determined from,

$$s_1 = \tau_0/\bar{p}b, \quad s_2 = \tau_c/\bar{p}b \tag{7}$$

The plug flow zone is within $|s| \leq s_1$; the low shear rate governed zones are within $s_1 < |s| \leq s_2$; and the high shear rate governed zones are within $s_2 < |s| \leq 1$. If the local pressure gradient is in the range of $2\tau_0/b < \bar{p} < 2\tau_c/b$ (i.e., when $s_1 < 1$ and $s_2 > 1$), only the plug flow zone and the low shear rate governed zones exist across the width direction.

In the rate form, the geometrical equation relates the shear strain rate $\dot{\gamma}$ to the flow velocity V_x through,

$$\dot{\gamma} = \frac{\partial V_x}{\partial y} \tag{8}$$

After combining the rheological equation, the balance of momentum and the geometrical equations with the no-slip condition at the walls (i.e., $V_x = 0$ at $s = \pm 1$), the flow velocity as a function of the local pressure gradient can be readily obtained. When $\tau_0/b < \bar{p} \leq \tau_c/b$,

$$V_x = \begin{cases} M_1 \left[(1 - s_1)^{1+\frac{1}{n_1}} - (|s| - s_1)^{1+\frac{1}{n_1}} \right] & s_1 < |s| \leq 1 \\ M_1 (1 - s_1)^{1+\frac{1}{n_1}} & 0 < |s| \leq s_1 \end{cases} \tag{9}$$

When $\bar{p} > \tau_c/b$,

$$V_x = \begin{cases} M_2 \left(1 - |s|^{1+\frac{1}{n_2}} \right) & s_2 < |s| \leq 1 \\ M_2 \left(1 - s_2^{1+\frac{1}{n_2}} \right) & \\ + M_1 \left[(s_2 - s_1)^{1+\frac{1}{n_1}} - (|s| - s_1)^{1+\frac{1}{n_1}} \right] & s_1 < |s| \leq s_2 \\ M_2 \left(1 - s_2^{1+\frac{1}{n_2}} \right) + M_1 (s_2 - s_1)^{1+\frac{1}{n_1}} & 0 < |s| \leq s_1 \end{cases} \tag{10}$$

where

$$\begin{aligned} M_1 &= \frac{b\dot{\gamma}_c}{(s_2 - s_1)^{\frac{1}{n_1}} \left(1 + \frac{1}{n_1} \right)} \\ M_2 &= \frac{b\dot{\gamma}_c}{s_2^{\frac{1}{n_2}} \left(1 + \frac{1}{n_2} \right)} \end{aligned} \tag{11}$$

For the case when $\bar{p} \leq \tau_0/b$, the fluid does not move.

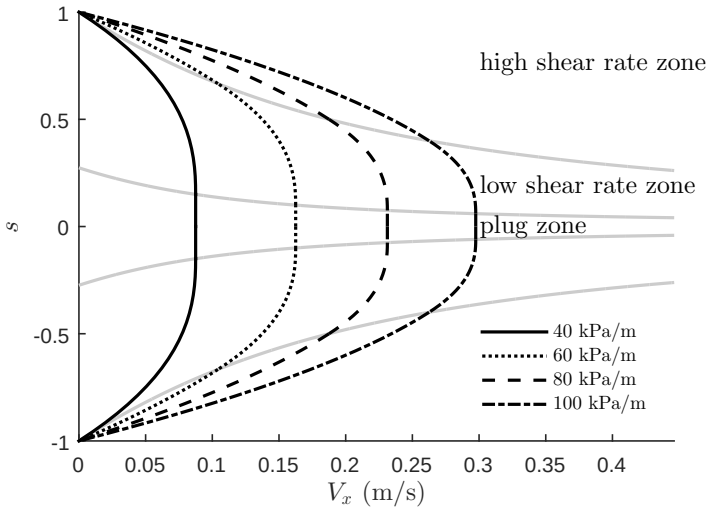

Figure 4: Variations of velocity profiles with respect to applied pressure gradients $\bar{p} =$ 40, 60, 80 and 100 kPa/m; interfaces between the plug flow zone, the low shear rate governed zone and the high shear rate governed zone are marked by solid grey lines; local fracture aperture is $2b = 0.5$ mm.

Fig. 4 shows the variation of the velocity profiles with respect to the applied pressure gradient $\bar{p} = 40,\ 60,\ 80$ and 100 kPa/m for the rheological parameters from fitting I in Table 1. As can be seen from Fig. 4, widths of both the plug flow zone and the low shear rate governed zone reduce as the pressure gradient $\bar{p}$ increases.

The local flow rate Q_x^s at a given pressure gradient $\bar{p}$ can be obtained by integrating the velocity across the fracture width,

$$Q_x^s = \begin{cases} 0 & 0 \le \bar{p} \le \tau_0/b, \\ Q_x^{s(\mathrm{I})}\left(\bar{p},\ b\right) & \tau_0/b < \bar{p} \le \tau_c/b, \\ Q_x^{s(\mathrm{II})}\left(\bar{p},\ b\right) & \bar{p} > \tau_c/b, \end{cases} \tag{12}$$

where

$$\begin{aligned} \frac{Q_x^{s(\mathrm{I})}}{2\dot{\gamma}_c b^2} = & \frac{\left(1 - \dfrac{s_1 + n_1 s_1^2}{n_1 + 1}\right)}{2 + \frac{1}{n_1}} \left(\frac{1 - s_1}{s_2 - s_1}\right)^{\frac{1}{n_1}} \\ \frac{Q_x^{s(\mathrm{II})}}{2\dot{\gamma}_c b^2} = & \frac{s_2^{-\frac{1}{n_2}}}{2 + \frac{1}{n_2}} + \left(\frac{1}{2 + \frac{1}{n_1}} - \frac{1}{2 + \frac{1}{n_2}}\right) s_2^2 \\ & + \left(\frac{1}{2 + \frac{1}{n_1}} - \frac{1}{1 + \frac{1}{n_1}}\right) s_1^2 + \left(\frac{1}{1 + \frac{1}{n_1}} - \frac{2}{2 + \frac{1}{n_1}}\right) s_1 s_2 \end{aligned} \tag{13}$$

The pressure gradient and the local flow rate relationships for the rheological parameters from fitting I & II are shown in Fig. 5. The result indicates that the flow rate is zero before

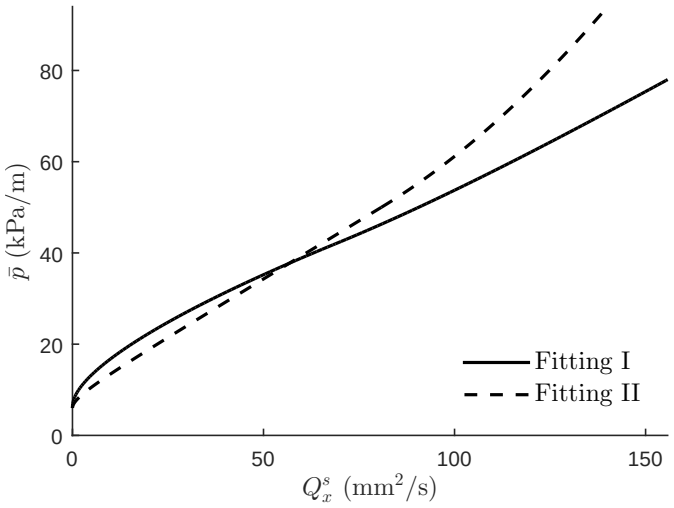

Figure 5: Variations of the pressure gradient with respect to the local flow rate; local fracture aperture is $2b = 0.5$ mm.

the yield stress is overcome by the pressure gradient along the flow direction.

The radial flow rate q_r (notation used to differentiate from the constant flow case) can be obtained by rewriting Eq. (12) using the fracture width w and the pressure gradient $\bar{p}$,

$$q_r = \begin{cases} 0 & 0 \le \bar{p} \le 2\tau_0/w \\ \dfrac{2\dot{\gamma}_c}{2+\frac{1}{n_1}}\left(\dfrac{w}{2}\right)^2 \left(\dfrac{\frac{\bar{p}w}{2\tau_0}-1}{\frac{\tau_c}{\tau_0}-1}\right)^{\frac{1}{n_1}} \left(1-\dfrac{\frac{2\tau_0}{\bar{p}w}+n_1\left(\frac{2\tau_0}{\bar{p}w}\right)^2}{n_1+1}\right) & 2\tau_0/w < \bar{p} \le 2\tau_c/w \\ 2\dot{\gamma}_c \left[\dfrac{\left(\frac{2\tau_c}{\bar{p}w}\right)^{-\frac{1}{n_2}}\left(\frac{w}{2}\right)^2}{2+\frac{1}{n_2}} + \left(\dfrac{1}{2+\frac{1}{n_1}}-\dfrac{1}{2+\frac{1}{n_2}}\right)\left(\dfrac{\tau_c}{\bar{p}}\right)^2 \right. & \bar{p} > 2\tau_c/w \\ \left. + \left(\dfrac{1}{2+\frac{1}{n_1}}-\dfrac{1}{1+\frac{1}{n_1}}\right)\left(\dfrac{\tau_0}{\bar{p}}\right)^2 + \left(\dfrac{1}{1+\frac{1}{n_1}}-\dfrac{2}{2+\frac{1}{n_1}}\right)\left(\dfrac{\tau_0}{\bar{p}}\right)\left(\dfrac{\tau_c}{\bar{p}}\right)\right] & \end{cases} \tag{14}$$

2.2.3 Fracture Deformation

The elastic response of the rock is assumed to be local, namely, deformation of the natural fracture at a given position depends on the local net pressure only, but not on the pressure everywhere else inside the fracture, i.e.,

$$w = w_0 + \frac{p}{K_n} \tag{15}$$

Eq. (15) implies that the fracture width w is related to the initial fracture width w_0, the net pressure p and the normal fracture stiffness K_n. The initial fracture width w_0 corresponds to the fracture aperture at zero net pressure. The local elasticity assumption relieves us of solving the integral form pressure-width relation required in other hydraulic fracture geometry models such as the Khristianovic-Geertsma-de Klerk (KGD) geometry model [57][32] and the penny-shaped fracture models [1]. Such an assumption is reasonable when the overbalance pressure is relatively small [61].

2.2.4 Local Fluid Mass Conservation

Local mass balance for one-dimensional lubrication flow can be written as,

$$\frac{1}{r}\frac{\partial\left(rq_r\right)}{\partial r}+\frac{\partial w}{\partial t}+u=0 \tag{16}$$

where q_r is the radial flow rate; t is the elapsed time from the onset of drilling mud invasion; and u is the fluid leakoff velocity accounting for both sides of the fracture faces. For a relatively low permeability formation, the fluid leakoff velocity may be approximated by the Carter's leak off model [13],

$$u=\frac{2C_L}{\sqrt{t-t_a\left(r\right)}} \tag{17}$$

where constant C_L is the leak off coefficient and $t_a\left(r\right)$ is the arrival time of the mud invasion front at radius r.

2.2.5 Boundary and Initial Conditions

To complete the formulation, boundary conditions both at the wellbore and at the mud invasion front need to be supplied. We may assume that the wellbore overpressure P_{in} is constant. Both the initial reservoir pore pressure and the reservoir stress are constant as well, which serve only as references.

$$\begin{aligned} &p=P_{\text{in}} \quad \text{at } r=r_{\text{in}} \qquad p=0 \text{ at } r=r_f \\ &w=w_0 \quad \text{at } r=r_f \end{aligned} \tag{18}$$

2.3 Numerical Implementation

The system of governing equations, Eqs. (15)-(18), is first transformed by introducing a moving coordinate system $\theta = (r - r_{\text{in}}) / (r_f - r_{\text{in}})$, $\theta \in [0, 1]$. The forgoing system of five equations contains five unknowns: $p(\theta, t)$, $q_r(\theta, t)$, $w(\theta, t)$, $r_f(t)$ and $u(\theta, t)$, which defines a complete system of solution. Such a system of equations can be solved by using an explicit finite-difference scheme proposed by Detournay *et al.* [22]. The line $0 \leq \theta \leq 1$ is discretized into N nodes to calculate $p(\theta, t)$, $w(\theta, t)$, and $u(\theta, t)$ with the first and last nodes corresponding to the fracture inlet and the tip. Flow rate $q_r(\theta, t)$ is evaluated at a system of $(N - 1)$ mid-nodes.

To choose the critical time step, the linearized form of the flow equation, Eq. (14), is combined with the continuity equation to form a "diffusion-type" of equation as follows,

$$\dot{w} = \frac{\theta \dot{r}_f}{r_f - r_{\text{in}}} \frac{\partial w}{\partial \theta} + c_w \frac{\partial^2 w}{\partial \theta^2} + c_s \left(\frac{\partial w}{\partial \theta} \right)^2 \tag{19}$$

where $\dot{(\,)} = d(\,)/dt$ is the material time derivative and c_w and c_s are functions of the material parameters, the fracture width w and the pressure gradient $\partial p / \partial \theta$. For brevity, expressions for c_w and c_s are omitted here. At a given time step, say, $t = t_{k+1}$, the critical time step to ensure numerical stability is chosen based on the criterion for numerical stability for a "diffusion-type" of equation for width w (Eq. 19),

$$\Delta t_c^{k+1} = \min \left[\frac{(\Delta \theta_i)^2}{2 (c_w)_i^k} \right]; \qquad i = 1, \cdots, N - 1 \tag{20}$$

Here the nodal number is denoted by the subscript i and the time step is denoted by the superscript k for simplicity, e.g., $(c_w)_i^k = c_w \left(\theta_i, t^k \right)$.

Since the numerical scheme is explicit, an initial guess is required to start the calculation. At early time, the process is expected to be governed by the high shear rate rheology. Power law parameters from the high shear rate rheology are therefore used as the input parameters for the initial guess solution. For the radial flow with a power law fluid, the flow rate is related to the pressure gradient through,

$$q_r = \frac{\dot{\gamma}_c w^2}{2 \left(2 + \frac{1}{n_2} \right)} \left(\frac{\bar{p} w}{2 \tau_c} \right)^{\frac{1}{n_2}} \tag{21}$$

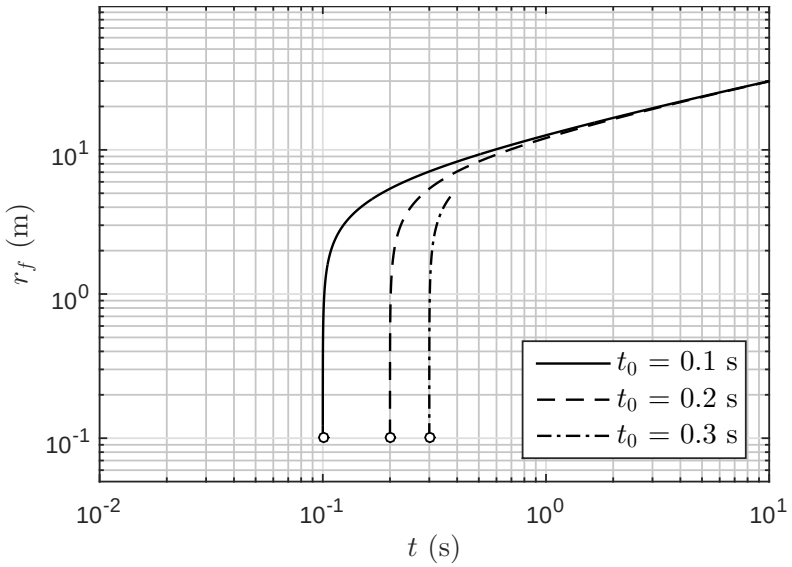

Figure 6: Effect of the initial guess for the radial fracture model - evolution of the mud invasion radius at small time with case I, $P_{\text{in}} = 10$ MPa with impermeable fracture walls.

Neglecting the leak off term and the rate of deformation of the fracture walls in Eq. 19 for early time and utilizing the boundary conditions at the wellbore, we can construct an initial guess for the fracture width, $w_0(r)$,

$$w_0(r) = w_{\text{in}} \left(\frac{r^{1-n_2} - r_f^{1-n_2}}{r_{\text{in}}^{1-n_2} - r_f^{1-n_2}} \right)^{\frac{1}{2n_2+2}} \tag{22}$$

where w_{in} is the fracture width at the wellbore. The initial rate of fluid front extension can be approximated by,

$$\dot{r}_{f0} = \frac{r_f - r_{\text{in}}}{t_0} \tag{23}$$

where t_0 is an arbitrarily small starting time. Effect of the initial guess on the mud invasion is shown in Fig. 6. Given the initial guesses obtained at $t_0 = 0.1,\ 0.2$ and 0.3 s for the rheological parameters from fitting I and with $P_{\text{in}} = 10$ MPa and $C_L = 6.3 \times 10^{-3}$ m/s$^{1/2}$, the differences resulted from the initial guess becomes largely negligible as $t > 2$ s. Fig. 6 suggest that the numerical scheme is not sensitive to the initial guesses given at different starting times.

Table 2: Fitting parameters for the rheology of drilling muds I and II.

	n_1	n_2	τ_0 (Pa)	τ_c (Pa)	$\dot{\gamma}_c$ (1/s)
I	0.7	1	3	20	500
I(b)	0.7	1	15	20	500
I(c)	0.7	1	15	50	500
II	1	1.9	3	25	560
II(b)	1	1.3	3	25	560
II(c)	1	1	3	25	560
II(d)	1	0.7	3	25	560

Table 3: Input parameters for the simulation cases.

Rock	Fracture stiffness, K_n	50 GPa/m
	Leak off coefficient, C_L	0, 5×10^{-3}, $5{\times}10^{-5}$ $5{\times}10^{-8}$ m/s$^{1/2}$
	Initial width, w_0	0.1, 0.2 mm
Wellbore	Overbalance pressure at inlet, P_{in}	1, 5, 10, 20, 50 MPa
	Wellbore radius, r_{in}	0.1 m

2.4 Numerical Results

Effects of rheological parameters on the drilling mud loss behaviors are investigated using the set of input parameters as listed in Table 2. Effects of the high shear rate rheology are examined by varying the power law index n_2. Other input parameters for the rock properties and the wellbore conditions are given in Table 3. These parameters are reasonable approximations of the realistic field conditions.

2.4.1 Evolution of the Fracture Width

Evolution of the fracture profile with respect to time for the radial fracture model can be seen in Fig. 7 with the rheological parameters from case I, $w_0 = 0$ mm, $P_{\text{in}} = 1$ MPa and $C_L = 5 \times 10^{-5}$ m/s$^{1/2}$. With the net pressure prescribed at fracture inlet, the fracture width at the inlet remains constant as the fracture propagates. Meanwhile, at a given location, the gradient of the fracture width, and thus the pressure gradient, decreases with time.

2.4.2 Effect of the Initial Width

In this model, the initial width of the natural fracture can be taken into account through Eq. 15. Fig. 8 shows the profiles of fracture width at $t = 10$ hours. The fracture width at the inlet is related solely to intial opening, the overbalance pressure at inlet and the fracture

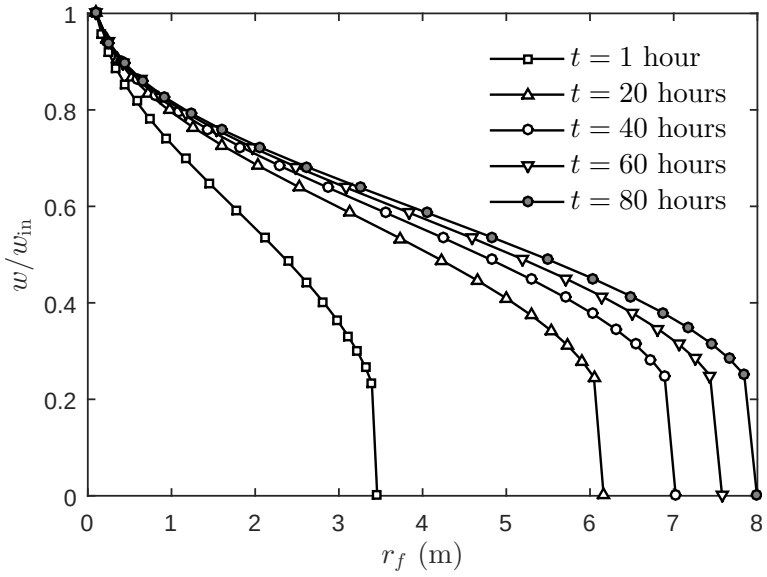

Figure 7: Evolution of fracture width with time for case I, $w_0 = 0$ mm, $P_{\rm in} = 10$ MPa and $C_L = 5 \times 10^{-5}$ m/s$^{1/2}$.

compliance. Given the same time, wider natural fractures yield longer invasion length. For that reason, mud invasion is more severe in formations with initially open natural fractures.

2.4.3 Effect of the Overbalance Pressure

Variations of the fracture length or the mud invasion radius with time for overpressure $P_{\rm in} = 1,\ 5,\ 10,\ 20,$ and 50 MPa, $C_L = 0$ m/s$^{1/2}$ and rheological parameters in cases I are compared in Fig. 9. The wellbore overbalance pressure plays a critical role in determining the mud invasion radius. For a smaller overbalance pressure, the mud invasion radius reaches a plateau earlier, which means the natural fracture is sealed faster.

2.4.4 Effects of the Yield Stress and the Critical Stress

Fig. 10 shows the variations of the mud invasion radius with time for overpressure $P_{\rm in} = 1$ and 10 MPa, $C_L = 0$ m/s$^{1/2}$, $w_0 = 0$ mm and rheological parameters in cases, I, I(b) and I(c). For the same overbalance pressure, the discrepancy in the invasion radius between cases I and I(b) can be attributed to the yield stress. A larger yield stress can stop the mud invasion faster. It should be noted that the yield stress has barely any influence on the mud invasion radius before $t \sim 10^4$ s ($\sim$3 hours) for $P_{\rm in} = 10$ MPa and $t \sim 10^2$ s ($\sim$2 min) for $P_{\rm in} = 1$ MPa. Comparing cases I(b) and I(c), the critical stress is increased from

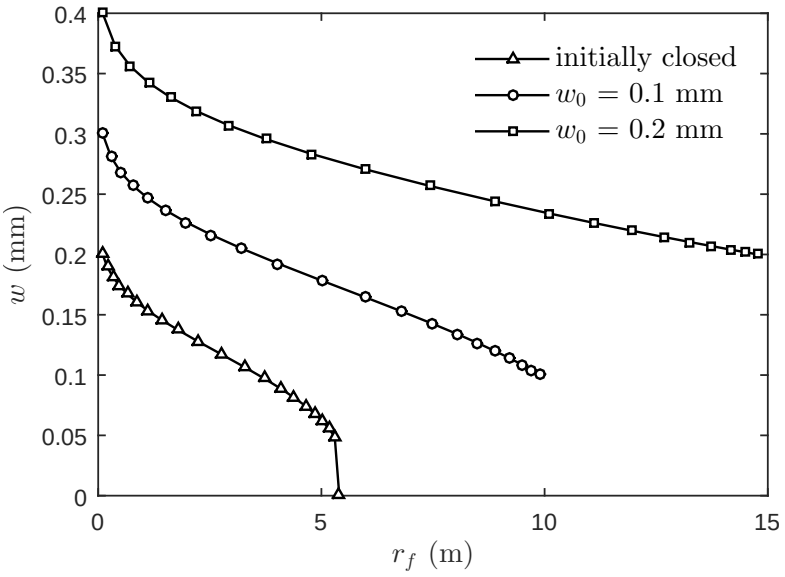

Figure 8: Effect of initial width for case I, $P_{\text{in}} = 10$ MPa and $C_L = 5 \times 10^{-5}$ m/s$^{1/2}$.

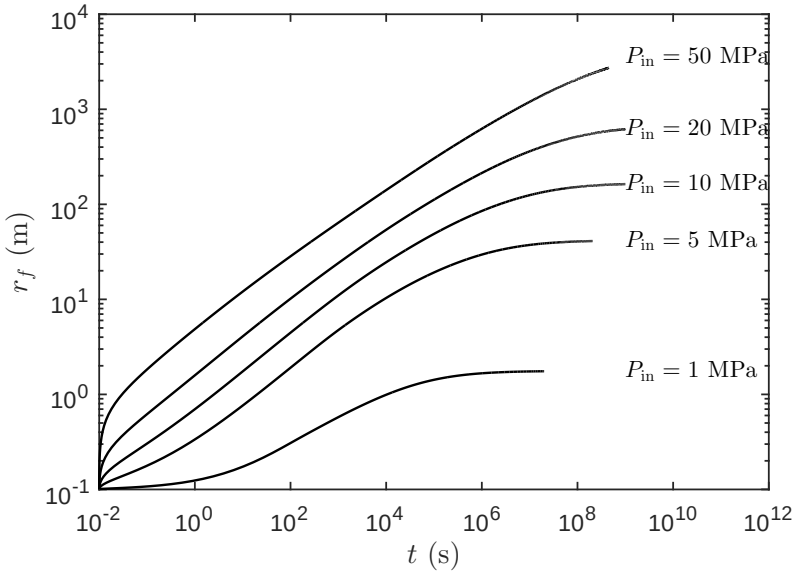

Figure 9: Mud invasion radius as a function of time with different overbalance pressures for case I, impermeable fracture walls.

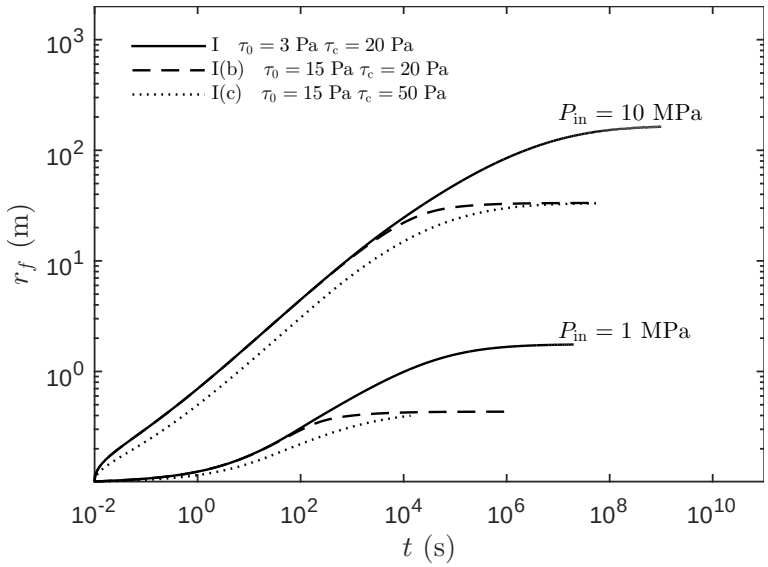

Figure 10: Mud invasion radius as a function of time with different overbalance pressure for case I, I(b), and I(c), $P_{\text{in}} = 1,\ 10$ MPa, impermeable fracture walls.

$\tau_c = 20$ Pa to 50 Pa and the invasion slows down at early time. But the differences in the invasion radius disappear at $t \sim 10^6$ s (∼11.6 days) for $P_{\text{in}} = 10$ MPa and $t \sim 10^5$ s (∼1 day) for $P_{\text{in}} = 1$ MPa. Here a higher critical stress τ_c translates to larger consistency indices K_1 and K_2. The apparent viscosity, $\eta' = \tau/\dot{\gamma}$, indeed has increased in all shear rate ranges. Therefore, it is not surprising that the mud invasion front is smaller when the critical shear stress τ_c is higher.

2.4.5 Effect of the Power Law Index for Shear Thickening

A series of simulations are conducted by varying the power index for the high shear rate behavior, $n_2 = 1.9,\ 1.3,\ 1,$ and 0.7, to investigate their influence on the invasion radius. Since fluid rheology in cases II and II(b-d) is only different in the power law index n_2, the discrepancy in the mud invasion radius at early time in Fig. 11 can be solely attributed to the effect of the power index n_2. The high shear rate power index does not affect the ultimate invasion radius, but it significantly affects the mud loss behavior at early time. Fig. 11 shows the influence of the high shear rate rheology lasts for $t \sim 10^5$ s (∼ 1 day), if the overpressure $P_{\text{in}} = 10$ MPa and the fracture walls are impermeable. Therefore, in the practice, the high shear rate rheology is a critical aspect for drilling mud engineering.

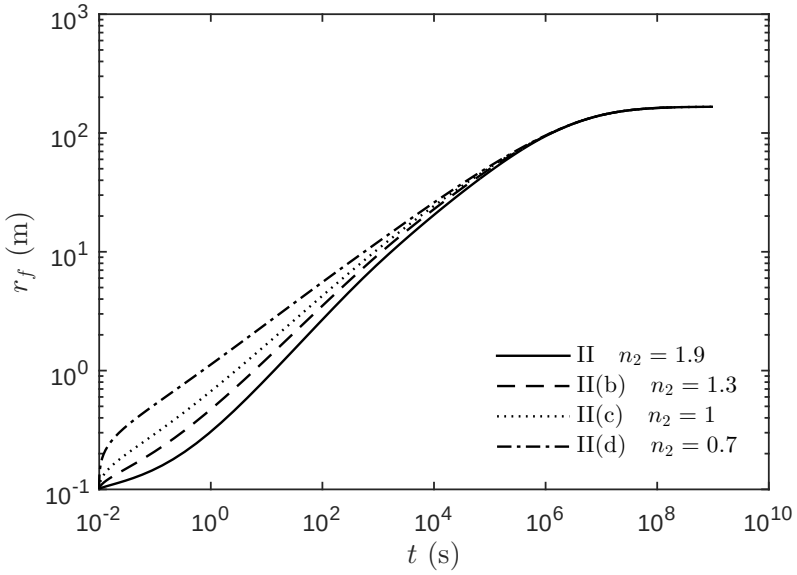

Figure 11: Mud invasion radius as a function of time for cases II, II(b-d), $P_{\text{in}} = 10$ MPa, impermeable fracture walls.

2.4.6 Effect of the Leak off Coefficient

A series of simulations are conducted by varying the leak off coefficient, $C_L = 0$, 5×10^{-3}, 5×10^{-5}, 5×10^{-8} m/s$^{1/2}$, to investigate their influence on the invasion radius.

Mud loss is either through leakoff from the fracture faces or inside the fracture. It should be noted that the leakoff coefficient has no effect on the ultimate invasion length, which is governed by the yield stress only. The leakoff coefficient, however, determines how fast the ultimate invasion radius is reached. As shown in Fig. 12, a small leakoff coefficient actually results in earlier termination of mud invasion.

2.5 Conclusions

In this work, a theoretical model is proposed to study drilling mud loss in a single natural fracture. The formulation is based on a radial fracture geometry model, assuming the fracture plane is perpendicular to the wellbore axis. A piecewise rheological model incorporating a yield stress and power laws for both the low shear rate and high shear rate is employed. The fracture could be closed or has an initial opening. The problem formulated is solved numerically using an explicit moving mesh algorithm. Effects of the overpressure, the initial fracture aperture, fluid rheology, in particular, the high shear rate rheology, and

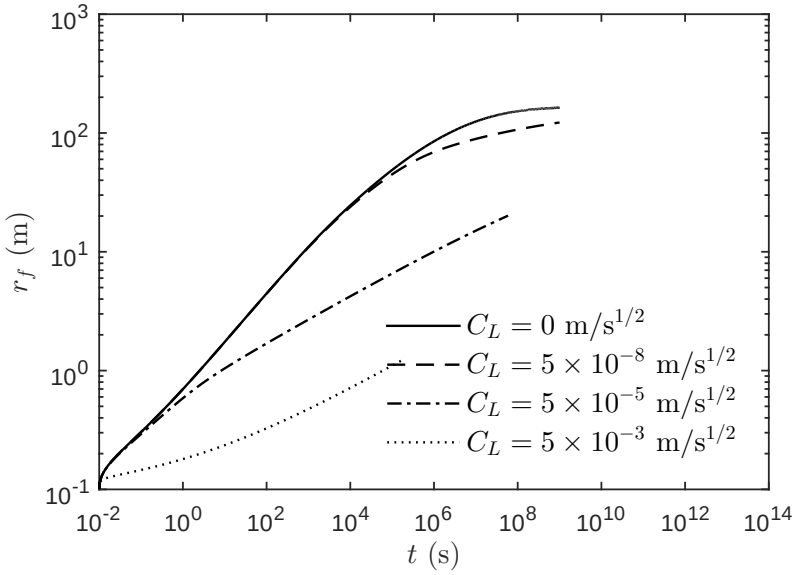

Figure 12: Mud invasion radius as a function of time with different leakoff coefficients for case I, $P_{\text{in}} = 10$ MPa.

the leakoff coefficient on the drilling mud loss behaviors are investigated.

The numerical analysis suggests that the high shear rheology is critical to control lost circulation since it takes effect at early time. The overbalance pressure and the yield stress of the fluid determines the ultimate invasion radius of the drilling mud at late time. The leakoff coefficient has no effects on the ultimate invasion radius, but it determines how fast the final invasion radius is approached. Numerical scheme outlined in this work provides a robust tool that allows not only systematic investigation of the effects of the formation and the fluid characteristics on the drilling mud loss, but also assessment for the improvement in the fluid design to control lost circulation.

CHAPTER III

THEORETICAL ANALYSIS OF DRILLING MUD INVASION INTO A NATURAL FRACTURE - A CONSTANT HEIGHT MODEL

3.1 Introduction

A theoretical model is formulated in this work to determine the drilling mud loss in a natural fracture intersected by a wellbore. We assume that the natural fracture is nearly parallel to the wellbore axis. The zone intersected by the wellbore is of constant height. The formulation is based on a PKN fracture geometry model [84, 80]. The drilling mud is treated as an incompressible and single-phase fluid. A piecewise rheological model incorporating a yield stress and power laws for both the low shear rate and high shear rate is employed. The reservoir formation is assumed to be permeable with the leakoff behavior following Carter's model [13]. Fluid flow along the fracture is assumed to be one-dimensional lubrication flow. Deformation of the fracture is governed by local elasticity. The borehole pressure and the pore pressure in the reservoir over the duration of the mud loss are assumed to be constant. The natural fracture could be initially closed or has a small opening. The problem defined above is solved numerically using an explicit moving mesh algorithm. Effects of the parameters such as the overbalance pressure, the yield stress and those for the high shear rate rheology on the drilling mud loss are evaluated.

Schematic of a PKN geometry model of length L and height H is shown in Fig. 13. Fluid flows along the $x-$direction only. The fracture is assumed to be fully bounded by the top and bottom layers and the cross section has a constant height and an elliptical shape.

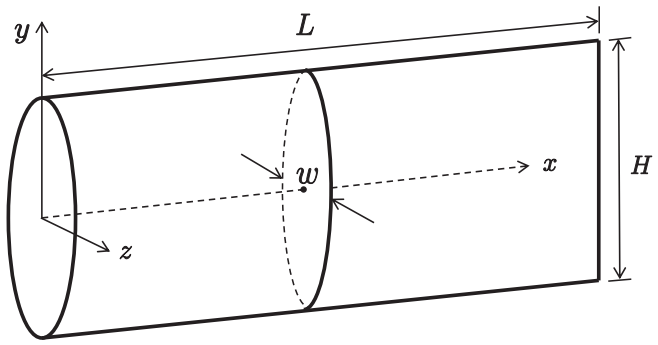

Figure 13: A PKN fracture of length L and height H; at a given cross section, the fracture width at the mid-height is denoted as w.

3.2 Mathematical Formulation

Fluid flow inside the fracture of a constant height is assumed to be one-dimensional, and lubrication theory can be applied. Therefore, field variables such as the net pressure p and the fracture width w therefore vary along the direction of propagation only. The net pressure p is the overpressure above the minimum *in-situ* stress that drives the drilling mud to flow inside the natural fracture. Poroelastic effect is considered to be negligible in this work. We aim to determine the fracture width $w\,(x,t)$ as a function of the position x and time t. The rheological model used in the PKN model is the same piecewise function as that proposed in Chapter II.

3.2.1 Balance of Fluid Momentum

The formulation of balance of fluid momentum starts with the Poiseuille slot flow solution for the piecewise fluid rheology, which has been given in Chapter II. Total flow rate Q_x^s is related to pressure gradient $\bar{p}$ and half width of the slot b,

$$Q_x^s = \begin{cases} 0 & 0 \le \bar{p} \le \tau_0/b, \\ Q_x^{s(\mathrm{I})}\,(\bar{p},\ b) & \tau_0/b < \bar{p} \le \tau_c/b, \\ Q_x^{s(\mathrm{II})}\,(\bar{p},\ b) & \bar{p} > \tau_c/b, \end{cases} \tag{24}$$

and

$$
\begin{aligned}
\frac{Q_x^{s(\mathrm{I})}}{2\dot{\gamma}_c b^2} &= \frac{\left(1-\dfrac{s_1+n_1 s_1^2}{n_1+1}\right)}{2+\frac{1}{n_1}}\left(\frac{1-s_1}{s_2-s_1}\right)^{\frac{1}{n_1}} \\
\frac{Q_x^{s(\mathrm{II})}}{2\dot{\gamma}_c b^2} &= \frac{s_2^{-\frac{1}{n_2}}}{2+\frac{1}{n_2}}+\left(\frac{1}{2+\frac{1}{n_1}}-\frac{1}{2+\frac{1}{n_2}}\right)s_2^2 \\
&\quad +\left(\frac{1}{2+\frac{1}{n_1}}-\frac{1}{1+\frac{1}{n_1}}\right)s_1^2+\left(\frac{1}{1+\frac{1}{n_1}}-\frac{2}{2+\frac{1}{n_1}}\right)s_1 s_2
\end{aligned}
\tag{25}
$$

where n_1 and n_2 are the power law indices, $\dot{\gamma}_c$ is the critical shear strain rate, s_1 and s_2 are scaled positions, $s_1 = \tau_0/\bar{p}b$, $s_2 = \tau_c/\bar{p}b$.

Next, we need to integrate the flow rate of the slot flow over the height of the fracture. However, the expression of $Q_x^{s(\mathrm{I})}$ in Eq. 25 is too complicated to obtain an analytic solution for the PKN model. We simplify the expression of $Q_x^{s(\mathrm{I})}$ in Eq. (25) by replacing $\left[(1-s_1)\,/\,(s_2-s_1)\right]^{1/n_1}$ with a linear approximation $1/s_2$,

$$
\frac{Q_{x(\text{approx.})}^{s(\mathrm{I})}}{2\dot{\gamma}_c b^2} = \frac{\left(1-\dfrac{s_1+n_1 s_1^2}{n_1+1}\right)}{2+\frac{1}{n_1}}\frac{1}{s_2} \tag{26}
$$

The error in the flow rate is evaluated by ϵ, which is defined as the ratio between the error and the flow rate at $\bar{p}b = \tau_c$, $\epsilon = \left[Q_{x(\text{approx.})}^{s(\mathrm{I})} - Q_x^{s(\mathrm{I})}\right]/Q_x^{s(\mathrm{I})}|_{\bar{p}b=\tau_c}$. This ratio is plotted as a function of pressure gradient and power index in Fig. 14. The error is relatively small, $|\epsilon| < 10\%$, for the chosen values of n_1, therefore the approximated expression can be used to solve for the PKN model.

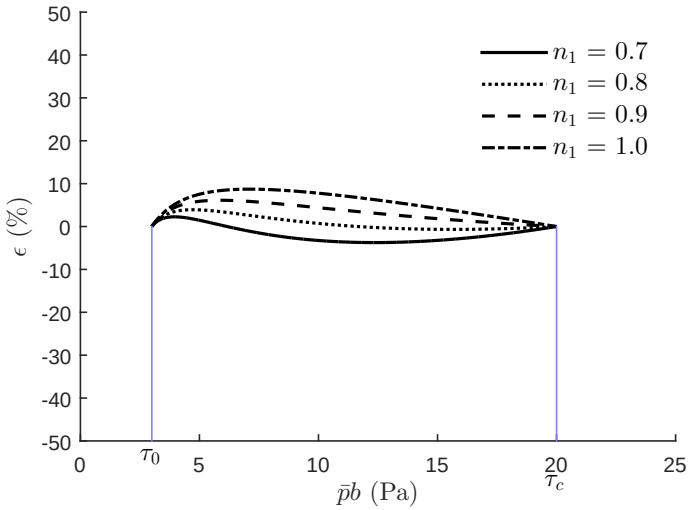

Figure 14: Error distribution for various n_1.

In the PKN fracture model, the cross-section can be divided into four types of zones according to the velocity profile of the fluid flow. The existence of the yield stress is manifested through the stagnation zones near the two ends of the fracture cross section, as shown in the gray areas in Fig. 15. The scaled height H_1 of the shear thickening zone and the scaled height H_2 of the moving fluid region can be determined from,

$$\frac{H_1}{H} = \sqrt{1 - \left(\frac{2\tau_c}{\bar{p}w}\right)^2}, \qquad \frac{H_2}{H} = \sqrt{1 - \left(\frac{2\tau_0}{\bar{p}w}\right)^2} \tag{27}$$

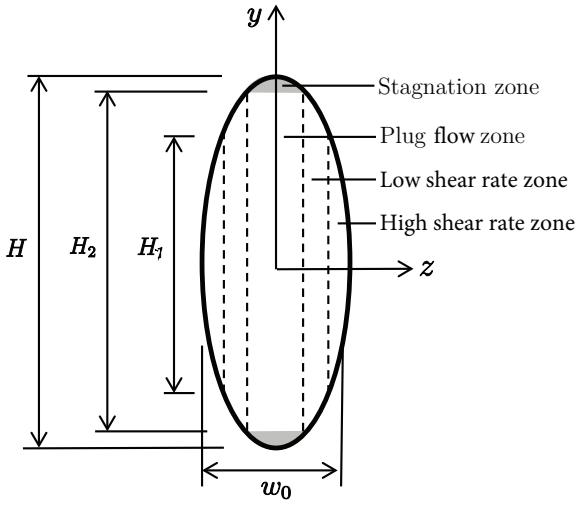

Figure 15: A PKN model cross section for the piecewise fluid.

At a given height position, the local flow rate Q_x can be obtained based on the approximated slot flow solution, Eq. (26),

$$\begin{aligned}
\frac{Q^{s(\mathrm{I})}_{x(\mathrm{approx.})}}{2\dot{\gamma}_c} = & \left(\frac{w_y}{2}\right)^2 \left(\frac{\bar{p}w_y}{2\tau_c}\right) \left(\frac{1}{2+\frac{1}{n_1}}\right) \left(1 - \frac{\frac{2\tau_0}{\bar{p}w_y} + n_1 \left(\frac{2\tau_0}{\bar{p}w_y}\right)^2}{n_1+1}\right) \\
\frac{Q^{s(\mathrm{II})}_x}{2\dot{\gamma}_c} = & \frac{\left(\frac{2\tau_c}{\bar{p}w_y}\right)^{-\frac{1}{n_2}} \left(\frac{w_y}{2}\right)^2}{2+\frac{1}{n_2}} + \left(\frac{1}{2+\frac{1}{n_1}} - \frac{1}{2+\frac{1}{n_2}}\right) \left(\frac{\tau_c}{\bar{p}}\right)^2 \\
& + \left(\frac{1}{2+\frac{1}{n_1}} - \frac{1}{1+\frac{1}{n_1}}\right) \left(\frac{\tau_0}{\bar{p}}\right)^2 + \left(\frac{1}{1+\frac{1}{n_1}} - \frac{2}{2+\frac{1}{n_1}}\right) \left(\frac{\tau_0}{\bar{p}}\right) \left(\frac{\tau_c}{\bar{p}}\right)
\end{aligned} \tag{28}$$

where w_y is the fracture width at a given height y, $w_y = w\sqrt{1-(2y/H)^2}$

The balance of momentum equation relating the total flow rate or the mud loss rate per unit height, q_x, to the local pressure gradient, $\bar{p}$, can be obtained by integrating Eq. (28) over the fracture height:

$$\begin{aligned}
q_x = & \frac{2}{H}\left(\int_0^{H_1/2} Q^{s(\mathrm{I})}_{x(\mathrm{approx.})} dy + \int_{H_1/2}^{H_2/2} Q^{s(\mathrm{II})}_x dy\right) \\
= & A_1 \left(\frac{w_0}{2}\right)^{2+\frac{1}{n_2}} \bar{p}^{\frac{1}{n_2}} + A_2 \bar{p}^{-2} \\
& + B_1 \left(\frac{w_0}{2}\right)^3 \bar{p} + B_2 \left(\frac{w_0}{2}\right)^2 + B_3 \left(\frac{w_0}{2}\right) \bar{p}^{-1}
\end{aligned} \tag{29}$$

and

$$\begin{aligned}
A_1 = & \frac{2\dot{\gamma}_c}{2+\frac{1}{n_2}} \tau_c^{-\frac{1}{n_2}} \frac{H_1}{H} \\
& \left({}_2F_1\left[\frac{1}{2}, -\frac{1}{2n_2}, \frac{3}{2}, \left(\frac{H_1}{H}\right)^2\right] - \frac{1}{3}\left(\frac{H_1}{H}\right)^2 {}_2F_1\left[\frac{3}{2}, -\frac{1}{2n_2}, \frac{5}{2}, \left(\frac{H_1}{H}\right)^2\right]\right) \\
A_2 = & 2\dot{\gamma}_c \tau_c^2 \frac{H_1}{H}\left[\frac{1}{2+\frac{1}{n_1}} - \frac{1}{2+\frac{1}{n_2}}\right. \\
& \left. + \left(\frac{1}{1+\frac{1}{n_1}} - \frac{2}{2+\frac{1}{n_1}}\right)\left(\frac{\tau_0}{\tau_c}\right)\right] + 2\dot{\gamma}_c \tau_0^2 \frac{H_2}{H}\left(\frac{1}{2+\frac{1}{n_1}} - \frac{1}{1+\frac{1}{n_1}}\right)
\end{aligned} \tag{30}$$

$$
\begin{aligned}
B_1 = \; & \frac{\dot{\gamma}_c}{\left(2+\frac{1}{n_1}\right)}\frac{1}{\tau_c}\left[\frac{1}{2}\left\{\sqrt{1-\left(\frac{H_2}{H}\right)^2}\left[\frac{5}{2}\frac{H_2}{H}-\left(\frac{H_2}{H}\right)^3\right]+\frac{3}{2}\arcsin\left(\frac{H_2}{H}\right)\right\}\right. \\
& \left.\frac{1}{2}\left\{\sqrt{1-\left(\frac{H_1}{H}\right)^2}\left[\frac{5}{2}\frac{H_1}{H}-\left(\frac{H_1}{H}\right)^3\right]+\frac{3}{2}\arcsin\left(\frac{H_1}{H}\right)\right\}\right] \\
B_2 = \; & 2\dot{\gamma}_c\left(\frac{\tau_0}{\tau_c}\right)\left(\frac{1}{1+\frac{1}{n_1}}-\frac{2}{2+\frac{1}{n_1}}\right)\left\{\left[\frac{H_2}{H}-\frac{1}{3}\left(\frac{H_2}{H}\right)^3\right]-\left[\frac{H_1}{H}-\frac{1}{3}\left(\frac{H_1}{H}\right)^3\right]\right\} \\
B_3 = \; & \dot{\gamma}_c\left(\frac{1}{1+\frac{1}{n_1}}-\frac{1}{2+\frac{1}{n_1}}\right)\left\{\left[\frac{H_2}{H}\sqrt{1-\left(\frac{H_2}{H}\right)^2}+\arcsin\left(\frac{H_2}{H}\right)\right]\right. \\
& \left.-\left[\frac{H_1}{H}\sqrt{1-\left(\frac{H_1}{H}\right)^2}+\arcsin\left(\frac{H_1}{H}\right)\right]\right\}
\end{aligned}
\tag{31}
$$

where ${}_2F_1[\,]$ denotes the hypergeometric function.

If $\tau_0 \leq \tau_w < \tau_c$, the shear thickening zone is not existent in the cross section , and therefore $H_1 \to 0$.

3.2.2 Fracture Deformation

We assume that opening of the natural fracture, w, can be related to the initial fracture width w_0, the local overpressure, p, and a fracture stiffness, K_n, i.e.,

$$
w = w_0 + \frac{p}{K_n} \tag{32}
$$

Local elasticity as assumed in Eq. 32 is reasonable when the fracture length is much larger than the height [33].

3.2.3 Local Fluid Mass Conservation

For an incompressible fluid, the local continuity equation can be written as,

$$
\frac{\partial q_x}{\partial x} + \frac{\partial w}{\partial t} + u = 0 \tag{33}
$$

in which q_x is the flow rate per unit height of a cross section, t is the elapsed time from the onset of drilling mud invasion, and u is the fluid leakoff velocity accounting for both sides of the fracture faces. For a relatively low permeability formation, fluid leakoff may be assumed to be one-dimensional obeying Carter's leakoff model [13]. The leakoff velocity u depends on the time of exposure at a given position, i.e.,

$$u = \frac{2C_L}{\sqrt{t - t_a(x)}} \tag{34}$$

where the constant C_L is the leakoff coefficient, $t_a(x)$ is the arrival time of the mud invasion front at location x.

3.2.4 Boundary Conditions

To complete the formulation, boundary conditions both at the inlet and at the invasion front need to be supplied. We may assume that the wellbore overpressure P_{in} is constant,

$$\begin{aligned} &p = P_{\text{in}} \quad \text{at } x = 0 \qquad p = 0 \text{ at } x = L \\ &w = w_0 \quad \text{at } x = L \end{aligned} \tag{35}$$

3.3 Numerical Implementation

An explicit finite difference scheme modified from [22] is employed in this work. The numerical scheme is constructed using a moving coordinate, θ,

$$\theta = \frac{x}{L(t)} \qquad \theta \in [0, 1] \tag{36}$$

The fracture is discretizing into N nodes along the length. In the time-marching algorithm, after all the nodal quantities in the previous time step are determined, a critical time step is first chosen. The fracture width w, the net fluid pressure p inside the fracture, the flow rate q_x, the leakoff velocity u, and the mud invasion length L, are then computed sequentially.

The equation for determining the fracture aperture is obtained from the system of governing equations Eqs. (32)-(35),

$$\dot{w} = \frac{\theta \dot{L}}{L}\frac{\partial w}{\partial \theta} + c_w \frac{\partial^2 w}{\partial \theta^2} + c_s \left(\frac{\partial w}{\partial \theta}\right)^2 \tag{37}$$

where $\dot{(\,)} = d(\,)/dt$ is the material time derivative and c_w and c_s are functions of the material parameters, the fracture width w and the pressure gradient $\partial p/\partial \theta$. For brevity, expressions for c_w and c_s are omitted here. At a given time step, say, $t = t^{k+1}$, the critical

time step is chosen based on the criterion for numerical stability for a "diffusion-type" of equation for width w (Eq. 37),

$$\Delta t_c^{k+1} = \min\left[\frac{(\Delta\theta_i)^2}{2\,(c_w)_i^k}\right]; \qquad i = 1, \cdots, N-1 \tag{38}$$

Here the nodal number is denoted by the subscript i and the time step is denoted by the superscript k for simplicity, e.g., $(c_w)_i^k = c_w\left(\theta_i, t^k\right)$.

Since the numerical scheme is explicit, an initial guess is required to start the calculation. The analytical solution for the PKN model in an impermeable formation with a power law fluid [79] is used as the initial guess for the fracture length, width and the flow rate at an arbitrarily small starting time. Effect of the initial guess on the mud invasion is shown in Fig. 16. Given the initial guesses obtained at $t_0 = 0.1,\ 0.2$ and 0.3 s for the rheological parameters from fitting I and with $P_{\text{in}} = 10$ MPa and $C_L = 6.3\times10^{-3}$ m/s$^{1/2}$, the differences resulted from the initial guess could be neglected as $t > 3$ s. Fig. 16 suggests that with the proper choice of the critical time step, the numerical scheme is robust and the solutions are not sensitive to the initial guesses.

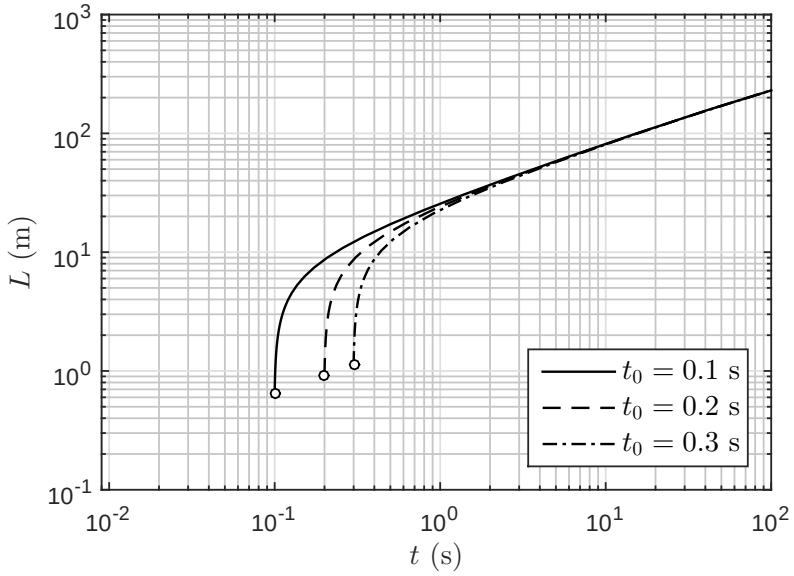

Figure 16: Effect of the initial guess for the PKN fracture model - evolution of the mud invasion length at small time for fitting I, $P_{\text{in}} = 10$ MPa with impermeable fracture walls.

3.4 Numerical Results

Effects of rheological parameters on the drilling mud loss behaviors are investigated using the set of input parameters as listed in Table 4. Effects of the high shear rate rheology are examined by varying the power law index n_2. Other input parameters for the rock properties and the wellbore conditions are given in Table 5. These parameters are similar to those for the radial model.

Table 4: Fitting parameters for the rheology of drilling muds I and II.

	n_1	n_2	τ_0 (Pa)	τ_c (Pa)	$\dot{\gamma}_c$ (1/s)
I	0.7	1	3	20	500
I(b)	0.7	1	15	20	500
I(c)	0.7	1	15	50	500
II	1	1.9	3	25	560
II(b)	1	1.3	3	25	560
II(c)	1	1	3	25	560
II(d)	1	0.7	3	25	560

Table 5: Input parameters for the simulation cases.

Rock	Fracture stiffness, K_n	50 GPa/m
	leakoff coefficient, C_L	0, 5×10^{-3}, $5{\times}10^{-5}$ $5{\times}10^{-8}$ m/s$^{1/2}$
	Bounding layer height, H	10 m
	Initial width, w_0	0.1, 0.2 mm
Wellbore	Overbalance pressure at inlet, P_{in}	1, 5, 10, 20, 50 MPa

3.4.1 Evolution of the Fracture Width

Fig. 17 shows evolution of the fracture profile with respect to time for the PKN fracture model with the rheological parameters from case I, $P_{\text{in}} = 1$ MPa and $C_L = 5 \times 10^{-5}$ m/s$^{1/2}$. The net pressure is constant at fracture inlet, therefore the fracture width at the inlet remains constant as the mud front advances. At a given location, the fracture width increases

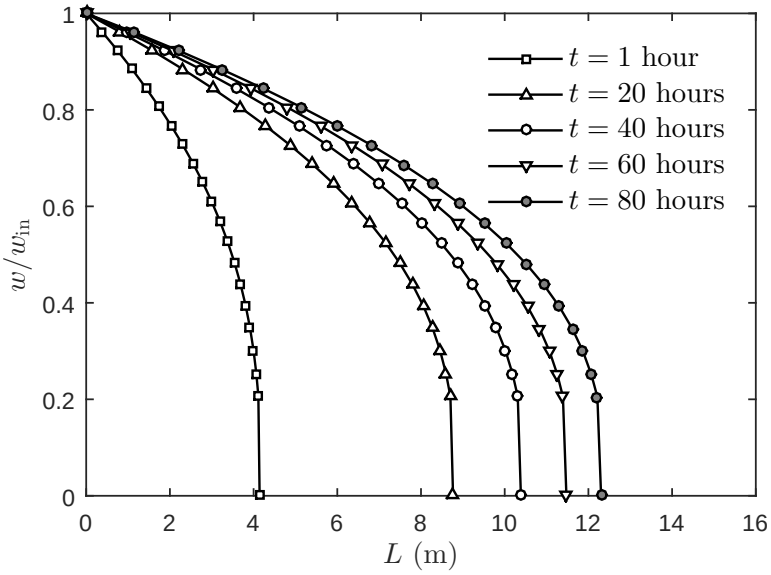

Figure 17: Evolution of fracture width with time for case I, $P_{\mathrm{in}} = 10$ MPa and $C_L = 5 \times 10^{-5}$ m/s$^{1/2}$.

with time, while the gradient of the fracture width, and thus the pressure gradient, decreases with time.

3.4.2 Effect of the Initial Width

Fig. 18 further illustrates the profiles of the fracture width by taking into account of an initial width. The fracture widths are plotted against the invasion length at $t = 10$ hours for three case with $P_{\mathrm{in}} = 10$ MPa, $C_L = 5 \times 10^{-5}$ m/s$^{1/2}$ and various initial widths. At the fracture inlet, the amount of elastic deformation due to fracture compliance is the same in all three cases, but the fractures with an initial width yield wider widths. The result agrees with that in the radial fracture: wider natural fractures lead to longer invasion length given the same amount of time.

3.4.3 Effect of the Overbalance Pressure

Variations of the mud invasion length with time for overpressure $P_{\mathrm{in}} = 1,\ 5,\ 10,\ 20,$ and 50 MPa and rheological parameters in case I are plotted in Fig. 19. Wellbore overbalance pressure is crucial in determining the mud invasion length. The invasion reaches a plateau eventually, indicating that the mud front is no longer propagating. The case with a smaller overbalance pressure not only yields a shorter ultimate invasion length but also reaches the

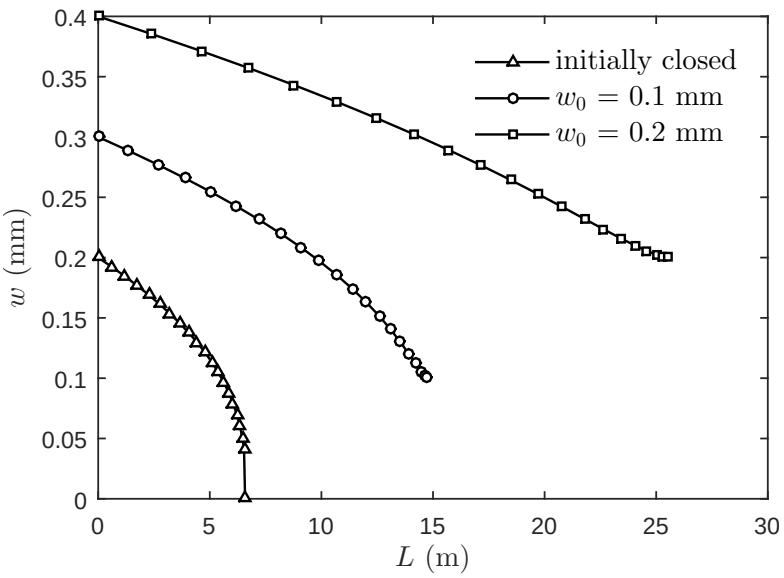

Figure 18: Effect of initial width for case I, $P_{\text{in}} = 10$ MPa and $C_L = 5 \times 10^{-5}$ m/s$^{1/2}$.

plateau earlier, which means the natural fracture is sealed faster.

3.4.4 Effect of the Yield Stress and the Critical Stress

A series of simulations are conducted by varying the yield stress, the critical stress and the inlet overpressure to investigate their influences on the mud invasion length. Fig. 20 shows the variations of the mud invasion length with time for overpressure $P_{\text{in}} = 1$ and 10 MPa and rheological parameters in cases, I, I(b) and I(c). Comparing case I(b) and I(c), the critical stress is increased from $\tau_c = 20$ Pa to 50 Pa and the invasion slows down at early time. However, the differences in the invasion length disappear at $t \sim 10^5$ s (∼1 day) for $P_{\text{in}} = 10$ MPa and $t \sim 10^4$ s (∼2.8 hours) for $P_{\text{in}} = 1$ MPa. For the same overbalance pressure, the solution of fluid I(b) coincides with that of fluid I at early time, but gradually deviates from the case I solution at late time. This means that fluid flow is governed by the high shear rate rheology at early time, but by the low shear rate rheology, namely, the yield stress, at late time. The yield stress starts to take effects on the mud invasion length at $t \sim 10^3$ s (∼17 min) for $P_{\text{in}} = 10$ MPa and $t \sim 10^2$ s (∼2 minutes) for $P_{\text{in}} = 1$ MPa, which are considerably earlier than those in the radial fracture model.

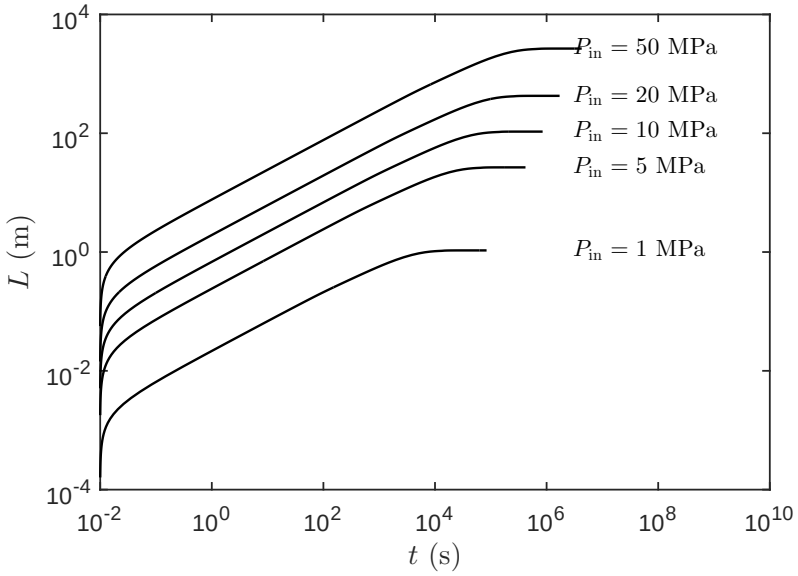

Figure 19: Mud invasion length as a function of time with different overbalance pressure for case I, impermeable fracture walls.

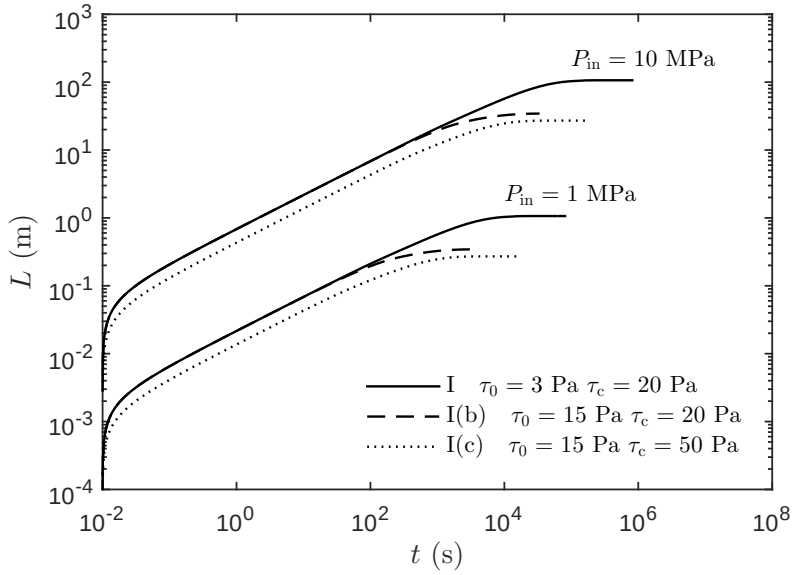

Figure 20: Mud invasion length as a function of time with different overbalance pressure for case I, I(b), and I(c), $P_{\text{in}} = 1,\ 10$ MPa, impermeable fracture walls.

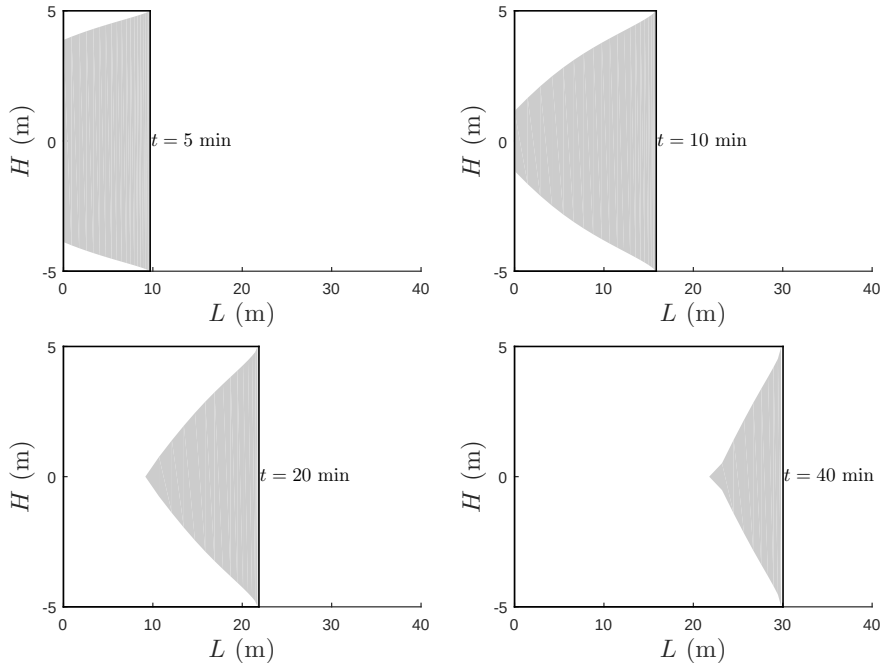

Figure 21: Evolution of height of shear thickening zone with time for case I, $P_{\text{in}} = 10$ MPa and $C_L = 0$ m/s$^{1/2}$.

3.4.5 Evolution of the Shear Thickening Zone

The position of the shear thickening zone, referred to as H_1 in Fig. 15, is plotted at different times in Fig. 21. The rectangle represents the shape of the fracture observing from the side. The shading area represents the position of shear thickening zone. It can be noted that the size of shear thickening zone is decreasing, and the shear thickening zone gradually disappears from the inlet to the mud front, which indicates that the drilling mud is subjected to large shear at early time and small shear at later time.

3.4.6 Evolution of the Stagnation Zone

Fig. 22 shows the zone of the moving fluid, which is characterized by height H_2. The shading area represents the stagnation zone, where the fluid is not moving. The eventual stop of mud invasion is due to the mud rheology: the stagnation zone forming in the fluid gradually occupies the entire cross section of the fracture when the pressure gradient drops below a certain threshold. Eventually, the mud invasion stops at a certain distance away from the borehole. It can be seen that the growth of stagnation zone is much slower than

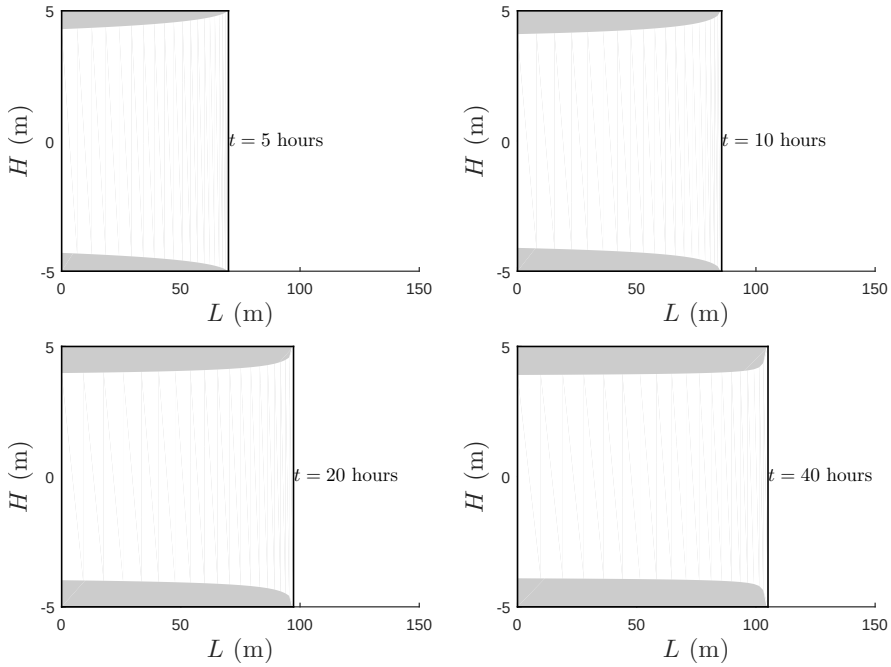

Figure 22: Evolution of height of moving fluid zone with time for case I, $P_{\text{in}} = 10$ MPa and $C_L = 0$ m/s$^{1/2}$.

that of the shear thickening zone in Fig. 21, since the stagnation is associated with the yield stress and the late time behavior.

3.4.7 Effect of the Power Index for the Shear Thickening Behavior

A series of simulations are conducted by varying the power index for the high shear rate behavior, $n_2 = 1.9,\ 1.3,\ 1,$ and 0.7, to further illustrate the effect of the high shear rate rheology upon mud loss. It can be seen in Fig. 23 that a greater shear thickening power index slows down the mud loss at early time, but it does not affect the ultimate invasion length. Fig. 23 shows the influence of the shear thickening behavior disappears after $t \sim 10^4$ s ($\sim$2.8 hours), if the overpressure $P_{\text{in}} = 10$ MPa and the fracture walls are impermeable.

3.4.8 Effect of the Leakoff Coefficient

A series of simulations are conducted by varying the leakoff coefficient, 0, 5×10^{-3}, 5×10^{-5}, 5×10^{-8} m/s$^{1/2}$, to investigate their influence on the invasion length. It can be noted that the leakoff coefficient has no effects on the ultimate invasion length, but it determines when the the ultimate invasion length is reached. For small leakoff coefficient, more fluid

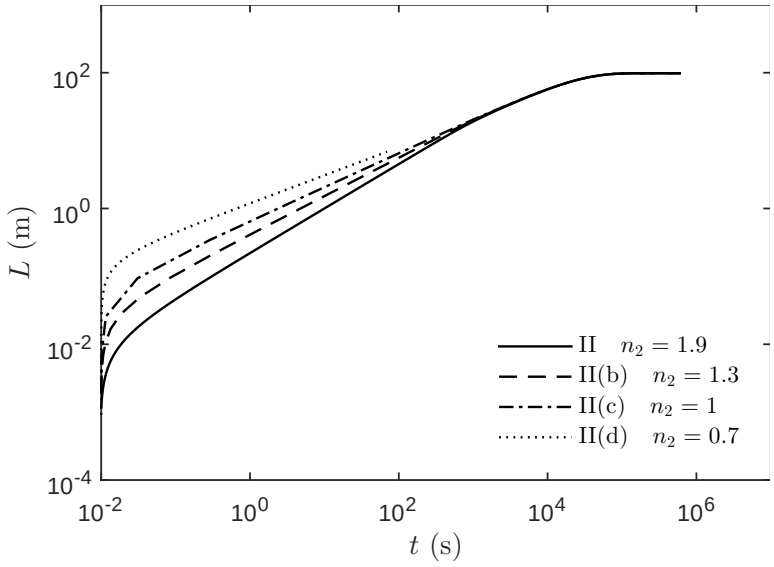

Figure 23: Mud invasion length as a function of time with different overbalance pressure for case II, II(b), II(c) and II(d), impermeable fracture walls.

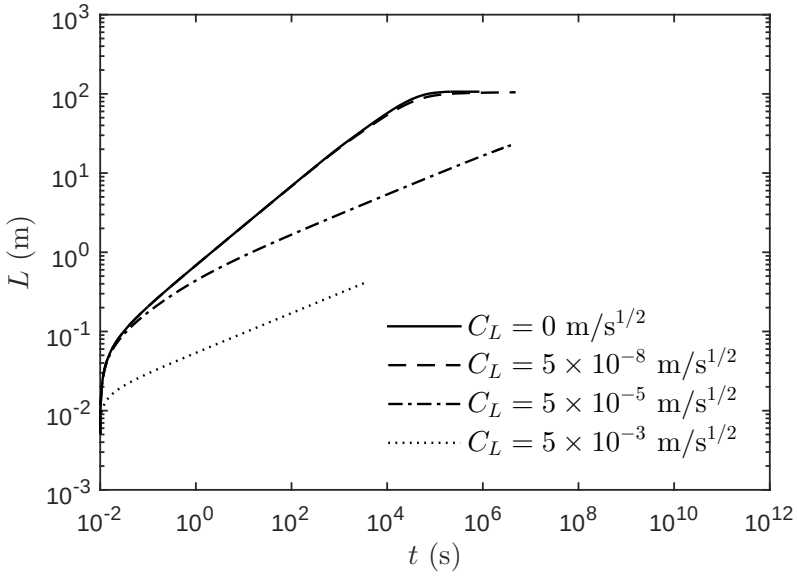

Figure 24: Mud invasion length as a function of time with different leakoff coefficients for case I, $P_{\text{in}} = 10$ MPa

is contained inside the fracture. Not surprisingly, as shown in both the radial model and the PKN model, a terminal mud invasion length is reached earlier with a smaller leakoff coefficient.

3.5 Conclusions

A drilling mud loss model based on the PKN fracture geometry model is formulated in this work to predict the transient mud loss behaviors in a natural fracture intersected by a wellbore. Qualitatively, effects of the formation characteristics, the overpressure and the fluid rheology on the mud loss behaviors are the same as those with a radial flow model. The numerical results support the arguments that the high shear rate rheology is the most critical aspect in controlling the mud loss at early time, while mud loss ultimately terminates if the local pressure gradient falls below the yield stress of the fluid.

CHAPTER IV

LIMIT EQUILIBRIUM ANALYSIS OF DRILLING MUD LOSS INTO AN INCLINED NATURAL FRACTURE

4.1 Introduction

Radial flow of a yield stress fluid between two parallel plates of a constant width has been extensively studied [65, 64, 44, 71, 72, 69, 100]. Extension of these models include linear [61, 62] and exponential [63] deformation laws of the fracture, roughness of the fracture wall [110, 81] and shut-in phase [63]. The main objective of these models is to predict the amount of circulation loss with various formation and fluid properties as well as operation conditions.

Limited studies were published for a natural fracture that intersects the borehole at an inclined angle, since modeling an arbitrarily orientated fracture can no longer be reduced to a mathematically one-dimensional problem due to the non-axisymmetric nature. Lavrov and Tronvoll [61] treated one-dimension linear flow along a fracture of finite length. The fracture could have a dip angle along the length direction. Sanfillippo *et al.* [90] assumed that the mud invasion profile for an inclined fracture is elliptical and can be translated into an equivalent radius in the diffusivity equation. Lavrov [60] conducted a numerical study of fluid flow from an arbitrarily-oriented compressible fracture into a sink. The dimensions of the rectangular fracture is assumed *a prior*.

In this work, we attempt to give an analytical solution for the ultimate invasion profile and consequently the mud loss volume in an inclined fracture without any prior geometrical assumptions. Even though the ultimate invasion profile may not be achieved during the life span of the drilling operation, it serves as a benchmark for the worst case scenario. The analysis is conducted based on limit equilibrium. The theoretical solutions for an arbitrarily oriented fracture and an incline wellbore are derived by considering: 1) the case of a circular wellbore trace when the wellbore and the fracture are perpendicular, i.e., when

the wellbore axis is perpendicular to both the dip and strike directions of the fracture; 2) the case of a colinear elliptical wellbore trace when the wellbore axis is only perpendicular to the strike direction of the fracture; and 3) the case of a rotated elliptical wellbore trace when the wellbore axis is no longer perpendicular to either the strike or the dip direction of the fracture. Parametric study is then carried out to show the effects of factors such as the yield stress and the fracture and wellbore orientations. The results are also compared with the numerical model for radial flow from Chapter II and with experimental data published in the literature. The solution is also used to approximate the fracture permeability from the mud loss data in the field. We also revisit the limit solution for radial flow of a yield stress fluid (Bingham or Herschel-Bulkley) within a horizontal fracture. It appears that the solution in the literature has an error in taking the limit at zero shear rate.

4.2 Model Description

The idealized problem of mud invasion into an arbitrarily oriented natural fracture with a hydraulic aperture w, intersected by an inclined wellbore of radius r_w, is shown in Figs. 25 and 26. Note that in Fig. 25 only the mid-plane of the fracture is shown for the sake of simplicity. A global Cartesian coordinate system $x_1x_2x_3$ is adopted to describe the geometrical configurations of the fracture and the wellbore, where origin O is located at the point of intersection between the wellbore axis and the fracture mid-plane. We choose x_3-axis to point upwards, opposite of the direction of gravity. $x_1-$and x_2-axes follow the right-hand-rule with x_1-axis pointing eastwards and x_2-axis northwards. Direction of the wellbore axis and the outward normal of the fracture mid-plane can be uniquely described by two unit vectors, $\mathbf{m}$ and $\mathbf{n}$. Denote the angles between x_3-axis and vectors $\mathbf{n}$ and $\mathbf{m}$ to be α and β, respectively (see Fig. 25). Angle α ($0 \leq \alpha \leq 90°$) is therefore the dip angle of the fracture plane, while angle β ($0 \leq \beta \leq 90°$) is the wellbore inclination angle.

A supplementary Cartesian coordinate system xyz is constructed also from origin O following the right-hand rule, with $x-$axis being on the fracture mid-plane and in the direction of the steepest descent, i.e., the direction of gravitational force component on the fracture plane (see Fig. 25), and $z-$axis in the direction of vector $\mathbf{n}$. Excluding the

cases when the natural fracture is either perpendicular to ($|\mathbf{n} \cdot \mathbf{m} = 1|$) or coplanar with ($\mathbf{n} \cdot \mathbf{m} = 0$) the wellbore axis, the intersection between the wellbore and the fracture mid-plane is an ellipse. Denote the angle between $x-$axis and the major axis of the ellipse to be γ. Note that the case when the fracture is perpendicular to the wellbore axis ($|\mathbf{n} \cdot \mathbf{m}| = 1$) can be treated as one of the special cases where $\gamma = 0°$, since the trace of the intersection is now a circle.

The drilling mud is assumed to be an incompressible single phase fluid with a yield stress and fluid flow occurs parallel to the fracture plane. In other words, the flow velocity in $z-$direction is assumed to be negligible. The invading mud and the preexisting fluid inside the fracture, if any, are immiscible, and the interface between the two fluids remain stable.

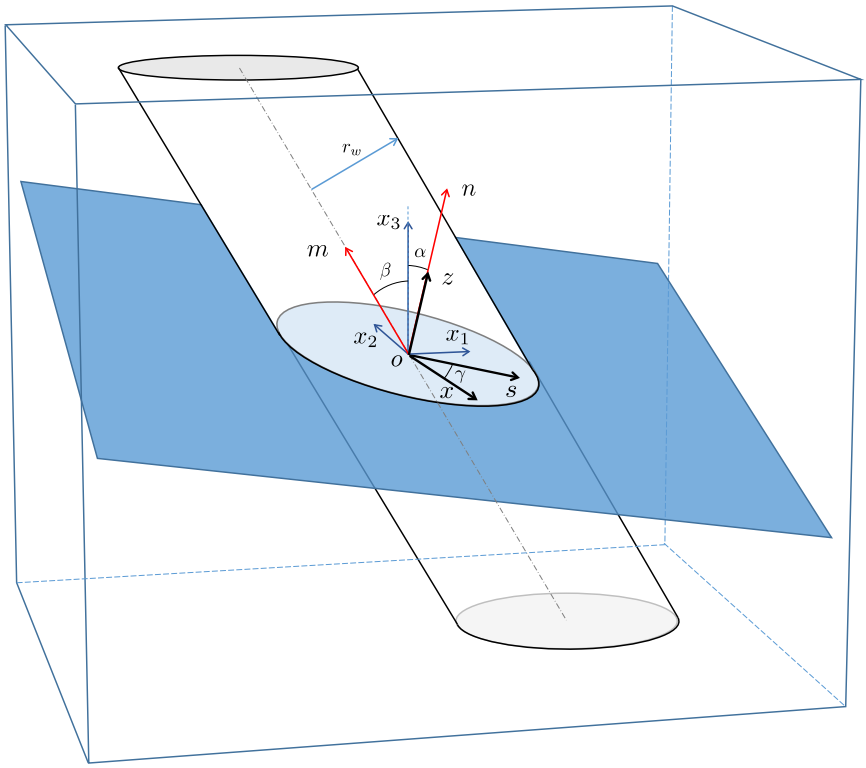

Figure 25: Schematic of an arbitrarily oriented natural fracture intersected by an inclined wellbore.

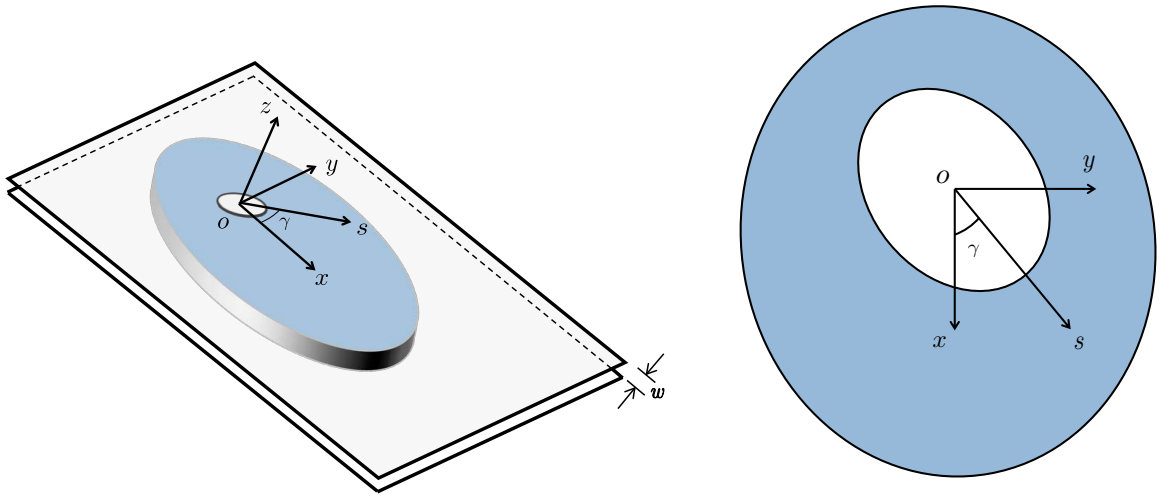

(a) (b)

Figure 26: Schematic of mud invasion from an inclined wellbore into an arbitrarily oriented natural fracture.

4.3 Case I - Circular Wellbore Trace

4.3.1 Mathematical Formulation

We start with the simplest case when the fracture is perpendicular to the wellbore axis ($|\mathbf{n} \cdot \mathbf{m}| = 1$), which leaves a circular wellbore trace on the fracture plane. When mud invasion ceases, impressibility of the fluid means that the entire fluid domain stops moving simultaneously and reaches static equilibrium. The stress components at any point inside in the mud, assuming tension positive, satisfy the equilibrium conditions,

$$\frac{\partial \sigma_x}{\partial x} + \frac{\partial \tau_{xy}}{\partial y} + \frac{\partial \tau_{xz}}{\partial z} + f_x = 0 \tag{39}$$

$$\frac{\partial \tau_{xy}}{\partial x} + \frac{\partial \sigma_y}{\partial y} + \frac{\partial \tau_{yz}}{\partial z} = 0 \tag{40}$$

$$\frac{\partial \tau_{xz}}{\partial x} + \frac{\partial \tau_{yz}}{\partial y} + \frac{\partial \sigma_z}{\partial z} + f_z = 0 \tag{41}$$

where f_x and f_z are the components of the body force per unit mass,

$$f_x = \rho g \sin \alpha \qquad f_z = \rho g \cos \alpha \tag{42}$$

where ρ is the mud density and g is the gravitational acceleration. We may assume that the equilibrium condition in $z-$direction, Eq. (41), is automatically satisfied, since we

approximate the mud flow to occur parallel to the $xy-$plane only. When the flow stops, variations of the shear stress on the fracture plane vanish, i.e,

$$\frac{\partial \tau_{xy}}{\partial x} = \frac{\partial \tau_{xy}}{\partial y} = 0 \tag{43}$$

Denote,

$$\sigma_x = \sigma_y = -p \tag{44}$$

where p is the net mud pressure, i.e., the overpressure above the initial fluid pressure inside the natural fracture. Eqs. 39-41 can be reduced to,

$$-\frac{\partial p}{\partial x} + \frac{\partial \tau_{xz}}{\partial z} + f_x = 0 \tag{45}$$

$$-\frac{\partial p}{\partial y} + \frac{\partial \tau_{yz}}{\partial z} = 0 \tag{46}$$

If the zone of interest is sufficiently deep and the hydraulic aperture w of the fracture is relatively small, we may assume that the net mud pressure is constant across the width, i.e., $\partial p/\partial z = 0$. Integrating the shear stresses over the width of the fracture, the wall shear stress is given by,

$$\tau_{xz}|_{z=\frac{w}{2}} = \int_0^{\frac{w}{2}} \left(\frac{\partial p}{\partial x} - f_x\right) \mathrm{d}z = \left(\frac{\partial p}{\partial x} - f_x\right) \frac{w}{2} \tag{47}$$

$$\tau_{yz}|_{z=\frac{w}{2}} = \int_0^{\frac{w}{2}} \left(\frac{\partial p}{\partial y}\right) \mathrm{d}z = \left(\frac{\partial p}{\partial y}\right) \frac{w}{2} \tag{48}$$

The wall shear stresses at $z = -w/2$ can be obtained by virtue of symmetry.

Resultant of these two shear stress components at the wall is balanced by the mud yield stress, τ_0, namely,

$$\left(\tau_{xz}|_{z=\frac{w}{2}}\right)^2 + \left(\tau_{yz}|_{z=\frac{w}{2}}\right)^2 = \tau_0^2 \tag{49}$$

Substituting Eq. (47)-(48) into Eq. (49) yields,

$$\left(\frac{\partial p}{\partial r} - f_x\right)^2 + \left(\frac{\partial p}{\partial y}\right)^2 = \left(\frac{2\tau_0}{w}\right)^2 \tag{50}$$

It is more convenient to solve Eq. (50) numerically in a cylindrical coordinate system, where $x = r\cos\theta$ and $y = r\sin\theta$. After applying the following chain rules,

$$\frac{\partial}{\partial x} = \cos\theta \frac{\partial}{\partial r} - \frac{1}{r}\sin\theta \frac{\partial}{\partial \theta} \tag{51}$$

$$\frac{\partial}{\partial y} = \sin\theta \frac{\partial}{\partial r} + \frac{1}{r}\cos\theta \frac{\partial}{\partial \theta} \tag{52}$$

Eq. (50) can be rewritten into,

$$\left(\frac{\partial p}{\partial x} - f_x \cos\theta\right)^2 + \left(\frac{1}{r}\frac{\partial p}{\partial \theta} + f_x \sin\theta\right)^2 = \left(\frac{2\tau_0}{w}\right)^2 \tag{53}$$

The following dimensionless parameters are introduced to facilitate the numerical calculation,

$$\widetilde{r} = \frac{r}{r_w} \quad \widetilde{p} = \frac{p}{P_{\text{in}}} \quad \widetilde{\tau}_0 = \frac{\tau_0 r_w}{P_{\text{in}} w} \quad \widetilde{f} = \frac{f_x r_w}{P_{\text{in}}} \tag{54}$$

Then Eq. (53) becomes

$$\Phi\left(\widetilde{r}, \theta, \widetilde{p}\right) = \left(\frac{\partial \widetilde{p}}{\partial \widetilde{r}} - \widetilde{f}\cos\theta\right)^2 + \left(\frac{1}{\widetilde{r}}\frac{\partial \widetilde{p}}{\partial \theta} + \widetilde{f}\sin\theta\right)^2 - \left(2\widetilde{\tau}_0\right)^2 = 0 \tag{55}$$

The normalized mud pressure $\widetilde{p}$ is in the range of $0 \le \widetilde{p} \le 1$ between the wellbore and the invasion front. In order to solve for the invasion profile, it is more convenient to write the partial derivatives in Eq. (55) with θ and $\widetilde{p}$ as variables. The objective of the formulation therefore reduces to solve for the coordinates $(\widetilde{r}, \theta)$ of the mud invasion front, where $\widetilde{p} = 0$ and $\Phi = 0$. Total derivative of function Φ can be expressed as,

$$d\Phi = \frac{\partial \Phi}{\partial \widetilde{p}} d\widetilde{p} + \frac{\partial \Phi}{\partial \widetilde{r}} d\widetilde{r} + \frac{\partial \Phi}{\partial \theta} d\theta \tag{56}$$

Partial derivative $\partial\widetilde{p}/\partial\theta$ is equivalent to $d\widetilde{p}/d\theta$, when $\widetilde{r}$ is held constant (i.e., $d\widetilde{r} = 0$). Since the equilibrium condition requires $\Phi = 0$, as a consistency condition, we also have $\Phi = 0$. Therefore,

$$\frac{\partial \widetilde{p}}{\partial \theta} = -\frac{\partial \Phi/\partial \theta}{\partial \Phi/\partial \widetilde{p}} \tag{57}$$

Similarly, we obtain,

$$\frac{\partial \widetilde{p}}{\partial \theta} = -\frac{\partial \Phi/\partial \theta}{\partial \Phi/\partial \widetilde{r}} \quad \text{and} \quad \frac{\partial \widetilde{r}}{\partial \widetilde{p}} = -\frac{\partial \Phi/\partial \widetilde{p}}{\partial \Phi/\partial \widetilde{r}} \tag{58}$$

It then follows,

$$\frac{\partial \widetilde{p}}{\partial \theta} = -\frac{\partial \widetilde{r}/\partial \theta}{\partial \widetilde{r}/\partial \widetilde{p}} \tag{59}$$

Based on the partial derivative rules derived above, $\Phi = 0$ can be rewritten into a quadratic equation of $\partial\widetilde{r}/\partial\widetilde{p}$,

$$\left(4\widetilde{\tau}_0^2 - \widetilde{f}^2\right)\left(\frac{\partial \widetilde{r}}{\partial \widetilde{p}}\right)^2 + 2\left(\widetilde{f}\cos\theta + \frac{1}{\widetilde{r}}\frac{\partial \widetilde{r}}{\partial \theta}\widetilde{f}\sin\theta\right)\frac{\partial \widetilde{r}}{\partial \widetilde{p}} - \left(\frac{1}{\widetilde{r}}\frac{\partial \widetilde{r}}{\partial \theta}\right)^2 - 1 = 0 \tag{60}$$

Applying the quadratic formula yields,

$$\frac{\partial \widetilde{r}}{\partial \widetilde{p}} = \frac{-\left(\widetilde{f}\cos\theta + \frac{1}{\widetilde{r}}\frac{\partial \widetilde{r}}{\partial \theta}\widetilde{f}\sin\theta\right) \pm \sqrt{\left(\widetilde{f}\cos\theta + \frac{1}{\widetilde{r}}\frac{\partial \widetilde{r}}{\partial \theta}\widetilde{f}\sin\theta\right)^2 + \left(4\widetilde{\tau}_0^2 - \widetilde{f}^2\right)\left[\left(\frac{1}{\widetilde{r}}\frac{\partial \widetilde{r}}{\partial \theta}\right)^2 + 1\right]}}{4\widetilde{\tau}_0^2 - \widetilde{f}^2} \tag{61}$$

Partial derivative $\partial\widetilde{r}/\partial\widetilde{p} \to \infty$, or, $4\widetilde{\tau}_0^2 - \widetilde{f}^2 = 0$, implies that flow of the mud will not stop at any position. Since $2\widetilde{\tau}_0$ represents the shear resistance from the walls while $\widetilde{f}$ corresponds to the driving mechanism resulted from gravity, for the mud to eventually stop flowing, the resistance must overcome the driving mechanism, i.e.,

$$2\widetilde{\tau}_0 - \widetilde{f} > 0 \tag{62}$$

Meanwhile, fluid pressure in the fracture always decreases with the radial distance, namely, $\partial\widetilde{r}/\partial\widetilde{p} < 0$. Consequently, the only admissible solution for Eq. (61) is,

$$\frac{\partial \widetilde{r}}{\partial \widetilde{p}} = \frac{-\left(\widetilde{f}\cos\theta + \frac{1}{\widetilde{r}}\frac{\partial \widetilde{r}}{\partial \theta}\widetilde{f}\sin\theta\right) - \sqrt{\left(\widetilde{f}\cos\theta + \frac{1}{\widetilde{r}}\frac{\partial \widetilde{r}}{\partial \theta}\widetilde{f}\sin\theta\right)^2 + \left(4\widetilde{\tau}_0^2 - \widetilde{f}^2\right)\left[\left(\frac{1}{\widetilde{r}}\frac{\partial \widetilde{r}}{\partial \theta}\right)^2 + 1\right]}}{4\widetilde{\tau}_0^2 - \widetilde{f}^2} \tag{63}$$

Formulation of the problem is complete if the boundary condition at the wellbore is supplied. We may assume that the wellbore overpressure P_{in} is constant and both the initial reservoir pore pressure and the reservoir stresses remain constant and serve only as references. The boundary condition at the wellbore can be expressed as,

$$\widetilde{p} = 1 \quad \text{at} \quad \widetilde{r} = 1 \tag{64}$$

Close-form solutions to Eq. (63) can be found for a particular case when $\gamma = 0°$, in other words, when the projection of the wellbore axis on the fracture plane is the same as the direction of the steepest descent. At $\theta = 0°$, by virtue of symmetry, $\cos\theta = 1$, $\sin\theta = 0$ and $\partial\widetilde{r}/\partial\theta$. Eq. (63) reduces to,

$$\frac{\partial \widetilde{r}}{\partial \widetilde{p}} = -\frac{1}{2\widetilde{\tau}_0 - \widetilde{f}} \quad \text{at} \quad \theta = 0° \tag{65}$$

Similarly,

$$\frac{\partial \widetilde{r}}{\partial \widetilde{p}} = -\frac{1}{2\widetilde{\tau}_0 + \widetilde{f}} \quad \text{at} \quad \theta = 180° \tag{66}$$

Theoretical solutions for radius $\widetilde{r}$ at $\theta = 0^\circ$ and 180° at a given $\widetilde{p}$ can be obtained from,

$$\widetilde{r} = \frac{1-\widetilde{p}}{2\widetilde{\tau}_0 - \widetilde{f}} \quad \text{at} \quad \theta = 0^\circ \tag{67}$$

$$\widetilde{r} = \frac{1-\widetilde{p}}{2\widetilde{\tau}_0 + \widetilde{f}} \quad \text{at} \quad \theta = 180^\circ \tag{68}$$

Eq. (63) can be solved numerically by using a finite difference scheme. We may discretize the fracture plane into a $N \times M$ mesh using N rays and M loops. The rays are of equal interval $\Delta\theta = 360^\circ/N$ and can be described by $\theta = \theta_1,\ \theta_2, ..., \theta_i, ..., \theta_N$, where $\theta_i = 360^\circ\,(i-1)\,/N$; the loops are the contour lines of the normalized overpressure $\widetilde{p}$ with an interval, $\Delta\widetilde{p} = 1/\,(M-1)$. Starting from the wellbore, the pressure at each loop is $\widetilde{p} = \widetilde{p}_1,\ \widetilde{p}_2,\ ...,\ \widetilde{p}_j,\ ...,\ \widetilde{p}_M$, where $\widetilde{p}_1 = 1$, $\widetilde{p}_M = 0$ and $\widetilde{p}_j = 1 - (j-1)\,/\,(M-1)$. Therefore, at a node $(i,\ j)$, where ith ray and jth loop intersect, θ_i and $\widetilde{p}_j$ are known; and the only unknown to be determined is the radial coordinate, $\widetilde{r}_{i,j}$, of the node. The partial derivatives in Eq. (63) can be replaced by finite differences according to

$$\left(\frac{\partial\widetilde{r}}{\partial\theta}\right)_{i,j} = \frac{\widetilde{r}_{i+1,j} - \widetilde{r}_{i-1,j}}{2\Delta\theta} \tag{69}$$

$$\left(\frac{\partial\widetilde{r}}{\partial\widetilde{p}}\right)_{i,j} = \frac{\widetilde{r}_{i,j+1} - \widetilde{r}_{i,j}}{\Delta\widetilde{p}} \tag{70}$$

The wellbore and the fracture geometry and orientation determine the first loop radial coordinates $\widetilde{r}_{i,1}$, which can be used to fully determine $\widetilde{r}_{i,2}$, after Eqs. (69) and (70) are substituted into Eq. (63). The algorithm can then march forward in the radial direction to find $\widetilde{r}_{i,j}$ based on $\widetilde{r}_{i,j-1}$ until the last loop $\widetilde{r}_{i,M}$, which is the mud invasion front profile corresponding to $\widetilde{p}_M = 0$.

4.3.2 Parametric Study

In this chapter, all the results are generated based on $M = N = 100$ using the set of input parameters listed in Table 6.

Table 6: Fluid properties, wellbore and fracture parameters

Fracture	Fracture width, w (mm)	1
Wellbore	Wellbore radius, r_w (mm)	100
	Overbalance pressure, P_{in}(kPa)	100
Fluid	Density, ρ $\left(\text{kg/m}^3\right)$	1800
	Yield stress, τ_0 (Pa)	10, 20, 30, 40
	Gravitational acceleration, g $\left(\text{m/s}^2\right)$	9.81

Effects of the natural fracture dip angle and the yield stress on the mud loss are first investigated. Fig. 27 (a) and (b) show loops of constant pressure with $\Delta\widetilde{p} = 0.1$ between two adjacent lines. Radial coordinates indicate the scaled radius. Red dot at the center represents the position of the wellbore. Black dots along the axis of symmetry mark the theoretical solution at $\theta = 0^\circ$ and 180°, which is consistent with the numerical solution. Fig. 27 (a) shows the invasion profile in a horizontal fracture. Since component of body force in the fracture plane is absent, the invasion profile is perfectly circular. Fig. 27 (b) shows the invasion into a fracture of a dip angle of 30°, $\alpha = 30^\circ$. The invasion has a a far endpoint at downstream and a close endpoint at upstream on the axis of symmetry, which are named the toe and the head, respectively.

To further study the effect of yield stress, invasion profiles into fractures with various yield stress are given in Fig. 28 . The mud invasion can be significantly reduced by a larger yield stress.

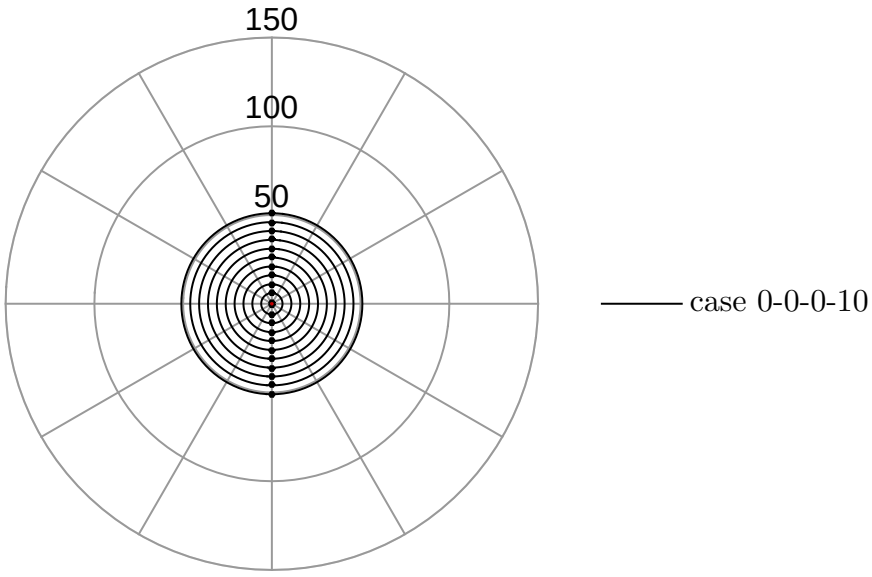

(a)

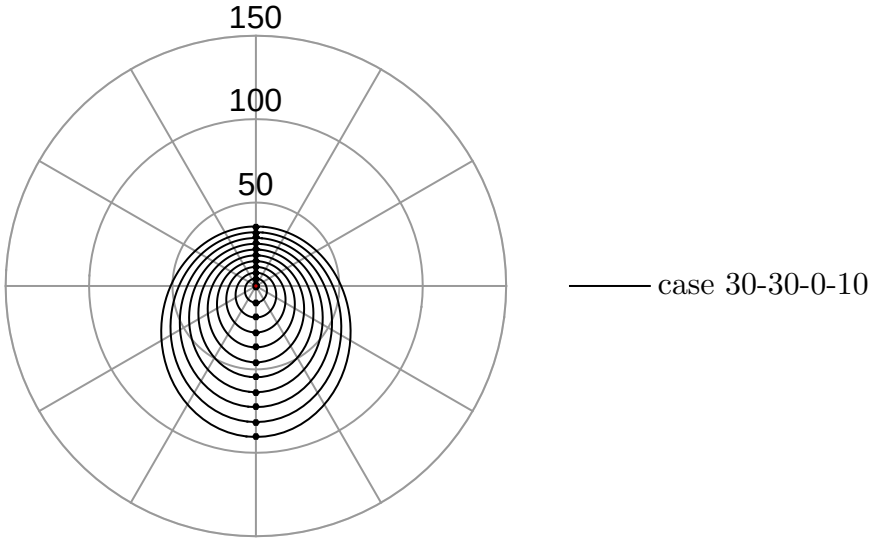

(b)

Figure 27: Mud invasion profiles with various fracture dip angle; the case numbers refer to fracture dip angle α in degrees, wellbore inclination angle β in degrees, angle between $x-$axis and the major axis γ in degrees, yield stress τ_0 in Pa; namely, case 30-30-0-10 is a test case with $\alpha = 30^\circ$, $\beta = 0^\circ$, $\gamma = 0^\circ$ and $\tau_0 = 10$ Pa.

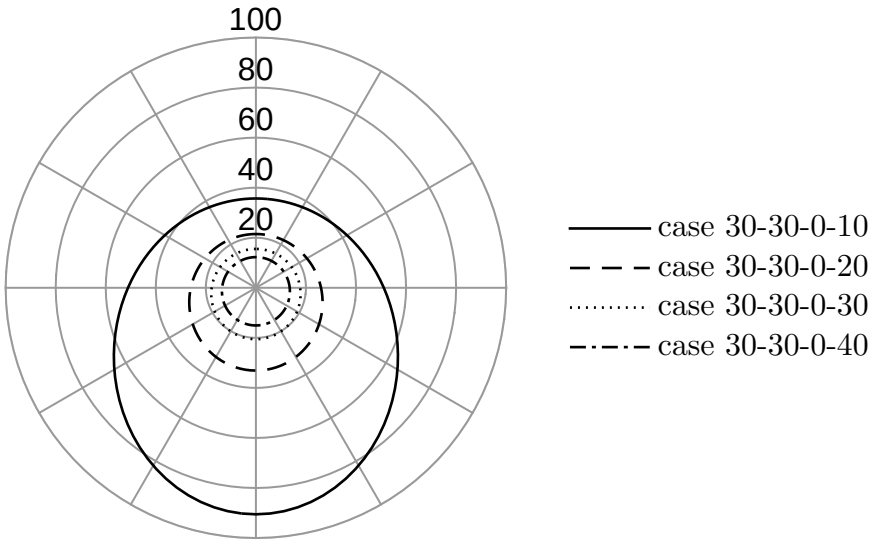

Figure 28: Mud invasion profiles with various yield stress.

4.4 Case II - Collinear Elliptical Wellbore Trace

4.4.1 Mathematical Formulation

Next, we consider a more complex case when the fracture is not perpendicular to the wellbore axis ($|\mathbf{n}\cdot\mathbf{m}| \neq 1$) while the angle between $x-$axis and the major axis of the ellipse is zero ($\gamma = 0^\circ$). The wellbore trace on the fracture plane is elliptical with the major axis of the ellipse being collinear with $x-$axis. Eqs. 39-63 and the numerical scheme in the last section remain the same for this case. The only difference is that now the wellbore boundary is an ellipse with major axis $a = 1/\cos\delta$ and minor axis $b = 1$,

$$\frac{\widetilde{r}^2\cos^2\theta}{a^2} + \frac{\widetilde{r}^2\sin^2\theta}{b^2} = 1 \tag{71}$$

Therefore, the boundary condition at the wellbore is expressed as,

$$\widetilde{p} = 1 \quad \text{at} \quad \widetilde{r} = \frac{1}{\sqrt{\cos^2\theta\cos^2\delta + \sin^2\theta}} \tag{72}$$

where δ is the angle between the unit vectors $\mathbf{m}$ and $\mathbf{n}$ ($\cos\delta = \mathbf{m}\cdot\mathbf{n}$) and is related to angles α and β via,

$$\cos\beta = \sin\alpha\sin\delta + \cos\alpha\cos\delta \tag{73}$$

Theoretical solutions for radius $\widetilde{r}$ at $\theta = 0^\circ$ and 180° at a given $\widetilde{p}$ can be obtained from,

$$\widetilde{r} = \frac{1-\widetilde{p}}{2\widetilde{\tau}_0 - \widetilde{f}} + \frac{1}{\cos\delta} \quad \text{at} \quad \theta = 0^\circ \tag{74}$$

$$\widetilde{r} = \frac{1-\widetilde{p}}{2\widetilde{\tau}_0 + \widetilde{f}} + \frac{1}{\cos\delta} \quad \text{at} \quad \theta = 180^\circ \tag{75}$$

In the limit when $\delta = 90^\circ$, that is the case when the wellbore axis is coplanar with the fracture plane, $\mathbf{m}\cdot\mathbf{n} = 0$, as shown in Fig. 29. Assuming that the interval where the fracture intersects the wellbore is much larger than the wellbore radius, the flow is approximately one-dimensional only in the direction of gravity, and the volume of mud loss mostly depends on the length of the fracture.

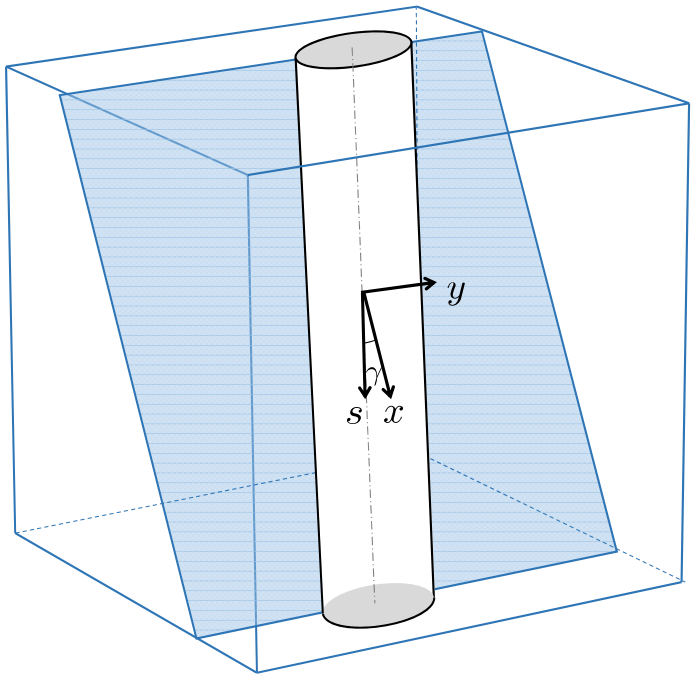

Figure 29: Schematic of a wellbore axis coplanar with the fracture plane.

4.4.2 Parametric Study

While the fracture dip angle determines the component of body force in the fracture plane, wellbore inclination angle β is only reflected in the boundary conditions through the trace of wellbore boundary. In other words, β defines the shape of mud inlet in the fracture through Eq. (72). Depending on the relative orientation of α and β, the trace of the wellbore is either circular or elliptical except for the extreme case when the wellbore axis is coplanar with the fracture plane. Wellbore inclination angle β determines the eccentricity of the wellbore trace, namely, how much the ellipse deviates from being circular. To study the

effect of β, cases of inclined wellbores intersecting a fracture with $\alpha = 30°$ are plotted in Fig. 30. As can be seen in Fig. 30, the mud invasion profiles from a vertical wellbore, a horizontal wellbore and a 45° inclined welllbore are about the same. What this means is that when the wellbore radius is small compared with the mud invasion length, the ultimate mud invasion profiles are not significantly affected by the wellbore radius.

It is noted that pairs of the wellbore of different inclination angles exist which intersect the fracture at different directions, but they project the same wellbore trace on the fracture plane. For example, consider a fracture plane of dip angle $\alpha = 30°$, based on Eq. (72) we can find $\beta = 0°$ and $60°$ are equivalent.

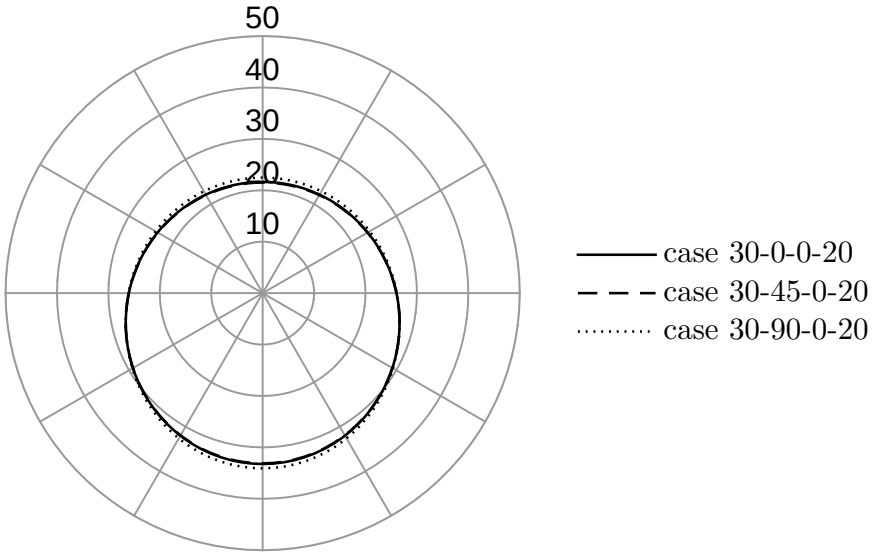

Figure 30: Mud invasion profiles with various wellbore inclination angles.

4.5 Case III - Rotated Elliptical Wellbore Trace

4.5.1 Mathematical Formulation

Now we add another layer of complexity and consider the case when the fracture is not perpendicular to the wellbore axis ($|\mathbf{n} \cdot \mathbf{m}| \neq 1$), and the wellbore trace on the fracture plane is elliptical with an offset between the major axis and $x-$axis ($\gamma \neq 0°$). Denote δ as the angle between the wellbore axis, represented by vector $\mathbf{m}$, and the outward normal for the fracture plane, vector $\mathbf{n}$.

$$\cos\delta = \mathbf{m} \cdot \mathbf{n} \tag{76}$$

In the global coordinate system, a unit vector along x_3-axis, can be decomposed into local Cartesian coordinate system xyz,

$$\vec{x}_3 = (-\sin\alpha, 0, \cos\alpha) \tag{77}$$

The trace of the wellbore on the fracture plane is an ellipse. Denote a and b as the major and minor half axis of the ellipse, respectively,

$$a = \frac{r_w}{\cos\delta} \qquad b = r_w \tag{78}$$

The unit vector representing the wellbore axis projected onto the fracture plane can be expressed in xyz coordinates as,

$$(-\sin\delta\cos\gamma, -\sin\delta\sin\gamma, \cos\delta) \tag{79}$$

The angle between the wellbore axis and $\vec{x}_3$ is rake angle β

$$\cos\beta = \sin\alpha\sin\delta\cos\gamma + \cos\alpha\cos\delta \tag{80}$$

Angle δ can therefore be determined by solving Eq. (80)

$$\delta = \arccos\left(\frac{\cos\beta}{\sqrt{\sin^2\alpha\cos^2\gamma + \cos^2\alpha}}\right) + \arctan\left(\frac{\sin\alpha\cos\gamma}{\cos\alpha}\right) \tag{81}$$

Inclination angles α and β can be arbitrarily chosen within the range $[0, \pi/2]$. However, according to Eq. 81, only the γ value that satisfies Eq. (82) is geometrically admissible,

$$\cos\beta/\sqrt{\sin^2\alpha\cos^2\gamma + \cos^2\alpha} \leq 1 \tag{82}$$

The wellbore trace on the fracture mid-plane can be expressed as,

$$\widetilde{r} = \frac{1}{\sqrt{\cos^2(\theta-\gamma)\cos^2\delta + \sin^2(\theta-\gamma)}} \tag{83}$$

Eqs. (39)-(63) and the numerical scheme in Section (4.3.1) remain the same for the case with rotated elliptical wellbore trace. The boundary condition at the wellbore is changed,

$$\widetilde{p} = 1 \quad \text{at} \quad \widetilde{r} = \frac{1}{\sqrt{\cos^2(\theta-\gamma)\cos^2\delta + \sin^2(\theta-\gamma)}} \tag{84}$$

Case III can only be solved numerically.

4.5.2 Parametric Study

The angle between the major axis of the ellipse and the $x-$axis, γ, is only reflected in the wellbore trace Eq. (84). Angle γ determines the relative offset of the major axis with respect to the $x-$axis. In Fig. 31, mud invasion profiles are plotted with a horizontal wellbore intersecting the fracture at different relative orientations so that γ varies between 30° and 165°. The results indicate that the mud invasion profiles only vary slightly with angle γ. Compared to the fracture dip angle and yield stress, both the wellbore inclination angle and the the angle of major axis with respect to $x-$axis are much less important to the mud loss behavior, unless the wellbore happens to be coplanar with the fracture plane .

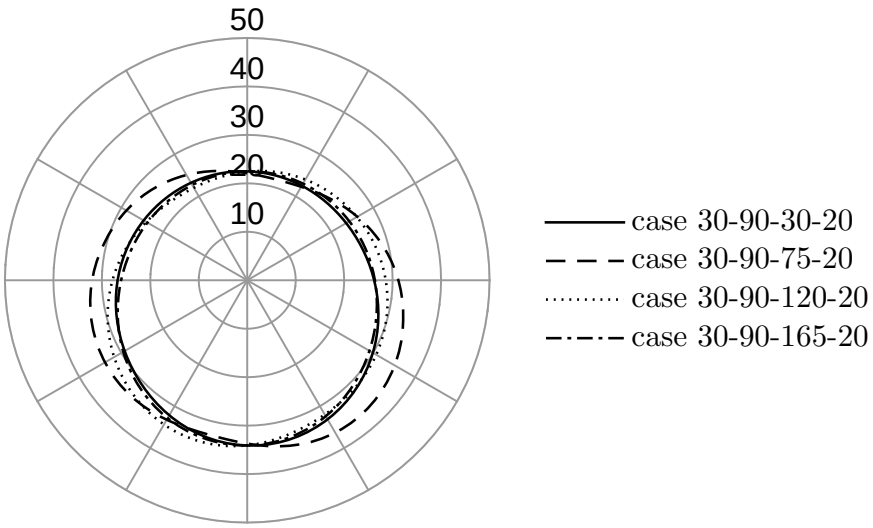

Figure 31: Mud invasion profiles with various γ.

4.6 Mud Loss Map

The mud invasion volume is plotted as a function of the inclination angles using a contour plot, see Figs. 32, 33 and 34. Each map is plotted by keeping one angle constant and varying the other two. The contour plot provides information of the unfavorable wellbore orientations with greater loss which should be avoided during drilling. In Fig. 32(a), we vary α and β and keep $\gamma = 0°$. In this case, when $\alpha + \beta = 90°$, wellbore lies in the fracture plane, which results in large volume of mud loss as indicated by Fig. 32 (a). In Fig. 32 (b), two zones of high volume are observed: $\alpha \approx 0°$ and $\beta \approx 90°$, i.e., a horizontal

wellbore inside a horizontal fracture, and $\alpha \approx 90°$, i.e., a vertical fracture intersected by an arbitrarily inclined wellbore. The mechanisms responsible for the mud loss in the two zones are different: in the first zone, mud loss is significant due to the large area of the wellbore cross-section on the fracture plane; in the second zone, fracture is vertical and therefore the increase of mud flow can be attributed to the increase in the gravitational force on the fracture plane.

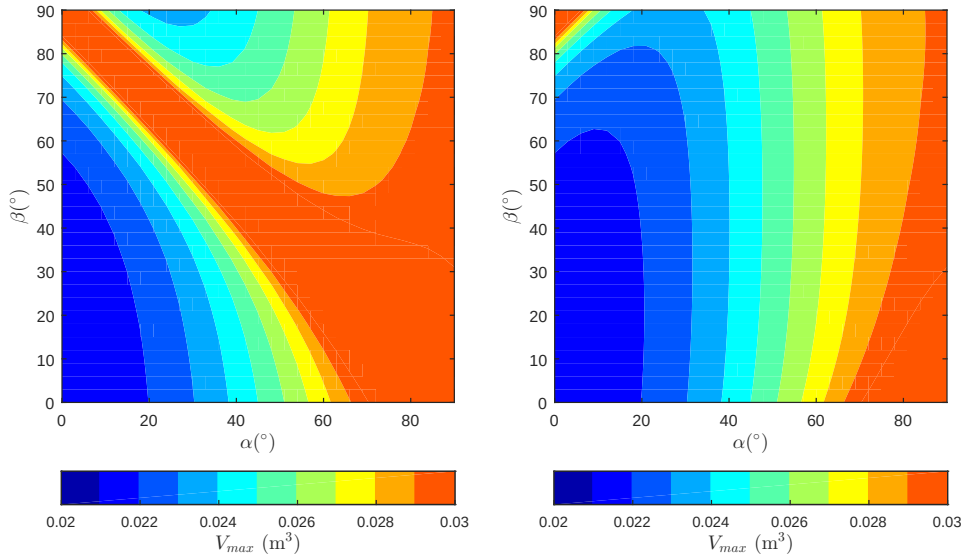

(a) $\gamma = 0°,\ \tau_0 = 20$ Pa (b) $\gamma = 180°,\ \tau_0 = 20$ Pa

Figure 32: Maximum mud invasion volume as a function of the fracture dip angle and the wellbore inclination angle.

In Fig. 33, effect of angle γ is examined. Even though inclination angles α, β and γ can be arbitrarily chosen, only the combinations of values that satisfy Eq. (82) are geometrically admissible. All the angles outside the admissible combinations are shown as blank spaces in Fig. 33 and 34. A band of high volume of mud loss can be identified for both $\beta = 45°$ and $\alpha = 15°$, around which wellbore axis is oriented close to the fracture plane. Outside of the band, mud loss is not sensitive to the variation in angle γ.

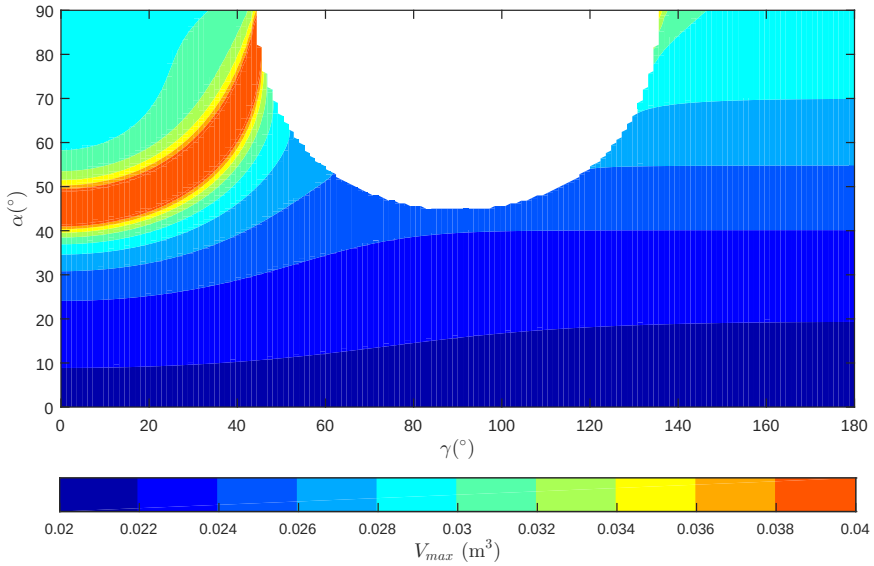

Figure 33: Maximum mud invasion volume as a function of the fracture dip angle and γ, $\beta = 45^\circ,\ \tau_0 = 20$ Pa.

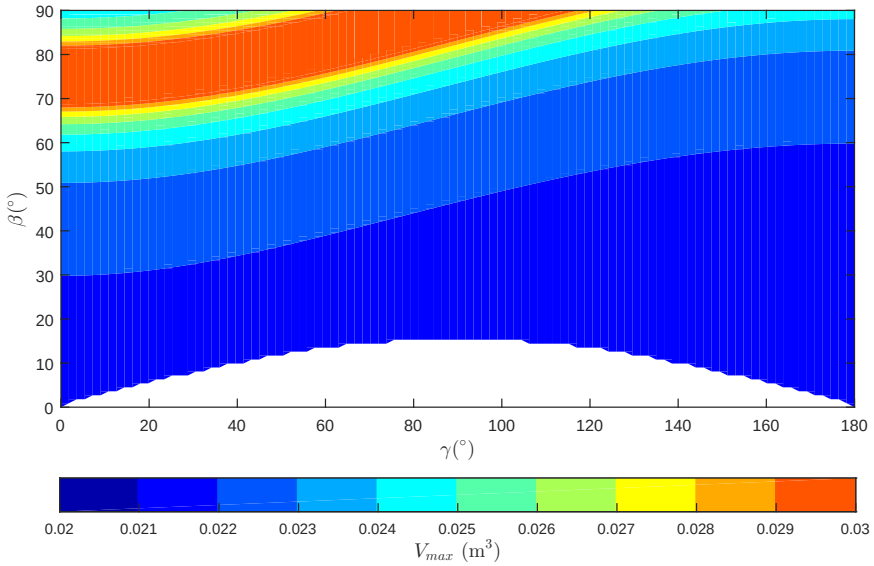

Figure 34: Maximum mud invasion volume as a function of the wellbore inclination angle and γ, $\alpha = 15^\circ,\ \tau_0 = 20$ Pa.

4.7 Comparison With the Numerical Model for Radial Flow

In this section, further analysis is performed with a numerical model for radial flow inside the fracture (Fig. 39). The fracture is assumed to be horizontal and the flow can be reduced to one-dimensional. Therefore, the velocities in θ and z direction are negligible compared with the velocity in the radial direction. With these assumptions, the basic equations are

- Continuity:

$$\frac{\partial Q}{\partial r} = 0 \tag{85}$$

where Q is the total flow rate in the fracture.

- Balance of Momentum:

$$-\frac{dp}{dr} = \frac{d\tau_{rz}}{dz} \tag{86}$$

where p is the net fluid pressure and τ_{rz} is the shear stress.

We assume that rheology of the drilling mud can be described by a piecewise power law model,

$$\tau = \begin{cases} \tau_0 + K_1\dot{\gamma}^{n_1} & 0 < |\dot{\gamma}| \leq \dot{\gamma}_c \\ K_2\dot{\gamma}^{n_2} & |\dot{\gamma}| > \dot{\gamma}_c \end{cases} \tag{87}$$

where K_1 and K_2 are the consistency parameters, and n_1 and n_2 are the power law indices. Symbol τ_0 denotes the yield stress and $\dot{\gamma}_c$ is a critical shear strain rate that characterizes the transition from the low shear rate rheology to the high shear rate rheology. Given the yield stress τ_0 and the critical shear stress τ_c at the critical shear strain rate $\dot{\gamma}_c$, the consistency parameters K_1 and K_2 can be determined from

$$K_1 = \frac{\tau_c - \tau_0}{\dot{\gamma}_c^{n_1}}, \qquad K_2 = \frac{\tau_c}{\dot{\gamma}_c^{n_2}} \tag{88}$$

A critical pressure gradient to initiate fluid flow can be determined from,

$$\bar{p}_{c1} = \frac{2\tau_0}{w} \tag{89}$$

A critical pressure gradient for the high shear rate behavior to occur can be expressed as,

$$\bar{p}_{c2} = \frac{2\tau_c}{w} \tag{90}$$

Combining Eqs. (86), (87) and the no slip condition at the fracture walls, we can obtain the expression of the total flow rate in the fracture.

If $\bar{p}_{c1} < \bar{p} \leq \bar{p}_{c2}$, only the plug flow region and the low shear rate rheology governed region are present.

$$Q^{(\mathrm{I})} = 4\pi r \dot{\gamma}_c \left(\frac{w}{2}\right)^2 \frac{1}{2+1/n_1} \left(\frac{\frac{\bar{p}w}{2} - \tau_0}{\tau_c - \tau_0}\right)^{1/n_1} \left[1 - \frac{1}{n_1+1}\left(\frac{2\tau_0}{\bar{p}w}\right) - \frac{n_1}{n_1+1}\left(\frac{2\tau_0}{\bar{p}w}\right)^2\right] \tag{91}$$

If $\bar{p} > \bar{p}_{c2}$, the plug flow region, the low shear rate governed and the high shear rate governed regions are all present.

$$Q^{(\mathrm{II})} = 4\pi r \dot{\gamma}_c \left[\begin{array}{c} \left(\frac{\left(\frac{w}{2}\right)^{2+1/n_2}}{2+1/n_2}\right)\left(\frac{\bar{p}}{\tau_c}\right)^{1/n_2} \\ + \left[\left(\frac{1}{2+1/n_1} - \frac{1}{2+1/n_2}\right)\tau_c^2 \right. \\ + \left(\frac{1}{2+1/n_1} - \frac{1}{1+1/n_1}\right)\tau_0^2 \\ \left. + \left(\frac{1}{1+1/n_1} - \frac{2}{2+1/n_1}\right)\tau_0\tau_c\right]\bar{p}^{-2} \end{array}\right] \tag{92}$$

$$Q = \begin{cases} Q^{(\mathrm{I})}\left(\bar{p},\ r\right) & \bar{p}_{c1} < \bar{p} \leq \bar{p}_{c2} \\ Q^{(\mathrm{II})}\left(\bar{p},\ r\right) & \bar{p} > \bar{p}_{c2} \end{cases} \tag{93}$$

The system of governing equations Eqs. (85), (91), (92) and (93) can be solved explicitly as described in Chapter 2. Various rheological parameters are chosen as input parameters (Table 7). The fracture width and the wellbore radius are taken as $w = 1$ mm and $r_w = 100$ mm, the same as in Table 6.

Table 7: Rheological parameters.

	n_1	n_2	τ_0 (Pa)	τ_c (Pa)	$\dot{\gamma}_c$ (1/s)
A	0.8	1.1	20	100	150
B	0.7	1.2	10	80	250
C	0.9	1.2	10	150	300

Variations of the mud invasion radius r_f with time for overpressure $P_{\mathrm{in}} = 100,\ 500$ kPa with three sets of rheological parameters are compared in Fig. 35. Wellbore overbalance

pressure plays a critical role in determining the mud invasion radius. For a smaller overbalance pressure, the mud invasion length reaches a plateau relatively earlier, which means the fracture is sealed faster. At late time, given the same overpressure, the mud invasion radius becomes more affected by the yield stress. For the same overbalance pressure, the yield stress only takes effect at late time while early time behavior is governed by the critical shear stress, which divides the invasion process into the low shear rate governed and high shear rate governed stages.

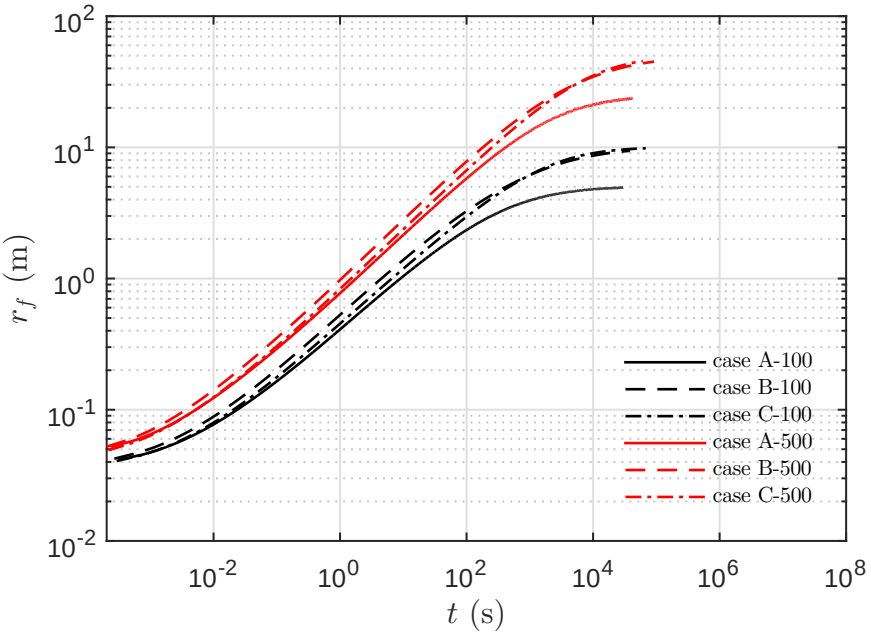

Figure 35: Invasion length vs. time with different overbalance pressure; the case numbers refer to the fluid type and overpressure in kPa; namely, case A-100 is a test case with type A fluid and $P_{\text{in}} = 100$ kPa.

Next, late time behaviors when invasion radius approaches a plateau are further studied. In a radial flow without the influence of gravity, the ultimate invasion radius depends on the wellbore radius, the yield stress, the fracture width and the overbalance pressure, as indicated in Eq. (94) (see derivation in Section (4.10)),

$$r_{max} = r_w + \frac{P_{\text{in}} w}{2\tau_0} \approx \frac{P_{\text{in}} w}{2\tau_0} \tag{94}$$

To verify the analytical solution in Eq. (94), the invasion radius from the numerical model

is normalized by $2\tau_0/wP_{\text{in}}$ in Fig. (36). Time is normalized by a representative small shear rate $\dot{\bar{\gamma}}_c = 1$ 1/s. The normalized ultimate invasion radius equals to 1 for all computation cases, which agrees with the theoretical solution. This comparison indicates that no matter what the rheological parameters are, the yield stress controls the mud loss behavior at late time and determines the final invasion length of the drilling mud.

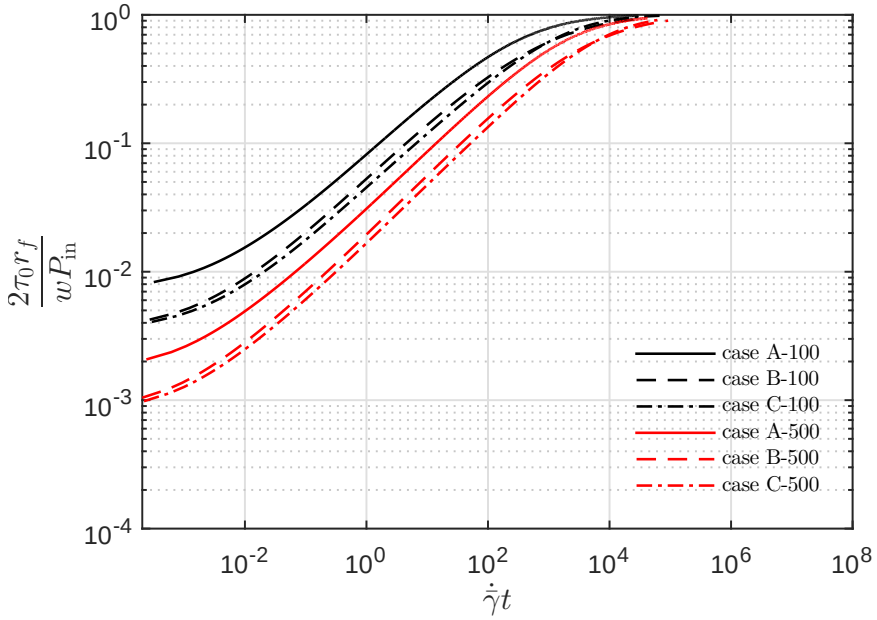

Figure 36: Normalized invasion length vs. normalized time with different overbalance pressure; the case numbers refer to the fluid type and overpressure in kPa; namely, case A-100 is a test case with type A fluid and $P_{\text{in}} = 100$ kPa.

4.8 Comparison with Experimental Data

In this section, we will compare the theoretical solution with the experimental data in Majidi *et al.* [70]. In their test, two different polymer solutions (Xanthan gum, 30 g/L and 40 g/L) are injected between two parallel plates from an inlet, where the pressure is maintained constant. The maximum invasion radius was measured from the injection experiments. Yield stress of the fluids is measured by a 12-speed rotational viscometer (Table 8).

Table 8: Yield Stress from test and calculation.

Fluid	Measured τ_0 (Pa)	Calculated τ_0 (Pa)
30 g/L Xanthan gum	9.6	9.09
40 g/L Xanthan gum	14	14.2

Data points in Fig. 37 show the maximum fluid invasion radius at various overbalance pressures from Majidi *et al.* [70]. According to Eq. (94), the maximum radius of fluid invasion increases linearly as the inlet pressure increases. Linear regressions are therefore applied to the experimental data. The yield stress is then determined from the linear regression based on Eq. 94. The theoretically determined yield stress is compared with the values measured from the rheometer in Table 8. Excellent agreement is indeed achieved.

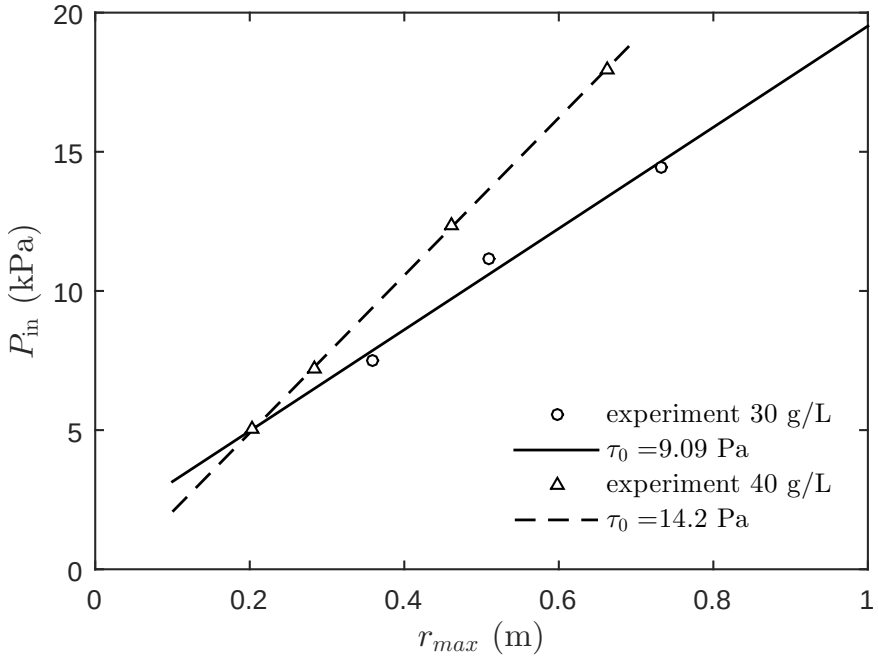

Figure 37: Maximum fluid invasion at various inlet pressures.

In practice, there are various methods for measuring the yield stress of a fluid ranging from direct measurement using a rheometer to indirect measurement in a flow test. However, direct measurement is rather difficult. Theoretically, the true yield stress should be measured in the limit of zero shear rate. Nevertheless, due to instrument limitations,

the rheometer measurement of the yield stress is generally obtained by extrapolating the shear stress under flow condition to the zero shear rate. Therefore, the yield stress could be rather inaccurate. A common indirect test is the slump test, which involves measuring the degree of slumping of a cylindrical volume of material on a horizontal plane [74] based on the "avanlanche behavior" [19] of yield stress fluid. Inclined plane test which involves measuring the equilibrium sample thickness on an inclined surface following an initial period of flow has also been suggested [18]. Since these indirect tests are less well-controlled, they are non-ideal either.

What we have shown is that our limit solution can not only predict the mud invasion length in a fracture, it can also be used as an alternative tool to determine the true yield stress of a fluid. Using squeeze flow between the parallel plates to determine the yield stress could have practical benefit as well. In practice, the maximum loss volume could also be affected by factors such as the roughness and the slip conditions of the fracture surfaces. If these conditions are known *a prior*, the parallel plates could be engineered to determine a nominal yield stress more relevant to the field condition.

4.9 Prediction of Fracture Permeability with Field Data

The maximum mud loss volume is given by

$$V_{max} = \pi w \left(r_{max}^2 - r_w^2\right) \tag{95}$$

Substituting Eq. (94) into Eq. (95) gives,

$$\Omega = \left(\frac{P_{\text{in}}}{\tau_0}\right)^2 w^3 - 4r_w \left(\frac{P_{\text{in}}}{\tau_0}\right) w^2 - \frac{V_{max}}{4\pi} = 0 \tag{96}$$

which is a cubic equation of the fracture width w, with coefficients dependent on wellbore radius r_w, overpressure ratio P_{in}/τ_0, and maximum mud loss volume V_{max}. Only one real, positive root of fracture width w is physically meaningful. Noticing that $\Omega|_{w=0} = -V_{max}/4\pi < 0$, $\Omega\left(w \to +\infty\right)$ and $\Omega'\left(w\right) > 0$, there will always be one and only one positive root. Solution of this equation for w is a simple and direct way of determining the fracture width.

Next, we will predict the fracture width using mud loss data from an Agip well reported in Sanllippo *et al* [90]. A calibration can be performed to find the overpressure ratio at the depth around 3892.8 m $\sim$ 3892.85 m, where a core sample was taken. On the core sample, a 4 cm thick band of fractures have been seen with the fracture width ranging from 0.2 mm to 0.8 mm. We can average the two mud loss readings at those two depths and take mid-value of the width, which gives a mud loss reading $V^* = 0.03$ m^3 and a width reading $w^* = 0.5$ mm. Substituting V^* and w^* into Eq. (96) and assuming $r_w = 0.1$ m gives overpressure ratio $P_{\text{in}}/\tau_0 = 4788.4$. The overpressure ratio is assumed to be constant over the depth 3892.8 m $\sim$ 4104.2 m. For every measurement of the circulation loss, the fracture width, namely, the root of Eq. (96), is computed through a numerical iteration. Since the inclination angles are not given in the report, we assume all the fractures to be horizontal. Table 9 and Fig. 38 summarize the results of such an analysis for this particular well. The calculated value of the fracture width can be used to predict the fracture permeability through the Poiseuille's law via the following equation,

$$k = \frac{w^2}{12} \tag{97}$$

where k is the permeability of the fracture. Note that here we are treating the real-time mud loss volume measurement as that of the worst case scenario to determine the fracture width. In reality, the ultimate mud loss volume will be larger than the real-time data. Therefore, the fracture width and the fracture permeability determined from our analysis are in fact lower bounds.

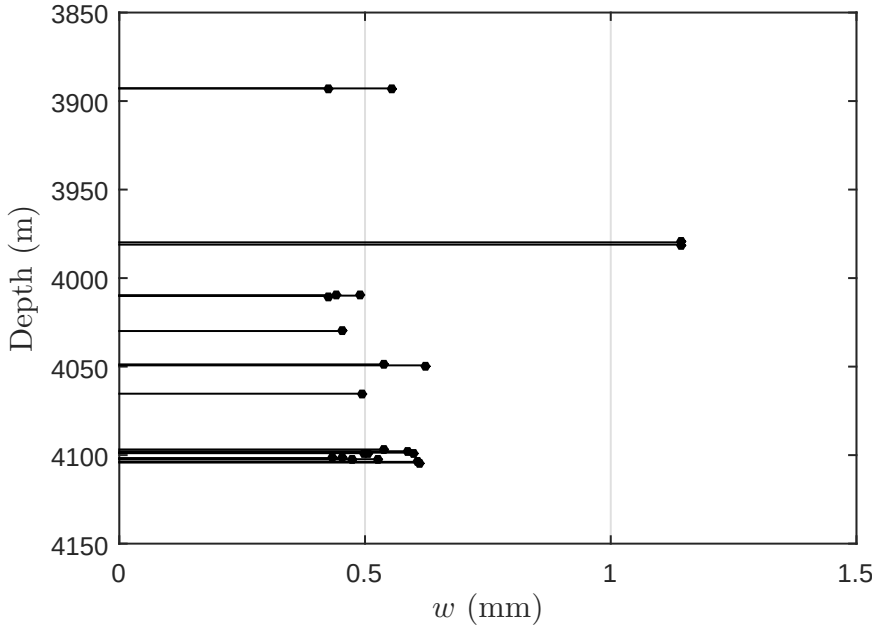

Figure 38: Location of the fractures and their estimated hydraulic apertures.

Table 9: List of the mud losses, the estimated hydraulic aperture and the permeability of the corresponding fractures

Depth (m)	V_{max} (m^3)	w (mm)	k (m^2)
3892.8	0.018	0.43	1.5×10^{-8}
3892.85	0.042	0.56	2.6×10^{-8}
3979.8	0.4	1.14	1.1×10^{-7}
3981.1	0.4	1.14	1.1×10^{-7}
4009.7	0.02	0.44	1.6×10^{-8}
4009.9	0.028	0.49	2.0×10^{-8}
4010.1	0.018	0.43	1.5×10^{-8}
4029.9	0.022	0.45	1.7×10^{-8}
4048.75	0.038	0.54	2.4×10^{-8}
4049.3	0.06	0.62	3.2×10^{-8}
4065.3	0.029	0.49	2.0×10^{-8}
4096.8	0.038	0.54	2.4×10^{-8}
4097.8	0.05	0.59	2.9×10^{-8}
4098.6	0.053	0.6	3.0×10^{-8}
4098.7	0.03	0.5	2.1×10^{-8}
4098.9	0.031	0.51	2.1×10^{-8}
4101.7	0.022	0.45	1.7×10^{-8}
4101.8	0.019	0.43	1.6×10^{-8}
4102.3	0.035	0.52	2.3×10^{-8}
4102.4	0.025	0.47	1.9×10^{-8}
4103.8	0.055	0.61	3.1×10^{-8}
4104.2	0.057	0.61	3.1×10^{-8}

4.10 Limit Solutions for Radial Flow of a Yield Stress Fluid in a Horizontal Fracture

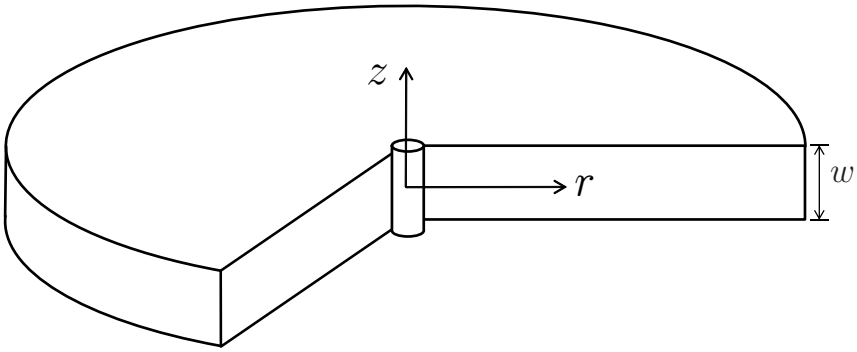

Figure 39: Schematic of radial flow in a fracture.

Steady state radial flow of a Bingham fluid between two horizontal parallel plates is presented here. Both the low shear limit and the high shear limit solutions are derived. We assume that the fluid is incompressible and the flow is axisymmetric in a laminar regime. Denote r and z as the coordinates in the direction of flow and across the parallel plates with $z = 0$ being the median plane of the opening between the parallel plates (Fig. 39). Assuming tension positive, the equilibrium equation in the radial flow direction can be written as,

$$\frac{\partial p}{\partial r} = \frac{\partial \tau_{rz}}{\partial z} \tag{98}$$

where p and τ_{rz} are the fluid pressure and the shear stress at an arbitrary position (r, z). Since we assume the flow is one-dimensional, $\partial p/\partial z = 0$. Integrating Eq. (98) over z and substituting the symmetry condition, $\tau_{rz} = 0$ at $z = 0$, yields,

$$\tau_{rz} = \int_0^z \left(\frac{\partial p}{\partial r}\right) dz = \left(\frac{\partial p}{\partial r}\right) z \tag{99}$$

Eq. (99) suggests that the shear stress at a given radial position is linearly distributed over the cross section and the maximum shear stress occurs at the walls of the parallel plates. The magnitude of the wall shear stress can be determined from,

$$\tau_w = \left(\frac{\partial p}{\partial r}\right) \frac{w}{2} \tag{100}$$

where w is the width of the opening between the parallel plates. Note that for radial flow, $\partial p/\partial r \leq 0$. For a Bingham fluid, the shear stress τ can be related to the shear strain rate $\dot{\gamma}$ through,

$$\tau = \tau_0 + \mu\dot{\gamma} \tag{101}$$

where τ_0 is the yield stress and μ is the plastic viscosity of the fluid. Existence of the yield stress means that fluid flow occurs only if the wall shear stress τ_w exceeds the yield stress τ_0 ($\tau_w > \tau_0$). Meanwhile, Eq. (99) also means that under flow condition, there is a plug zone within $|z| \leq z_p$, where the flow velocity does not vary in z-direction. The half width of the plug zone, z_p , can be calculated from,

$$z_p = -\frac{\tau_0}{\partial p/\partial r} \tag{102}$$

The shear strain rate $\dot{\gamma}_{rz}$ is related to the radial flow velocity v_r through the geometrical equation,

$$\dot{\gamma}_{rz} = \frac{\partial v_r}{\partial z} \tag{103}$$

Combining the rheological equation, the equilibrium and geometrical equations and applying the no-slip condition at the walls (i.e., $v_r = 0$ at $|z| = w/2$), the flow velocity as a function of the plug zone half width z_p , which in turn is a function of the local pressure gradient, can be readily obtained,

$$v_r = \begin{cases} \dfrac{1}{\mu}\left[\dfrac{\tau_w}{w}\left(\dfrac{w^2}{4} - z^2\right) - \tau_0^2\left(\dfrac{w}{2} - z\right)\right] & z_p < |z| \leq \dfrac{w}{2} \\ \dfrac{1}{\mu}\left[\dfrac{\tau_w}{w}\left(\dfrac{w^2}{4} - z_p^2\right) - \tau_0^2\left(\dfrac{w}{2} - z_p\right)\right] & 0 \leq |z| \leq z_p \end{cases} \tag{104}$$

The total flow rate can be determined from,

$$Q_r = 2\int_0^{w/2} v_r dz = \frac{2\tau_w}{3\mu}\left(\frac{w^2}{4} - \frac{2z_p^3}{w}\right) - \frac{\tau_0}{\mu}\left(\frac{w^2}{4} - z_p^2\right) \tag{105}$$

The average velocity at a given cross section is,

$$\bar{v} = \frac{2\tau_w}{3\mu w}\left(\frac{w^2}{4} - \frac{2z_p^3}{w}\right) - \frac{\tau_0}{\mu w}\left(\frac{w^2}{4} - z_p^2\right) \tag{106}$$

Define,

$$\psi = \frac{\tau_0}{\tau_w} = \frac{2z_p}{w} \tag{107}$$

Eq. (106) becomes

$$\frac{6\mu\bar{v}}{w\tau_0} = \frac{1}{\psi}\left(1 - \frac{3}{2}\psi + \frac{1}{2}\psi^3\right) \tag{108}$$

When the flow rate is large ($\psi \ll 1$), we may discard the higher order term ψ^3 and obtain the high shear limit solution for the local pressure gradient, i.e.,

$$-\frac{\mathrm{d}p}{\mathrm{d}r} = \frac{12\mu\bar{v}}{w^2} + \frac{3\tau_0}{w} \tag{109}$$

When the flow rate is small and the flow is about to stop, we have, $\bar{v} \to 0$ and $\psi \to 1$, which yields a low shear limit solution,

$$-\frac{\mathrm{d}p}{\mathrm{d}r} = \frac{2\tau_0}{w} \tag{110}$$

Yield stress is the only the rheological parameter governing the low shear limit soluton. Though the solution is derived based on the Bingham rheology, the low shear limit solution is the same if the fluid rheology is Herschel-Bulkley.

Note that the low shear limit solution in Liétard *et al.* (1999) [65], Verga *et al.* (2000) [100], Majidi *et al.* (2010) [70], and Huang, *et al.* (2011) [44] was obtained by simply setting $\bar{v} = 0$ in Eq. (109). Since Eq. (109) is only true for large flow rate ($\psi \ll 1$), it cannot be used to approximate the low shear limit solution at $\bar{v} = 0$. Therefore, their limit solution $-\mathrm{d}p/\mathrm{d}r = 3\tau_0/w$ is incorrect. The implication is that a pressure gradient smaller than $3\tau_0/w$ could still drive the fluid to flow. The solutions for the mud volume loss in these studies have therefore erred on the unconservative side.

4.11 Conclusions

In this work, a theoretical solution is provided to study the mud invasion into an arbitarily oriented isolated fracture from an inclined wellbore. The component of gravity in the fracture plane is taken into account, therefore the invasion profile is not axisymmetric. The fracture is assumed to has a constant width and bounded by rigid walls. The ultimate invasion profile when the mud eventually stops flowing is solved based on limit equilibrium conditions. Effects of the fluid yield stress, the overbalance pressure, the fracture inclination angle and the wellbore trace on the fracture upon the mud loss behaviors are analyzed. A limit solution for the particular case of radial flow in a horizontal fracture is compared with

the transient numerical model for radial flow. Excellent agreement is achieved between our analytical solution and published experimental data. The theoretical model can be used to give the lower bound for the fracture permeability based on the mud loss data from the field.

CHAPTER V

DEM MODELING OF FLUID INJECTION INTO A NEARLY UNCONSOLIDATED MEDIUM SUBJECTED TO ISOTROPIC STRESS

5.1 Introduction

Better understanding of failure induced by fluid injection in unconsolidated formations or weakly consolidated formations is crucial. On the one hand, fluid pressurization could lead to undesirable consequences. For example, overpressure in horizontal directional drilling may cause upheaval and rupture of the ground surface [29, 94]. On the other hand, fluid injection can be engineered to achieve specific goals in engineering applications such as, grouting for ground improvement [3, 31, 92, 93], construction of permeable reactive barriers for environmental remediation [4, 40, 41], sand control in unconsolidated reservoirs [37, 101], enhanced production by fracturing or water flooding [53, 54] and cuttings reinjection for waste storage [16, 52, 98].

Different from hydraulic fracturing in competent rocks, failure mechanisms due to fluid injection in a nearly unconsolidated formation are not yet well understood due to the highly nonlinear and coupled nature of the problem. It is generally assumed that onset of failure may occur in a tensile or a shear mode, depending on whether cohesion is present or not. In a cohesive medium, fluid pressurization in a borehole is assumed to lead to tensile crack initiation and propagation. However, in an unconsolidated or weakly consolidated medium, classical linear elastic fracture mechanics for solids becomes inapplicable since either no new surface areas are created and/or excessive irreversible deformation occurs. There could be also be other additional complexities, e.g., when the medium is highly permeable, leakoff behavior becomes nonlinear.

This work is set out to address fundamental questions such as whether the failure resulted from fluid pressurization would lead to a shear or in an opening mode of growth, how to

predict the onset of localized failure and how to relate the breakdown pressure to the formation characteristics and the fluid properties.

Though the openings or the localized features created by fluid injection in a weak medium can hardly be called fractures or fluid fingers in the classical sense, these terms are used loosely to describe any narrow opening features in this work. It is also necessary to differentiate the growth modes of the localized features from the failure mechanisms in the host medium. We refer to the growth mode as an opening mode when the opening feacture extends along the tangent of its original trajectory, and as a branched or shear mode when the extension deviates from its original path.

5.2 Literature Review

Studies related to fluid injection into the unconsolidated or weakly consolidated materials, including laboratory experiments, theoretical analyses, and numerical simulations, are reviewed in this section.

5.2.1 Laboratory Experiments

5.2.1.1 Experimental Setup

Laboratory hydraulic fracturing experiments are commonly conducted with an injection outlet embedded in the center of the specimen. Fluid is then pumped into the specimen via the outlet at a constant flow rate. Two common types of configurations are a triaxial cell for a cylindrical sample [75, 82, 55, 20, 92, 67, 15, 10, 34, 21, 23, 45] and a true triaxial cell for a cubical or rectangular sample [78, 76, 104, 49, 47, 54, 56, 35, 50, 48]. For the cylindrical cell, the sample is usually contained within a flexible membrane, and is subjected to a lateral confining stress and a vertical load independently. On the other hand, the true triaxial chamber allows independent control of three principal stresses. The chamber consists of six sides and usually has at least one movable side allowing loading, compaction and removal of the specimen. Among them, X-ray CT was used during the injection experiments in [20, 10, 21]. Real time acoustic emission monitoring was employed in [36].

The configurations mentioned above are for three dimensional samples, which does not allow for direct real time visualization. Huang *et al.* [44] conducted a radial flow injection

test into dry sand using a Hele-Shaw cell with transparent sides. This approach allows observing the tip propagation and the leakoff behavior in real time.

5.2.1.2 Material Properties

According to Mitchel *et al.* [73], the boundary between cohesionless versus cohesive soils is when the fraction of silt or clay exceeds 50%. Earlier studies were mostly using cohesive materials as the specimen [75, 66, 78, 76, 104, 92]. Recently, tests on either pure silica sand [20, 10, 21, 23, 45, 15, 47, 44, 55, 54, 56, 35, 50, 48] or a mixture of sand and fine-grained material [45, 49, 58, 87, 47, 48] have been performed. The particle size of the sands is about 100 μm in most of the tests. Fine-grained materials, e.g., kaolinite flour, silica flour, sugar and plaster, are added to the mixture to introduce cohesion, so as to make the granular samples hold their shape, or to reduce permeability. Experimental results from Hurt [45] show that adding 20% silica flour to sand can reduce sample permeability by an order of magnitude while not affecting the cohesionless nature of the material. However, an apparent cohesion may be introduced in a mixture of sand grains and fluid due to the presence of surface tension [44].

The experiments were performed on fully-saturated [66, 20, 21, 10, 92, 45, 82, 104, 91], partially-saturated [78, 35, 50, 82] or dry samples [15, 44]. Most of the samples were saturated by water, a few studies used *KCL* brine [55] or oil [56, 91, 35, 50] to wet the soil. These studies show that hydraulic fractures can be created regardless of the degree of saturation.

5.2.1.3 Fluid Type

A variety of fluids have been used in the laboratory experiments: water [91, 82, 104, 75, 66, 49, 47, 58], glycerin [78, 44], bentonite slurry [20, 10, 21], cross-linked gel [87, 20, 67, 10, 21, 23, 35, 50, 45], silicone adhesives [15], oil [48, 91, 10], and epoxy resin [92]. These fluids differ in their rheological behaviors and also in the ability in creating internal or external filter cakes. Some of the cross-linked gels are used in practice as fracturing fluids.

Khodaverdian and Mcelfresh [55] performed the test with a guar-based cross-linked polymer. Three distinct zones were identified, including a "filter cake" zone, a "gel-invaded"

zone, and a "filtrate-invaded" zone. Existence of the filter cake increases the rate of pressure build-up inside the borehole and consequently enhances fracturing. According to Khodaverdian and Mcelfresh, the cross-linked fluids can create relatively long fractures, but may result in extensive formation damage, whereas non-filter cake building fluids result in relatively short fractures due to excessive leakoff.

Similarly, a group of researchers in Delft University of Technology [10, 20, 21, 23] used viscasil oil, borate cross-linked gel and bentonite slurry, among which they found viscasil oil was the least efficient fluid in creating a fracture. On the other hand, borate cross-linked gel plus quartz powder yielded fractures in all the tests due to its effective leakoff control.

5.2.1.4 Boundary Conditions

Boundary conditions in most experiments are stress-controlled [78, 20, 10, 21, 23, 24, 55, 54, 56, 35, 50, 67, 82, 104, 75, 49, 47, 48, 45, 15], with the confining stress up to 40 MPa [20]. Only a small number of tests are displacement-controlled [87, 92, 45, 15, 43].

The tests performed by Bohloli and de Pater [10] showed that the ratio of maximum injection pressure to confining stress decreases with an increasing confining stress while the maximum injection pressure shows an ascending trend with increasing confining stress. At a low confining stress ($\sim$1 MPa), the ratio in the tests with bentonite slurry is much higher than those with other fluids. At higher confining stresses ($\sim 10 - 20$ MPa), the ratios are about the same for all types of fluids used. It was noted that the fracture initiation pressure is not sensitive to the fluid type used at the high confining stress.

The experiments by Hurt [45] indicated that the fracture initiation pressure greatly depends on the magnitude of the confining stresses. He performed dimensional analysis, which suggests a power-law relationship between the peak injection pressure and the confining stress.

5.2.1.5 Failure Near the Borehole

Prior to the breakdown of the borehole, cavity expansion was observed in the experiments, e.g., [15][36] Meanwhile, experiments by Bohloli and de Pater [10] and de Pater and Dong [21] showed evidence of both an opening mode and a shear growth mode in sand near the

injection borehole. Fractures obtained at high stresses are short, branched and tortuous while those obtained at low stresses are relatively longer, straight and less tortuous. Shear bands manifested through localized density variations was detected by CT scan.

5.2.1.6 Failure at Fracture Tip

Murdoch [78] found that the hydraulic fractures generated in partially saturated silty clay are narrow, normal to the direction of the least principal compression, and have similar features of the tensile fractures in hard rocks. At a high water content, a fluid lag was found behind the leading edge of the fracture, which is also present in fluid-driven fractures in rocks.

Khodaverdian and Mcelfresh [55] injected a guar-based cross-linked polymer into sand. They considered that fracture tip propagation in unconsolidated sand is dominated by fluid invasion and shear failure within a process zone ahead of the tip. Besides the main fracture, multiple sub-parallel fractures are observed.

In the experiments by Dong [24], a cross-linked gel was injected into sand. Shear bands were observed ahead of the crack tip by CT imaging. They also found that fractures were relatively wider in the granular media compared to those in competent rocks.

Chang's experiments [15] were primarily in dry silica flour and sand. Three main types of fracture fronts were observed: round, beveled and fingered. The front geometry was attributed to three physical mechanisms: cavity expansion, shear banding and induced cohesion. The results also showed an increase in the fracture aperture with an increasing confining pressure.

Hurt [45] extended Chang's study to saturated materials. A leakoff zone was observed ahead of the fracture tip and showed that fractures cannot be generated in cohesionless materials if there is excessive leakoff. An important characteristic feature of the fracture propagation process is tip blunting, which is attributed to plastic deformation at the tip.

Golovin *et al.* [35] and Jasarevic *et al.* [50] injected the cross-linked gel into partially saturated sand. They found that the fractures could change from simple planar forms to a "multi-branched stochastic fracture network" by increasing the injection rate or lowering

the solids concentration in the injection fluid.

In the experiment by Ito *et al.* [47], water was injected into pure silica sand or a mixture of sand and kaolin. The fracture patterns greatly depend on injection flow rate: a lower flow rate resulted in a single and straight fracture and a higher rate resulted in branching fractures.

In Zhang's experiment [107], the fractures are produced by injecting an aqueous glycerin solution into silica sand. The velocity field of near the fracture tip was analyzed by using Particle Image Velocimetry (PIV) technique, which indicates the tip propagation has the sequence of tip blunting and splitting. The new tip grows into a direction of 45° with respect to the main branch, suggesting that the tip grows as a result of shear failure. The shear failure mechanism was also confirmed by the highly localized shear strain rates near the tip from the PIV results.

5.2.2 Theoretical Analyses

In theoretical analyses, it is typically assumed that the medium fails in a tensile or shear mode, depending on whether cohesion is present or not. Many theoretical analyses have been proposed to study the failure near a cavity to address fracture initiation, and the failure near a fracture tip to explain the propagation process.

5.2.2.1 Tensile Failure of A Pressurized Cylindrical Cavity

The tensile fracture near a cylindrical cavity was analyzed based on a tensile strength criterion [9, 51, 66, 104]. The formation is considered failed when the circumferential stress near the borehole exceeds the tensile strength of the formation. In a weakly consolidated formation, the tensile strength is very low or negligible. Based on this assumption, an empirical expression was first given by Bjerrum *et al.* [9] and then modified by Jaworski *et al.* [51] to predict the fracture initiation pressure,

$$u_f = m\sigma_H + \sigma_t \tag{111}$$

where u_f is the hydraulic fracturing pressure; σ_H is the horizontal total stress; σ_t is the tensile strength; and m is a material constant.

5.2.2.2 Tensile Failure at Fracture Tip

Conventional linear or non-linear fracture mechanics has been employed to constructed the failure criteria for fracture propagation. Saada *et al.*, Fang *et al.*, Murdoch, and Hanson *et al.* [89, 30, 97, 77, 38] based their studies on Linear Elastic Fracture Mechanics (LEFM). Fracture initiates and propagates if the stress intensity factor at the fracture tip exceeds the fracture toughness of the material. Both a mode I [77] fracture and a mixed mode I/II fracture [97] have been studied.

Nevertheless, in practice, a toughness much larger than that is typical for a competent rock is often needed as an input to predict the fracturing pressure in the nearly unconsolidated formations. This may be an indication that the theoretical models based on LEFM is not sufficient in describing the failure mechanisms in those media.

5.2.2.3 Shear Failure of A Cylindrical Cavity

The ideal radial expansion of the borehole can be described by the theory of cavity expansion, first introduced by Bishop *et al.* in 1945 [8] and was modified over the next few decades [14, 59, 12] to consider large, radially symmetric deformation of a cavity in an infinite domain with hydrostatic far field stress. Since the experiments are generally conducted in a finite domain, the elastic-perfectly plastic solutions for radial expansion of a thick-walled cylinder [105, 42] could also apply. To analyze the onset of non-uniform shear deformation, experiments are compared with theoretical studies based on bifurcation analysis in [2]. The thick-walled cylinder solution and the bifurcation analysis will be further discussed in Chapter VI.

5.2.2.4 Shear Failure at Fracture Tip

Papanastasiou [83] numerically investigated the influence of the plastic behavior using an elasto-plastic model coupled with fluid flow inside the fracture. A strain softening model was employed at the fracture tip to describe fracture propagation. It was concluded that a higher net pressure is needed to propagate a fracture in an elasto-plastic medium than in an elastic medium. Plastic deformation results in a shorter and wider fracture. The difference

is strongly affected by the size of the plastic zones.

Chang [15] suggested two mechanisms for fracture propagation: fluidization, i.e., when the grains lost contact as a result of fluid pressurization, and shear band formation. A localized process zone model and a super-dislocation model were examined in Wu [102]. The localized process zone model assumes a linear softening law according to the Dugdale-Barenblatt model [26, 5]. In the super-dislocation model, the shear band is modeled by a single dislocation. Hurt [45] found evidences of both shear and tensile deformation near the tip, which suggests potential competing mechanisms for the fracture propagation.

5.2.3 Numerical Simulations

Hydraulic fracturing models for hard rocks usually assume a planar mode I fracture geometry. This assumption is invalid for cohesionless and weakly unconsolidated formations that are prone to shear failure. Shear failure could cause the fracture to become tortuous. Modeling fracture growth thus becomes rather challenging since in any numerical model, whether it is based on finite difference or finite element method (FEM), the criterion for fracture propagation is the most crucial element.

A smeared-fracture approach has been implemented into both the FEM model [6] and the finite difference model [95] to simulate the fracture propagation in weakly consolidated formations. The use of the smeared-fracture approach could be justified by the random nature of the micro-structure. In the model by Khodaverdian *et al.* [54], the criterion for fracture propagation was approximated by an "equivalent" fracture toughness, which was chosen to represent that of unconsolidated sand. Xu and Wong [103] treated the hydraulic fracture as a large area of shear dilated plastic zone with low effective stress and high hydraulic conductivity.

DEM modeling has been used to simulate the fluid injection process into unconsolidated or weakly consolidated formations. An advantage of the DEM in modeling the fluid injection problem is that the propagation of the fracture is automatically taken care of by the local force-displacement laws. Fluid injection could be realized by a coupled CFD-DEM model [11, 109, 108] or a coupled pore-network model [20, 21, 108]. A limitation of the coupled

CFD-DEM model is that the simulated fracture morphologies are relatively simple, since the fluid pressure is averaged over the fluid element, which is generally much larger than the particle sizes. The pore-scale pressure information is thus not accurate. For the pore-network model, a main challenge is to deal with the large pressure gradient from fluid leakoff when the viscosity of the injected fluid is large.

Bruno *et al.* [11] utilized a coupled CFD-DEM model to simulate the fracturing process during waste injection. When formations are weakly cemented with limited shear strength, the failure transitions from brittle, discrete fracture extension, to relatively large-scale dilation and inelastic deformation.

Cook *et al.* [17] simulated the near-wellbore failure in a loosely cemented rock based on the DEM approach in [88]. Fluid flow is modeled by streaming disc particles from the source to collide with the larger particles on the borehole boundary, which results in a radial, outward force along the borehole wall. The simulation produced multiple radial fractures.

Wu [102] conducted the analysis with a coupled CFD-DEM model and suggested that opening of a fracture is a result of fluidization of the particle-fluid mixture when the loss of contacts between the particles occurs in all directions.

De Pater *et al.* [20, 21] simulated the injection process based on a pore-network model. The hydraulic conductivity of the contacts near the injection source was assigned to decrease exponentially to simulate the pressure drop over the external filter cake. The numerical simulations agreed with their experimental results and predicted the trend of the stress dependence of the fracturing pressure.

Zhang *et al.* [108] modeled the fluid injection process into a dense granular medium based on both the coupled CFD-DEM and the pore-network coupling model. The numerical analysis examined the effects of parameters such as the fluid viscosity, the injection rate, the elastic modulus and the permeability of the medium and verified the scaling relationships among them.

5.3 Numerical Model Setup

As we can see from the literature review, extensive efforts have been devoted to the subject over the last two decades. However, failure of the host medium and the fracture growth mechanisms due to fluid injection in a nearly unconsolidated medium are not fully understood due to the highly nonlinear and coupled nature of the problem. It is generally assumed that onset of failure may occur in a tensile or a shear mode, depending on whether cohesion is present or not. In a cohesive medium, fluid pressurization in a borehole is assumed to lead to tensile crack initiation and propagation. On the other hand, for a cohesionless material, a constitutive model of Coulomb type predicts that the material must fail in shear and failure may be manifested in the medium in form of spiral-shaped shear bands.

Evidences of shear band development are observed in the cavity expansion experiments in dry sands in Alsiny *et al.* [2] where borehole pressurization is realized by inflating a membrane. In these experiments, the membrane does not penetrate into the sands. Meanwhile, the experiments in Chang [15], performed by injecting a highly viscous fluid into dry sands or silica flour, demonstrate that planar features resembling an opening mode crack can be created in a purely frictional granular material. A major difference between these two experiments is the pressurization mechanism. We therefore conjecture that the action of fluid penetration to cause grain displacements is a critical element in producing the opening mode crack- or finger-like features.

In this study, the effect of fluid penetration on the fluid-grain displacement patterns in a nearly cohesionless medium is investigated using the DEM code *PFC2D*®[46]. A numerical scheme is devised to consider a particular case, where the injected fluid is highly viscous and can penetrate into open spaces in between grains if the gap size between two neighboring grains exceeds a threshold value. Such an implementation could be considered analogous to taking into account the effect of surface tension without leakoff; the larger the critical gap size, the higher the surface tension or the fluid viscosity. We focus here only on the case when the fluid leakoff is negligible and the matrix is dry or in a drained condition. Numerical implementation in this work can be viewed as a simplification for modeling a fully-coupled process. It overcomes the difficulties in dealing with the large pressure gradient from fluid

leakoff when the viscosity of the injected fluid is large.

The numerical analysis is carried out in two types of two-dimensional (2D) domains: a circular particle assembly under isotropic stress field with a borehole in the center and a rectangular particle assembly under anisotropic stress field with a center slot, a side slot or a center hole. The circular assembly is used to study the near-wellbore failure mechanisms under an isotropic stress field. The rectangular assembly is used to investigate the mechanisms of fracture propagation under both isotropic and anisotropic stress conditions. This chapter and Chapter VI focus on expansion from a cylindrical cavity subjected to an isotropic confining stress, while the case with a rectangular assembly is investigated in Chapter VII. Discussions on the numeical simulation results in this chapter will focus mainly on the morphology or displacement patterns created by fluid injection. The injection pressure and the comparison between the numerical results and theoretical solutions are discussed in Chapter VI.

A 2D hollow circular domain is set up as shown in Fig. 40. The particle are generately randomly to create a dense packing inside the hollow circular domain. A servo-controlled scheme is applied to the outer boundary to maintain a prescribed confining stress by adjusting its radial velocity.

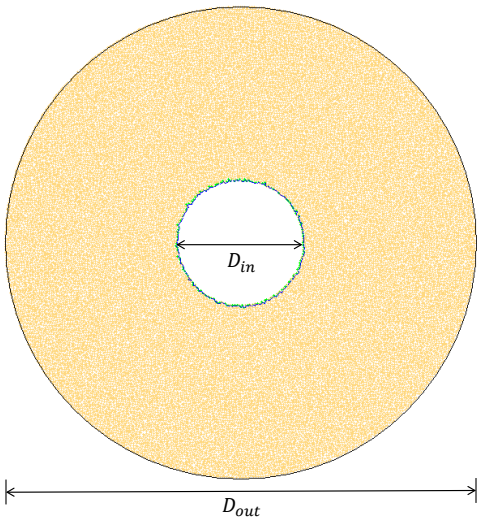

Figure 40: Schematic of a circular assembly with a hole.

A linear contact model is employed to relate the contact forces and the relative displacements between two particles through,

$$F_n = k_n U_n \quad F_s = -k_s \Delta U_s \tag{112}$$

where F_n and F_s are the normal and shear contact forces; k_n and k_s are the normal and shear contact stiffness; U_n and ΔU_s are the normal displacement and shear displacement increment. A positive force means compression. If there are bond strengths assigned to the contacts, the contact forces are limited by these normal and shear bond strengths. The contact forces reduce to zero if the normal bond strength $\overline{F}_n$ is reached (in tension). If the shear bond strength $\overline{F}_s$ is reached, the contact forces then follow a slip model of Coulomb type so that the shear force at a contact remains less than or equal to a limiting value that equals to the friction coefficient times the normal force.

5.3.1 Fluid Modeling Strategy

The fluid-grain interface is identified first by searching for a closed chain of particles nearest to the borehole, where the gap, δ, between any two neighboring particles does not exceed a threshold value, δ_c. As fluid front advances, new particles are added to the chain, if the growth criterion, $\delta \geq \delta_c$, is met. The interface therefore acts like a very flexible membrane. A schematic illustrating the growth of the fluid front is shown in Fig. 41. The initial fluid-grain interface consists of balls I, II and III. Ball IV becomes part of the interface chain when the gap between balls I and II exceeds the critical value. An example showing details of the fluid-grain interface from an advanced simulation stage is given in Fig. 42. Resultants of the fluid pressure are applied to individual particles on the fluid-grain interface as body forces, similar to the shining-lamp algorithm proposed by Potyondy [85]. In this study, the fluid flow time step is set to be 20 times the mechanical time step. Both the fluid pressure and the fluid-grain interface are updated at every fluid flow time step.

Two sets of parameters are used to define the chain properties: the critical gap δ_c as well as the normal and shear stiffnesses of the contact bond k_{nc} and k_{sc} between two adjacent particles. The stiffnesses of the bonds on the chain are set to be 10% of the contact stiffnesses for the grains, to simulate a very flexible membrane. For a cohesive assembly

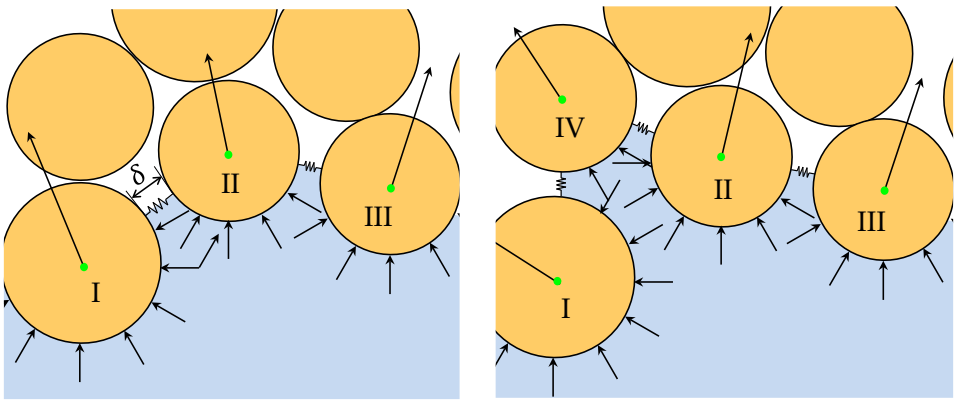

Figure 41: Schematic of (a) the initial fluid-grain interface consisting of balls I, II and III; (b) the updated fluid-grain interface with the new addition of ball IV; fluid pressure is applied to the particles via body forces.

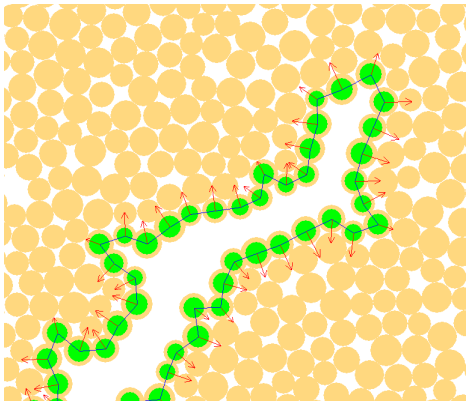

Figure 42: An example showing details of the fluid-grain interface at an advanced stage of simulation. The particles on the interface are marked in green, and the resultant forces from the fluid pressure are marked by the red arrows.

with the contact bond strengths, at the interface the chain properties are implemented after the contact bonds are broken.

5.3.2 Constant Flow Rate Implementation

Fluid injection is assumed to be at a constant rate. To implement the constant rate boundary condition, we assume that fluid pressure is constant in the borehole within one fluid flow time step. A cylindrical wall is initially used to support the cavity. At the start of the simulation, the reaction on the wall is replaced by an equivalent pressure applied at the fluid-grain interface. The fluid pressure is then updated at each time step. Given an

injection rate, Q, fluid bulk modulus, K_f, and current borehole area, A, the change in the borehole pressure, ΔP, can be related to the volume of fluid being injected into the borehole within one time step, $Q\Delta t$, and the area of borehole expansion during that time step, ΔA, through,

$$\Delta P = \frac{K_f}{A}\left(Q\Delta t - \Delta A\right) \tag{113}$$

The fluid bulk modulus is set to be $K_f = 1 \times 10^7$ Pa in this study, which is lower than a typical value for water. The value is chosen primarily for the reason of maintaining numerical stability. A large bulk modulus could result in a large pressure change within one time step, causing the interface chain to become unstable.

A detailed fluid pressure calculation cycle is shown in the flow chart in Fig. 43. After the start of the simulation, the amount of fluid being injected into the borehole is calculated for a given fluid flow step time Δt. The change in the fluid pressure is then calculated based on Eq. (113). Position of the fluid-grain interface chain as well as the fluid pressure is updated. Mechanical calculation steps then follow. Borehole deformation and the particle movements during the mechanical calcuation steps alter the relative positions of the particles. After 20 mechanical time steps, a new fluid pressure calculation cycle starts.

5.3.3 Simulation Parameters

Both the cohesionless and weakly consolidated media are modeled in this study. The outer diameter of the domain is chosen to be $D_{\text{out}} = 160$ mm and the inner diameter of the borehole is varied, $D_{\text{in}} = 8$ mm, 16 mm and 32 mm, which gives $D_{\text{out}}/D_{\text{in}} = 20$, 10 and 5. The micro-scale parameters and fluid properties are summarized in Table 10. The macro-scale material strength parameters of the particle assembly with three particle friction coefficients, i.e. $\phi_b = 15^\circ$, 30° and 45° are measured separately using the biaxial tests under different confining stress σ_o ranging from 0.5 MPa to 3 MPa. A rectangular specimen of height 200 mm and width 100 mm is used. The specimen has a uniform particle radius distribution between 0.5 mm and 0.7 mm and the total number of the particles is about $15,000$. Since the stress-strain behaviors of the particle assembly are nonlinear, the tangent

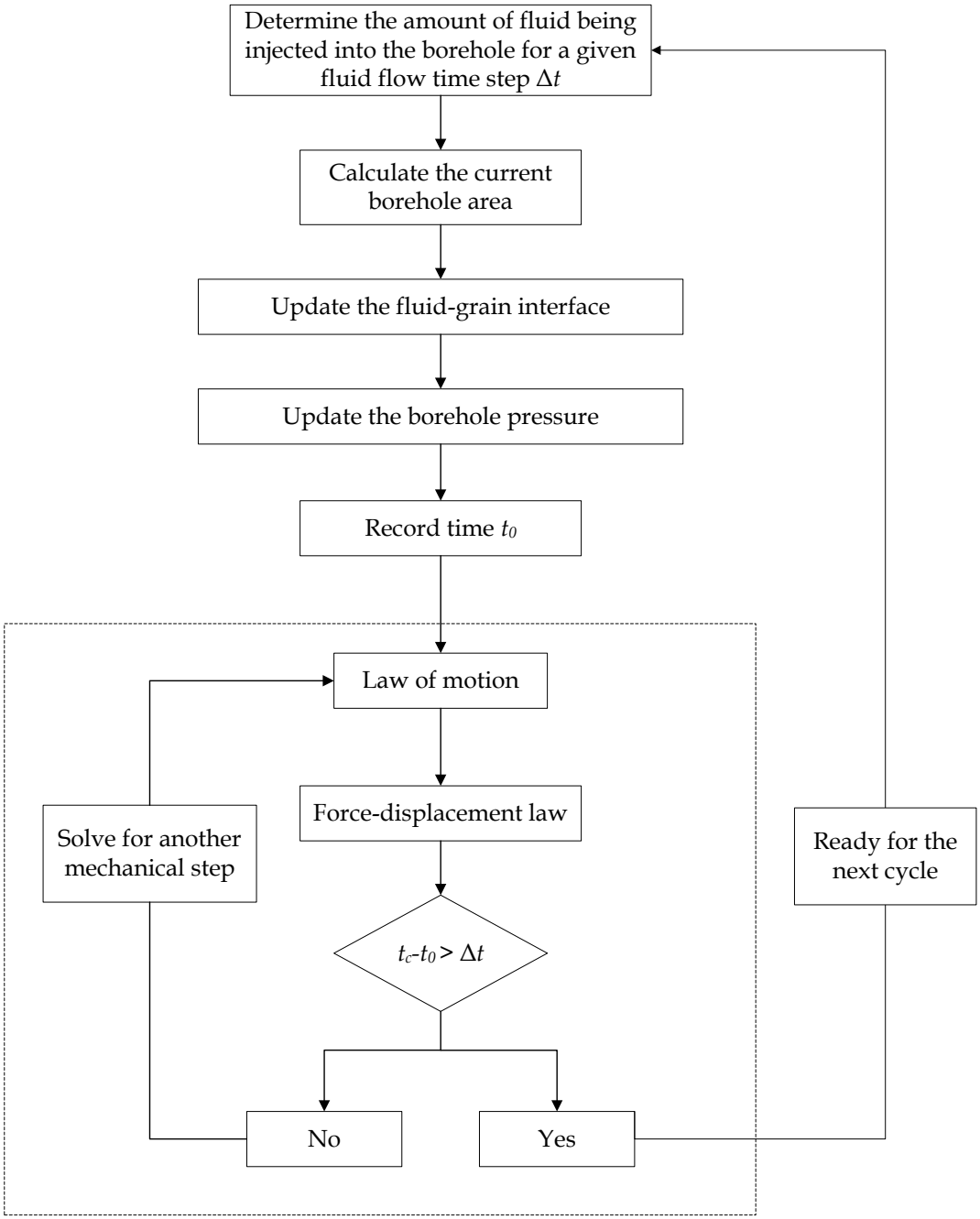

Figure 43: Flow chart of the constant flow rate implementation.

elastic modulus and the friction angle at the level of 50% peak stress are obtained as the index properties. Figs. 44 and 45 plot the elastic moduli and the peak friction angles of the three assemblies at different confining stresses. The macro-scale material constants for the cohesionless case are summarized in Table 11.

Table 10: Micro-scale properties of the particle assembly.

Grains	density	$\rho = 2650$ kg/m^3
	particle radius	$0.5 - 0.7$ mm
	friction	$\phi_b = 15^\circ,\ 30^\circ,\ 45^\circ$
	contact stiffness	$k_n = k_s = 0.417 \times 10^8$ N/m
	contact bond strength	$\bar{F}_n = \bar{F}_s = 0,\ 100,\ 500,\ 1000$ N
Interface chain	contact stiffness	$k_{nc} = k_{sc} = 0.417 \times 10^7$ N/m
	critical gap	$\delta_c/\bar{r} = 0.1,\ 0.3,\ 0.5$

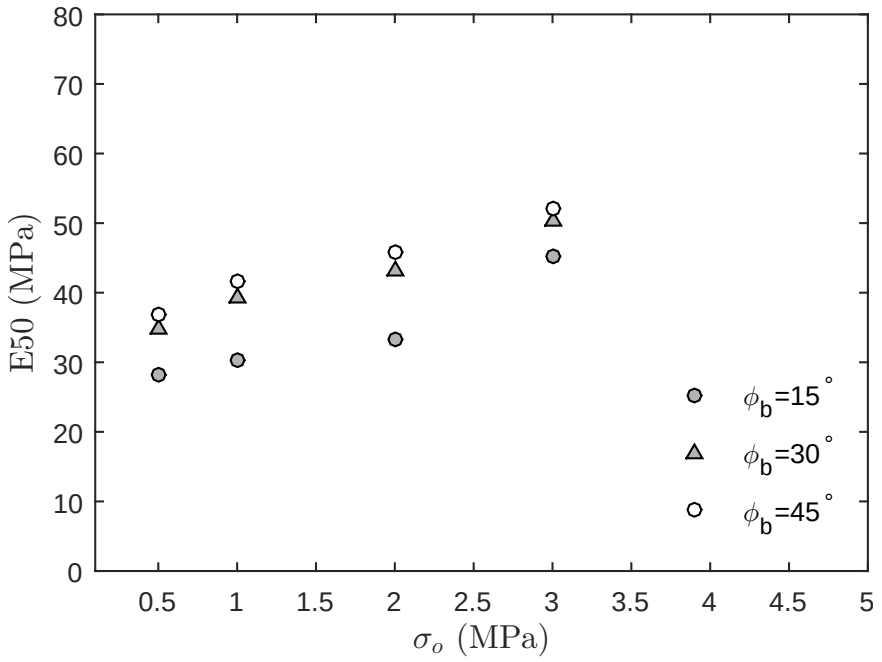

Figure 44: Variations of the elastic moduli of the purely frictional particle assembly as functions of the confining stress.

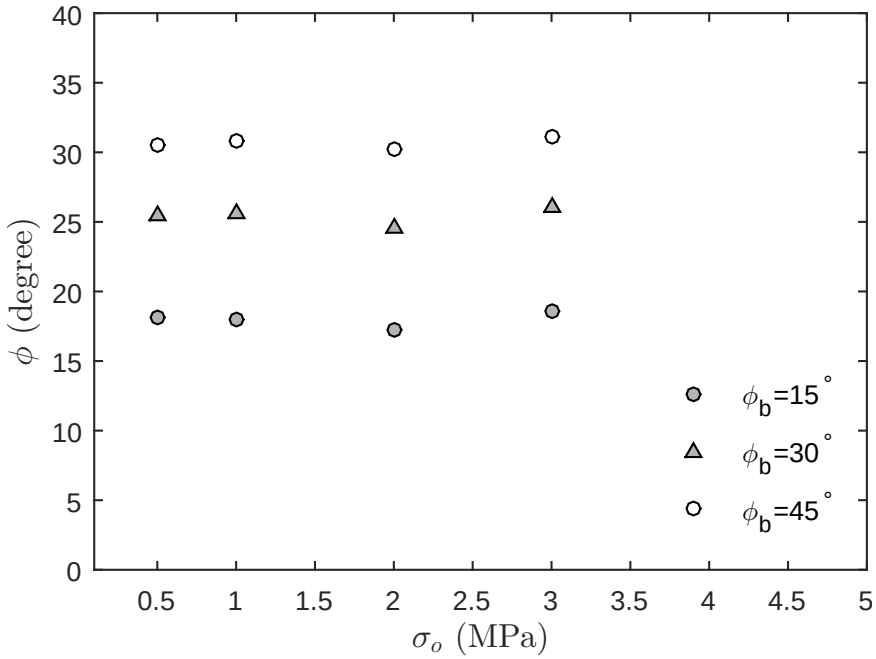

Figure 45: Variations of the peak friction angle of the purely frictional particle assembly as functions of the confining stress.

Table 11: Macro-scale properties of the purely frictional medium.

ϕ_b (°)	σ_o (MPa)	E50 (MPa)	ϕ (°)
15	0.5	28.2	18.08
	1	30.3	17.92
	2	33.2	17.29
	3	45.1	18.59
30	0.5	34.7	25.49
	1	39.2	25.67
	2	43.0	24.58
	3	50.4	26.03
45	0.5	36.9	30.46
	1	41.6	30.87
	2	45.8	30.16
	3	52.1	31.19

The macro-scale material strength parameters of the particle assembly with various normal and shear bond strengths are measured separately by the direct tension test, the uniaxial compression test, and the biaxial test under the confining stress of $\sigma_o = 1$ MPa (Table 12). The elastic modulus is mostly related to the particle stiffness and is therefore not significantly affected by the bond strengths. The maximum contact strengths assigned to the bonds are $\bar{F}_n = \bar{F}_s = 1000$ N, which result in a uniaxial compressive strength σ_c of 1227.5 kPa and a tensile strength σ_t of 446.2 kPa. After the start of the uniaxial compression and direct tension tests with $\bar{F}_n = \bar{F}_s = 100$ N, since the initial locked-in contact forces in the particle assembly are mostly larger than the bond strengths, the load drops instantaneously once it's applied. In other words, the particle assembly is effectively cohesionless. Therefore, σ_c and σ_t are both taken as zero for the case with $\bar{F}_n = \bar{F}_s = 100$ N.

Table 12: Macro-scale properties of the cohesive medium.

$\bar{F}_n,\ \bar{F}_s$ (N)	E50 (MPa)	ϕ (°)	σ_c (kPa)	σ_t (kPa)
100	39.2	25.87	0	0
500	40.2	26.49	576.4	181.0
750	41.2	28.23	910.3	318.1
1000	41.8	31.08	1227.5	446.2

5.4 Parametric Study

In this section, we uses the proposed numerical methodology to study the fluid injection process into the unconsolidated or weakly consolidated medium. Parametric analysis on the effects of the confining stress, the critical opening size for the fluid to penetrate through, the particle friction angle, the size of the initial borehole, the injection rate and the contact bond strengths is performed. A total of 39 numerical are conducted (details of the parameters in each test are listed in Appendix A), which includes 30 tests for the cohesionless medium and 9 tests for the cohesive medium. The test name refers to the ratio of the critical gap size over the average radius $\delta_c/\bar{r}$, confining stress σ_o in MPa, the ratio of the outer over inner diameter $D_{\text{out}}/D_{\text{in}}$, the injection rate Q in m^2/s, the particle friction angle ϕ_b in degree, and the contact bond strengths $\bar{F}_n$ and $\bar{F}_s$ in N, if there is cohesion. For

example, test 0.1_0.5_20_0.1_30 is a case with a cohesionless particle assemby and $\delta_c/\bar{r} = 0.1$, $\sigma_o = 0.5$ MPa, $D_{\text{out}}/D_{\text{in}} = 20$, $Q = 0.1$ m^2/s and $\phi_b = 30°$. Test 0.5_1_10_0.1_30_c1000 is a case with a cohesive particle assembly and $\delta_c/\bar{r} = 0.5$, $\sigma_o = 1$ MPa, $D_{\text{out}}/D_{\text{in}} = 10$, $Q = 0.1$ m^2/s, $\phi_b = 30°$, and $\bar{F}_n = \bar{F}_s = 1000$ N.

5.4.1 Effect of the Critical Gap Size and the Confining Stress

A series of 9 tests are carried out at a constant injection rate $Q = 0.1$ m^2/s with various confining stresses $\sigma_o = 0.5,\ 1$, and 5 MPa and critical gap sizes $\delta_c/\bar{r} = 0.1$, 0.3, and 0.5. The displacement patterns from the series of the injection tests around the peak pressure stage and at a post peak stage are shown in Figs. 46 and 47. The particles on the interface chain are marked in green. Red circle indicate initial borehole positions.

Overall, a transition from radial expansion of the cavity at initial stage and the growth of localized features is observed. At the early stage of injection, the wellbore expands and the shape remains more or less circular. However, as the injection continues, the borehole shape becomes distorted. Localized features start to form. The injection pressure reaches the peak around the moment when these localized features form. Fig. 48 plots the schematic of particle arrangement near the cavity and two possible failure modes. Starting from the state shown in Fig. 48 (a), if the medium is nearly homogeneous and the initial borehole is perfectly circular, the cavity should remain circular and expands radially. Nevertheless, the assembly is randomly generated with particle size following a uniform distribution and the interface chain itself is flexible. Borehole distortion and localized deformation are therefore expected.

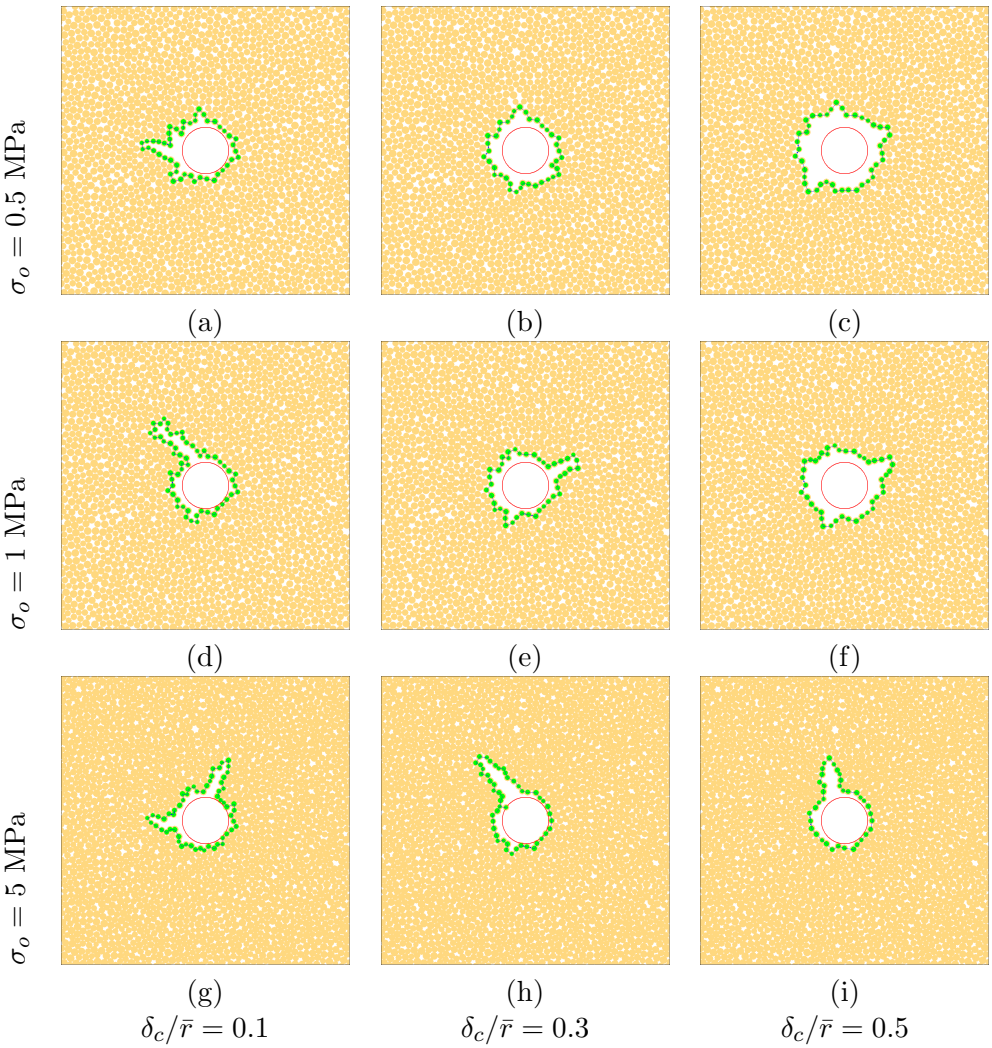

Figure 46: Morphologies of the fluid-grain interface for the tests with $\phi_b = 30°$, $Q = 0.1$ m^2/s and $D_{\text{out}}/D_{\text{in}} = 20$ around the peak pressure stages, showing only the near-borehole vicinity; injected fluid volume, (a) $Qt = 50.2$ mm^2 (b) $Qt = 95.3$ mm^2 (c) $Qt = 147.4$ mm^2; (d) $Qt = 55.7$ mm^2 (e) $Qt = 95.0$ mm^2 (f) $Qt = 153.1$ mm^2; (g) $Qt = 50.2$ mm^2 (h) $Qt = 51.1$ mm^2 (i) $Qt = 52.9$ mm^2.

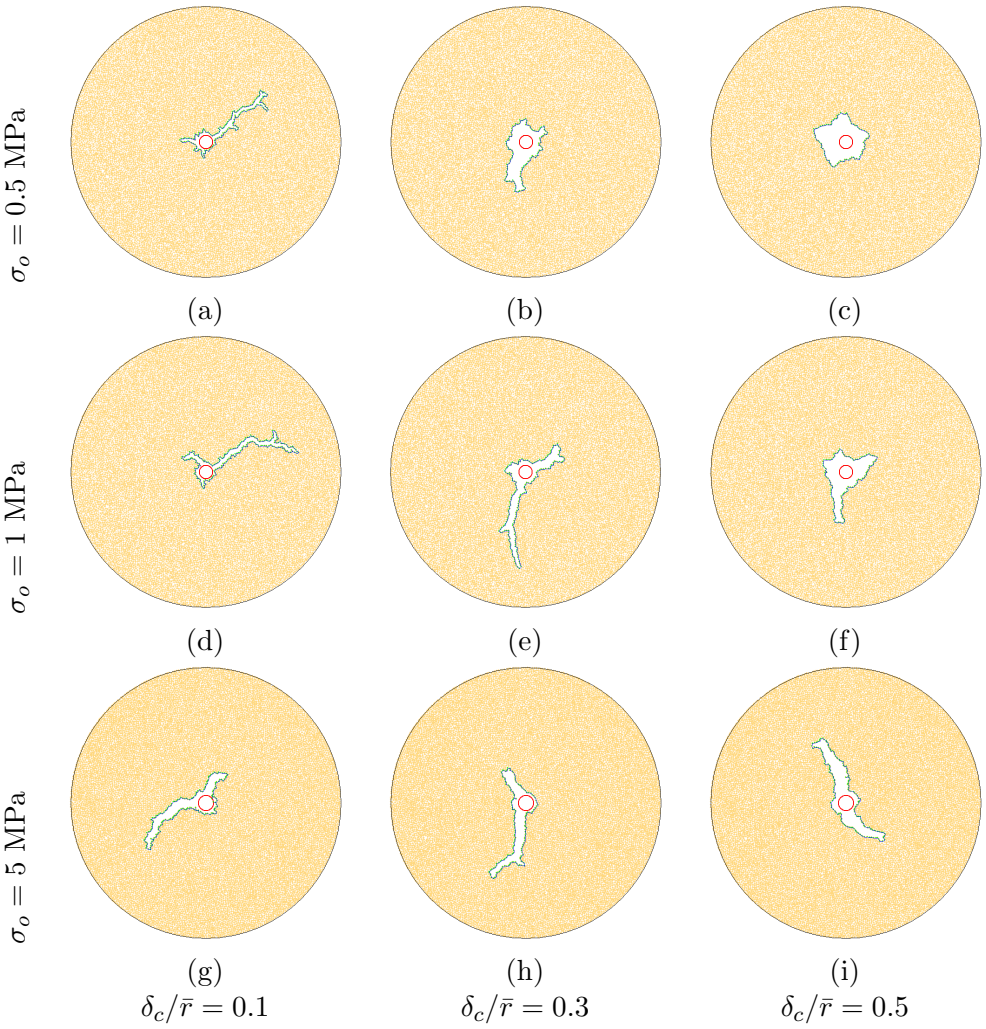

Figure 47: Morphologies of the fluid-grain interface for the tests with $\phi_b = 30°$, $Q = 0.1$ m^2/s and $D_{\text{out}}/D_{\text{in}} = 20$ at post peak stages; (a) $Qt = 247.7$ mm^2 (b) $Qt = 694.5$ mm^2 (c) $Qt = 894.9$ mm^2 (d) $Qt = 307.8$ mm^2 (e) $Qt = 644.8$ mm^2 (f) $Qt = 739.3$ mm^2 (g) $Qt = 405.3$ mm^2 (h) $Qt = 499.1$ mm^2 (i) $Qt = 640.1$ mm^2.

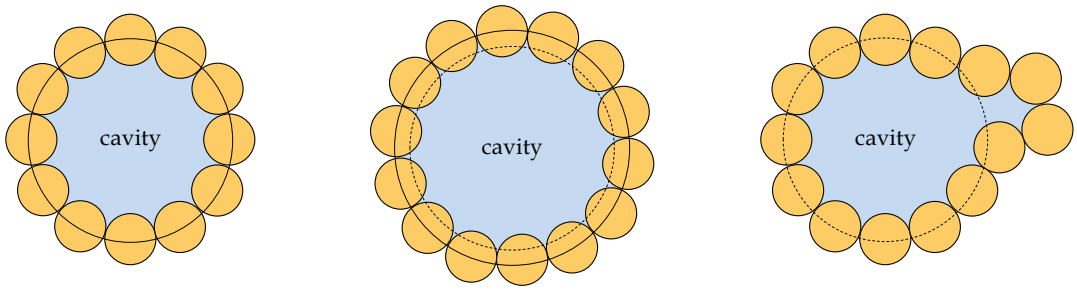

(a) (b) (c)

Figure 48: Schematic of the particle arrangement around the cavity and the two possible displacement modes: (a) initial state, (b) radial expansion of the borehole and (c) borehole distortion.

It can be seen from the first test series in Figs. 46 and 47 (a)-(c) with a low confining stress, $\sigma_o = 0.5$ MPa, borehole expansion is more significant in the pre-peak stage if the critical gap size $\delta_c/\bar{r}$ is larger. For $\delta_c/\bar{r} = 0.1$ and $\sigma_o = 0.5$ MPa, one small "branch" first appears around the peak injection pressure. But it does not extend outwards immediately. Instead, another branch is developed from the other side of the borehole. At the injection volume of $Qt = 247.7$ mm^2, a thin long finger-like feature with side branches (or kinks) can be observed. For $\delta_c/\bar{r} = 0.5$ and $\sigma_o = 0.5$ MPa, borehole expansion is the dominant growth mode for both the peak stage and the post peak stage. The amount of fluid being injected at the peak pressure for the $\delta_c/\bar{r} = 0.5$ case is more than that for the $\delta_c/\bar{r} = 0.1$ case. Furthermore, the relatively large critical gap size leads to notch-like features, instead of the finger-like features, even at a relatively large injection volume. The displacement patterns in the simulations with $\sigma_o = 1$ MPa are similar to their corresponding cases with $\sigma_o = 0.5$ MPa. The injection volumes at the peak stages are comparable too. When the confining stress increases to $\sigma_o = 5$ MPa, there is no longer substantial cavity expansion prior to the peak when $\delta_c/\bar{r} = 0.5$. The peak pressures are reached with much smaller injection volumes. The fingers are now wider, see Figs. 47 and 46 (g)-(i). At $\delta_c/\bar{r} = 0.1$ and 0.5, the fingers appear to be curved.

At the early stage, if the trajectory of a localized feature is in the radial direction, we may relate it to an opening mode growth mechanism. Meanwhile, if the trajectory deviates from

the radial direction, i.e., not perpendicular to the circumference of the borehole, we may then relate it to a shear mode. Judged by this simple criterion, both growth mechanisms are present in Fig. 46. For example, in Fig. 46 (h), the branch in the top appears to be of shear origin, whereas the one in Fig. 46 (i) seem to be of an opening mode. In the propagation stage in Fig. 47 (a), after the primary branch grows to a certain length, tip of the opening starts to split. One of the splitted tips becomes dominant and the main branch changes direction to propagate in a zig-zag fashion. When the critical gap size increases from $\delta_c/\bar{r} = 0.1$ to 0.3, or the confining stress increases from $\sigma_o = 0.5$ MPa to 5 MPa, the tortuosity decreases and the branch walls become relatively smooth. It is interesting to note that some of the branches in Fig. 47 (e)-(i) seem to be in a spiral-like shape, a signature associated with a shear band. The finger orientations are fitted by a spiral function and futher analyzed in Section 5.3.1.4.

5.4.1.1 Borehole Evolution

By tracking the centroids of the particles at the borehole boundary, evolution of the borehole geometry in terms of shape and the rate of borehole expansion is recorded at a constant time interval, see Fig. 49. For small critical gap size, the borehole develops into multiple fingers at very early stage. The fingers extends in length but the width remains nearly constant, as shown in Fig. 49 (a). For large critical gap size, the borehole expands uniformly prior to becoming distorted. The localized feature grows in both length and width, as shown in Fig. 49 (c).

If we translate the effect of the critical gap size to the effect of surface tension or fluid viscosity, this means that injection with a low viscosity fluid at a low confining stress is likely to create long thin features of nearly constant width, while injection with a high viscosity fluid at a high confining stress is likely to create the fractures with the aperture decreasing with its length. Width at the tip of the fingers also increases with the critical gap size as well as the confining stress. These observations are similar to those from Chang's experiments [15], where the fracture created with a larger viscosity has a beveled fracture front while the fracture created with a lower viscosity has a relatively sharp fracture front.

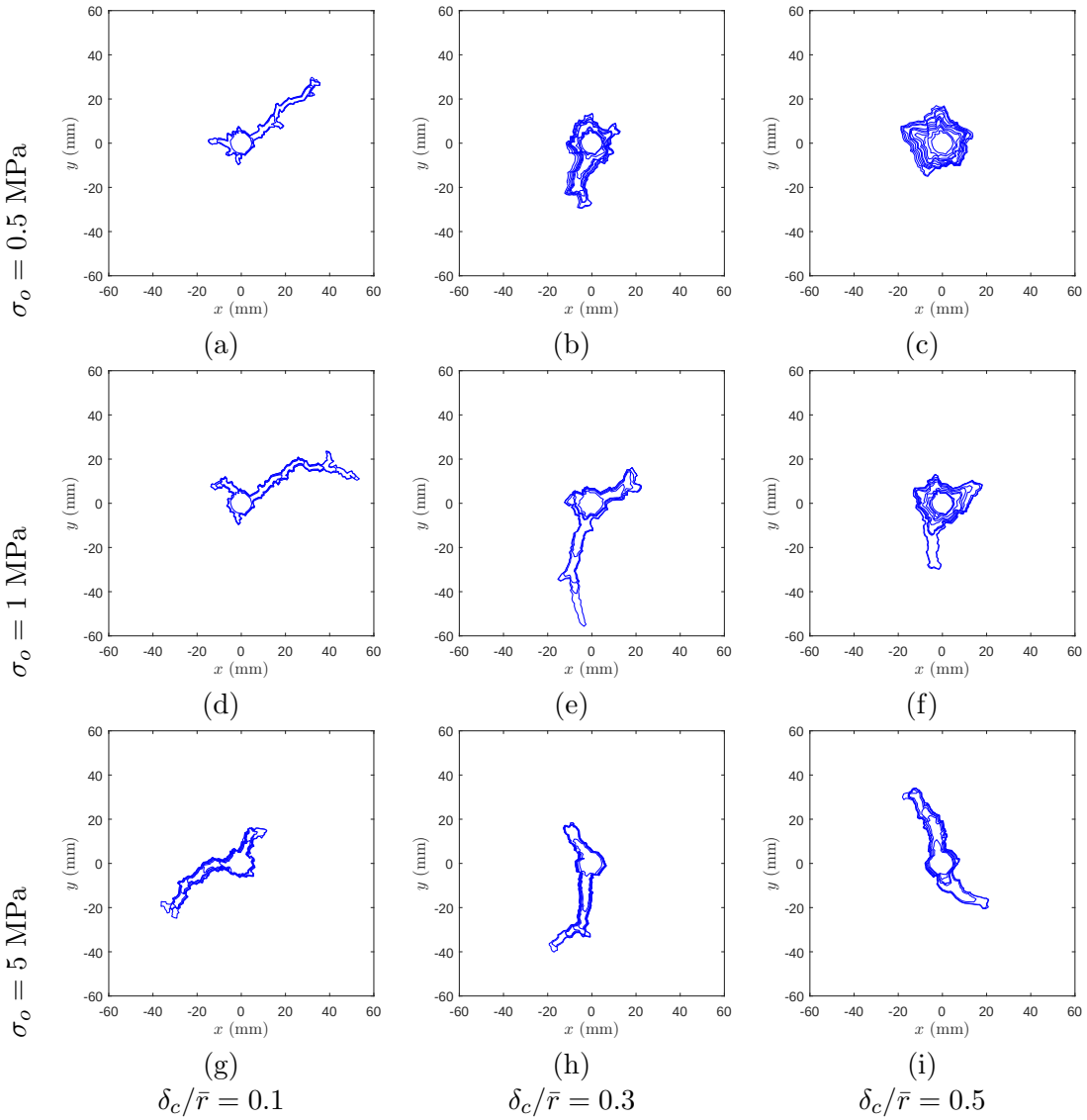

Figure 49: Evolution of the borehole profiles at $Q = 0.1$ m^2/s and $D_{\text{out}}/D_{\text{in}} = 20$.

The borehole profiles can be approximated by a discrete Fourier series [28],

$$R(\theta) = R_0 + \sum R_n \cos(n\theta - \phi_n) \tag{114}$$

where θ is the polar angle; n is the harmonic order; R_0 is the average borehole radius; R_n is the nth harmonic amplitude and ϕ_n is the phase angle. The Fourier analysis of the wellbore profiles for a representative test with $\sigma_o = 0.5$ MPa and $\delta_c/\bar{r} = 0.5$ is shown in Fig. 50. The amplitudes of the harmonic orders $n = 4$ and 5 are about the same as that of $n = 1$. This means that at the peak pressure stage, though the borehole shape is no longer a perfect circle, it remains nearly circular.

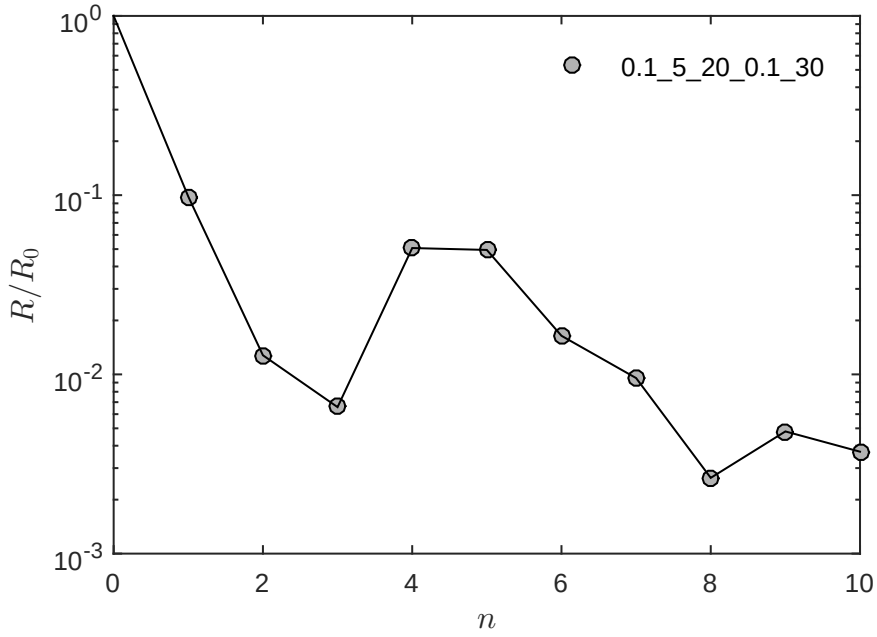

Figure 50: Normalized amplitude of the first ten harmonics at the peak stage for the case with $Q = 0.1$ m^2/s, $D_{\text{in}} = D_{\text{out}}/20$ and $\sigma_o = 0.5$ MPa.

5.4.1.2 Fracture Width and Orientation

To quantify the growth of the borehole and initiation of the fingers, we define three parameters: radius of the inscribed circle for the distorted wellbore, R_{max}, an apparent fracture width of the opening, $\bar{w}$, and a pitch angle ϕ of the spiral function fitted by the finger mid-line.

The inscribed circle is the largest possible circle that can be drawn on the inside of the

borehole profile as shown in Fig. 52 (a) and (b). The radius of the inscribed circle, R_{max}, is measured to reflect the amount of radial expansion.

The apparent fracture width of the opening is defined as,

$$\bar{w} = \frac{A - A^*}{S - S^*} \tag{115}$$

where A and S are the current area and the perimeter of the borehole respectively, $A^*$and S^* are the area and the perimeter of the maximum inscribed circle, defined as

$$A^* = \pi \left(R_{max}\right)^2, \qquad S^* = 2\pi R_{max} \tag{116}$$

The area and the perimeter of the maximum inscribed circle are subtracted from the current values to eliminate the amount of radial expansion while calculating the apparent width. Both the areas and the perimeters are determined based on the centroid-to-centroid distances of the particles on the interface chain.

Variations of the apparent width of the opening, $\bar{w}$, with the radius, R_{max}, are shown in Fig. 51 for the three tests with $\sigma_o = 0.5$ MPa, where $\bar{d}$ is the mean particle diameter and R_0 is the initial borehole radius. Since the borehole area is excluded in Eq. 115, the apparent width $\bar{w}$ can be considered as a measure of the half-width of the branches; $\bar{w}/\bar{d} \approx 1$ means the opening is about twice the mean particle diameter (including one particle diameter from the interface chain). It can be seen from Fig. 51, as the borehole expands, the width $\bar{w}$ increases nearly linearly in the tests with $\delta_c/\bar{r} = 0.3$ and 0.5. For the test with $\delta_c/\bar{r} = 0.1$, the width and the radius remain more or less a constant of 1. At the same injection volume, the width increases with the critical gap size δ_c.

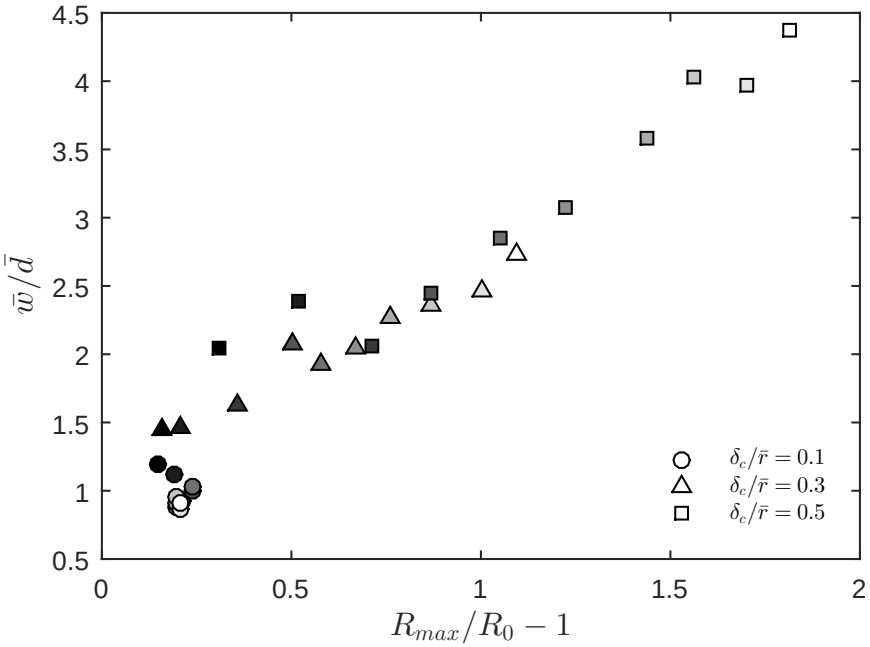

Figure 51: Variations of the apparent width of the opening, $\bar{w}$, with the radius, R_{max}, of the largest inscribed circle at various stages of the simulations for the three tests with $\sigma_o = 0.5$ MPa; the grey scale indicates the injection stage, black corresponds to early stages and white late stages.

The numerical results imply that if the fluid viscosity is relatively low (small $\delta_c/\bar{r}$), the localized feature tends to be narrow (small $\bar{w}/\bar{d}$). The injected volume mostly goes into extending the finger-like features in length, instead of expanding the borehole or widening the localized features. On the other hand, if the fluid viscosity is high, significant borehole expansion should be expected and the localized features tend to be wider.

To fit the finger by a spiral function, we need to identify the mid-lines of the fingers. The boundary of the borehole is first converted to a binary image. Each point inside the borehole boundary is assigned a number indicating the distance between that point and the nearest point on the boundary. The information is then processed by plotting a contour plot, see Fig. 52 (c) and (d) . The mid-line, which consists of points with the furthest distance from the boundary, is therefore plotted as white dots in Fig. 52 (e) and (f). Finally, the white dots representing fracture mid-lines are fitted by logarithmic spiral functions in polar

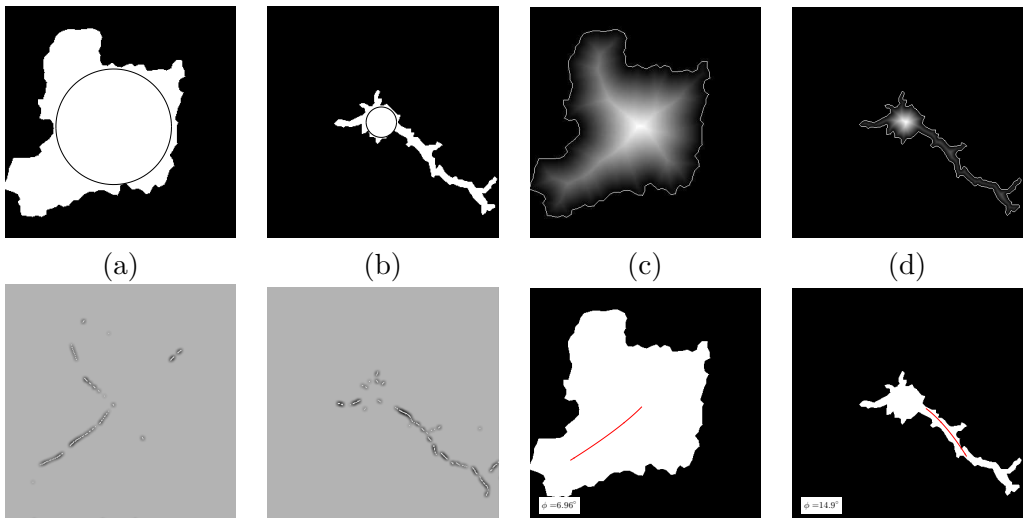

Figure 52: Procedure to find inscribed circles, fracture mid-lines and pitch angles, (a) and (b): inscribed circles of two borehole profiles; (c) and (d): contour plots of the distance to the nearest boundary; (e) and (f): fracture mid-lines; (g) and (h): fitted fracture mid-lines

coordinates (r, θ) in the form of,

$$r = a \exp(b\theta) \tag{117}$$

with a and b being constant coefficients. For an arbitrary point on the spiral, the angle between the tangent and radial line is constant, which is called the pitch angle ψ.

$$\psi = \arctan \frac{1}{b} \tag{118}$$

The larger the pitch angle, the tighter the spiral. In the limit when $\psi = 90°$, the spiral is a circle; and when $\psi = 0°$, the spiral becomes a straight line.

In Fig. 53, the pitch angles for the fingers in the 9 tests are plotted. For the tests with multiple fingers, the pitch angle of each fracture is represented by a marker of the same color and style in Fig. 53. Overall, the fingers at low confining stress are less tortuous than those at high confining stress.

5.4.1.3 Shear Deformation

Fig. 54 plots contours of the particle rotational velocity for the 9 numerical tests. The magnitude of the color map represents the rotational velocity in rad/s. The particle rotational velocity can be considered as a measure of the shear strain rate. The larger the particle

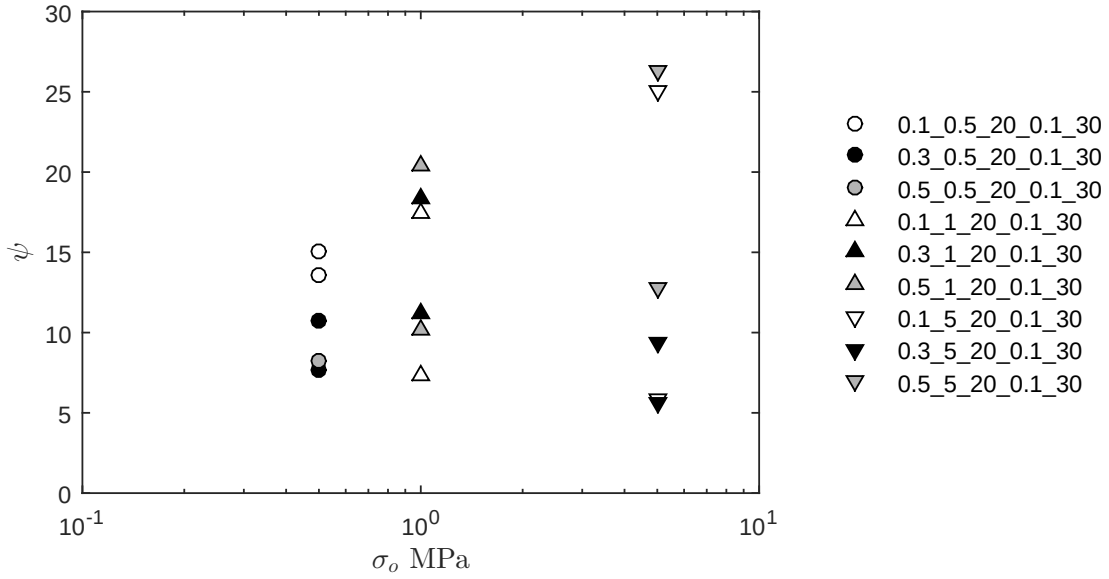

Figure 53: Fracture pitch angle with various confining stress and critical gap size at $Q = 0.1$ m^2/s and $D_{\text{out}}/D_{\text{in}} = 20$.

rotational velocity, the greater the shear strain rate. Though these contours are only snapshots at those particular post peak moments, we can still infer from the plots that active growth of the localized features are related to intense shear deformation. For the finger-like features, the shear deformation is localized near the tips. However, large borehole expansion could result in growth of long spiral shaped shear bands emitting from the inner wall and extending all the way to the outer boundary, see Fig. 54(c), as would be expected from an elasto-plastic analysis when the full domain is in plastic yield. Shear banding associated with fluid injection has also been observed in a DEM coupled CFD analysis in Zhang and Huang [106] and experimental work in MacMinn *et al.* [68].

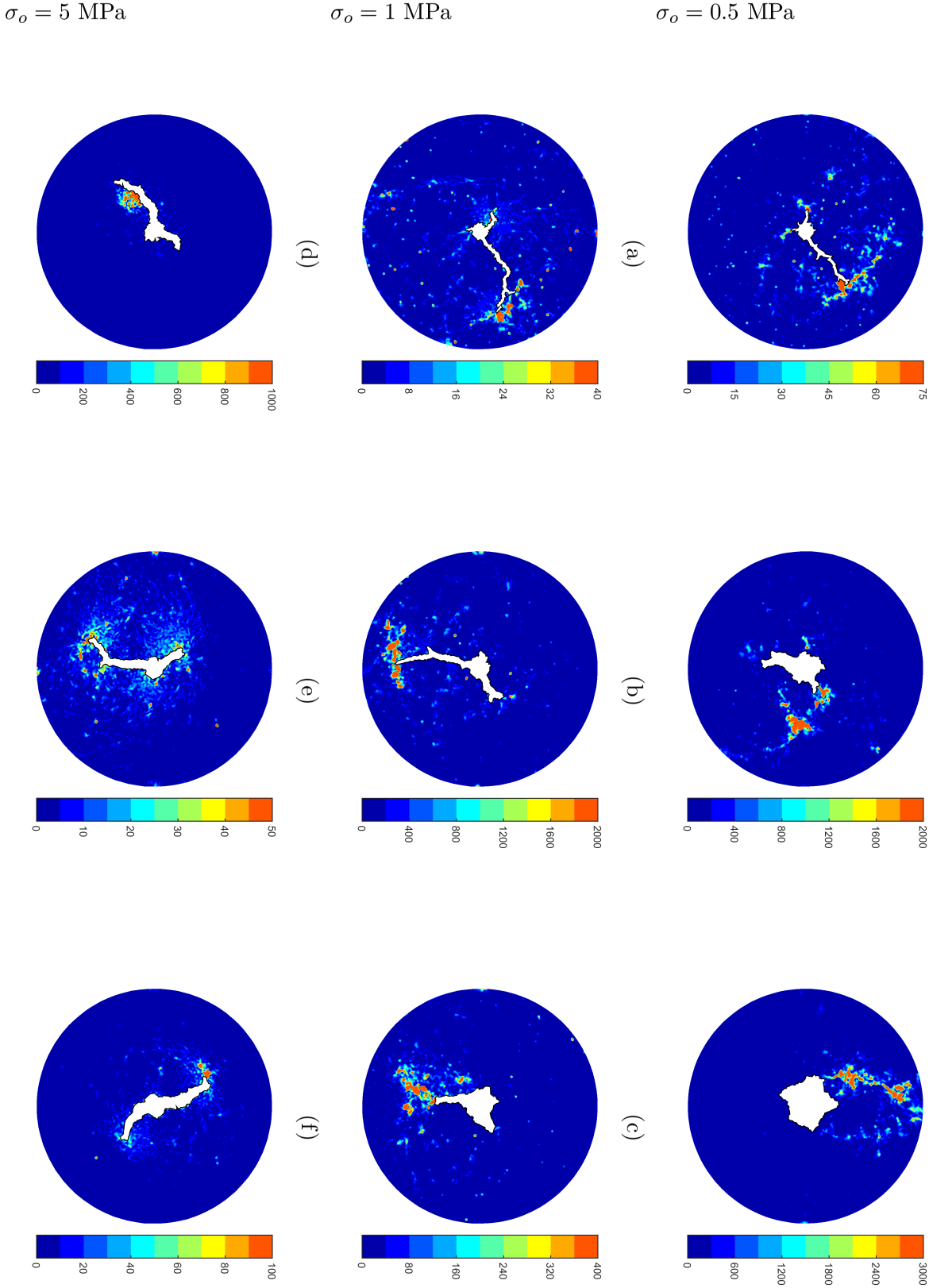

Figure 54: Particle rotational velocity at $Q = 0.1$ m^2/s and $D_{\text{out}}/D_{\text{in}} = 20$.

5.4.1.4 Pressure History

Histories of the net borehole pressure, ΔP, from the three numerical simulation cases at $\sigma_o = 1$ MPa are plotted in Fig. 55. The net borehole pressure is defined as $\Delta P = P - \sigma_o$, where P is the absolute borehole pressure and σ_o is the confining stress. As can be seen from Figs. 55, the pressure histories from the numerical simulations all exhibit sudden drops and rebounds. The drops and the rebounds are partly reflecting the physical process of borehole expansion or the extension of the finger-like features and partly due to the discretization in time in implementing the constant rate boundary condition.

In general, the pressure histories from the numerical simulations may be divided into two stages. The first stage is the early rising part before the pressure reaches a peak. Note that in Figs. 46 (d)-(f), at the end of this first stage, the borehole shape remains nearly circular, but there are initiations of localized features. The first stage ends earlier if the critical gap size is smaller. Pressure histories in this first stage are compared with theoretical solutions in Chapter VI. The second stage corresponds to the extension of the finger-like features or further expansion and distortion of the borehole. In this stage, the pressure remains nearly constant or declines slightly within the observation period.

The results in Fig. 55 suggest that given the same injection rate, the fracturing pressure is lower if $\delta_c/\bar{r}$ is smaller. This is not surprising since the critical gap size embodies an energy dissipation mechanism for fracture growth. What the numerical results mean is that if less energy is spent in propagating the fracture, the fracture pressure is then lower, which is consistent with fracture mechanics in a continuum.

Injection pressure and the injection volume at the peak stages for the 9 tests is complied in Table 13. Overall, the net injection pressure at the peak stage shows an increasing trend with the confining stress. However, the ratio $\Delta P_{max}/\sigma_o$ decreases with the confining stress. Simillar observation was made in Bohloli and de Pater [10], where the ratio $\Delta P_{max}/\sigma_o$ increases from 1.1 to around 3 when the concentration of cross-linked gel increases from 20 lb/1000 gal to 50 lb/1000 gal. The increase in concentration results in a higher viscosity, which is analogous to the increased critical gap size in our numerical tests.

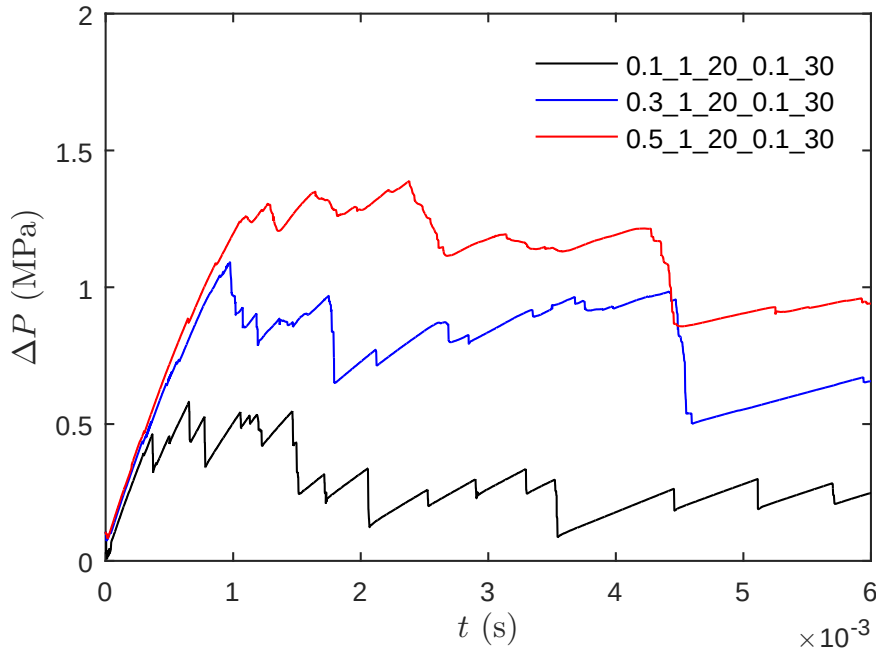

Figure 55: Pressure history at $Q = 0.1$ m^2/s, $D_{\text{out}}/D_{\text{in}} = 20$ and $\sigma_o = 1$ MPa

Table 13: Injection pressure and the injection volume at the peak stages for the tests with $D_{\text{out}}/D_{\text{in}} = 20$, $Q = 0.1$ m^2/s and $\phi_b = 30°$.

Test Name	$\delta_c/\bar{r}$	σ_o (MPa)	ΔP_{max} (MPa)	$\frac{\Delta P_{max}}{\sigma_o}$	P_{max} (MPa)	$\frac{P_{max}}{\sigma_o}$	Qt (mm^2) around peak
0.1_0.5_20_0.1_30	0.1	0.5	0.55	1.11	1.05	2.10	50.2
0.3_0.5_20_0.1_30	0.3	0.5	0.84	1.65	1.34	2.68	95.3
0.5_0.5_20_0.1_30	0.5	0.5	0.94	1.88	1.44	2.88	147.4
0.1_1_20_0.1_30	0.1	1	0.58	0.58	1.58	1.58	55.7
0.3_1_20_0.1_30	0.3	1	1.09	1.09	2.09	2.09	95.0
0.5_1_20_0.1_30	0.5	1	1.39	1.39	2.39	2.39	153.1
0.1_5_20_0.1_30	0.1	5	1.35	0.27	6.35	1.27	50.2
0.3_5_20_0.1_30	0.3	5	1.74	0.35	6.74	1.35	51.1
0.5_5_20_0.1_30	0.5	5	2.10	0.42	7.10	1.42	52.9

5.4.2 Effect of Borehole Size

Fig. 56 shows morphologies of the fluid-grain interface of 9 tests with different initial borehole sizes, $D_{\text{out}}/D_{\text{in}} = 20,\ 10$ and 5, various confining stresses, $\sigma_o = 0.5$, 1, and 5 MPa and $\delta_c/\bar{r} = 0.3$. Overall, the displacement patterns depend on both the borehole size and the degree of confinement. At low confining stress $\sigma_o = 0.5$ MPa, for about the same injection volume, the large borehole with $D_{\text{out}}/D_{\text{in}} = 5$ still remains circular, while notch-like features have already developed in the small borehole with $D_{\text{out}}/D_{\text{in}} = 20$. This could be explained by the fact that there are fewer particles around the borehole with $D_{\text{out}}/D_{\text{in}} = 20$. Given the same radial expansion, the average gap between particles resulted from the expansion is inversely proportional to the number of particles and is larger in the smaller borehole radius case. Localization and the peak injection pressure are therefore reached earlier in the case with a smaller initial borehole. At high confining stress $\sigma_o = 5$ MPa, the finger-like features have all developed in all three cases.

5.4.3 Effect of Flow rate

A series of 9 tests were performed to vary the injection rate, $Q = 1,\ 10,$ and 50 m^2/s, and the confining stress, $\sigma_o = 0.5,\ 1,\ 5$ MPa, to investigate their influences on the displacement patterns at $\delta_c = 0.1$, as shown in Fig. 57. One or more fingers are created from the borehole boundary. With an increasing injection rate, the number of fingers increases. Most of the fingers are aligned radially. It is also observed that with greater injection rate side branches and tip splitting occur at later stages, e.g. Fig. 57 (c)(f)(i). Two representative cases are selected to further investigate the initiation and propagation processes.

Two types of fracturing processes are observed at a low or high injection rate. Fig. 58 shows the early time behaviors for the test in Fig. 57 (h) with $\sigma_o = 5$ MPa and $Q = 10$ m^2/s. After the injection starts, a short finger is created from the borehole. As the injection continues, the thin feature starts to widen, and the sharp tip becomes blunt and starts to split. At the same time, a second fracture is developed from the borehole and the first one is arrested. Eventually, two main fractures are developed near the borehole.

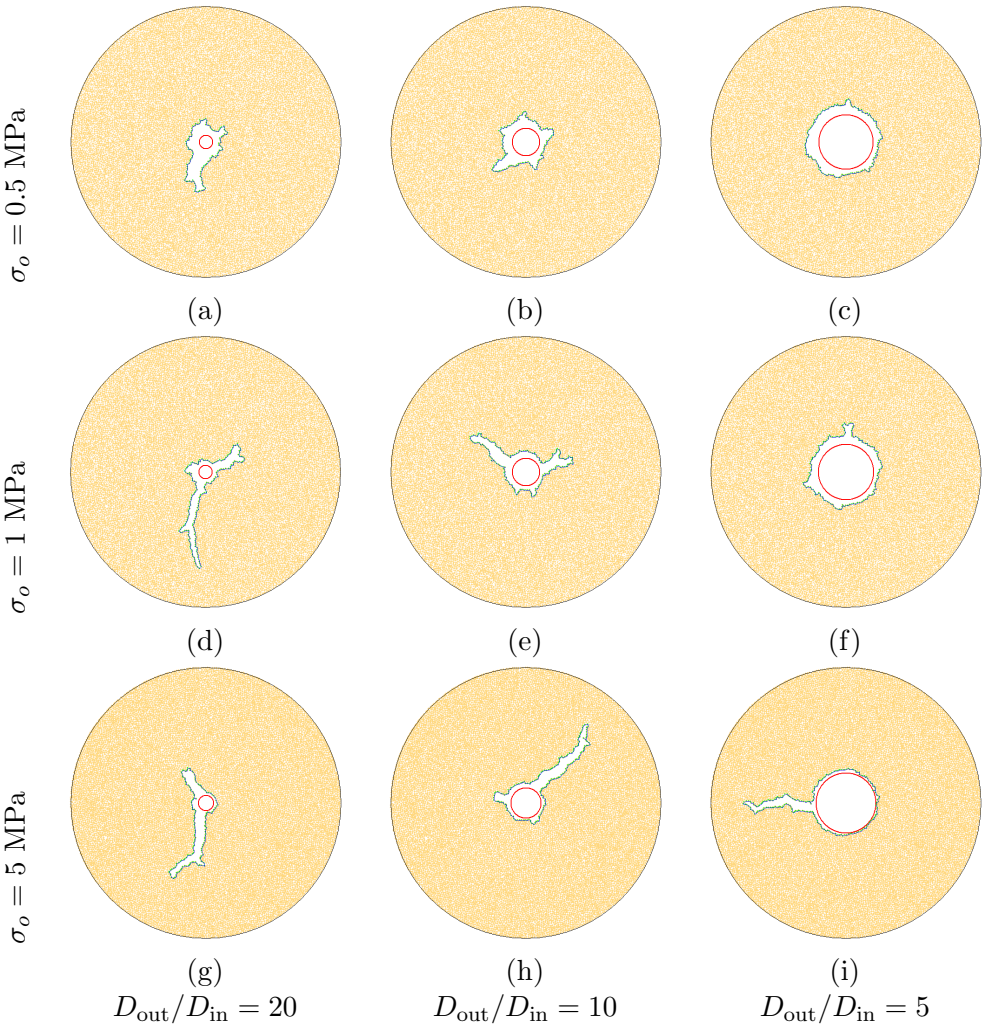

Figure 56: Morphologies of the fluid-grain interface for the tests with $\phi_b = 30°$, $Q = 0.1$ m^2/s and $\delta_c/\bar{r} = 0.3$; (a) $Qt = 694.5$ mm^2 (b) $Qt = 752.0$ mm^2 (c) $Qt = 760.5$ mm^2 (d) $Qt = 644.8$ mm^2 (e) $Qt = 701.9$ mm^2 (f) $Qt = 750.9$ mm^2 (g) $Qt = 499.1$ mm^2 (h) $Qt = 459.5$ mm^2 (i) $Qt = 395.3$ mm^2 .

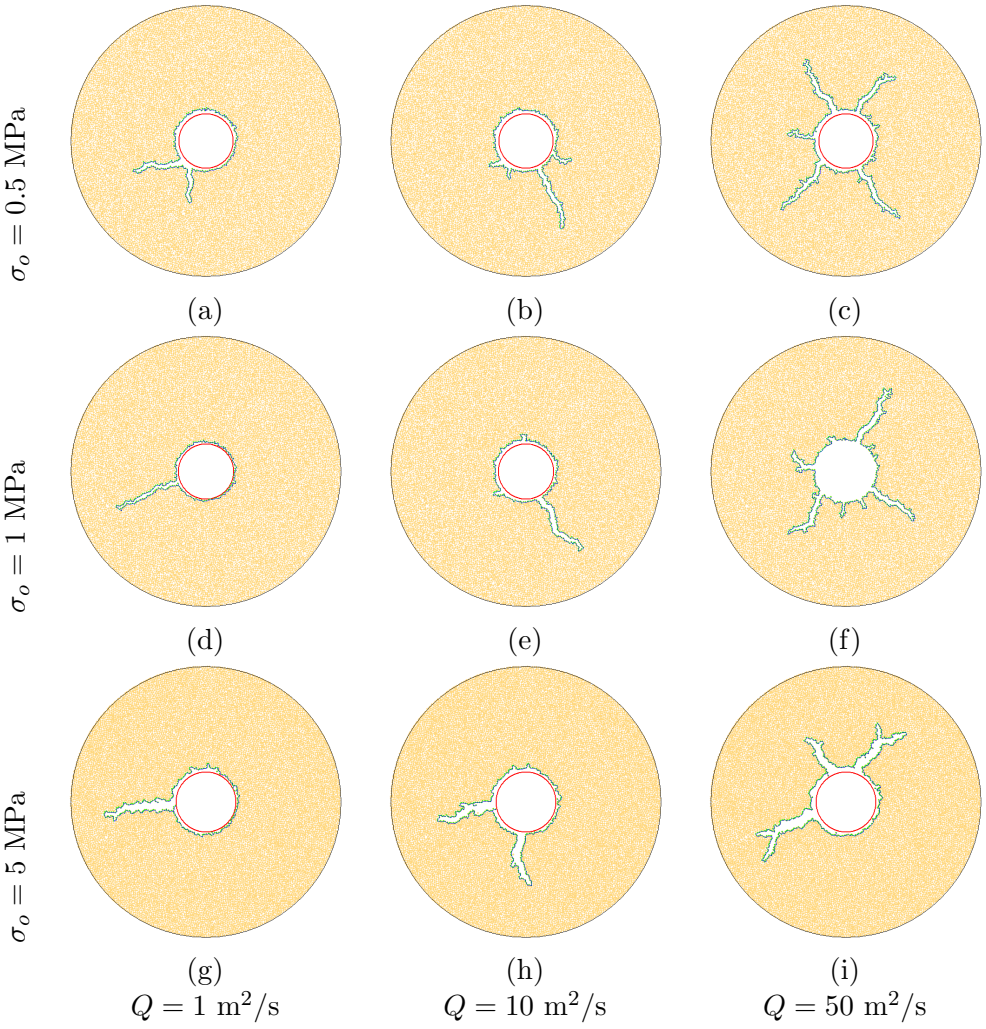

Figure 57: Morphologies of the fluid-grain interface for the tests with $\phi_b = 30°$, $D_{\text{out}}/D_{\text{in}} = 5$ and $\delta_c/\bar{r} = 0.1$ at a post peak stage; (a) $Qt = 492.5$ mm^2 (b) $Qt = 543.4$ mm^2 (c) $Qt = 907.7$ mm^2 (d) $Qt = 205.0$ mm^2 (e) $Qt = 486.3$ mm^2 (f) $Qt = 852.8$ mm^2 (g) $Qt = 407.5$ mm^2 (h) $Qt = 611.5$ mm^2 (i) $Qt = 901.6$ mm^2 at

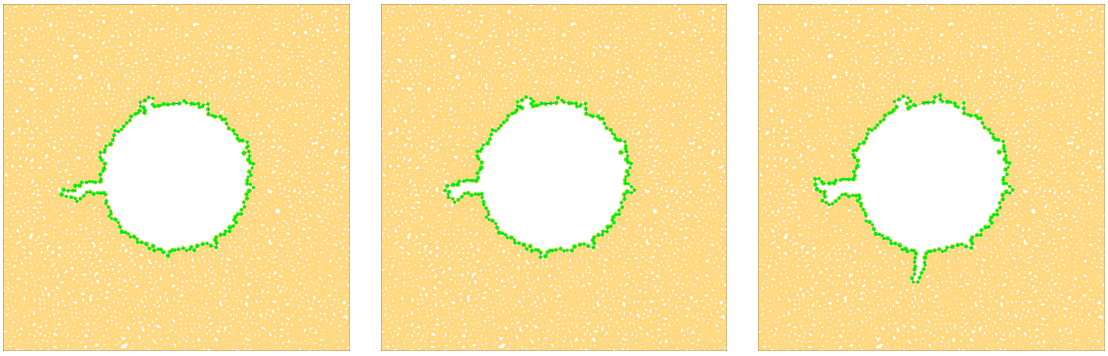

(a) (b) (c)

Figure 58: Evolution of displacement patterns for test with $D_{\text{out}}/D_{\text{in}} = 5$, $\delta_c/\bar{r} = 0.1$, $\sigma_o = 5$ MPa and $Q = 10$ m^2/s, showing only the near borehole region.

The early time behaviors from the test in Fig. 57 (f) with $\sigma_o = 0.5$ MPa and $Q = 50$ m^2/s are shown in Fig. 59. Different from the previous case, multiple small fingers are initiated near the borehole simultaneously after the injection starts. Some of the fingers are able to extend outward, while the others are arrested. Further extension of the fingers lead to a borehole with multiple more or less radial cracks of various lengths in Fig. 59 (c). The arrest of some shorter fingers could perhaps be attributed to the compaction of the materials resulted from the extension and widening of the neighboring fingers.

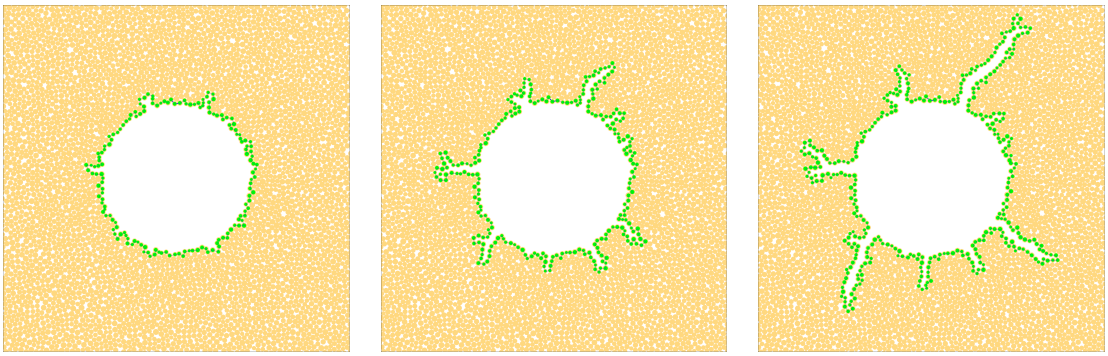

(a) (b) (c)

Figure 59: Evolution of displacement patterns for test with $D_{\text{out}}/D_{\text{in}} = 5$, $\delta_c/\bar{r} = 0.1$, $\sigma_o = 0.5$ MPa and $Q = 50$ m^2/s, showing only the near borehole region.

5.4.4 Effect of Friction Angle

Fig. 47 includes a series of 9 test carried out at various particle friction angles, $\phi_b = 15°$, $30°$ and $45°$, and critical gap sizes, $\delta_c/\bar{r} = 0.1,\ 0.3$ and 0.5. The macro-scale friction angles are $\phi = 17.92°$, $25.67°$ and $30.87°$, respectively. The effect of friction with $\delta_c/\bar{r} = 0.1$ is not obvisous: thin fingers are formed in all three particle assemblies with different friction angles. Comparing cases (c) and (i) in Fig. 47 at $\delta_c/\bar{r} = 0.5$, given about the same injection volume, the particle assembly with $\phi_b = 45°$ has two fingers while that with $\phi_b = 15°$ only exhibits a slightly distorted borehole. The results indicate that the borehole in a high friction assembly is more susceptible to opening mode growth, while the borehole in low friction assembly is more likely to expand radially.

Fig. 61 plots contours of the particle rotational velocity for the 9 numerical tests. The magnitude of the color map represents the rotational velocity in rad/s. For the test with the lower friction angle, the high viscosity fluid case ($\delta_c/\bar{r} = 0.5$) results in growth of multiple long spiral shaped shear bands emitting from the inner wall; the low viscosity fluid cases ($\delta_c/\bar{r} = 0.1$) produces thin fingers localized shear failure near the tip. For the tests with the higher friction angle, finger-like features are developed, with fluids of both high and low $\delta_c/\bar{r}$. However, the fingers in the test with high δ_c are wider. It can be seen that shear bands are easier to develop in formations with lower friction angle. With greater particle friction, the resistance to the sliding is greater, the the medium tends to deform in an opening mode.

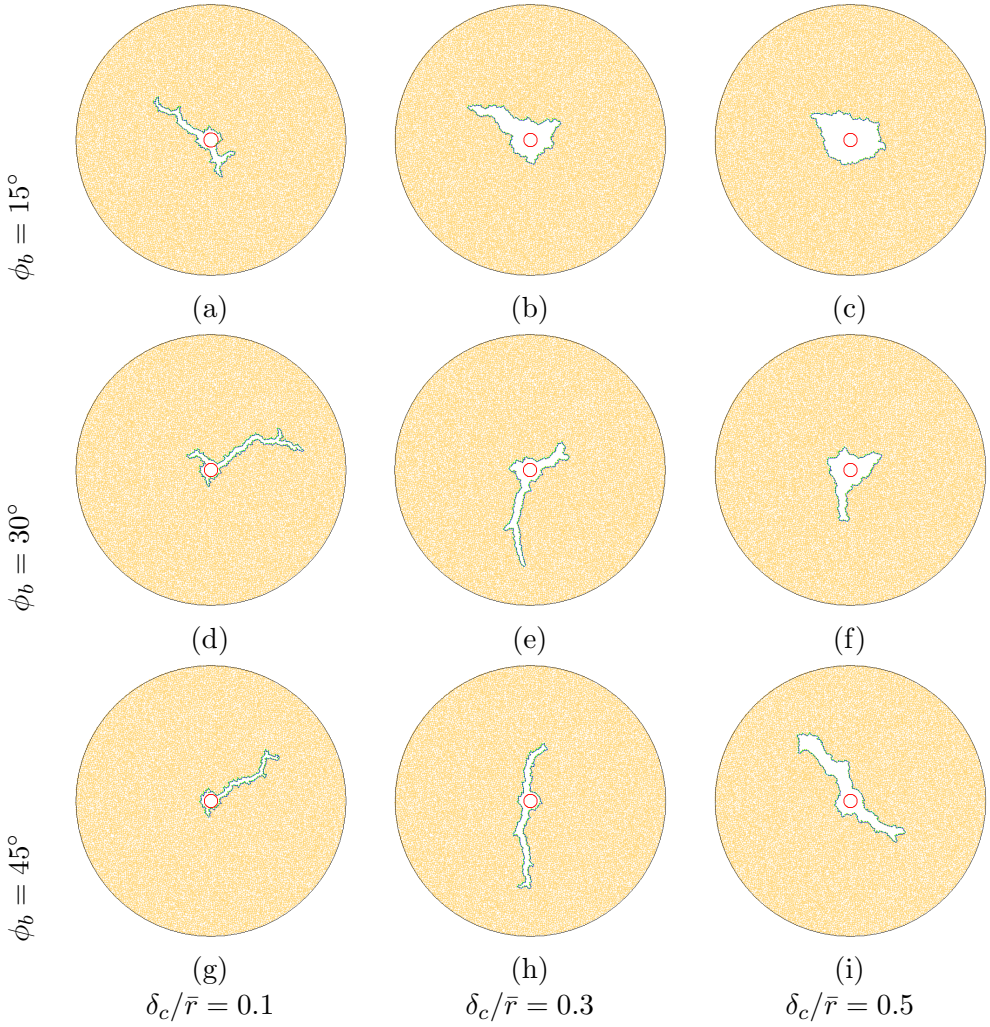

Figure 60: Morphologies of the fluid-grain interface with different particle friction angle and gap size at $D_{\text{out}}/D_{\text{in}} = 20$ and $\sigma_o = 1$ MPa for: (a) $Qt = 346.4$ mm^2 (b) $Qt = 993.9$ mm^2 (c) $Qt = 1292.7$ mm^2 (d) $Qt = 307.8$ mm^2 (e) $Qt = 644.8$ mm^2 (f) $Qt = 739.3$ mm^2 (g) $Qt = 204.7$ mm^2 (h) $Qt = 493.3$ mm^2 (i) $Qt = 1063.3$ mm^2.

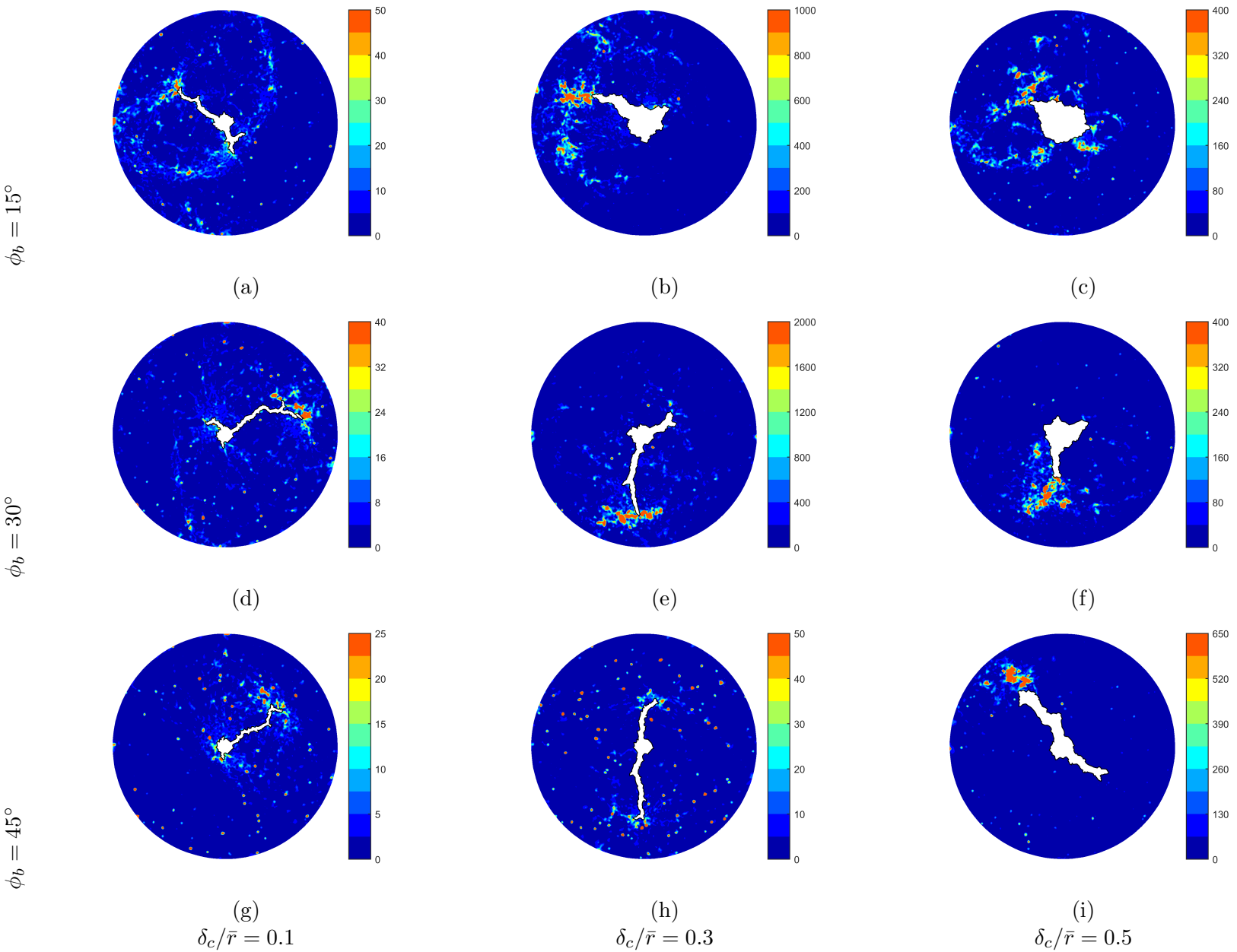

Figure 61: Particle rotational velocity with different friction angles and critical gap sizes at $Q = 0.1$ m^2/s and $D_{\text{out}}/D_{\text{in}} = 20$.

5.4.5 Effect of Cohesion

A series of 9 tests are carried out at a constant injection rate $Q = 0.1$ m^2/s and confining stress $\sigma_o = 1$ MPa with various critical gaps sizes $\delta_c/\bar{r} = 0.1,\ 0.3,\ 0.5$ and contact bond strengths $\bar{F}_s = \bar{F}_n = 100,\ 500,\ 1000$ N. Fig. 62 shows the displacement patterns for the 9 tests. The maximum bond strengths 1000 N corresponds to $\sigma_c = 1227.5$ kPa and $\sigma_t = 446.2$ kPa. Based on Eq. (112), a bond strength of $\bar{F}_s = \bar{F}_n = 1000$ N can be translated into a normal displacement of 0.024 mm, which is always smaller than the critical gap size, even for the $\delta_c = 0.1\bar{r}$ case ($\delta_c \sim 0.06$ mm). In other words, based on the parameters we select, for the particles on the interface chain, the contact bonds are expected to break before the critical gap criterion is met.

Overall, the dispacement patterns transition from an opening mode to a shear growth mode with the increasing $\delta_c/\bar{r}$ in the tests with all levels of cohesion. The differences in failure morphologies between the cohesionless and the cohesive cases are not very noticeable, even though shear failure is expected to be less favored and the medium tends to fail in tension in cohesive materials. Given these simulation parameters, the results show that the critical gap size is still the dominating factor in determining failure mode in our simulations since fluid advancement is controlled by δ_c, not by the cohesion.

In Figs. 63-65, the tensile forces in the contact bonds are plotted at three stages through the injection process. The color indicates the magnitude of the tensile force in each contact bond, if it is not broken. Overall, both the number of the active tensile bonds and the magnitude of the tensile forces in those bonds increase with the bond strength. In cases A1 and A3, only scattered tensile bonds exisit in the midium.

In cases C1 and C3, a ring of high density of active tensile bonds is present around the expanding cavity before localized deformation occurs. In the case with $\delta_c/\bar{r} = 0.1$, the ring soon disappears after fingers are developed. In the case with $\delta_c/\bar{r} = 0.5$, the ring gradually expands and always encloses the near borehole region where the majority of the bonds are broken.

In cases B1 and B3, the number of active bonds in tension is much less. However, the ring of high density of active tensile bonds is still found in B3.

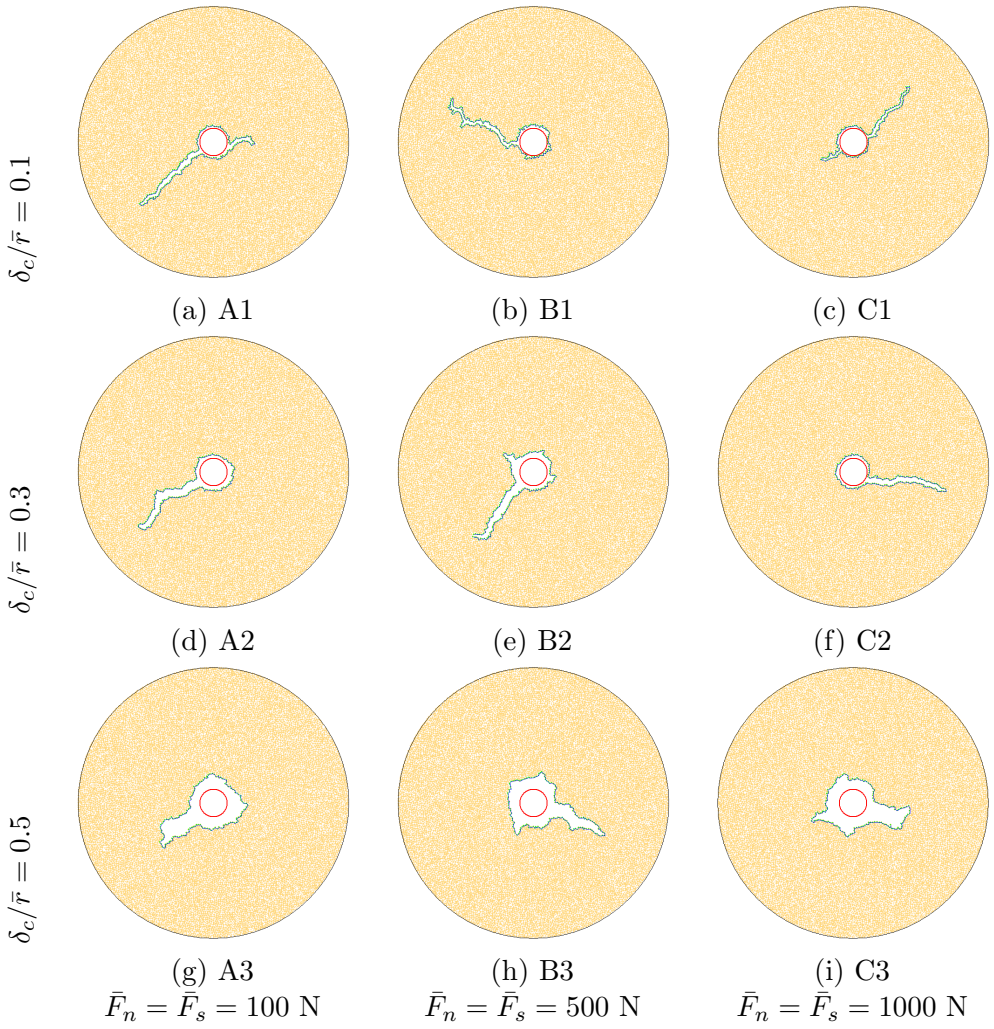

Figure 62: Morphologies of the fluid-grain interface with various critical gap sizes and contact bond strengths at $Q = 0.1$ m^2/s, σ_o=1 MPa and $\phi_b = 30°$: (a) $Qt = 290.4$ mm^2 (b) $Qt = 206.7$ mm^2 (c) $Qt = 149.5$ mm^2 (d) $Qt = 507.7$ mm^2 (e) $Qt = 557.9$ mm^2 (f) $Qt = 295.5$ mm^2 (g) $Qt = 1145.7$ mm^2 (h) $Qt = 1060.3$ mm^2 (i) $Qt = 1158.6$ mm^2.

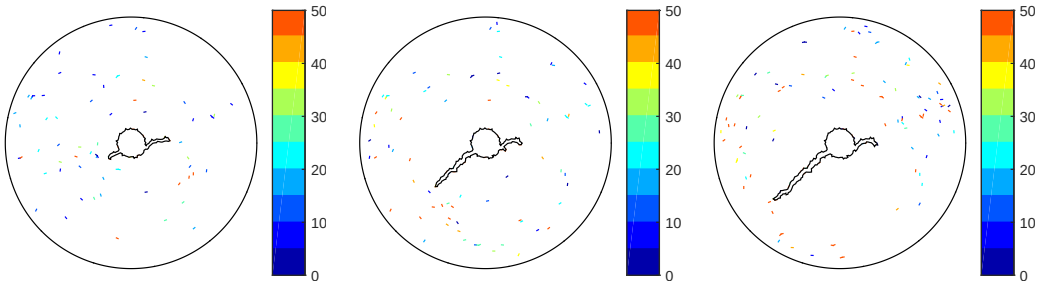

A1: $\delta_c/\bar{r} = 0.1$ and $\bar{F}_n = \bar{F}_s = 100$ N

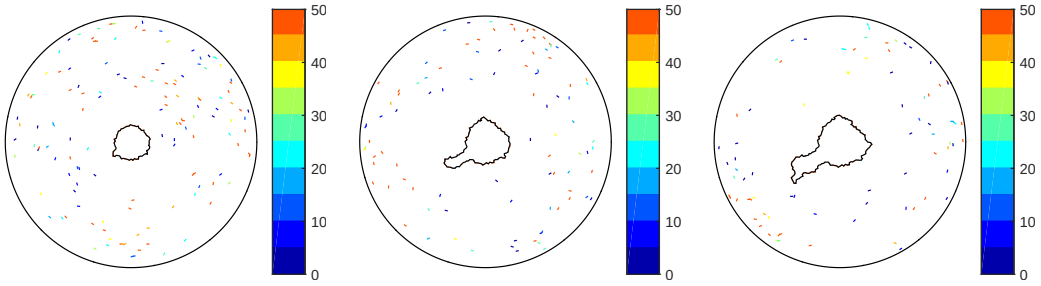

A3: $\delta_c/\bar{r} = 0.5$ and $\bar{F}_n = \bar{F}_s = 100$ N

Figure 63: Evolution of tensile forces in tests A1 and A3. The color indicates magnitude of tensile forces in N.

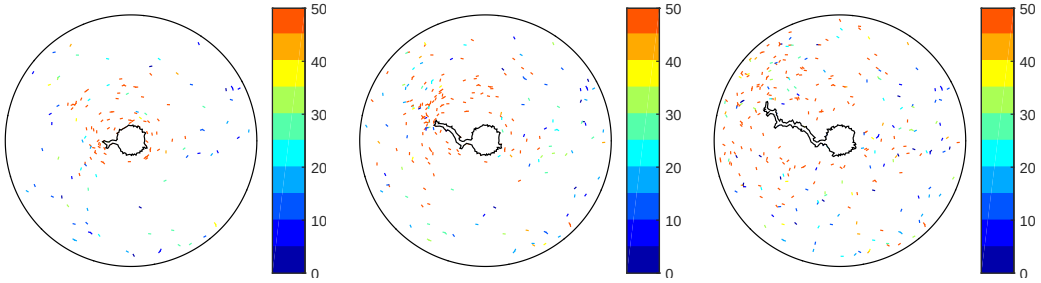

B1: $\delta_c/\bar{r} = 0.1$ and $\bar{F}_n = \bar{F}_s = 500$ N

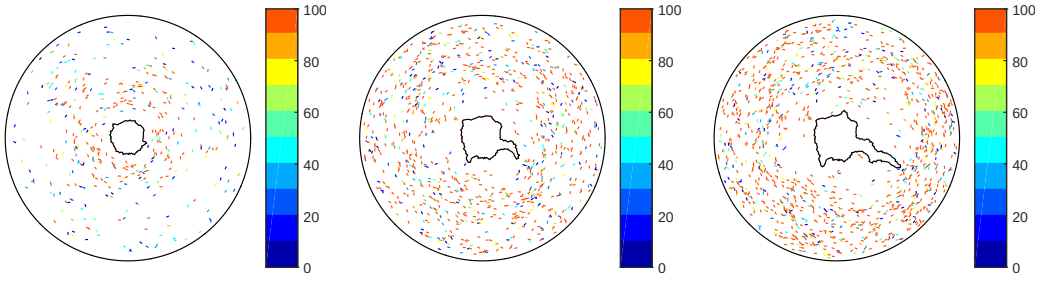

B3: $\delta_c/\bar{r} = 0.5$ and $\bar{F}_n = \bar{F}_s = 500$ N

Figure 64: Evolution of tensile forces in tests B1 and B3. The color indicates magnitude of tensile forces in N.

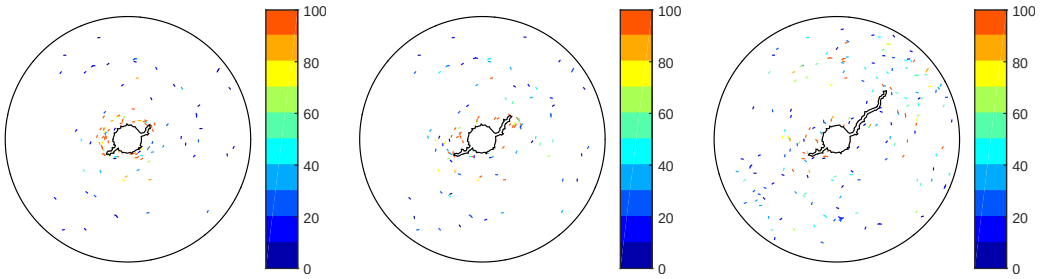

C1: $\delta_c/\bar{r} = 0.1$ and $\bar{F}_n = \bar{F}_s = 1000$ N

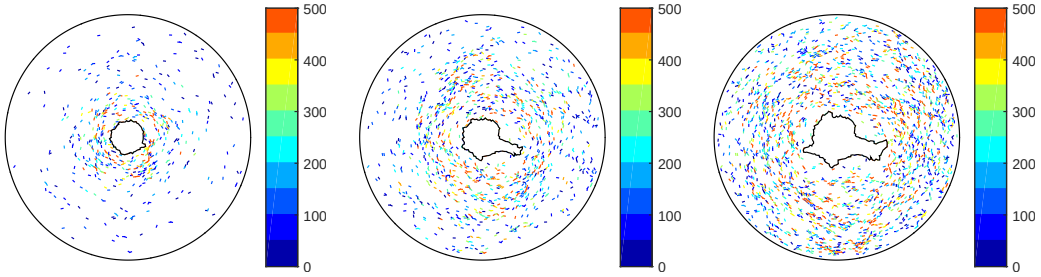

C3: $\delta_c/\bar{r} = 0.5$ and $\bar{F}_n = \bar{F}_s = 1000$ N

Figure 65: Evolution of tensile forces in tests C1 and C3. The color indicates magnitude of tensile forces in N.

In Figs. 66 and 67, the tensile and shear micro-cracks are plotted for the four representative cases B1, B3, C1 and C3. Color indicates the elapsed simulation time. In the cases with $\delta_c/\bar{r} = 0.1$, most of the micro-cracks are formed at early stage around the initial cavity. Once fluid is forced to open a channel, only scattered local micro-cracks are generated near the tip. The number of the shear micro-cracks significantly outweighs that of the tensile micro-cracks. In the cases with $\delta_c/\bar{r} = 0.5$, the transition from radial expansion to localized deformation happens much later. The progressive growth of plastic zone generates micro-cracks throughout the injection process. Note that in B1 and B3, a number of the micro-cracks are formed outside of the plastic zone at early stage. This is because the initial locked-in contact forces in those bonds are already close to the bond strengths.

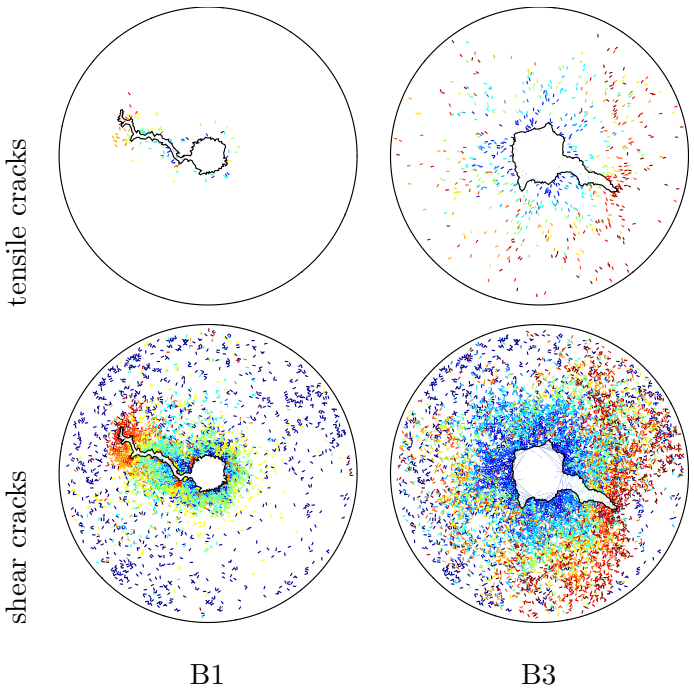

Figure 66: Tensile and shear cracks occurred in tests B1 and B3. The color indicates the time sequence: blue cracks are earlier, red cracks are later.

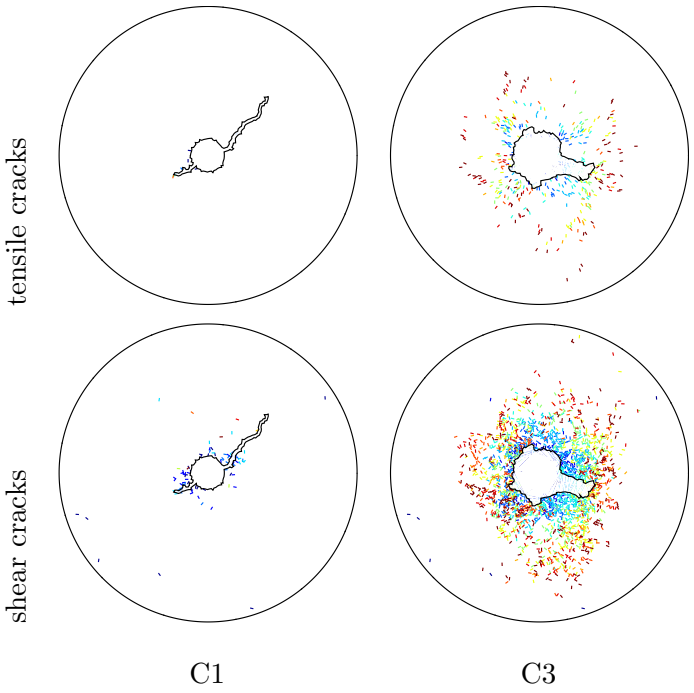

Figure 67: Tensile and shear cracks occurred in tests C1 and C3. The color indicates the time sequence: blue cracks are earlier, red cracks are later.

5.5 Conclusions

Fluid injection into an unconsolidated or weakly consolidated medium is modeled numerically using the DEM code *PFC2D*®. The injection process is modeled with the simplification that fluid leakoff is negligible and the fluid can penetrate in between grains if the gap size between two neighboring grains exceed a critical value δ_c. Such a simplification can be made analogous to considering the effect of surface tension or viscosity.

The numerical results suggest that the critical gap size plays a critical role in determining the failure mechanism. If the critical gap size δ_c is relatively small, fluid-grain displacement has three stages: borehole expansion, initiation of localized feature and extension of finger-like features; at large δ_c, borehole expansion is dominant and the localized features are notch-like. Evidences from the trajectories of localized features as well as particle rotational velocity suggest both opening and shear modes of initiation and growth mechanisms are plausible. What this means is that from the point of view of theoretical modeling at the continuum scale, a growth criterion should be able to capture both the opening and shear modes.

The confining stress, the initial borehole size, the injection rate, the particle friction angle of the particles and the cohesion of the particles also affect the failure modes. Wide and tortuous fingers are obtained at high confining stresses. At low confining stress, thin and straight fingers are obtained with a small δ_c, and notch-like localized features are observed at large δ_c. The numerical results also indicate that large boreholes generally develop thinner features, even with weak confinement. Conversely, small boreholes will generally exhibit localized notch-like features, even with high confinement. With an increasing injection rate, the fractures tend to align radially and the number of the main fractures increases. At small injection rate, the fingers grow in an alternating manner, only one fracture is propagating at one time; at large injection rate, multiple small fingers are initiated but only a number of them are able to extend outward. Shear bands are easier to develop in formations with a lower friction angle. With a higher friction angle, the resistance to the sliding is greater, the medium tends to fail in an opening mode. With a relatively large cohesion, shear failure is less favored and the medium tends to fail in tension.

CHAPTER VI

THEORETICAL ANALYSIS OF THE BREAKDOWN PRESSURE

In theoretical analyses, it is typically assumed that the cavity may fail in a tensile or shear mode, depending on whether cohesion is present or not. In the limit of a cohesionless material, a constitutive model of Coulomb type predicts that the material must fail in shear and failure may be manifested in the formation of spiral shaped shear bands. For a competent rock, tensile brittle failure is expected, the formation could be modeled as an elastic-perfectly plastic material obeying the Mohr-Coulomb yield criterion. In this chapter, numerical results in Chapter V on the breakdown of the cavity are analyzed and compared with those from the bifurcation analysis for the cohesionless case as well as elasto-plasticity solutions for the cohesive case.

6.1 Bifurcation Analysis

Prior to the growth of the finger-like features or the borehole shape being severely distorted, the numerical simulation is effectively modeling cavity expansion of a thick-walled cylinder, where the relationship between the borehole pressure and the volume is amenable to bifurcation analysis. In general, bifurcation or incipient shear banding could occur if the Jacobian matrix for the velocities loses positive definiteness, allowing jumps in velocities to occur.

The formulation in Alsiny *et al.* [2] is adopted here to analyze the pressure versus volume relationship and the critical pressure corresponding to the onset of bifurcation. Their theoretical model assumes progressive failure where a shear band initiates from the inner cavity wall and progresses into the interior of the domain as the borehole size increases. In this analysis, the cylindrical domain is first discretized into a total of 100 adjacent rings (Fig. 68) with the thickness of the rings following a geometric sequence with a factor $GF = 1.05$. Local bifurcation analysis for each ring is conducted, assuming each ring is in a uniform axisymmetric stress and strain state. Stresses and displacements are continuous

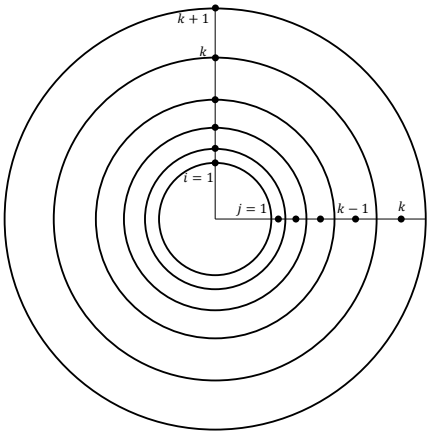

Figure 68: The thick-walled hollow cylinder is discretized into N rings.

at the interfaces between two adjacent rings.

In this formulation, the material is purely frictional and the load acting on the sample is only mechanical. The response of the cylindrical sample is modeled by the incremental elastoplastic constitutive equations proposed by Vardoulakis [99]. The constitutive equations include an incrementally linear Hooke's law, a linear Mohr-Coulomb yield condition, and a non-associative flow rule. The yield condition f and the potential function g can be written as,

$$f = \tau/s - \mu\left(e_0, \gamma^p\right) \tag{119}$$

$$g = \tau/s - \beta\left(e_0, \gamma^p\right) \tag{120}$$

where τ is the shear stress intensity; s is the mean stress; γ^p is the plastic shear strain intensity; and e_0 is the initial void ratio. The expressions for τ, s, and γ are $\tau = \left|\sigma_{rr} - \sigma_{\theta\theta}\right|/2$, $s = \left|\sigma_{rr} + \sigma_{\theta\theta}\right|/2$, and $\gamma = \left|\epsilon_{rr} - \epsilon_{\theta\theta}\right|$, respectively. In the yield condition and the potential function, μ and β are the friction and dilatancy function, respectively. Hardening-softening functions of μ and β are employed.

6.1.1 Effect of Critical Gap Size

The analysis is first performed to compare with tests 0.1_1_10_0.1_30, 0.3_1_10_0.1_30 and 0.5_1_10_0.1_30 where $\delta_c/\bar{r} = 0.1,\ 0.3,\ 0.5$, $\sigma_o = 1$ MPa, $D_{\text{out}}/D_{\text{in}} = 10$, $Q = 0.1$ m^2/s and $\phi_b = 30°$. Elastic modulus E, the functions μ and β are evaluated from the material tests

conducted in Chapter V. The biaxial compression test with $\sigma_o = 1$ MPa, $\phi_b = 30^\circ$ and $\bar{F}_n = \bar{F}_s = 0$ N gives an elastic modulus $E = 39.2$ MPa. The Poisson's ratio is taken as $\nu = 0.17$, which gives $G = 16.8$ MPa. The bifurcation condition for incipient shear banding is met if the hardening modulus, $h = d\mu/d\gamma^p$, reaches a critical value,

$$h = \frac{G\left(\mu - \beta\right)^2}{8s\left(1 - \nu\right)} \tag{121}$$

The hardening/softening form of function μ is approximated by,

$$\mu = \begin{cases} C_1 \left\{1 - \exp\left[C_2 \left(\gamma^p\right)^{C_3}\right]\right\} & \gamma^p \leq \gamma^p_{peak} \\ C_4 \exp\left\{-\left[C_5\left(\gamma^p - \gamma^p_{peak}\right)\right]^2\right\} & \gamma^p > \gamma^p_{peak} \end{cases} \tag{122}$$

Regression of the hardening part of the numerical simulation data yields coefficients $C_1 - C_3$: $C_1 = 0.496$, $C_2 = -26.723$ and $C_3 = 0.911$. The peak shear strain $\gamma^p_{peak} = 0.0734$ and $C_4 = \mu_{max} = 0.454$. Since we focus mostly on the onset of bifurcation, the coefficient C_5, which characterizes the softening part, is set to be $C_5 = 3.5$, the same as that from the experimental results by Alsiny *et al.* [2], see Fig. 69.

Function β can be obtained by differentiating the relationship between the volumetric plastic strain and the shear plastic strain, which is fitted by,

$$\epsilon^p = \frac{C_6 \gamma^p}{1 + C_7\left(\gamma^p\right)^2} + C_8 \ln\left(1 + C_9 \gamma^p\right) \tag{123}$$

where $C_6 = 0.576$, $C_7 = 1$, $C_8 = 1.7 \times 10^{-3}$, and $C_9 = 390.194$, see Fig. 70.

Theoretical prediction of the borehole pressure as a function of the expansion volume is shown in Fig. 71. Onset of bifurcation, or initiation of a shear band, at the inner wall occurs at $\Delta R = 2$ mm, $Qt = 115$ mm^2 and $P = 2.0$ MPa. Afterwards, the borehole pressure continues to increase and reaches a peak around $\Delta A = 600$ mm^2, which corresponds to a borehole radius increment of $\Delta R = 8$ mm. The shear band reaches the outer boundary in the post peak stage as indicated by the open dot in Fig. 71.

Fig. 72 shows the borehole pressure histories of tests 0.1_1_10_0.1_30, 0.3_1_10_0.1_30 and 0.5_1_10_0.1_30. The pressure histories from the numerical simulations all exhibit an early rising part, which corresponds to the radial expansion of the borehole. Pressure histories

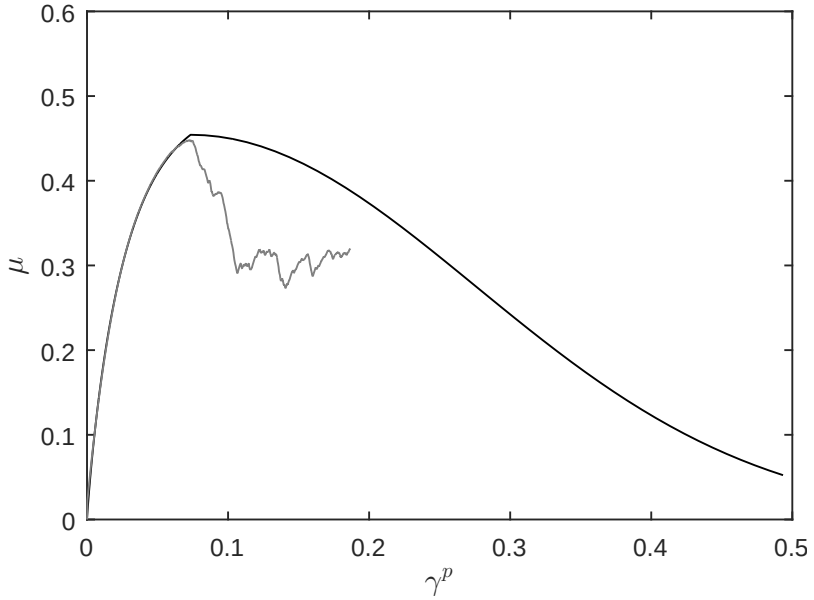

Figure 69: Material function μ as a function of the plastic shear strain from the numerical biaxial compression test (grey line) and the fitting function (black line) for the cohesionless medium with $\sigma_o = 1$ MPa, $\phi_b = 30°$.

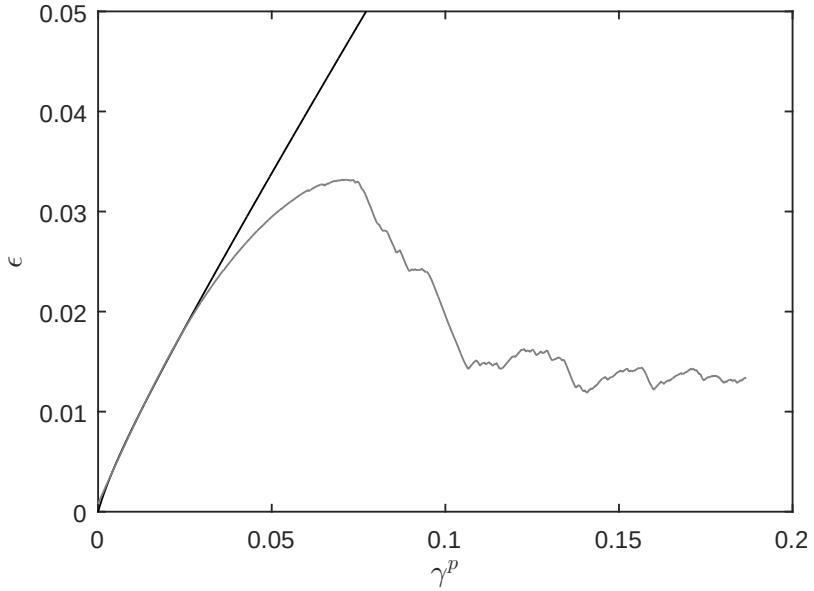

Figure 70: Plastic volumetric strain as a function of the shear plastic strain from the numerical biaxial compression test (grey line) and the fitting function (black line) for the cohesionless medium with $\sigma_o = 1$ MPa, $\phi_b = 30°$.

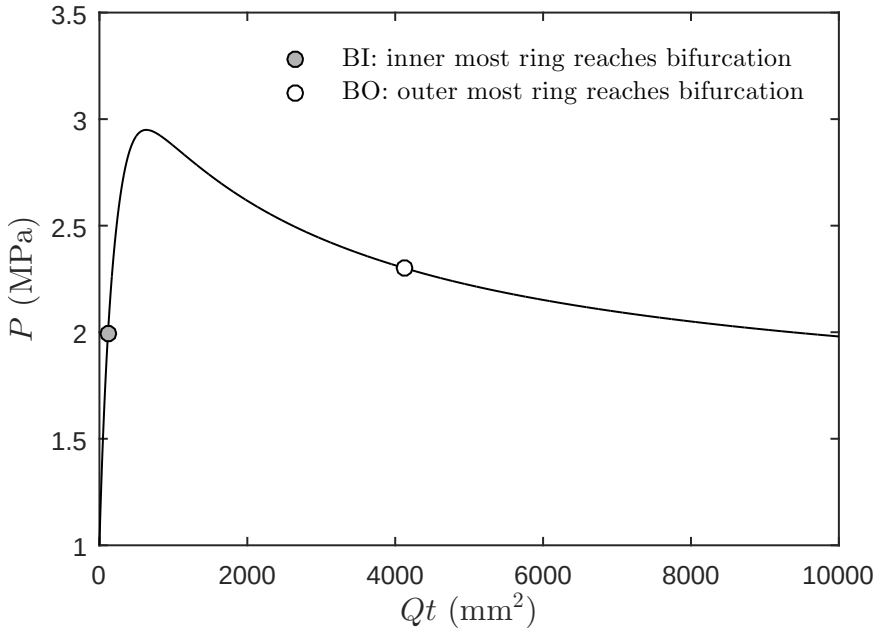

Figure 71: Internal pressure as a function of borehole area change is predicted by the bifurcation analysis. The solid circle and hollow circle mark the pressure when the innermost and outermost rings reach the bifurcation condition, respectively.

in this first stage in fact can be very well described by the theoretical prediction. The first stage ends earlier if the critical gap size is smaller. During the second stage, the pressure remains nearly constant or declines slightly within the observation, corresponding to the extension of the finger-like features or further expansion and distortion of the borehole. The most interesting part of the comparison is perhaps the excellent agreement between the pressure for the onset of bifurcation and the peak pressure at $\delta_c/\bar{r} = 0.5$, despite one being a DEM simulation at a given fluid injection rate and the other being an elasto-plastic solution where the pressurization rate is not taken into account.

Figs. 73 and 74 show the distribution of the radial and circumferential stresses for the $\delta_c/\bar{r} = 0.5$ case (test 0.5_1_10_0.1_30) at $t = 1.5 \times 10^{-3}$ s, around the time when the borehole pressure of the numerical test first reaches the predicted bifurcation pressure of $P = 2$ MPa. All the stresses are in compressive. The local variation of the stress field indicates the existence of force chains, as a result of the random nature of the micro-structure. As expected, the radial forces near the cavity are higher than those at the far field, while the circumferential forces are lower.

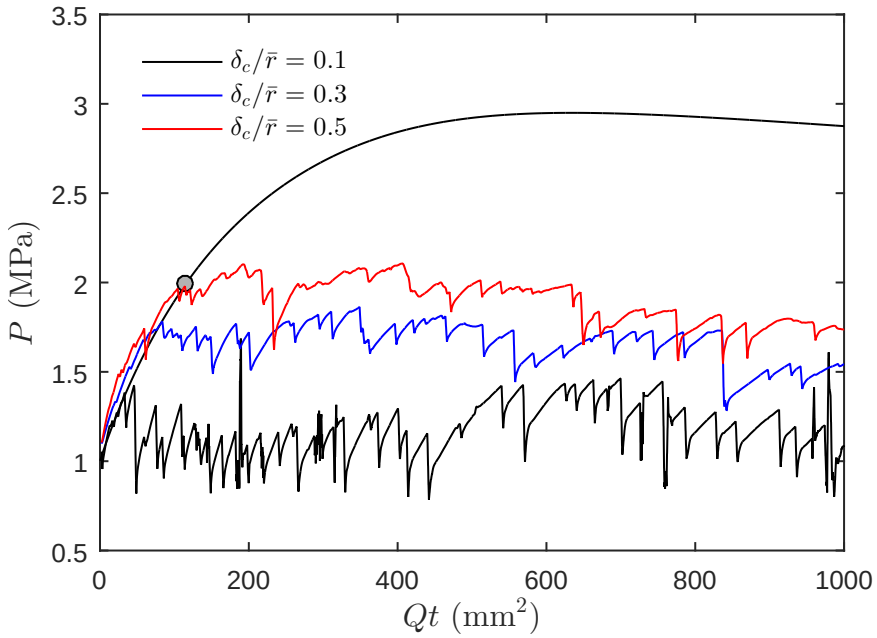

Figure 72: History of the injection pressure for tests with $\delta_c/\bar{r} = 0.1, 0.3$ and 0.5 are compared with part of the internal pressure curve.

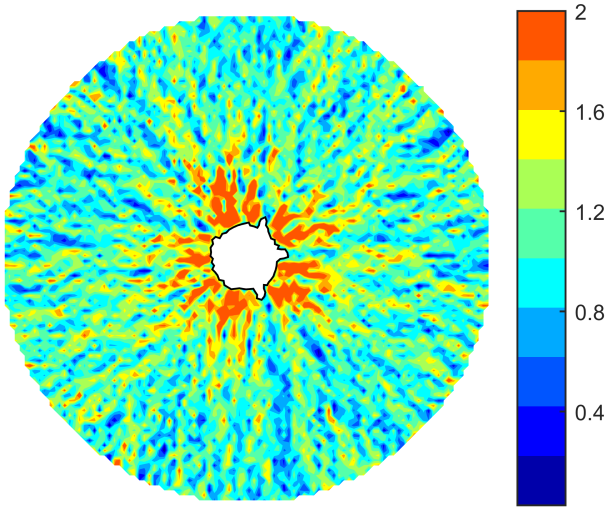

Figure 73: Radial stress of test 0.5_1_10_0.1_30 at $t = 1.5 \times 10^{-3}$ s. The color bar indicates the magnitude of the stresses (MPa).

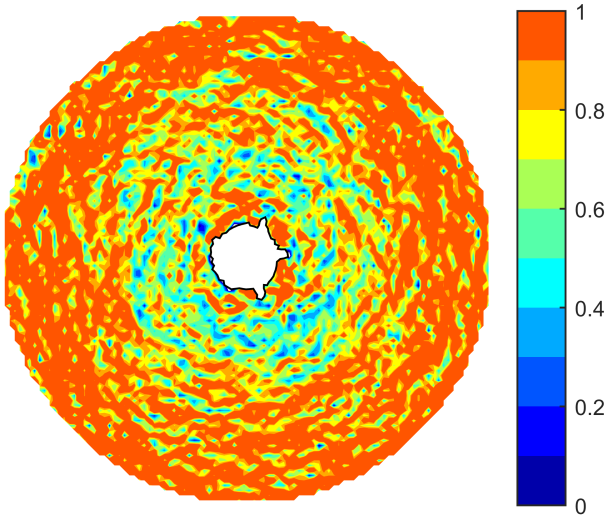

Figure 74: Circumferential stress of test 0.5_1_10_0.1_30 at $t = 1.5 \times 10^{-3}$ s. The color bar indicates the magnitude of the stresses (MPa).

In Fig. 75, variations of the theoretical radial and circumferential stresses as a function of the scaled radius, r/a, with a being the borehole radius, at onset of shear banding are predicted by the bifurcation analysis, and plotted in smooth lines. The radial and circumferential stresses in the numerical test are averaged in the circumferential direction and plotted as a function of radius in dotted lines. Overall, the radial stress field obtained in the numerical test agrees with the theoretical analysis despite some local variations. However, the theoretical circumferential stress is higher than that in the numerical test.

6.1.2 Effect of Friction Angle

In this section, the bifurcation analysis is performed for three tests with various particle friction angles, and the theoretical results are compared with the numerical results. The numerical tests to be compared with in this section are tests 0.5_1_20_0.1_15, 0.5_1_20_0.1_30, and 0.5_1_20_0.1_45 with $\phi_b = 15°,\ 30°,\ 45°$, $\delta_c/\bar{r} = 0.5$, $\sigma_o = 1$ MPa, $D_{\text{out}}/D_{\text{in}} = 20$ and $Q = 0.1$ m^2/s. Elastic modulus E, and coefficients in the functions μ and β are evaluated from the biaxial compression tests conducted in Chapter V. The friction and dilatancy functions μ and β are plotted in Figs. 76 and 77.

The parameters in the friction and dilatancy functions are summarized in Table 14.

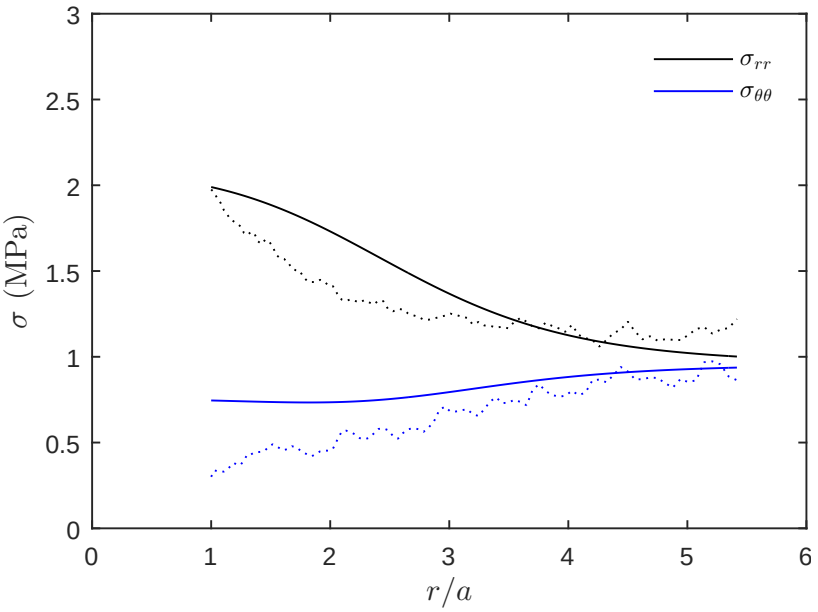

Figure 75: Predicted radial and circumferential stresses by bifurcation analysis when the innermost ring reaches the bifurcation condition.

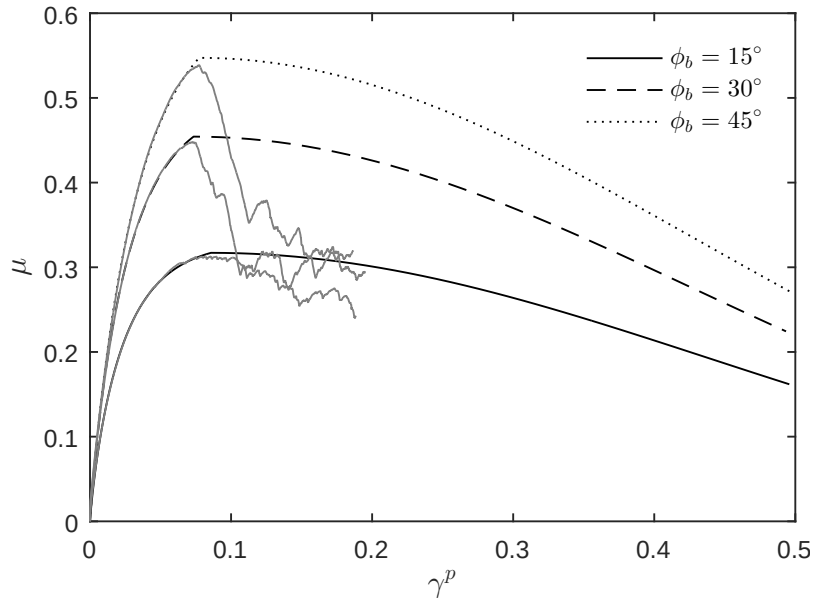

Figure 76: Material function μ as a function of the plastic shear strain from the numerical biaxial compression tests (grey line) and the fitting function (black line) for the cohesionless medium with $\sigma_o = 1$ MPa, $\phi_b = 15°,\ 30°,$ and $45°$.

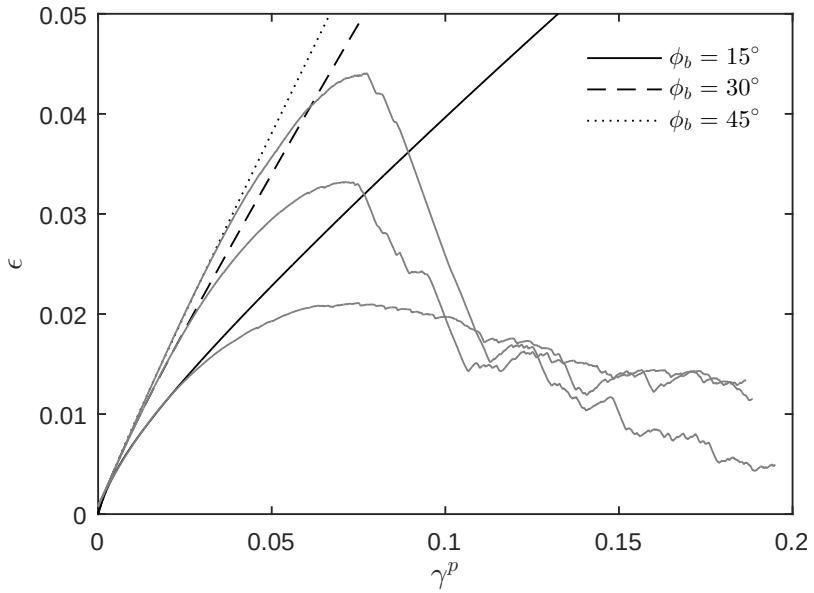

Figure 77: Plastic volumetric strain as a function of the shear plastic strain from the numerical biaxial compression tests (grey line) and the fitting function (black line) for the cohesionless medium with $\sigma_o = 1$ MPa, $\phi_b = 15°,\ 30°,$ and $45°$.

Table 14: Material constants and fitted parameters for the material functions in the bifurcation analysis for tests with various particle friction angles $\phi_b = 15°,\ 30°$ and $45°$.

	C_1	C_2	C_3	C_4	C_5	C_6	C_7	C_8	C_9	E (MPa)
$\phi_b = 15°$	0.332	-27.456	0.883	0.317	3.5	0.310	1	0.0024	398.194	30.3
$\phi_b = 30°$	0.496	-26.723	0.911	0.454	3.5	0.582	1	0.0016	400.356	39.2
$\phi_b = 45°$	0.622	-22.441	0.921	0.547	3.5	0.701	1	0.001	512.15	41.6

Poisson's ratio ν is taken as 0.17.

Fig. 78 shows the variations of the internal pressure as a function of borehole area for the three cases with various friction angles. The internal pressures for the three tests reach the peak at about the same expansion volume. The symbols in Fig. 78 mark the onset of shear banding for the innermost and outermost rings. It can be seen that local bifurcation occurs first for the material with a lower particle friction. The internal pressure corresponding to onset of bifurcation is 1.70 MPa for $\phi_b = 15°$, 2.04 MPa for $\phi_b = 30°$ and 2.27 MPa for $\phi_b = 45°$.

Pressure histories from the three numerical simulation cases, Tests 0.5_1_20_0.1_15, 0.5_1_20_0.1_30, and 0.5_1_20_0.1_45 with $\phi_b = 15°,\ 30°,\ 45°,\ \delta_c/\bar{r} = 0.5,\ \sigma_o = 1$ MPa, $D_{\text{out}}/D_{\text{in}} = 20$ and $Q = 0.1$ m^2/s, are compared with the theoretical prediction in Fig. 79.

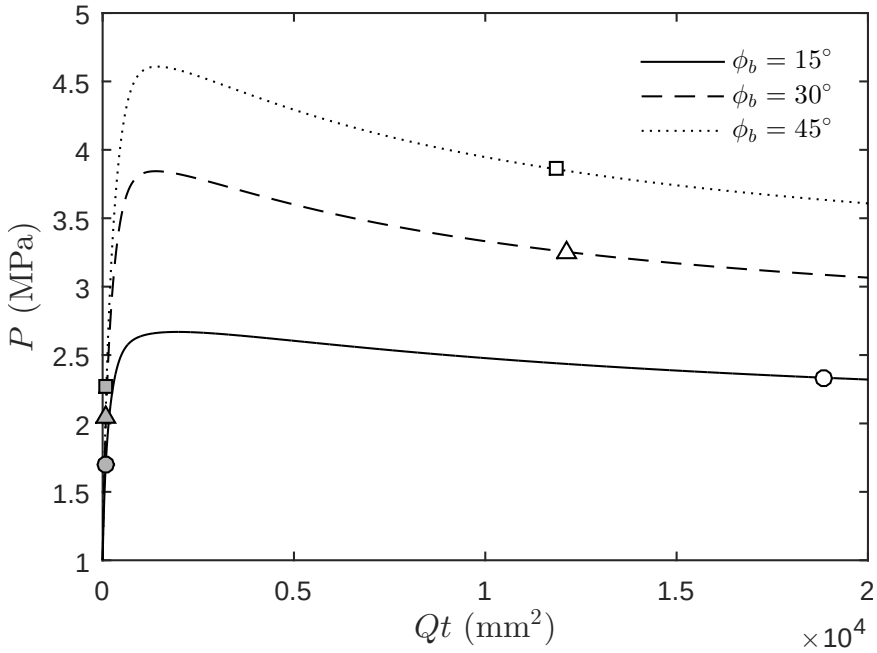

Figure 78: Internal pressure as a function of borehole area change is predicted by the bifurcation analysis. The filled and hollow markers indicate the pressure when the innermost and outermost rings reach bifurcation condition, respectively.

Only the histories of the $\delta_c/\bar{r} = 0.5$ cases are plotted in Fig 79 since Fig. 72 suggests a good agreement between the predicted pressure for onset of bifurcation and the peak injection pressure for the $\delta_c/\bar{r} = 0.5$ case. Overall, the breakdown pressures in the numerical tests are slightly higher than the theoretical predictions for this series of tests. Comparing the two cases with the same friction angle, $\phi_b = 30°$, but different initial borehole radius, $D_{\text{out}}/D_{\text{in}} = 10$ in Fig. 72 and $D_{\text{out}}/D_{\text{in}} = 20$ in Fig. 79, the results suggest that the bifurcation analysis yields a more precise prediction for the case with a larger borehole. A possible explanation for the discrepancy could be that a smaller borehole has fewer particles on the interface chain, which makes the chain less prone to distortion and eventually leads to a breakdown pressure higher than predicted. For $D_{\text{out}}/D_{\text{in}} = 20$, the number of particles on the initial borehole perimeter is about 21, while for $D_{\text{out}}/D_{\text{in}} = 10$, that number is about 42.

As internal pressure increases, the shear band starts to form from a given point at the inner boundary and progresses toward the outer boundary. Based on Alsiny *et al.*'s solution [2], The inclination angle of the shear band with respect to the direction of the algebraically

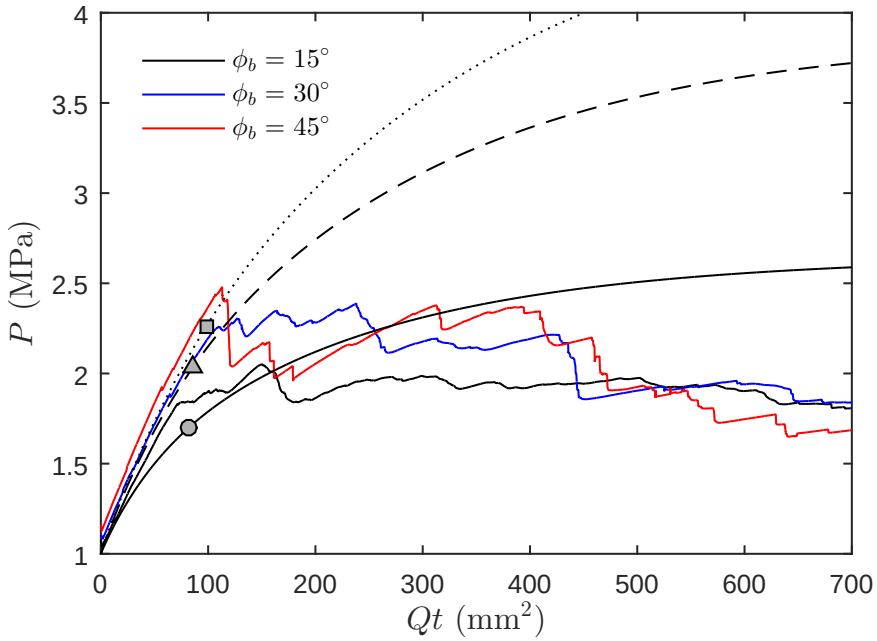

Figure 79: History of the injection pressure for tests with $\phi_b = 15°,\ 30°,$ and $45°$ are compared with part of the internal pressure curve.

greater principal stress can be calculated from,

$$\Omega_B = \pm\left[45° + \left(\phi^* + \psi^*\right)/4\right] \tag{124}$$

where ϕ^* is mobilized friction angle and ψ^* mobilized dilatancy angle.

Angle Ω_B is calculated at the peak internal cavity pressure for the rings that have reached the bifurcation condition along the radius. The trajectory of the shear band is drawn starting from the inner boundary, as shown in Fig. 80. The shear band trajectories for the three representative cases with different particle friction angles, $\phi_b = 15°,\ 30°,$ and $45°$, are all in spiraling shape, but exhibits a significant difference in the "tightness", namely, the medium with a greater friction angle results in a more tightly shaped shear band.

Contours of the particle rotational velocity for the three corresponding numerical tests are shown in Fig. 81. Although the shear bands in Fig. 80 predicted from bifurcation analysis correspond to the peak cavity pressure, while contour plots from the numerical tests are obtained at peak injection pressure, which is comparable to the pressure for onset of bifurcation, we can still find that the numerical shear bands resemble the relative tightness in the theoretical ones. In Fig. 81 (a), long shear bands are able to extend outward further

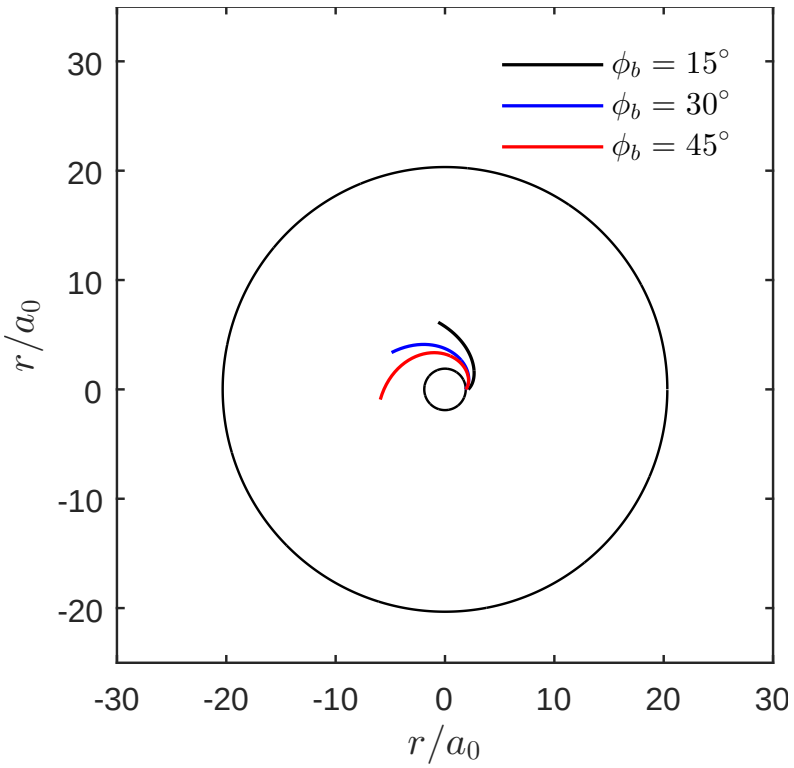

Figure 80: Predicted trajectory of shear band at peak internal pressure. Black circles are the outer and inner boundaries of the thick-walled cylinder.

from the inner boundary. In Figs. Fig. 81 (b) and (c), the shear failure is limited within a smaller region near the borehole, as would be expected from the predicted inclination angles of the shear bands for the higher friction angles.

6.2 Analysis of the Tensile Failure

When a thick-walled cylinder is internally pressurized, the circumferential stress changes from compressive to tensile. The fracture is assumed to initiate when the maximum tensile stress, σ_{tmax}, in the domain exceeds the tensile strength of the material, σ_t, namely, $\sigma_{tmax} \geq \sigma_t$. Theoretical prediction based on the Lamé's solutin for a thick-walled cylinder is compared with the pressure histories from the numerical tests.

Consider a hollow cylinder of an outer radius, b_0, and an inner radius, a_0, subjected to uniformly distributed internal and external pressures p_a and p_b. According to Lamé's solution, the radial and tangential stresses can be expressed as [96],

$$\sigma_r = -\left[\frac{\left(\frac{b_0}{r}\right)^2 - 1}{\left(\frac{b_0}{a_0}\right)^2 - 1}\right] p_a - \left[\frac{1 - \left(\frac{a_0}{r}\right)^2}{1 - \left(\frac{a_0}{b_0}\right)^2}\right] p_b \tag{125}$$

$$\sigma_\theta = \left[\frac{\left(\frac{b_0}{r}\right)^2 + 1}{\left(\frac{b_0}{a_0}\right)^2 - 1}\right] p_a - \left[\frac{1 + \left(\frac{a_0}{r}\right)^2}{1 - \left(\frac{a_0}{b_0}\right)^2}\right] p_b \tag{126}$$

Positive sign denotes tensile. Tensile failure is expected to first occur at the cavity wall, since the circumferential stress is most tensile at the inner boundary, $r = a_0$. The maximum tensile stress in the cylindrical domain is expressed as,

$$\sigma_{tmax} = \frac{\left[\left(\frac{b_0}{a_0}\right)^2 + 1\right] p_a - 2\left(\frac{b_0}{a_0}\right)^2 p_b}{\left(\frac{b_0}{a_0}\right)^2 - 1} \tag{127}$$

Therefore

$$p_{a,max} = \frac{\left[\left(\frac{b_0}{a_0}\right)^2 - 1\right] \sigma_t + 2\left(\frac{b_0}{a_0}\right)^2 \sigma_o}{\left(\frac{b_0}{a_0}\right)^2 + 1} \tag{128}$$

where $p_{a,max}$ is the maximum internal pressure before tensile failure occurs. If $\sigma_t = 0$,

$$p_{a,max} = \left(\frac{2b_0^2}{b_0^2 + a_0^2}\right) \sigma_o \tag{129}$$

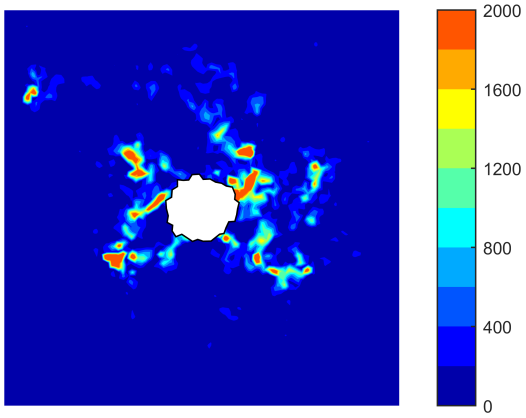

(a)

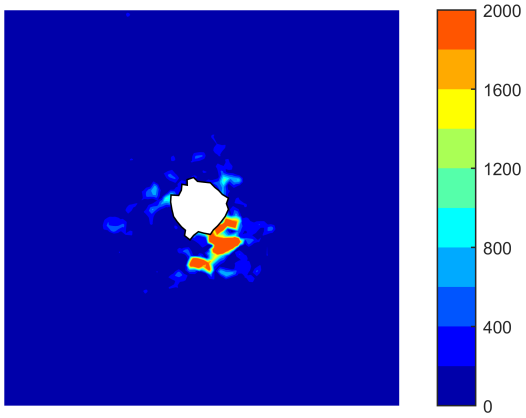

(b)

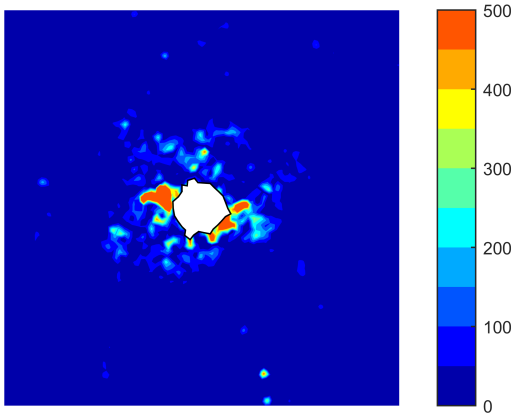

(c)

Figure 81: Contours of the particle rotational velocity with (a) $\phi_b = 15°$, (b) $\phi_b = 30°$, and (c) $\phi_b = 45°$, showing only the near-borehole region, around the peak pressure stage, value of the color map indicates magnitude of rotational velocity in rad/s.

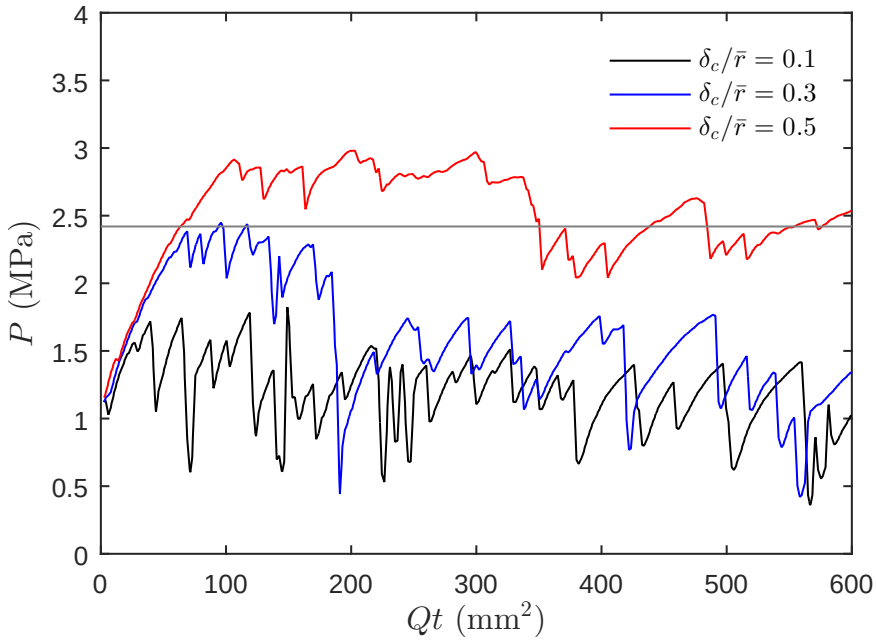

Figure 82: History of the injection pressure for tests with $\phi_b = 15°$, $30°$, and $45°$ are compared with the maximum internal pressure (grey line).

when $b_0 \gg a_0$, $p_{a,max} = 2\sigma_0$.

Maximum internal pressure $p_{a,max}$ is calculated to be compared with tests 0.1_1_10_0.1_30_c1000, 0.3_1_10_0.1_30_c1000 and 0.5_1_10_0.1_30_c1000 with $\delta_c/\bar{r} = 0.1,\ 0.3,\ 0.5$, $\sigma_c = 1$ MPa, $D_{\text{out}}/D_{\text{in}} = 10$, $Q = 0.1$ m^2/s, $\phi_b = 30°$ and $\bar{F}_n = \bar{F}_s = 1000$ N. Fig. 82 shows the borehole pressure history of the three tests. The tensile strength of the medium, $\sigma_t = 446.2$ kPa, for $\sigma_o = 1$ MPa and $\bar{F}_n = \bar{F}_s = 1000$ N is obtained from the direct tension test. The outer and inner radii are $a_0 = 8$ mm, and $b_0 = 80$ mm, respectively. The maximum internal pressure is calculated according to Eq.128, $p_{a,max} = 2.42$ MPa, which is plotted as a straight grey line in Fig. 82. In test 0.3_1_10_0.1_30_c1000 with $\delta_c/\bar{r} = 0.3$, the predicted maximum internal pressure is consistent with the peak borehole pressure, while the peak borehole pressure for test 0.5_1_10_0.1_30_c1000 with $\delta_c/\bar{r} = 0.5$ is slightly higher than the predicted pressure.

Distribution of the radial and circumferential stresses for 0.3_1_10_0.1_30_c1000 at $t = 7.5 \times 10^{-4}$ s, around the time when the borehole pressure reaches the predicted maximum internal pressure, $p_{a,max} = 2.42$ MPa, is shown in Figs. 83 and 84. Similarly, the radial stress is compressive everywhere in the domain. However,the circumferential stress has some local tensile variations near the borehole vicinity.

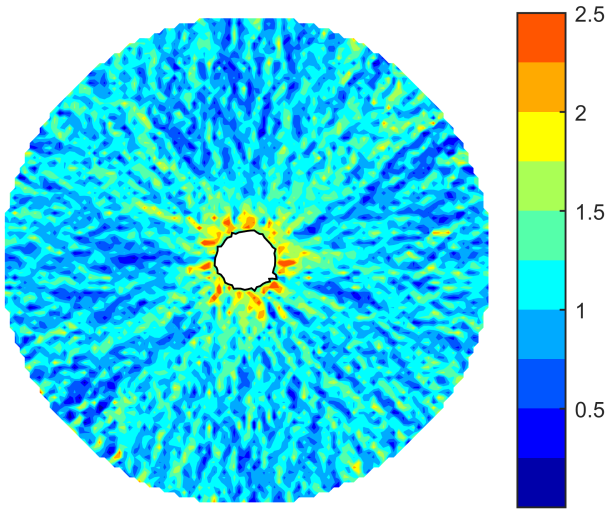

Figure 83: Radial stress of test 0.3_1_10_0.1_30_c1000 at $t = 7.5 \times 10^{-4}$ s. The color bar indicates the magnitude of the stresses (MPa).

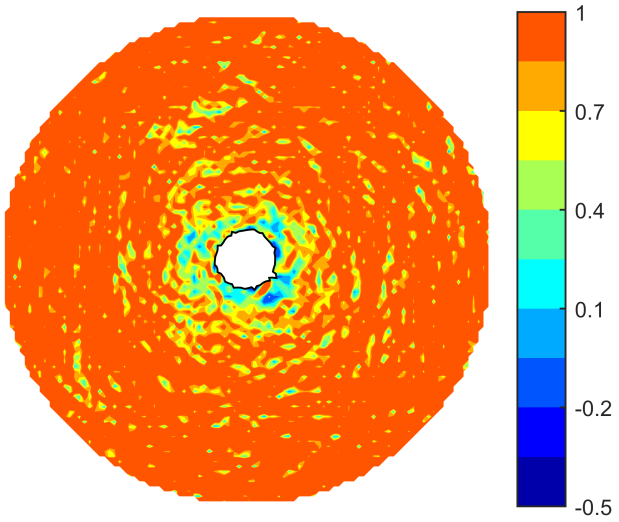

Figure 84: Circumferential stress of test 0.3_1_10_0.1_30_c1000 at $t = 7.5 \times 10^{-4}$ s. The color bar indicates the magnitude of the stresses (MPa).

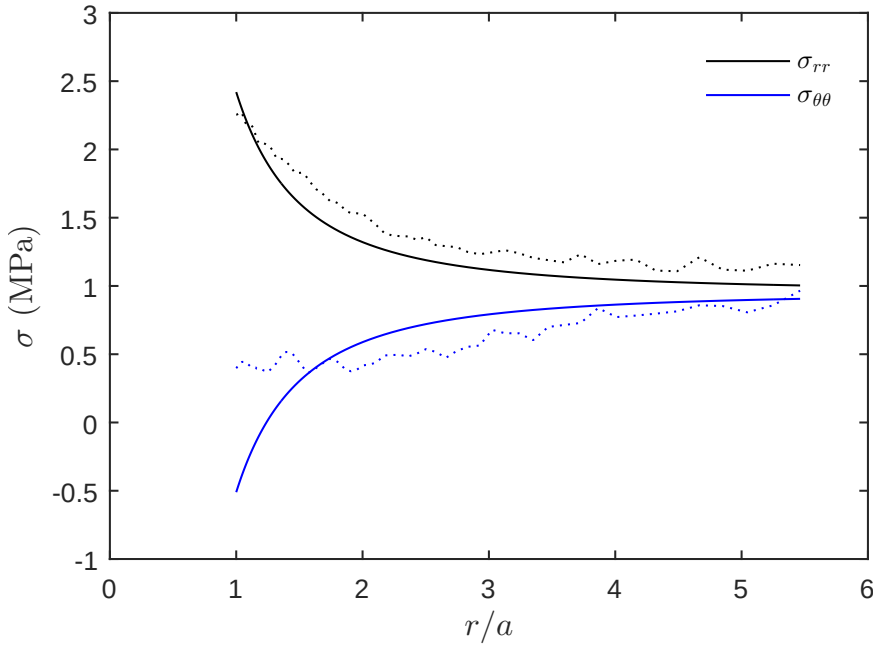

Figure 85: Averaged radial and circumferential stresses (dotted lines) are compared with predicted radial and circumferential stresses given by Lamé's solution (smooth lines) when $\sigma_{t,max} = \sigma_t$.

Fig. 85, the theoretical radial and circumferential stresses along the scaled radius of the hollow cylinder when subjected to an external pressure of 1 MPa and a cavity pressure of 2.42 MPa are plotted in solid lines according to Lamé's solution. The radial and circumferential stresses in the numerical test are averaged in the circumferential direction and plotted as a function of radius in dotted lines. The numerical solution for $\delta_c/\bar{r} = 0.3$ case shows good agreement with the the theoretical prediction. However, the averaged circumferential stress is in compression near the borehole vicinity, while the theoretical circumferential stress is tensile for $r/a < 1.24$. Though negative values are observed in the contour plot in Fig 85, the local features of the tensile stress disappear after taking the average along the circumferential direction.

6.3 Analysis with Elastic-Perfectly Plastic Solution

In this section, we estimate the relationship between the injection pressure P and the injection volume using the expansion of thick-walled cylinder model proposed by Yu [105]. In the analysis, the soil is modeled as an elastic-perfectly plastic material obeying the

Table 15: Properties of the medium and geometric parameters in the elastic-perfectly plastic solution.

$\bar{F}_n,\ \bar{F}_s$ (N)	E (MPa)	ϕ (°)	c (kPa)	b_0/a_0	σ_o (MPa)	ν
0	39.2	25.67	0	10	1	0.17
100	39.2	25.87	0	10	1	0.17
500	40.2	26.49	144.6	10	1	0.17
1000	41.8	31.08	243.8	10	1	0.17

Mohr-Coulomb yield criterion. The analysis provides a closed-form solution to determine the elastic-plastic deformation and stresses when a thick-walled cylinder is subjected to a constant confining stress and an increasing internal pressure. The effect of large strain in the plastic zone is accounted for by the logarithmic strain, instead of using the definition for strains in the small strain analysis. The large strain analysis takes into account the effect of geometry changes and therefore able to predict the softening behavior in the cavity pressure-cavity volume relation.

The theoretical analysis is performed with the parameters in tests 0.5_1_10_0.1_30, 0.5_1_10_0.1_30_c100, 0.5_1_10_0.1_30_c500 and 0.5_1_10_0.1_30_c1000 with $\bar{F}_n = \bar{F}_s = 0$, 100, 500 and 1000 N, $\delta_c/\bar{r} = 0.5$, $\sigma_o = 1$ MPa, $D_{\text{out}}/D_{\text{in}} = 10$, $Q = 0.1$ m^2/s and $\phi_b = 30°$. The properties of the medium, loading conditions, and the geometrical parameters for the analysis are the same as those in the DEM numerical tests, which are summarized in Table 15.

Fig. 86 shows the variation of the internal pressure as a function of the cavity area change for the parameters in Table 15. The curves show that the peak injection stress increases with strengthened bonds. For the case with $\bar{F}_n = \bar{F}_s = 1000$ N, the curve starts to show softening behavior at a normalized radius of $a/R_0 = 1.62$ and a corresponding radial displacement of 4.96 mm.

Pressure histories from the three numerical simulation cases, 0.1_1_10_0.1_30_c1000, 0.3_1_10_0.1_30_c1000, and 0.5_1_10_0.1_30_c1000 with $\delta_c/\bar{r} = 0.1,\ 0.3,\ 0.5$, $\sigma_o = 1$ MPa, $D_{\text{out}}/D_{\text{in}} = 10$, $Q = 0.1$ m^2/s, $\phi_b = 30°$ and $\bar{F}_n = \bar{F}_s = 1000$ N are compared with the theoretical prediction in Fig. 86. The numerical pressure histories reach the peaks and deviate from the theoretical prediction, at 2.98 MPa for $\delta_c/\bar{r} = 0.5$, 2.38 MPa for $\delta_c/\bar{r} = 0.3$, and

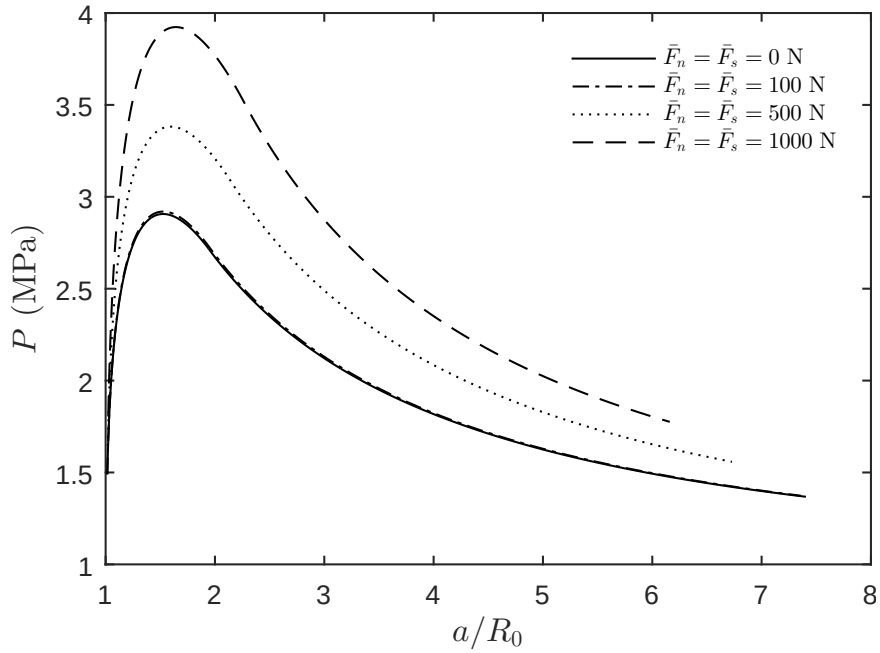

Figure 86: Internal pressure as a function of borehole area change is predicted by the elastic-perfectly plastic solution.

1.71 MPa for $\delta_c/\bar{r} = 0.1$, respectively, before the theoretical peak arrives. With increasing $\delta_c/\bar{r}$, or fluid viscosity, the peak injection pressure gradually approaches the theoretical peak as expected. A possible explanation is that as the critical gap size increases, the amount the localized deformation is limited, the pressurized borehole deforms more like a expanding circular cavity.

In Fig. 88, the theoretical radial and circumferential stresses along the radius of the hollow cylinder when subjected to an external pressure of 1 MPa and a cavity pressure of 2.98 MPa are plotted in solid lines according to the elastic-perfectly plastic solution. The averaged stresses in the numerical test 0.5_1_10_0.1_30_c1000 when the borehole pressure is about 3 MPa are plotted in dotted lines. The red lines mark the positions of the boundaries between the borehole, the plastic zone and the elastic zone. By taking into account the plastic zone, the thick-walled cylinder solution shows better agreement with the stress field in the numerical test, especially for the circumferential stress in the near-borehole vicinity.

The breakdown pressures of a series of 12 tests with $\delta_c/\bar{r} = 0.1,\ 0.3,\ 0.5$, $\sigma_o = 1$ MPa, $D_{\text{out}}/D_{\text{in}} = 10$, $Q = 0.1$ m^2/s, $\phi_b = 30°$ and $\bar{F}_n = \bar{F}_s = 0,\ 100,\ 500,\ 1000$ N are plotted in

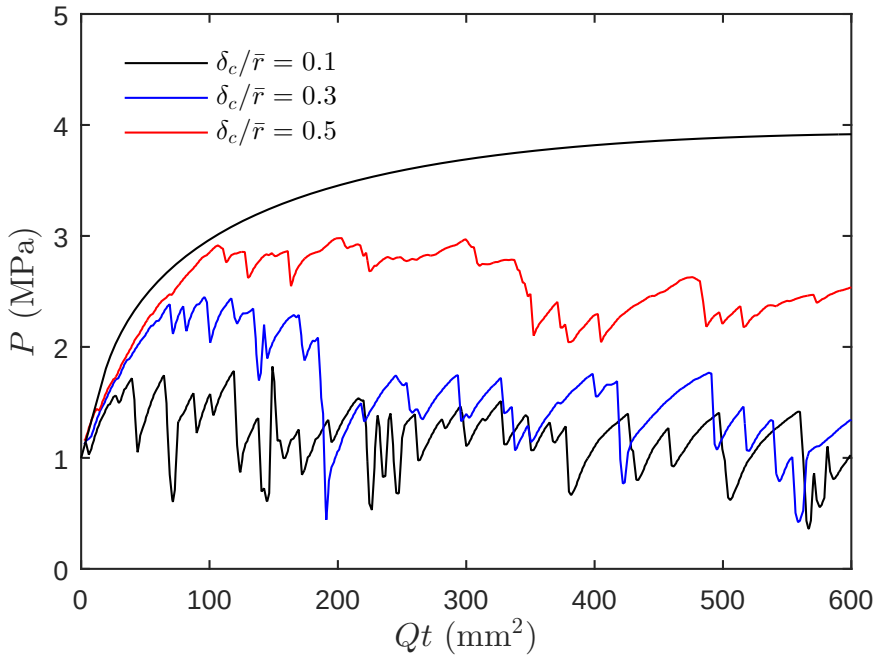

Figure 87: History of the injection pressure for tests with $\delta_c/\bar{r} = 0.1,\ 0.3,\ 0.5$, $\bar{F}_n = \bar{F}_s = 1000$ N are compared with part of the internal pressure curve predicted by the elastic-perfectly plastic solution.

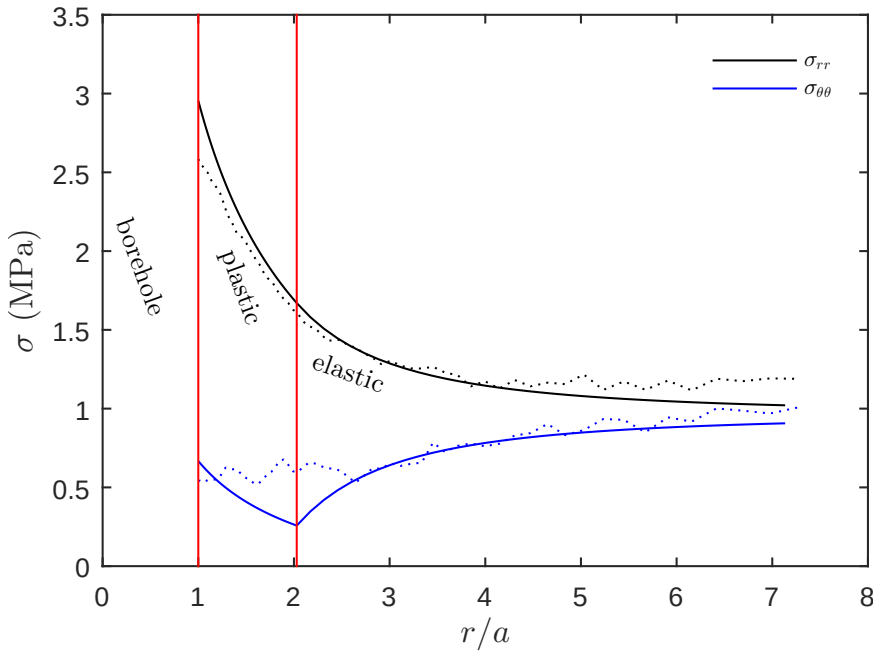

Figure 88: Averaged radial and circumferential stresses (dotted lines) are compared with predicted radial and circumferential stresses given by the elastic-perfectly plastic solution (smooth lines).

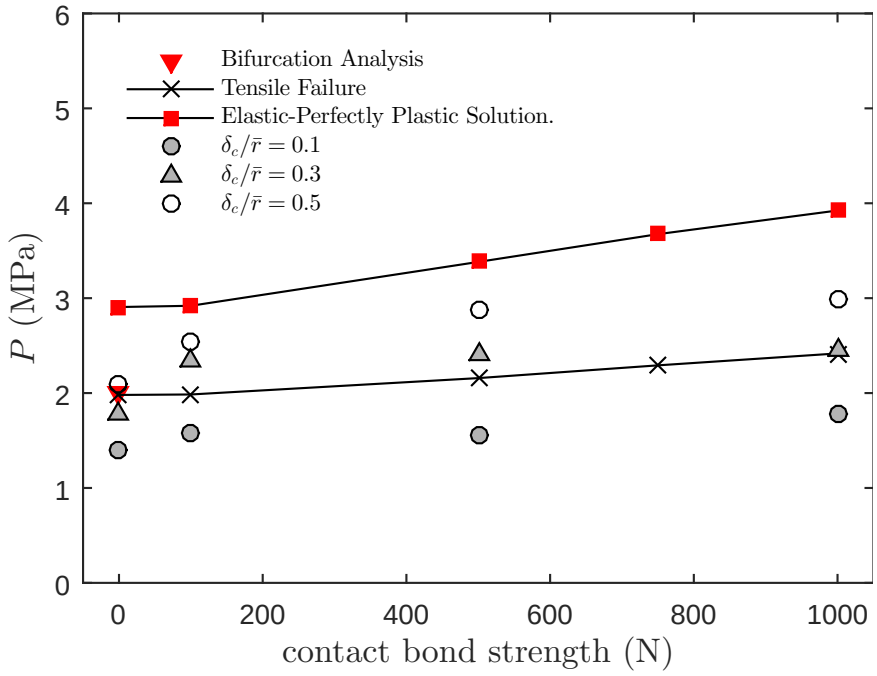

Figure 89: Summary of theoretical analysis and numerical results. The numerical tests are performed with $\delta_c/\bar{r} = 0.1,\ 0.3,\ 0.5$, $\sigma_o = 1$ MPa, $D_{\text{out}}/D_{\text{in}} = 10$, $Q = 0.1$ m^2/s, $\phi_b = 30°$ and $\bar{F}_n = \bar{F}_s = 0,\ 100,\ 500,\ 1000$ N. The theoretical analysis is obtained with corresponding parameters.

Fig 89, along with the theoretical predictions: the cavity pressure for onset of bifurcation, the cavity pressure for the tensile failure to occur and the predicted peak cavity pressure from the elastic-perfectly plastic solution. Fig. 89 summarizes the overall accuracy of the three theoretical prediction methods for various bond strengths of the medium and various $\delta_c/\bar{r}$ of the fluid. The bifurcation analysis is assumed to be for purely frictional material, therefore it is denoted as only one marker at $\bar{F}_n = \bar{F}_s = 0$ N in Fig. 89. For the cohesionless medium, both the tensile prediction and the bifurcation analysis show an excellent agreement with the numerical test with $\delta_c/\bar{r} = 0.5$ and $\bar{F}_n = \bar{F}_s = 0$ N. As the contact bond strength increases, the medium transitions from a cohesionless material to a cohesive material. The numerical breakdown pressures for the $\delta_c/\bar{r} = 0.5$ cases increase above the tensile failure prediction and fall within the range between the tensile failure solution and the elastic-perfectly plastic solution. It is also noted that as $\delta_c/\bar{r}$ increases, the breakdown pressure gradually approaches the elastic-perfectly plastic solution.

Table 16: Results of the maximum injection pressure at $Q = 0.1$ m^2/s and $\phi_b = 30°$.

Test Name	$\delta_c/\bar{r}$	σ_o (MPa)	$D_{\text{out}}/D_{\text{in}}$	P_{max} (MPa)	P_{max}/σ_o	$\Delta P_{max}/\sigma_o$
0.1_0.5_20_0.1_30	0.1	0.5	20	1.05	2.11	1.11
0.3_0.5_20_0.1_30	0.3	0.5	20	1.33	2.65	1.65
0.5_0.5_20_0.1_30	0.5	0.5	20	1.44	2.88	1.88
0.1_1_20_0.1_30	0.1	1	20	1.58	1.58	0.58
0.3_1_20_0.1_30	0.3	1	20	2.09	2.09	1.09
0.5_1_20_0.1_30	0.5	1	20	2.39	2.39	1.39
0.1_5_20_0.1_30	0.1	5	20	6.35	1.27	0.27
0.3_5_20_0.1_30	0.3	5	20	6.74	1.35	0.35
0.5_5_20_0.1_30	0.5	5	20	7.10	1.42	0.42
0.3_0.5_10_0.1_30	0.3	0.5	10	1.15	2.29	1.29
0.3_1_10_0.1_30	0.3	1	10	1.78	1.78	0.78
0.3_5_10_0.1_30	0.3	5	10	6.47	1.29	0.29
0.3_0.5_5_0.1_30	0.3	0.5	5	0.98	1.96	0.96
0.3_1_5_0.1_30	0.3	1	5	1.87	1.87	0.87
0.3_5_5_0.1_30	0.3	5	5	5.98	1.20	0.20

6.4 Parametric Analysis of the Breakdown Pressure

To further explore the factors affecting the breakdown pressure, the pressure information of the 15 tests with $Q = 0.1$ m^2/s and $\phi_b = 30°$ is complied in Table 16. The pressure ratio $\Delta P_{max}/\sigma_o$, is defined as the ratio of maximum net injection pressure ΔP_{max} and confining stress σ_o. The lowest ratio, $P_{max}/\sigma_o = 1.2$, is obtained in test 0.3_5_5_0.1_30 with $\delta_c/\bar{r} = 0.3$, $\sigma_o = 5$ MPa and $D_{\text{out}}/D_{\text{in}} = 5$. The highest ratio, $p_{max}/\sigma_o = 2.88$, is obtained in test 0.5_0.5_20_0.1_30 with $\delta_c/\bar{r} = 0.5$, $\sigma_o = 0.5$ MPa and $D_{\text{out}}/D_{\text{in}} = 20$. The effects of the critical gap size, the confining stress, and the initial borehole size upon the breakdown pressure are analyzed.

Variations of the pressure ratio, $\Delta P_{max}/\sigma_o$, with the critical gap size, are shown in Fig. 90. In general, the pressure ratio increases with the critical gap size. If $\delta_c/\bar{r}$ is greater, the surface tension, or the fluid viscosity, is larger, the fluid needs to overcome a higher pressure gradient to penetrate through. In Fig. 90, we can see similar trend for the numerical tests under different confining stresses.

Fig. 91 illustrates an increasing trend of pressure ratio with initial borehole size. Overall, a small initial borehole leads to a higher peak injection pressure, which is consistent with the theoretical solutions. The small pressure ratio corresponds to early occurrence of localized

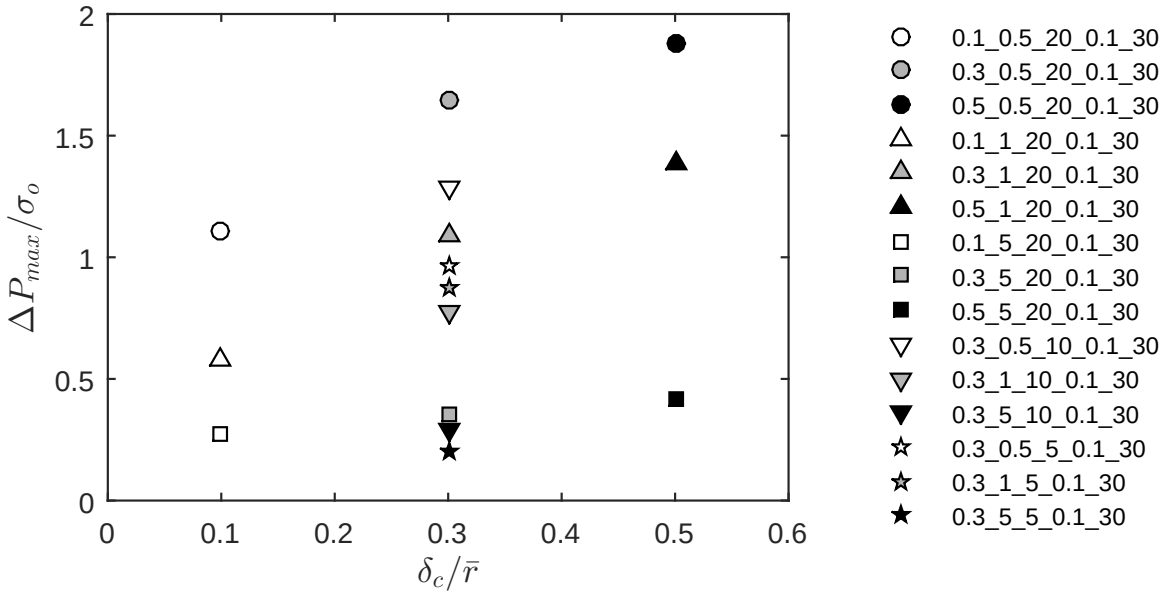

Figure 90: Variations of ratio between the maximum net injection pressure and the confining stress, $\Delta P_{max}/\sigma_o$, with critical gap size $\delta_c/\bar{r}$ for tests at $Q = 0.1$ m^2/s and $\phi_b = 30°$

deformation. The results in Fig. 91 suggests that the tests with larger initial boreholes tend to develop finger-like local features. This trend is also reflected by the displacement patterns in Section 5.3.2.

Variations of the pressure ratio, $\Delta P_{max}/\sigma_o$, and the peak net injection pressure, ΔP_{max}, with the confining stress, are shown in Figs. 92 and 93, respectively. Even though the actual breakdown pressure increases with confining stress σ_o, the pressure ratio is lower if σ_o is greater. According to Bohloli and de Pater [10], the confining stress is the dominating factor of the fracturing pressure.

6.5 Conclusion

Theoretical analyses are performed to predict the breakdown pressures in the numerical tests for both the cohesionless and cohesive media. For the cohesionless material, bifurcation analysis is performed to model the progressive failure where a shear band initiates from the inner cavity wall and progresses into the interior of the domain as the borehole increases. Theoretical prediction on the borehole pressure versus expansion volume relationship agrees well with the pressure histories from the borehole expansion stage of the numerical simulations. The pressure corresponding to the onset of bifurcation from the

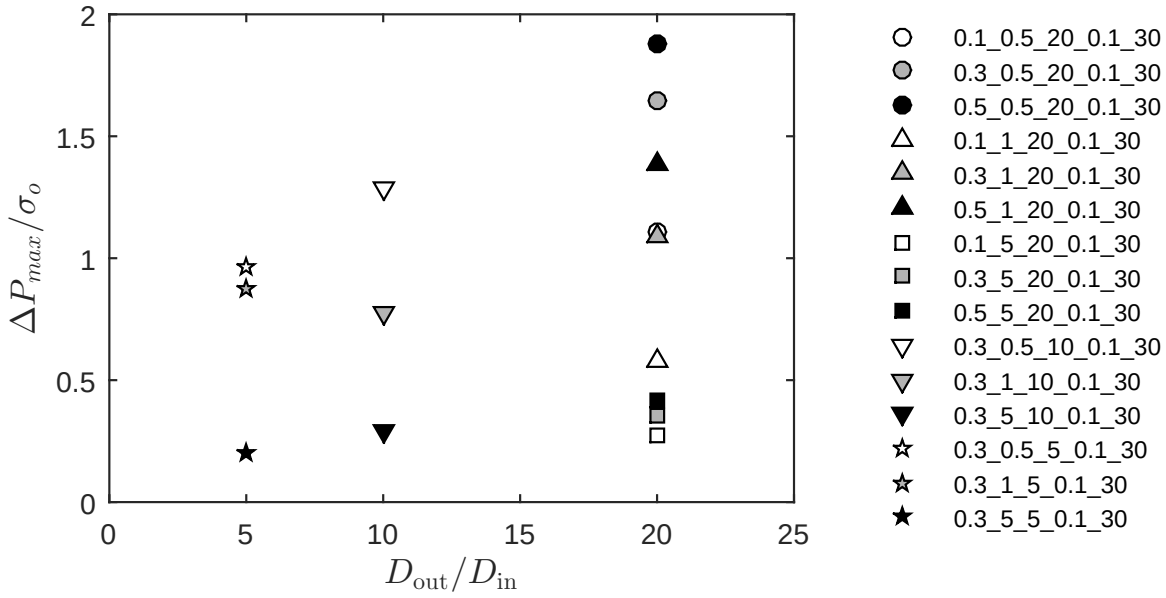

Figure 91: Variations of ratio between the maximum net injection pressure and the confining stress, $\Delta P_{max}/\sigma_o$, with the ration of initial diameter and initial borehole size $D_{\text{out}}/D_{\text{in}}$ for tests at $Q = 0.1$ m^2/s and $\phi_b = 30°$

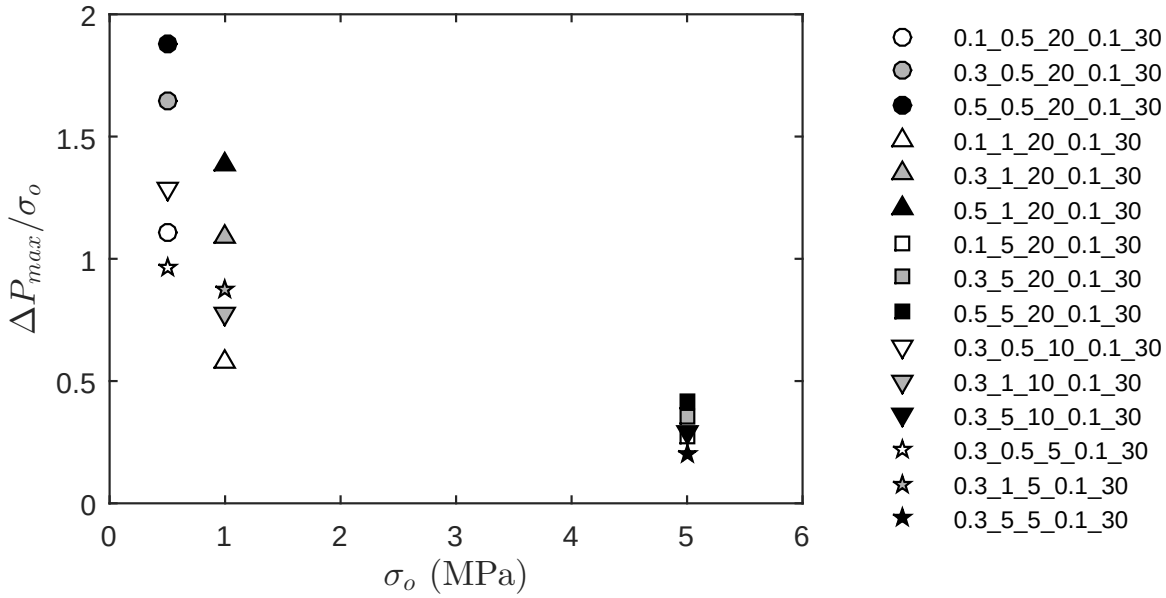

Figure 92: Variations of ratio between the maximum net injection pressure and the confining stress, $\Delta P_{max}/\sigma_o$, with confining stress σ_o for tests at $Q = 0.1$ m^2/s and $\phi_b = 30°$

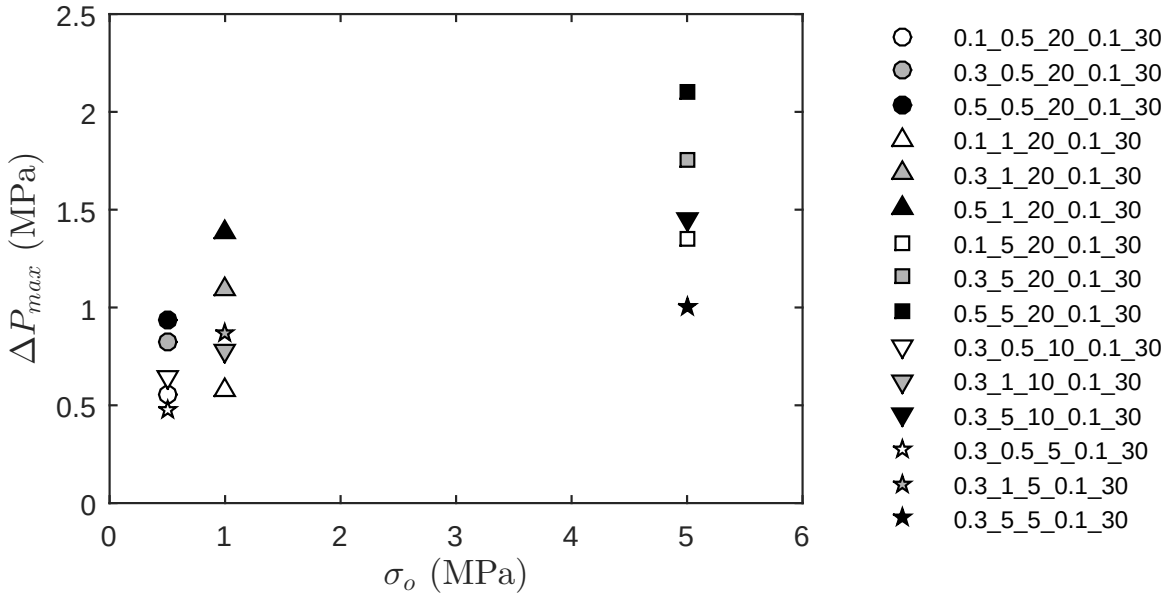

Figure 93: Variations of the maximum net injection pressure, ΔP_{max}, with confining stress σ_o for tests at $Q = 0.1$ m^2/s and $\phi_b = 30°$

inner wall is in fact in an excellent agreement with the peak pressure from the simulation case with $\delta_c/\bar{r} = 0.5$ and $b_0/a_0 = 10$.

For both cohesionless and cohesive materials, the critical cavity pressure is calculated when the tensile failure first occurs based on the elastic stress field and the tensile strength of the material. The cavity pressure corresponding to the occurrence of tensile failure is consistent with the peak pressure in the cohesionless case with $\delta_c/\bar{r} = 0.5$, but it is lower than the peak pressure in the cohesive case with $\delta_c/\bar{r} = 0.5$.

For the cohesive material, the medium is also modeled as an elastic-perfectly plastic material obeying the Mohr-Coulomb yield criterion. The peak pressure from the simulation case with $\delta_c/\bar{r} = 0.5$ falls within the range of tensile failure solution and the elastic-perfectly plastic solution. It is also noted that as δ_c increases, the breakdown pressure gradually approaches the elastic-perfectly plastic solution.

Parametric study is performed to analyze the effects of the critical gap size, the borehole size, and the confining stress upon the ratio of breakdown pressure ΔP_{max} and confining stress σ_o. Overall, a greater δ_c, a smaller initial borehole and a lower confining stress lead to a greater ratio $\Delta P_{max}/\sigma_o$.

CHAPTER VII

DEM MODELING OF FLUID INJECTION INTO AN UNCONSOLIDATED MEDIUM SUBJECTED TO ANISOTROPIC STRESS

7.1 Introduction

Fluid injection into a cohesionless formation under both isotropic and anisotropic stress fields is studied using DEM modeling in *PFC2D*®. The numerical methodology proposed in Chapter V is used to model the injection process. We focus here only on the case when the fluid leakoff is negligible and the matrix is dry or in a drained condition. We attempt to explore the complex morphology of the fractures in cohesionless materials. Effects of the stress anisotropy on the fracture trajectory are investigated. In addition, the progressive propagation of fracture tip as well as the evolution of fracture width and length is analyzed.

The numerical analysis is carried out in three types of two-dimensional DEM domains: a rectangular assembly with a center hole, a center or side slot. The outer boundary is implemented by two fixed walls at the bottom and left sides as well as two servo-controlled walls at the top and right sides. All the walls are frictionless, and their stiffness is set to be the same as that of the particles.. The biaxial assembly is used to investigate the mechanisms of fracture propagation under both isotropic and anisotropic stress conditions. The micro-scale parameters specified for the particle assembly and the interface chain are summarized in Table 17.

Table 17: Micro-scale properties of the cohesionless particle assembly.

Grains	density	$\rho = 2650$ kg/m^3
	particle radius	$0.5 - 0.7$
	friction	$\phi_b = 30°$
	contact stiffness	$k_n = k_s = 0.417 \times 10^8$ N/m
	bond strength	$\bar{F}_n = \bar{F}_s = 0$ N
Interface chain	contact stiffness	$k_{nc} = k_{sc} = 0.417 \times 10^7$ N/m
	critical gap	$\delta_c/\bar{r} = 0.1$

7.2 A Rectangular Sample with a Center Hole

Fluid injection from a circular borehole into a cohesionless rectangular domain is modeled here. The domain is subjected to horizontal and vertical confining stresses as shown in Fig. 94. The width and the height of the assembly are $W = H = 200$ mm. The hole has a diameter $D_{\text{in}} = 15$ mm. The assembly consists of about 30,600 particles with radii ranging from 0.5 to 0.7 mm ($W/\bar{r} = 333$ and $D_{\text{in}}/R = 25$).

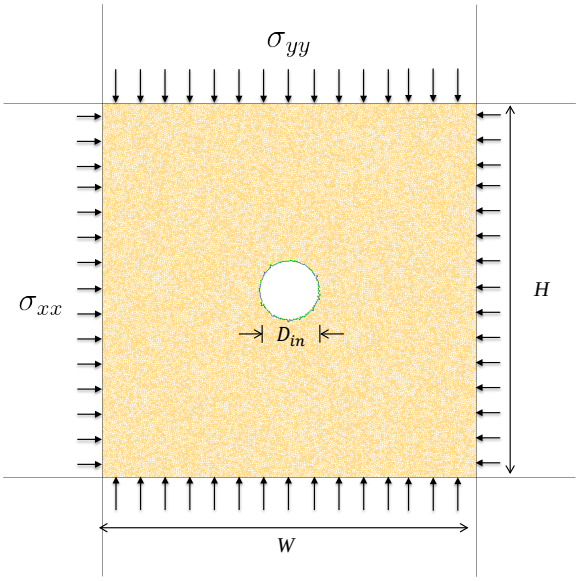

Figure 94: Schematic of biaxial setup with a center hole.

The displacement patterns from the series of injection tests into a center hole with various confining stresses are shown in Fig. 95. The ratio between horizontal stress σ_{xx}

and vertical stress σ_{yy} is defined as stress ratio λ to quantify the stress anisotropy, namely, $\lambda = \sigma_{xx}/\sigma_{yy}$. In Fig. 95, the horizontal stress is maintained constant $\sigma_{xx} = 1$ MPa, and the vertical stress is varied, $\sigma_{yy} = 1,\ 1.25,\ 1.5$ MPa , which gives a varying stress ratio $\lambda = 1,\ 0.8$, and 0.67. As a result, the borehole breakdown pressures are 2.68 MPa, 3.21 MPa and 3.37 MPa, respectively, in tests A1, A2 and A3. In the test with an isotropic confining stress, three main fractures are developed, as shown in Fig. 95 (a), while in the tests with an isotropic stress field, only one fracture is able to extend outward, as shown in Fig. 95 (b)(c).

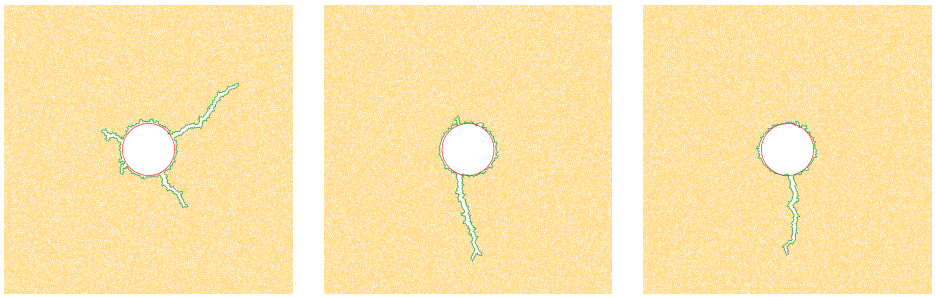

A1 A2 A3

Figure 95: Morphology of the fluid-grain interface initiated from a center hole under different stress anisotropy: A1, $\sigma_{xx} = 1$ MPa, $\sigma_{yy} = 1$ MPa; A2, $\sigma_{xx} = 1$ MPa, $\sigma_{yy} = 1.25$ MPa; A3, $\sigma_{xx} = 1$ MPa, $\sigma_{yy} = 1.5$ MPa.

For the isotropic case, the three fractures initiated from the borehole boundary are almost equally spaced on the circumference. The initiation is likely governed by the weakest contacts on the borehole perimeter. After the fractures are initiated, the propagation is mainly in the radial direction. Based on the elastic solution, the circumferential stress should be the least compressive at the upper and lower ends of the borehole, given the far field stress $\sigma_{yy} > \sigma_{xx}$. It is noted that with a greater stress anisotropy in test A3, the initiation location is closer to the theoretical prediction than that in A2. The initiation is likely affected by both the far field stress as well as local variation in the contact forces due to the random nature of the particle assembly. If the effect of the stress anisotropy overweights that of the local effect, the initiation location of the fracture is then governed by the stress field. In both tests A2 and A3, the fracture starts to align itself with the

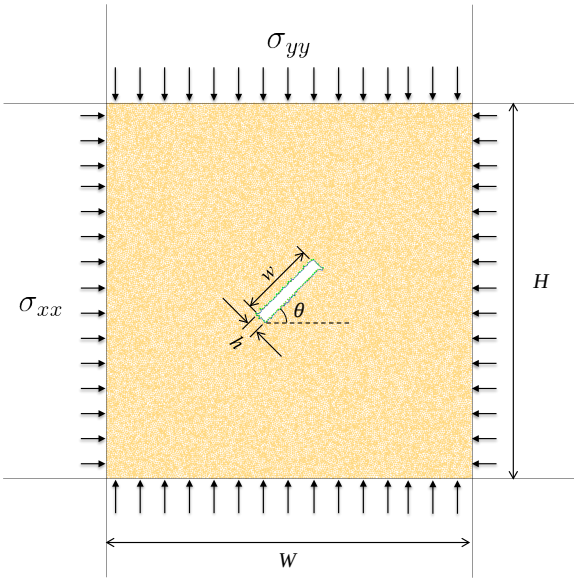

Figure 96: Schematic of biaxial setup with a center slot.

major principal direction after initiated.

7.3 A Rectangular Sample with a Center Slot

Fluid injection from a slot-shaped defect into a cohesionless biaxial domain is modeled in this section. The rectangular domain is subjected to the horizontal and vertical confining stresses as shown in Fig. 96. Orientation angle of the slot is θ with respect to the horizontal direction, θ is taken as 0° or 45°. The assembly consists of about 31,000 particles. The width and the height of the assembly are $W = H = 200$ mm. The slot has a width $w = 40$ mm and a height of $h = 4.8$ mm ($W/w = 5$ and $h/\bar{r} = 8$).

To investigate the influence of the stress anisotropy on the fracture path, a series of 10 numerical tests are performed at a constant injection rate $Q = 0.1$ m^2/s with various confining stress and slot orientation. Both σ_{xx} and σ_{yy} are varied among 1 MPa, 1.25 MPa and 1.5 MPa, which produce a varying stress ratio $\lambda = 1.5,\ 1.25,\ 1,\ 0.8$, and 0.67.

7.3.1 $\theta = 0^\circ$

Fig. 97 shows the morphologies of the fluid-grain interface for the 5 tests with a horizontal center slot. Red block indicate initial slot positions. Magnified views are presented in Fig. 98 to illustrate the details.

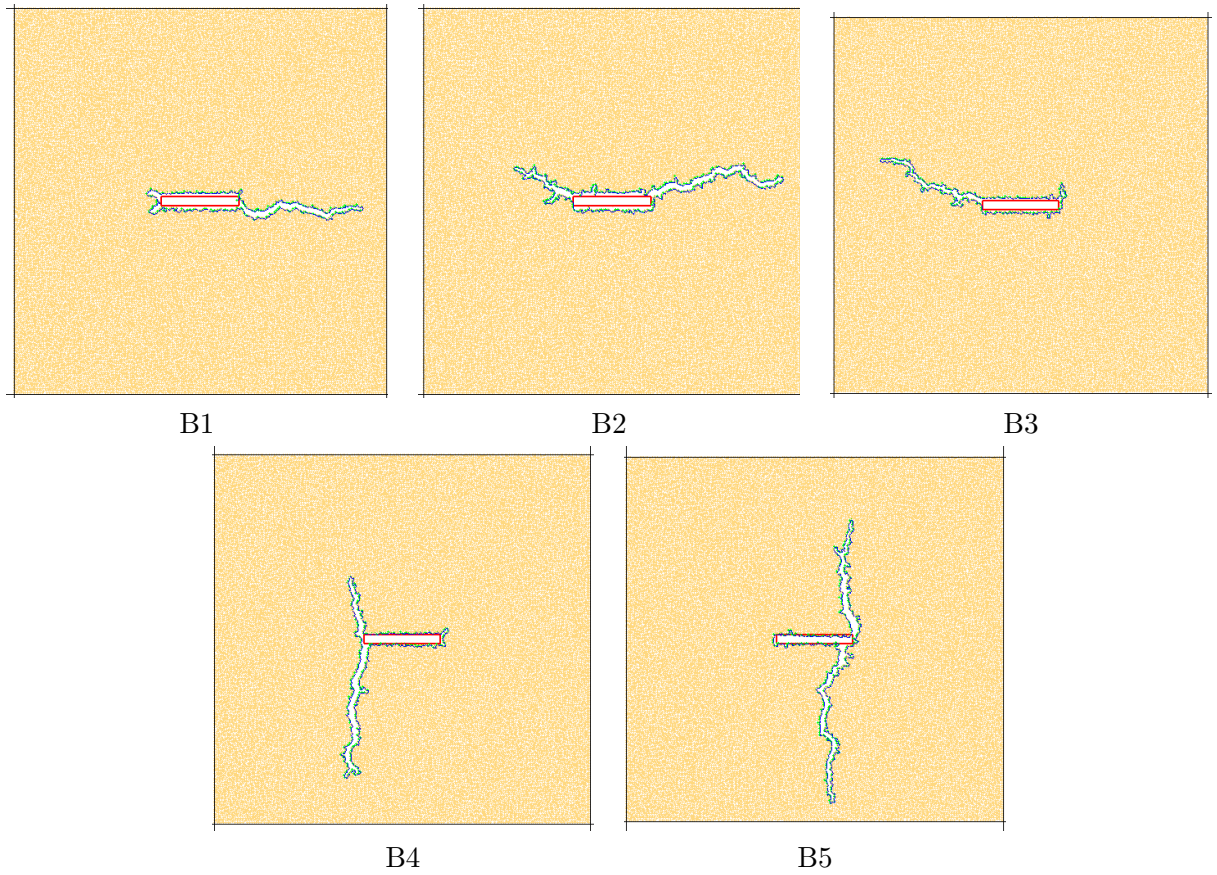

Figure 97: Morphology of the fluid-grain interface with a horizontal slot under different stress anisotropy: B1, $\sigma_{xx} = 1.5$ MPa, $\sigma_{yy} = 1$ MPa; B2, $\sigma_{xx} = 1.25$ MPa, $\sigma_{yy} = 1$ MPa; B3, $\sigma_{xx} = 1$ MPa, $\sigma_{yy} = 1$ MPa; B4, $\sigma_{xx} = 1$ MPa, $\sigma_{yy} = 1.25$ MPa; B5, $\sigma_{xx} = 1$ MPa, $\sigma_{yy} = 1.5$ MPa.

Fig. 97 shows that the direction of fracture path is strongly affected by stress anisotropy. In test B1-B3, the fracture starts at an angle with respect to the slot plane and then propagates in a zig-zag pattern, though overall the fracture path is more or less oriented to the principal direction. With a stress contrast of $\lambda = 1.5$ (Test B1), zig-zag is the most obvious, but the amplitude of oscillation gradually decreases as the fracture grows longer. Such a zig-zag propagation pattern can be considered as an indication of shear deformation in the host medium. For tests B4 and B5, the slot plane is paralle to the minor principal stress in the far-field. The fractures do not extend along the slot plane. Instead, two branches immediately develops and propagates along the vertical direction, indicating the path could be rather well defined when the initial flaw is parallel to the minor principal stress direction.

Fig. 98 shows the magnified views of one branch of the fracture in each test. Boundaries of the fractures formed under greater stress contrast are relatively smooth while those formed under smaller stress contrast have more side branches and irregularities. It is also noted that in the three cases with $\lambda \geq 1$ (B1-B3), the initial fracture orientation is at about $\pi/4 - \phi/2$ with respect to the horizontal direction. For stress contrast $\lambda < 1$ (B4 and B5), the initial fracture orientation is at a greater angle of about $\pi/4 + \phi/2$, suggesting that the onset of the fracture growth is related to shear failure. Notice that in these tests, while the slot width increases in Tests B1-B3 as the fractures extend, the width actually becomes smaller than the initial value in Test B4-B5. This could be explained by the fact that the propagation fracture is within the range of $\sigma_3 < P < \sigma_1$. The pressure the slot faces is smaller than σ_1 in Tests B4-B5.

7.3.2 $\theta = 45°$

Fig. 99 shows the morphologies of the fluid-grain interface for the 5 tests with a center slot inclined at an angle of 45°. The initial slot positions are marked in red. Magnified views are presented in Fig. 100 to illustrate the details.

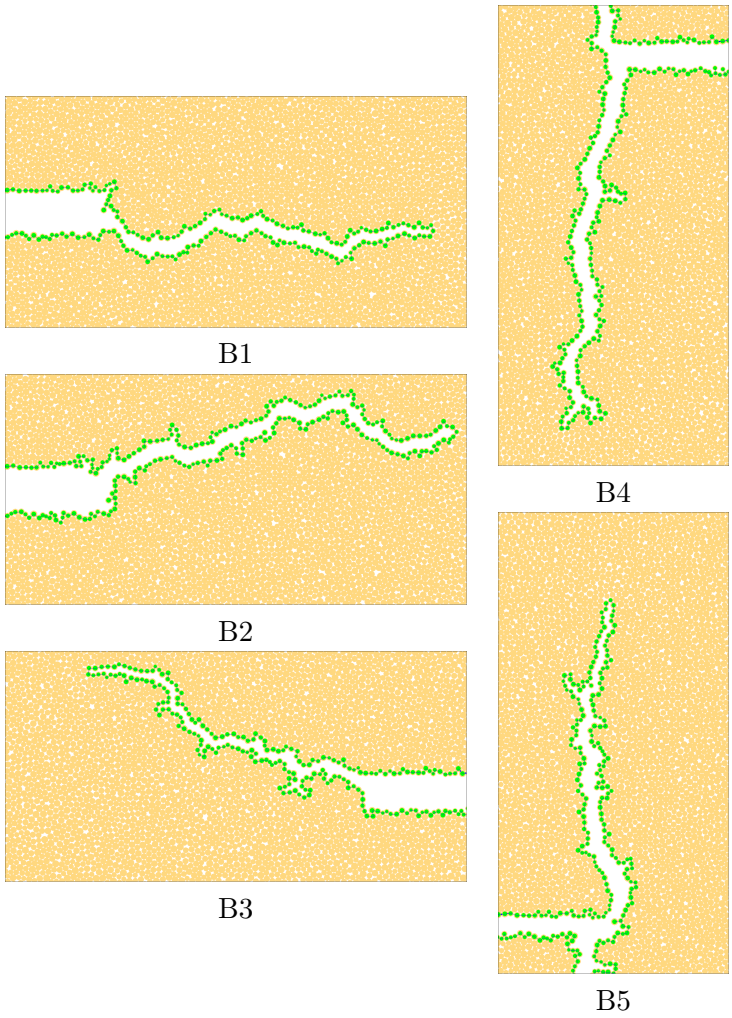

Figure 98: Magnified views of the morphology of the fluid-grain interface with a horizontal slot under different stress anisotropy: B1, $\sigma_{xx} = 1.5$ MPa, $\sigma_{yy} = 1$ MPa; B2, $\sigma_{xx} = 1.25$ MPa, $\sigma_{yy} = 1$ MPa; B3, $\sigma_{xx} = 1$ MPa, $\sigma_{yy} = 1$ MPa; B4, $\sigma_{xx} = 1$ MPa, $\sigma_{yy} = 1.25$ MPa; B5, $\sigma_{xx} = 1$ MPa, $\sigma_{yy} = 1.5$ MPa.

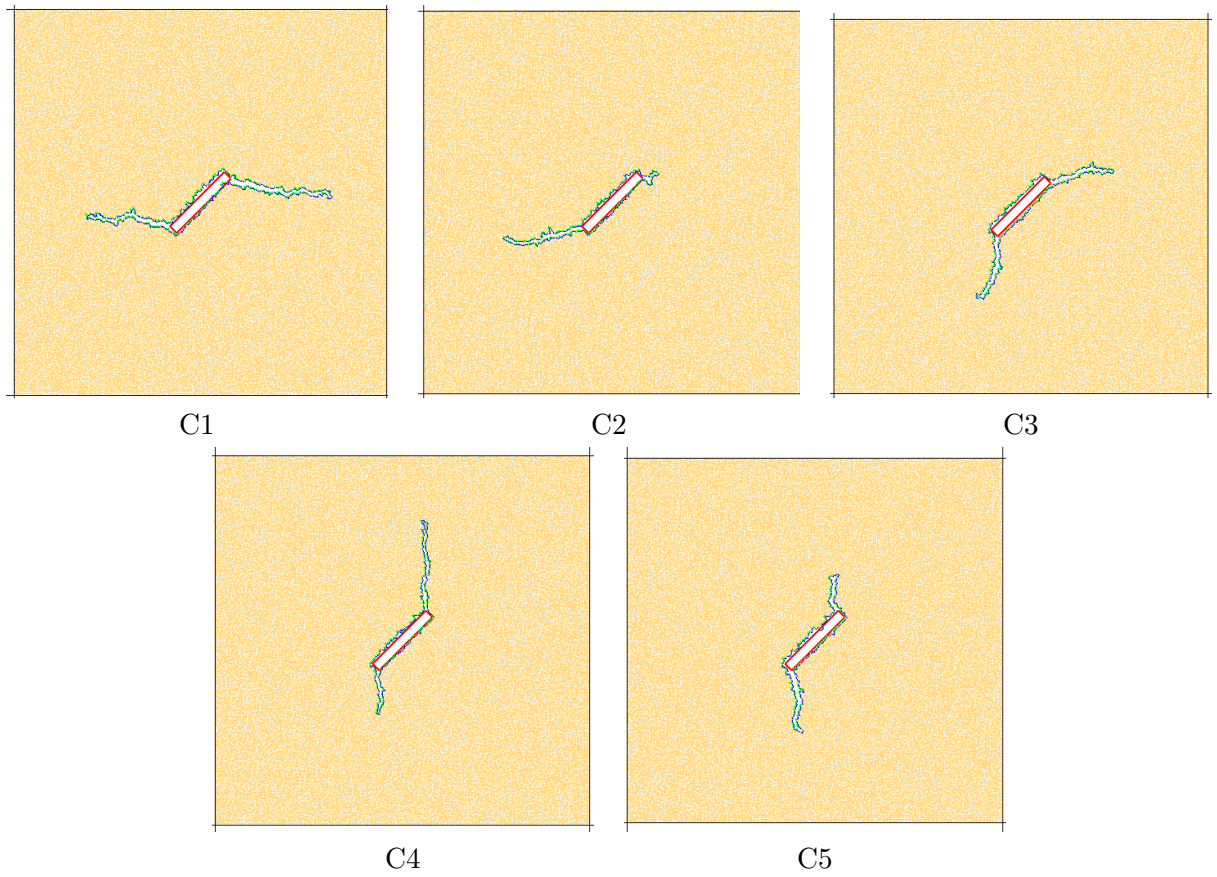

Figure 99: Morphology of the fluid-grain interface with a center slot inclined at 45° under different stress anisotropy: C1, $\sigma_{xx} = 1.5$ MPa, $\sigma_{yy} = 1$ MPa; C2, $\sigma_{xx} = 1.25$ MPa, $\sigma_{yy} = 1$ MPa; C3, $\sigma_{xx} = 1$ MPa, $\sigma_{yy} = 1$ MPa; C4, $\sigma_{xx} = 1$ MPa, $\sigma_{yy} = 1.25$ MPa; C5, $\sigma_{xx} = 1$ MPa, $\sigma_{yy} = 1.5$ MPa.

Table 18: Pressure information of the anisotropic tests with a center slot; the stress unit is in MPa.

Test	σ_{xx}	σ_{yy}	λ	σ_m	p_{ini}	p_{ini}/σ_m	Δp_{ini}	$\Delta p_{\text{ini}}/\sigma_m$
B1	1.5	1	1.5	1.25	2.44	1.95	1.44	1.15
B2	1.25	1	1.25	1.125	2.50	2.22	1.50	1.33
B3	1	1	1	1	2.35	2.35	1.35	1.35
B4	1	1.25	0.8	1.125	3.09	2.75	2.09	1.86
B5	1	1.5	0.67	1.25	3.57	2.86	2.57	2.06
C1	1.5	1	1.5	1.25	3.07	2.46	2.07	1.66
C2	1.25	1	1.25	1.125	2.63	2.34	1.63	1.45
C3	1	1	1	1	2.61	2.61	1.61	1.61
C4	1	1.25	0.8	1.125	2.79	2.48	1.79	1.59
C5	1	1.5	0.67	1.25	2.98	2.38	1.98	1.58

Fig. 100 shows the magnified views of one branch of the fracture in each test for the cases with the center slot orientated at 45°. Similar to the cases with $\theta = 0°$, after the fractures are initiated, they start to align themselves with the direction of the major principal stress. However, the tortuosity of the fracture path seems to be dependent of the stress anisotropy. Tortuosity of the fracture path will be analyzed quantitatively for the configuration with a side slot in Section 7.4.

7.3.3 Breakdown Pressure

The ratio of the breakdown pressure and the mean confining stress are summarized for both test series B and C in Table 18. In test series B, the ratio is the lowest for test B1 with the initial slot aligned with the major principal direction and is the highest for test B5 with the initial slot perpendicular to the the major principal direction. It is noted that when the fracture needs least effort to be oriented to the major principal direction, the pressure required to initiate the fracture is also minimized. In test series C, the fracture initiation pressure is the lowest in Test C3. The fracture initiation pressure increases with the major principal stress. But the ratio between the net pressure, $\Delta p_{\text{ini}} = p_{\text{ini}} - \sigma_{\text{min}}$, over the mean far field stress do not vary much. This perhaps should be expected since the orientation of the slot with respect to the minor principal stress is the same in all these cases. From the perspective of the boundary conditions, Tests C1 and C5 as well as Tests C2 and C4 are equivalent. They indeed have about the same fracturing pressure as expected.

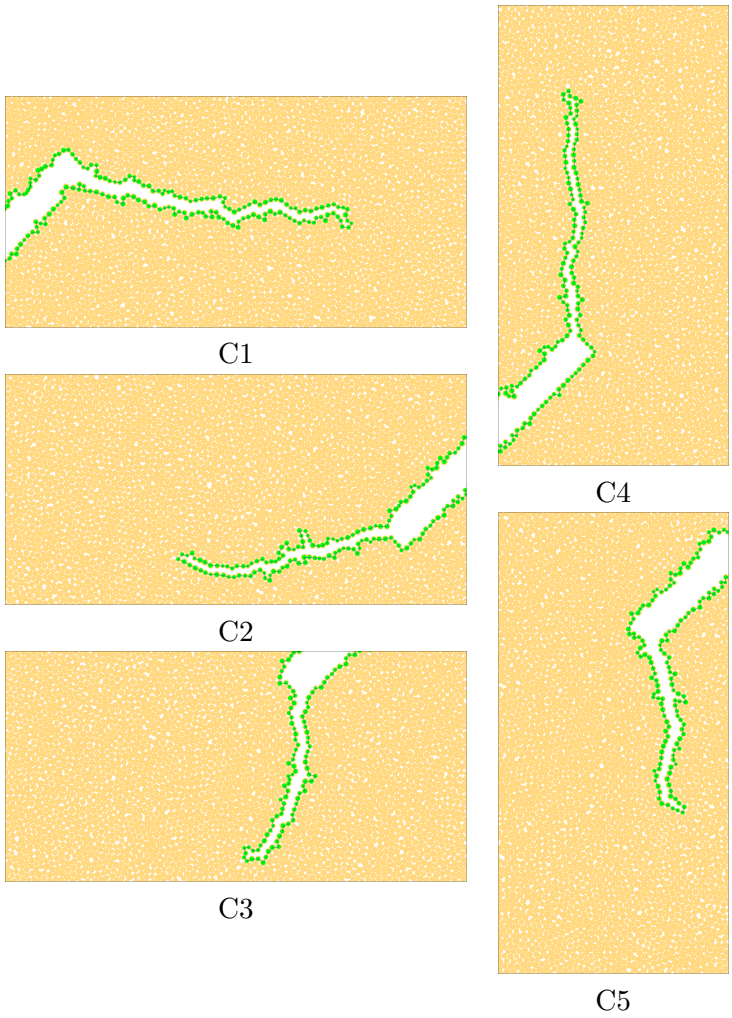

Figure 100: Magnified view of morphology of the fluid-grain interface with a center slot inclined at 45° under different stress anisotropy: C1, $\sigma_{xx} = 1.5$ MPa, $\sigma_{yy} = 1$ MPa; C2, $\sigma_{xx} = 1.25$ MPa, $\sigma_{yy} = 1$ MPa; C3, $\sigma_{xx} = 1$ MPa, $\sigma_{yy} = 1$ MPa; C4, $\sigma_{xx} = 1$ MPa, $\sigma_{yy} = 1.25$ MPa; C5, $\sigma_{xx} = 1$ MPa, $\sigma_{yy} = 1.5$ MPa.

7.4 A Rectangular Sample with a Side Slot

To further investigate fracture initiation and propagation in a larger domain with randomly generated assembly, a rectangular domain with a side slot is subjected to horizontal and vertical confining stresses as shown in Fig. 101. The assembly has about 28,600 particles with radii ranging from 0.5 mm to 0.7 mm. The width and the height of the assembly are $W = H = 200$ mm. The side slot has a width $w = 20$ mm ($W/w = 10$) and a height of $h = 6$ mm ($h/\bar{r} = 10$). Four groups of tests are performed at a constant injection rate $Q = 0.1$ m^2/s with various confining stress. Each group includes 5 statistical realizations of the random packing with all the parameters being the same. The fracture is initiated from a preexisting slot at the left side of the assembly. Four sets of confining stress are chosen: D1: $\sigma_{xx} = 1.5$ MPa, $\sigma_{yy} = 1$ MPa; D2: $\sigma_{xx} = 1$ MPa, $\sigma_{yy} = 1$ MPa; D3: $\sigma_{xx} = 1$ MPa, $\sigma_{yy} = 1.5$ MPa; D4: $\sigma_{xx} = 3$ MPa, $\sigma_{yy} = 3$ MPa.

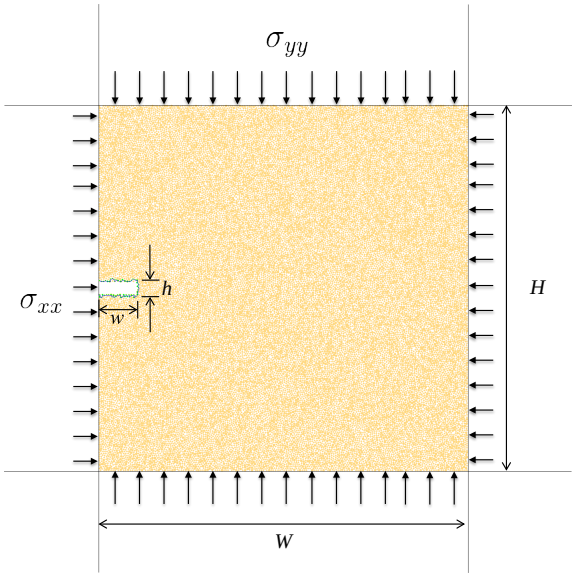

Figure 101: Schematic of biaxial setup with a side slot.

Fig. 102 shows the displacement patterns of the four test series. On each graph, final displacement patterns of the five tests with the same set of parameters are stacked on top of each other. Fig. 102 illustrates differences of the failure patterns as a result of both stress contrast and the magnitude of mean stress. Considering spatial variation of the fracture

path, it is obvious that the fracture path for the isotropic stress condition (D3 and D4) is more tortuous as opposed to a more straight pattern for the anisotropic stress condition (D1 and D2).

7.4.1 Fracture Depth

To measure the differences in the fracture paths quantitatively, we defined two parameters to characterize the spatial variation and tortuosity of the fracture trajectory. The first parameter is called fracture depth Y, which is expressed as

$$Y = y - \bar{Y} \tag{130}$$

where y is the distance from a point on the fracture mid-line (black line) to the horizontal axis; $\bar{Y}$ is the averaged value of y, which is denoted by a red line, as shown in Fig. 103. The probability density of the fracture depth is calculated. The fracture depth is sampled at an interval of lateral distance Δx along the mid-line. The values of the fracture depth are then partitioned into bins, and the count in each bin can be plotted as histograms.

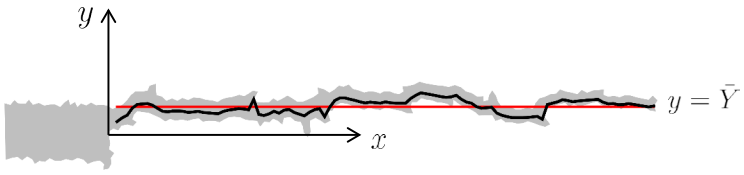

(a)

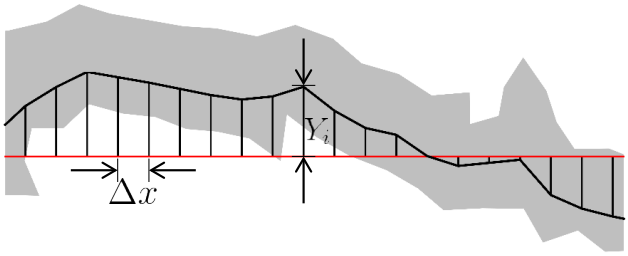

(b)

Figure 103: Schematic of the fracture depth.

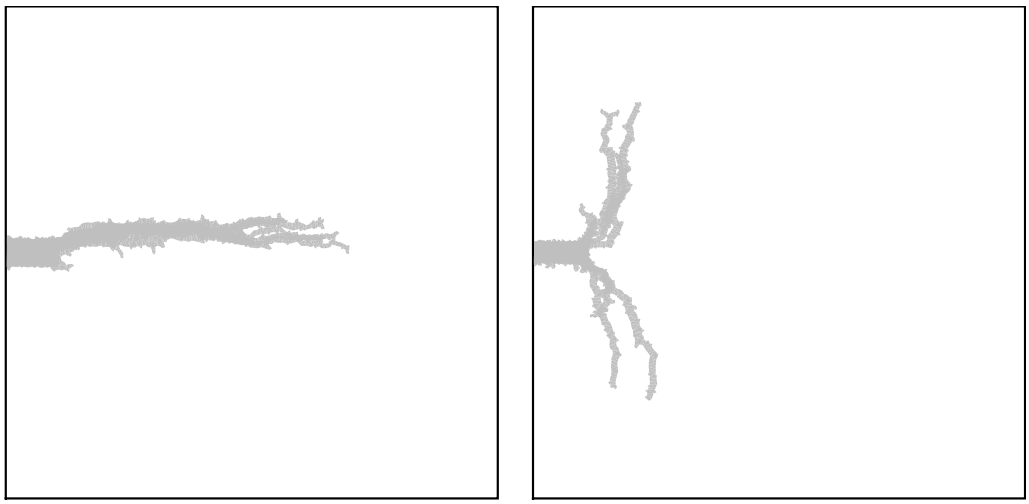

(a) D1

(b) D2

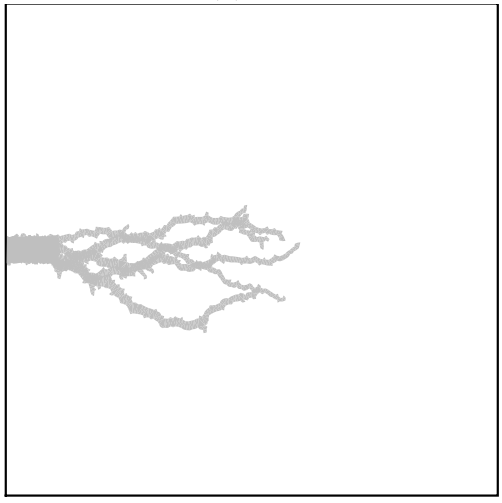

(c) D3

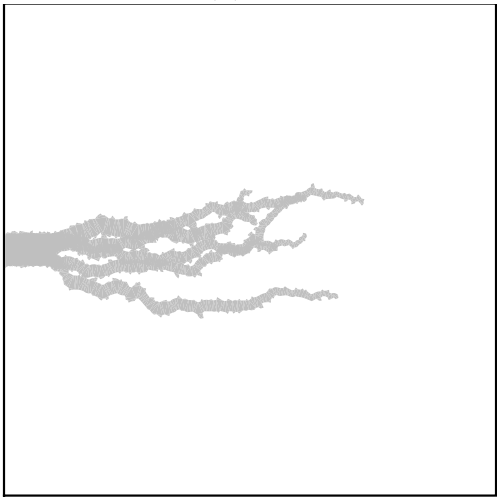

(d) D4

Figure 102: Overlay displacement patterns of four test series with a side slot under different confining stresses: D1: $\sigma_{xx} = 1.5$ MPa, $\sigma_{yy} = 1$ MPa; D2: $\sigma_{xx} = 1$ MPa, $\sigma_{yy} = 1.5$ MPa; D3: $\sigma_{xx} = 1$ MPa, $\sigma_{yy} = 1$ MPa; D4: $\sigma_{xx} = 3$ MPa, $\sigma_{yy} = 3$ MPa. Each series include five statistical realizations.

Figs. 104-106 show the histograms of the tests at various confining stresses (Note this analysis is not meaningful for Test D2 since the fracture path has turned to become perpendicular to the initial slot orientation). Each graph contains plots of five colors, representing the histograms for the five tests. The peaks represent the most common values. Since the fracture depth is taken with respect to the average depth, the peaks are all located around zero. The spread of the histogram indicates how much the fracture trajectory deviates from the center line of the initial slot. In test D1, the variation of the fracture depth is limited to a narrow range of about 10 mm, while that ranges for tests D3 and D4 are relatively larger, but similar, since now there is no stress anisotropy. The variation of the fracture depth for D3 is about 35 mm while that number for D4 is about 30 mm.

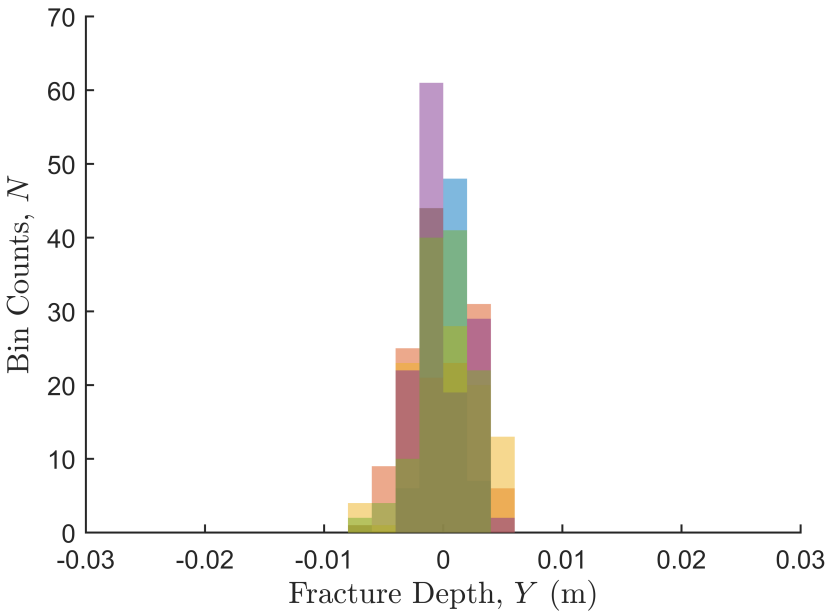

Figure 104: Histograms of the fracture depth for test series D1.

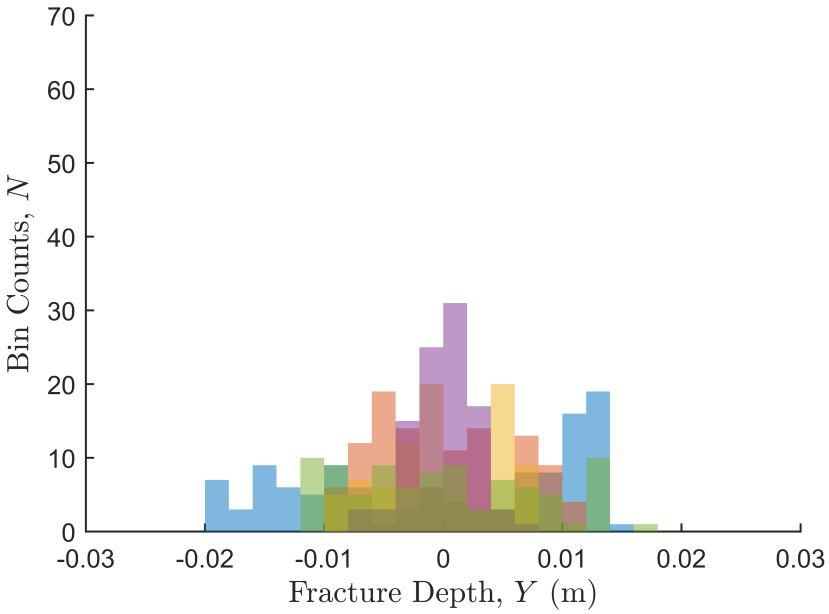

Figure 105: Histograms of the fracture depth for test series D3.

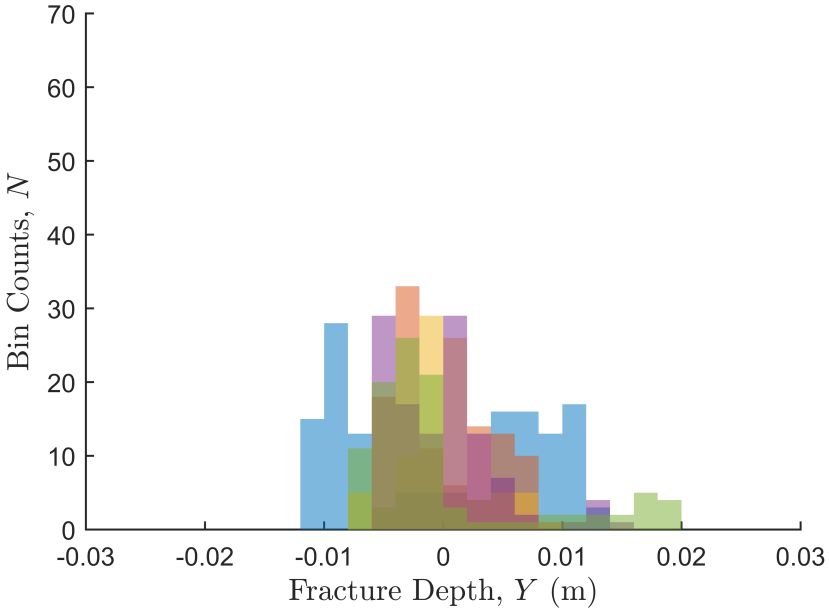

Figure 106: Histograms of the fracture depth for test series D4.

7.4.2 Fracture Sinuosity

Even though the histogram clearly indicates the range of global variation, it is not able to reflect the tortuosity of the fracture path, in other words, the local variation. A parameter defined as the fracture path sinuosity is used to measure the tortuosity. The sinuosity is expressed as the ratio of the actual length of the fracture path, denoted by S, and the straight line distance between the ends, denoted by L.

$$\text{sinuosity} = \frac{S}{L} \tag{131}$$

Fig. 107 shows two examples of the sinuosity calculation. We can clearly see the path is more meandering with a greater sinuosity.

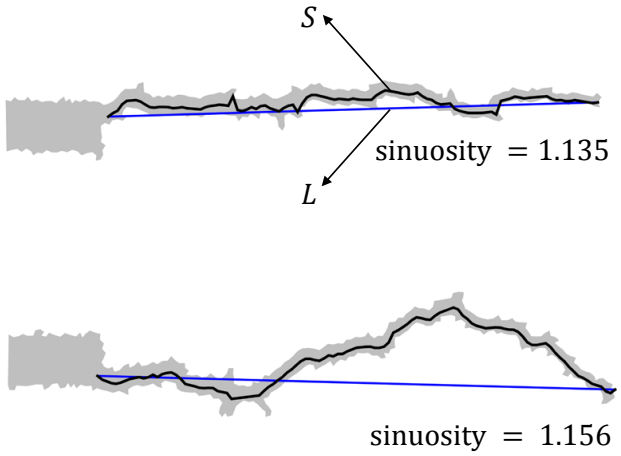

Figure 107: Illustration of fracture sinuosity.

In Fig. 107 the actual fracture path passes through the shortest path multiple times since the path follows an oscillating zig-zag pattern. We assume that every time when the fracture changes its direction, the intersection angle is a constant ω. Next, we aim to relate the sinuosity with the intersection angle. Considering two fracture paths $ABCD$ and $AB'C'D$ in Fig. 108, the total length of the two paths are exactly the same as long as the intersection angle is a constant. In other words, the length of the actual fracture path is not

affected by where the fracture changes direction but solely attributed to the intersection angle. Based on geometric relations, the sinuosity is expressed as a function of intersection angle ω,

$$\text{sinuosity} = \frac{1}{\sin\frac{\omega}{2}} \tag{132}$$

It should be pointed out the intersection angle is only an apparent measurement but not the true angle.

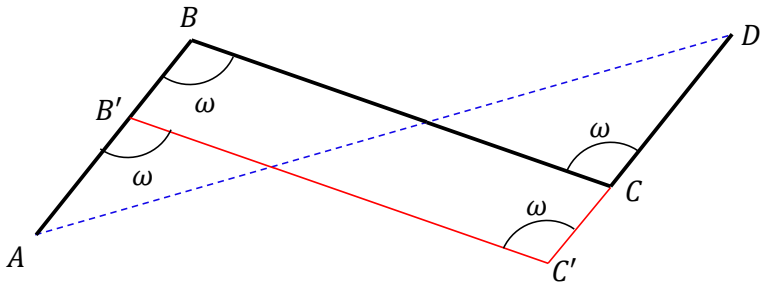

Figure 108: Schematic of fracture intersection angle.

To analyze the sinuosity for each group of tests, the range of sinuosity (vertical bars) as well as the mean values (circles) are plotted in Fig. 109. Overall, the sinuosity varies within the range of 1 to 1.25. It is able to differentiate the tortuosity of the fracture paths in different tests. Again, the result from Test D2 is not very meaningful since the fracture path has turned. It is still presented just for reference. Test group D3 exhibits the highest sinuosity with the average of 1.13, slightly greater than that of test group D4 which is 1.12. Both D3 and D4 are under isotropic stress field, therefore the difference in sinuosity is solely attributed to the degree of confinement. It is observed that the failure patterns under a greater confining stress is more linear.

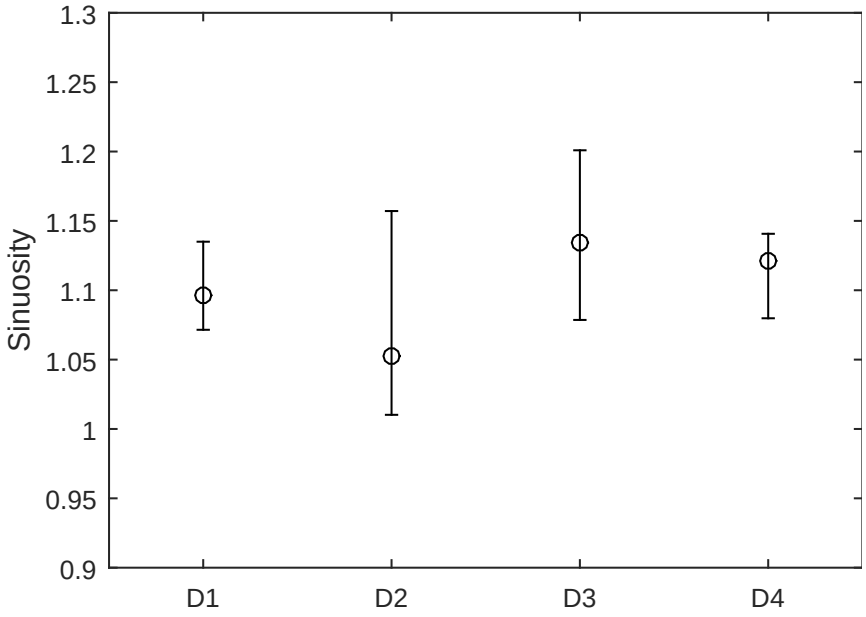

Figure 109: Variation of the fracture sinuosity for test series D1, D2, D3 and D4.

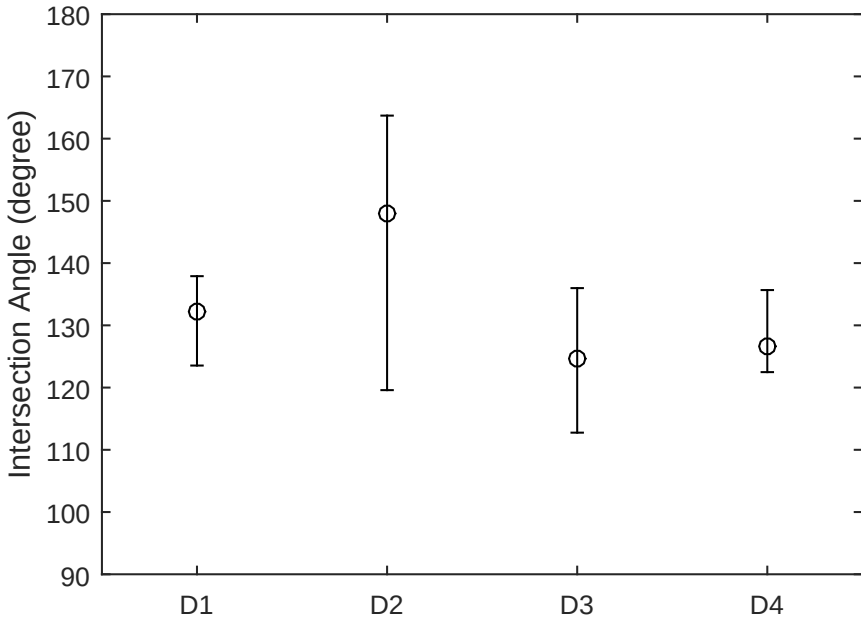

Figure 110: Variation of the fracture intersection angle for test series D1, D2, D3 and D4.

The values for the sinuosity can be translated to intersection angles based on Eq. 132, as shown in Fig. 110. The intersection angles vary within the range of $110° - 165°$. The mean intersection angles for D1, D2, D3 and D4 are 132°, 149°, 125°, and 126°, respectively.

By introducing stress anisotropy, the fracture paths in D1 and D2 become more linear and the zig-zagging is significantly reduced. Under isotropic stress field, the intersection angle is about 125°, and the corresponding supplementary angle is 55° in both D3 and D4. Given friction angle $\phi = 26°$, the new branch turns to a direction of about $\pi/4 + \phi/2$ with respect to the old branch, which is an indication that the tip propagates as a result of shear failure.

7.4.3 Evolution of Fracture Width, Length and Displacement Field

In order to track the growth of the fracture in both width and length as a function of time, a case with the isotropic stress field, $\sigma_{xx} = \sigma_{yy} = 1$ MPa, and a case with the anisotropic stress field, $\sigma_{xx} = 1.5$ MPa, $\sigma_{yy} = 1$ MPa, are selected for further analysis. In each case, three pairs of particles are chosen as marker balls based on the final failure pattern so that each pair of particles are located on the opposite sides of the fracture. Then the numerical test is repeated, and the relative distance between the two particles is monitored as the fracture width. Here the fracture length is defined as the horizontal distance from the center to the outer tip, which is denoted by L_{tip} as indicated in Fig. 111.

7.4.3.1 Case I: $\sigma_{xx} = \sigma_{yy} = 1$ MPa

Fig. 111 indicates the morphology of the fluid-grain interface for case I and the final locations of the marker balls. Since the stress field is isotropic, the fracture is initiated at the upper corner of the slot due to the stress concentration. The fracture path turns after initiation, but then continues to grow in about the same direction. The sinuosity and the intersection angle of the fracture path in case I are sinuosity = 1.084 and $\omega = 134.72°$, respectively.

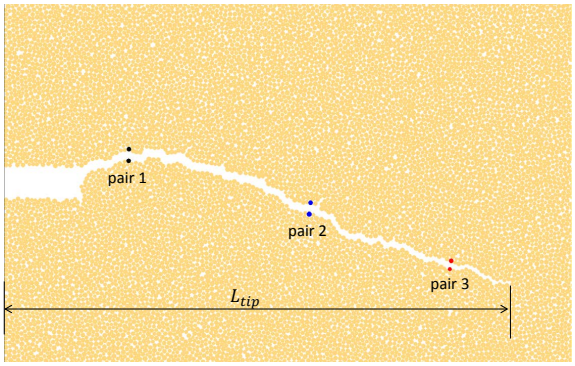

Figure 111: Morphology of the fluid-grain interface for case I with$\sigma_{xx} = \sigma_{yy} = 1$ MPa, showing only part of the domain. The balls in color represent the three pairs of markers.

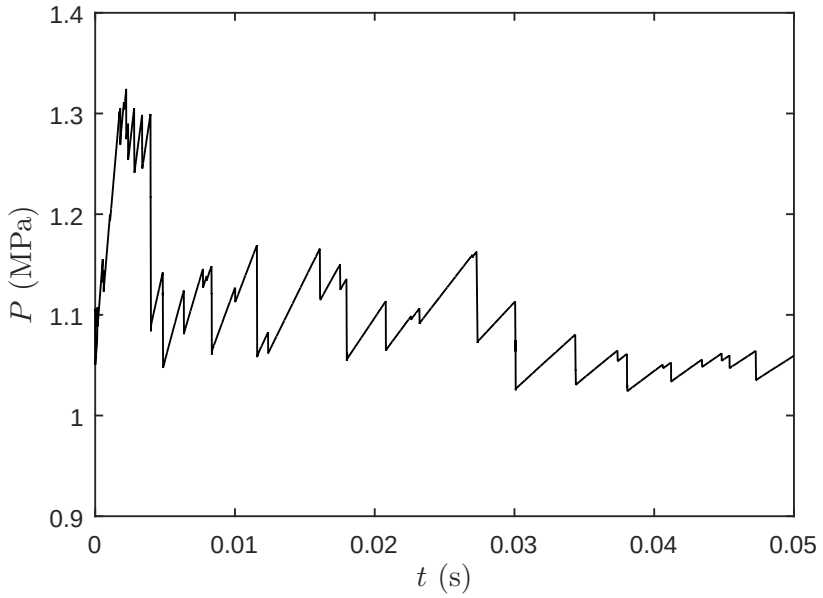

Figure 112: Pressure history for case I with$\sigma_{xx} = \sigma_{yy} = 1$ MPa.

Fig. 112 shows the injection pressure history for case I with $Q = 0.1$ m^2/s and $\delta_c/\bar{r} = 0.1$. After an initial spike, associated with the sudden application of the velocity at the slot, the pressure significantly drops as the main fracture is initiated and starts to propagate. The pressure then declines with many small drops due to the continued growth and propagation of the fracture. Since in this test the far field boundaries are subjected to a constant hydrostatic mechanical stress, the fluid pressure is expected to re-establish a state of static equilibrium. As a result, at the end of the injection the fluid pressure tends to level off at

about 1.05 MPa, which equals to the far field stress.

The evolution of the fracture widths is shown in Fig. 113. Overall, the earlier segments are wider than the later segments. Before the fracture tip arrives a certain pair of markers, the contact in compression with a small overlap, indicated by a negative width in Fig. 113. When fracture tip arrives that pair of markers, it is reflected in Fig. 113 as a sudden jump in the fracture width. It is also noted that the oscillation of fracture width coincides with the pressure change. Once a new segment is opened, the pressure in the old segments declines, causing a reverse movement of the particles near the fluid-grain interface.

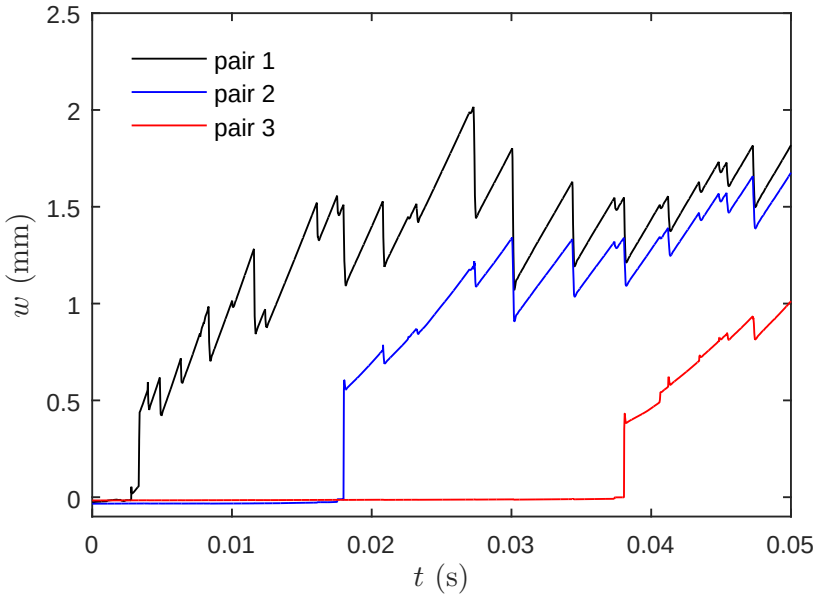

Figure 113: Evolution of the fracture width for case I with$\sigma_{xx} = \sigma_{yy} = 1$ MPa.

The history of fracture length is plotted in Fig. 114. In case I, the fracture length is increased steadily in a staircase like fashion with small steps. The rate of increase gradually slows down as the fracture extends and the tip becomes closer to the boundary.

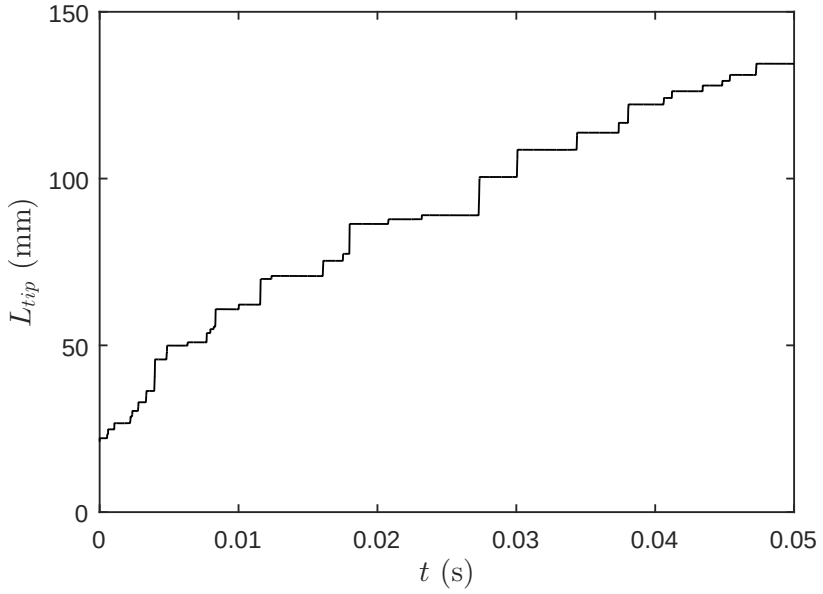

Figure 114: Evolution of the fracture length for case I with$\sigma_{xx} = \sigma_{yy} = 1$ MPa.

Fig. 115 shows the displacement fields at four different times. The color in the disks indicates magnitude of the displacement from large (red) to small (grey). As can be seen, the development of fracture starts with two localized process zones at the fracture tip in Fig. 115 (a). The process zones is manifested as two lobes that are inclined with respect to the fracture plane, which is in agreement with elasto-plasticity theory. Once a new segment of fracture is opened, injection pressure drops, the propagation is arrested. Instead, the injection pressure steadily increases followed by continued expansion of the fracture. Fig. 115 (b) shows that the earlier segments have the greatest deformation as opposed to the later segments, which is also confirmed by the history of fracture width in Fig. 113. In Fig. 115 (c), new process zone starts to form at the tip, leading to the propagation of new segments. The propagation process can be described as alternation of two stages: propagation of a new segment followed by a decrease in injection pressure and fracture width; steady increase in injection pressure and gradual expanding of the width.

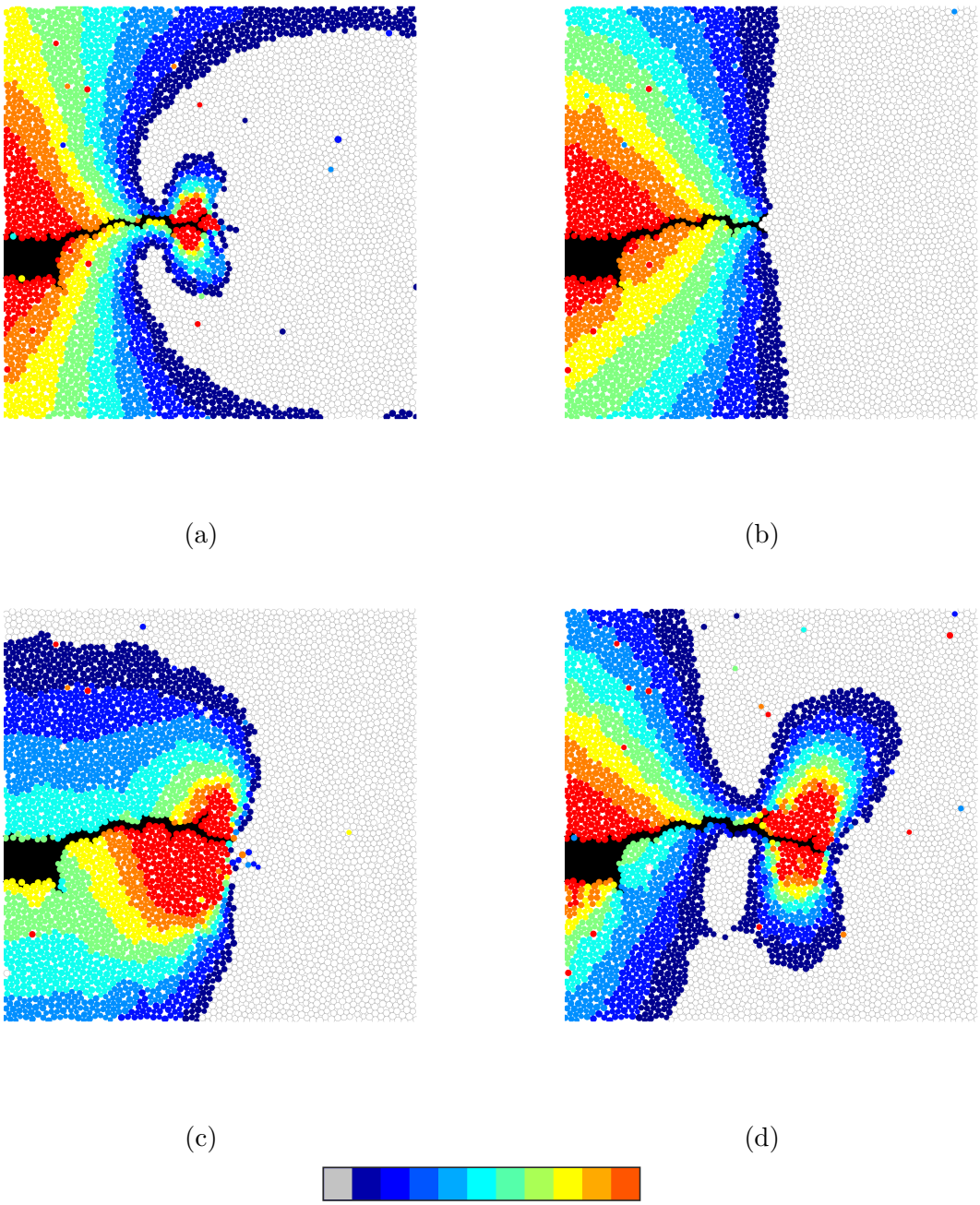

Figure 115: Evolution of the displacement field for case I with$\sigma_{xx} = \sigma_{yy} = 1$ MPa. Color indicates of the amount of displacement for each particle during $\Delta t = 1$ ms. Maximum value of the color map: (a) 0.389 mm, (b) 0.232 mm, (c) 0.384 mm, (d) 0.727 mm.

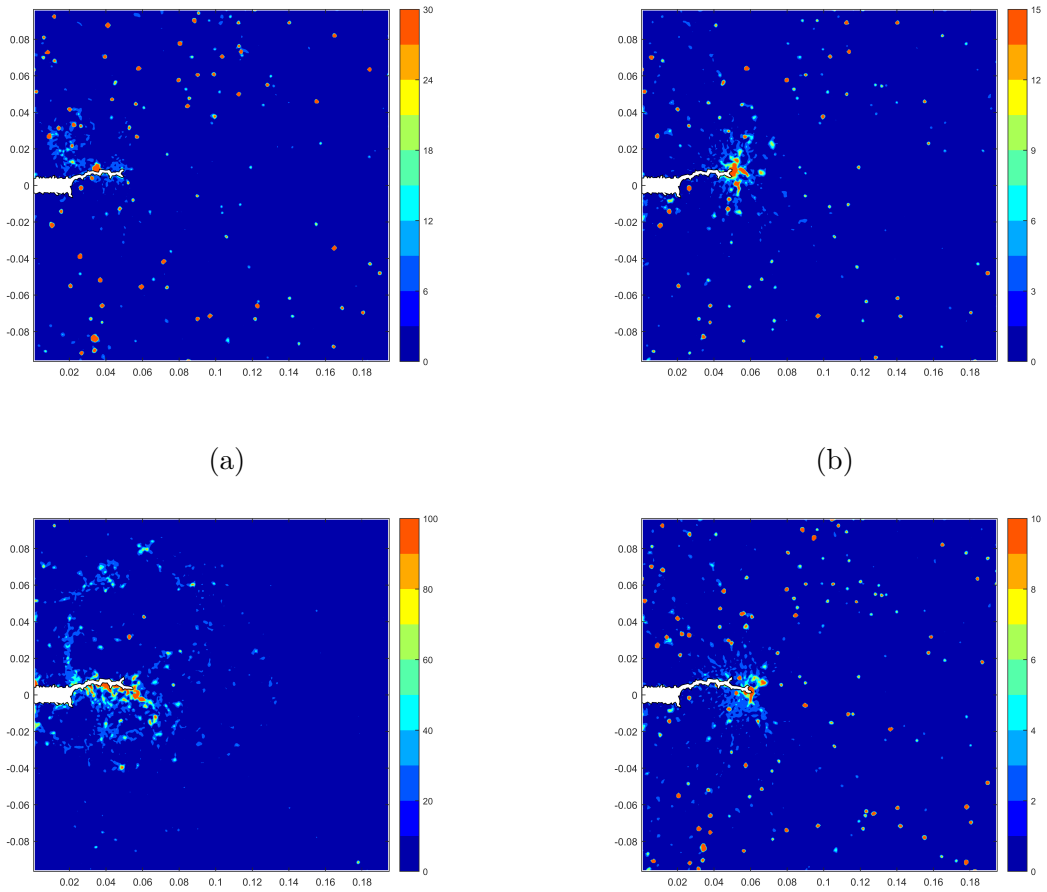

(a) (b)

(c) (d)

Figure 116: Particle rotational velocity for case I with $\sigma_{xx} = \sigma_{yy} = 1$ MPa, value of the color map indicates magnitude of rotational velocity in rad/s.

Fig. 116 plots contours of the particle rotational velocity for the four time stages. The magnitude of the color map represents the rotational velocity in rad/s. The shear deformaiton is localized near the tip as well as along the side of the fracture, which indicates the alternating propagation process: extension in the fracture length and expansion in the fracture width.

7.4.3.2 Case II: $\sigma_{xx} = 1.5$ MPa, $\sigma_{yy} = 1$ MPa

Fig. 117 indicates the final locations of the marker balls for case II with $\sigma_{xx} = 1.5$ MPa and $\sigma_{yy} = 1$ MPa. Since the stress field is anisotropic, the fracture path is more or less

aligned with the major principal direction soon after initiation. The zig-zagging pattern is very obvious. The sinuosity and the intersection angle of the fracture path in case II are $sinuosity = 1.128$ and $\omega = 117.53°$, respectively.

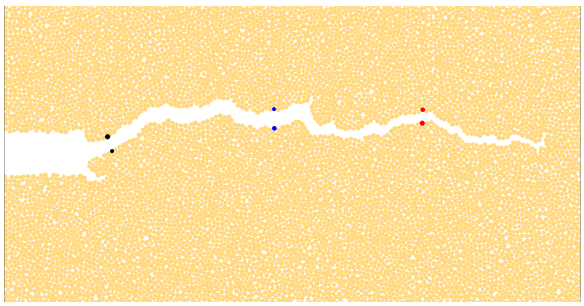

Figure 117: Morphology of the fluid-grain interface with $\sigma_{xx} = 1.5$ MPa, $\sigma_{yy} = 1$ MPa, showing only part of the domain. The balls in color represent the three pairs of markers.

Fig. 118 shows the injection pressure history for the second representative case at $Q = 0.1$ m^2/s and $\delta_c/\bar{r} = 0.1$. The peak stress is about 1.8 MPa as opposed to 1.3 MPa in case I, due to the increase in the far field confining stress. After the initial spike, the injection pressure gradually declines with oscillation and finally approaches 1.1 MPa. Though the decline process is longer in case II, the eventual fracture propagation pressure is similar to that in the first case.

Figs. 119-122 show the history of fracture width, the history of fracture length, and displacement field for case II. A significant difference between case I and case II is that the pressure history for case II is more staircase-like with larger steps. With a greater magnitude of the confining stress, the width expansion phase in case II is longer. In Fig. 122 (a), two clear shear bands can be observed at the fracture tip. The two shear bands are inclined with respect to the fracture trajectory, which suggests shear failure mode.

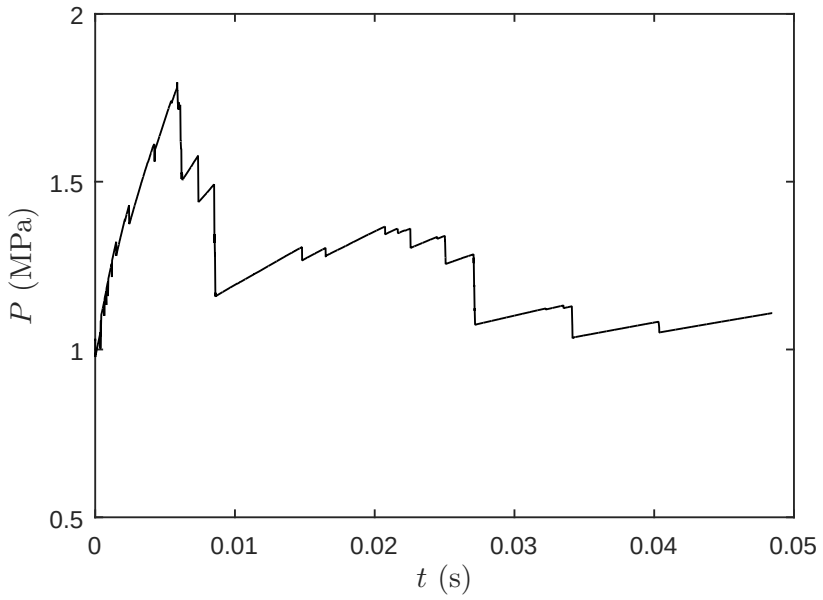

Figure 118: Pressure history for case II with$\sigma_{xx} = 1.5$ MPa, $\sigma_{yy} = 1$ MPa.

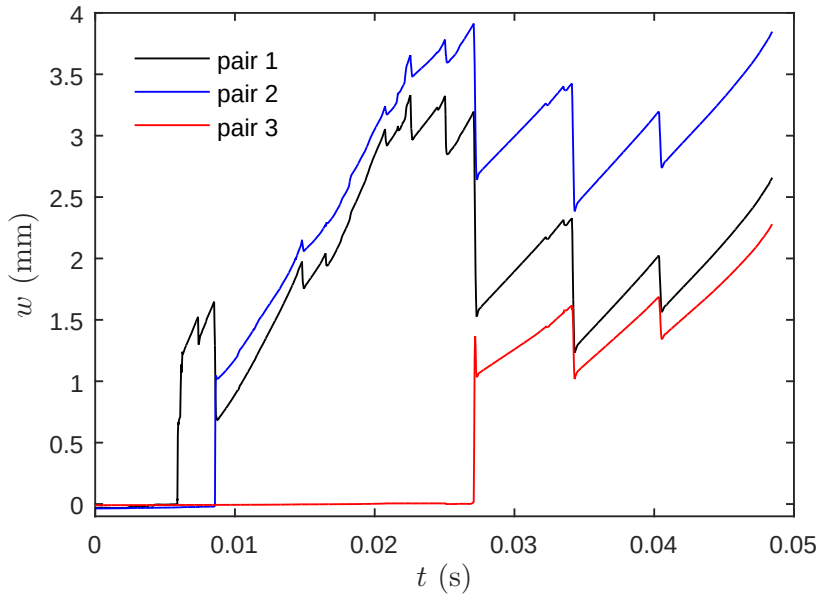

Figure 119: Evolution of the fracture width for case II with $\sigma_{xx} = 1.5$ MPa, $\sigma_{yy} = 1$ MPa.

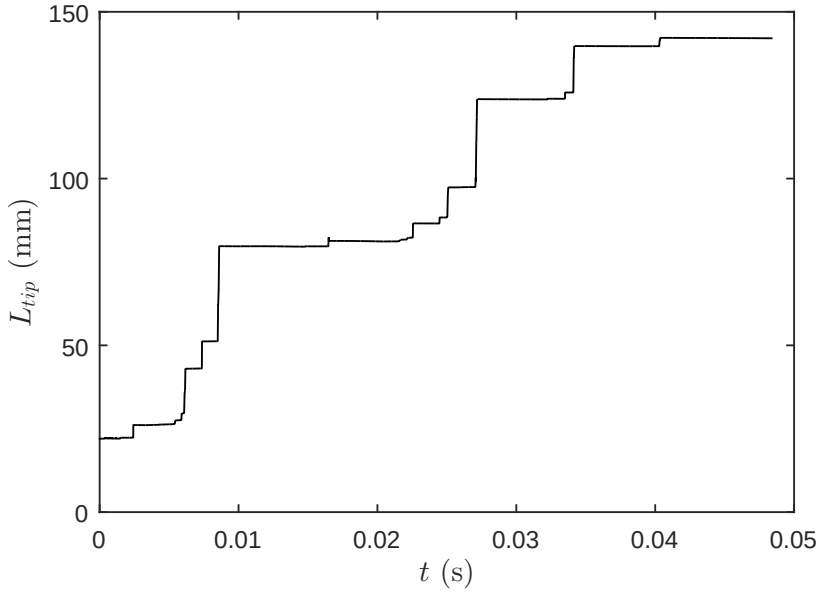

Figure 120: Evolution of the fracture length for case II with $\sigma_{xx} = 1.5$ MPa, $\sigma_{yy} = 1$ MPa.

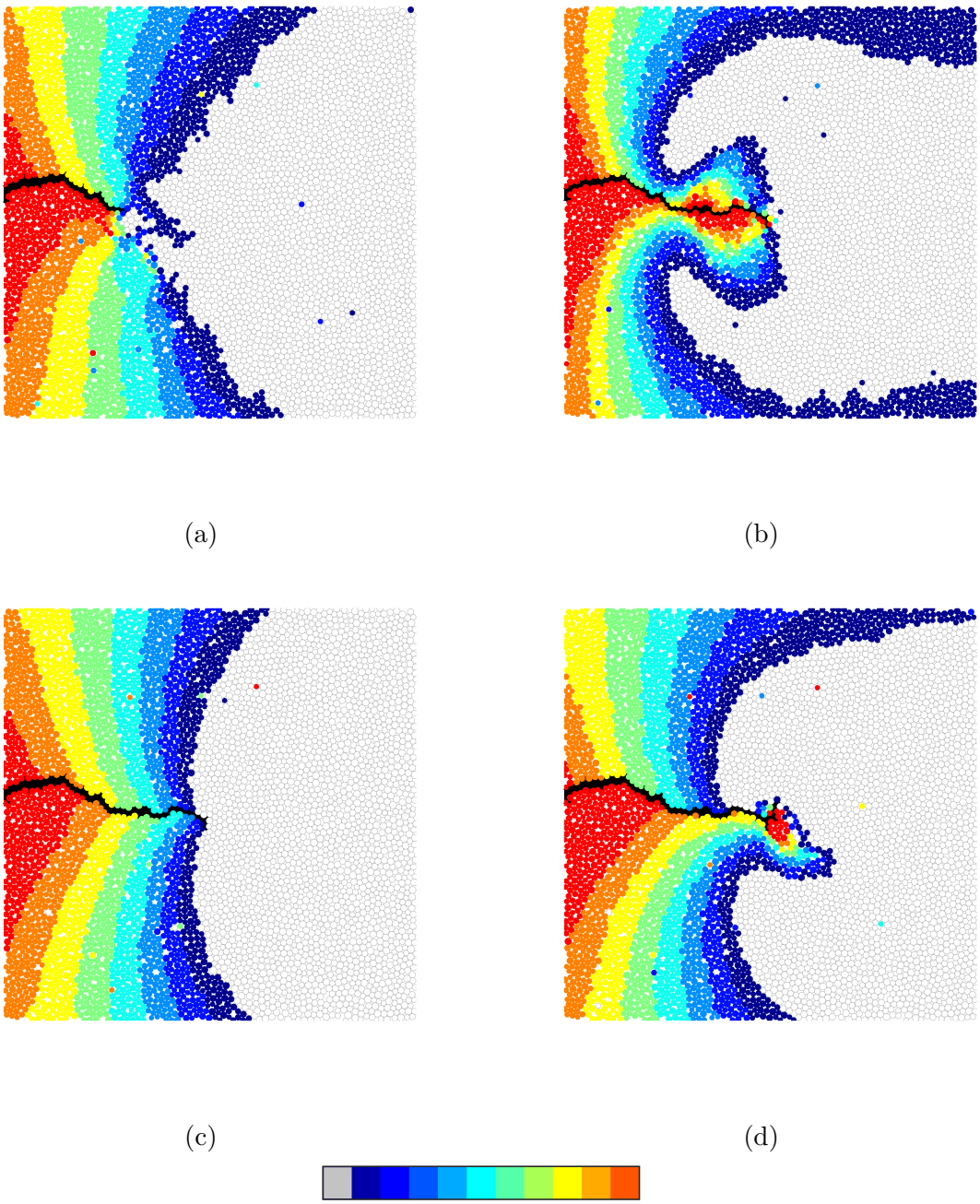

Figure 121: Evolution of the displacement field for case II with $\sigma_{xx} = 1.5$ MPa, $\sigma_{yy} = 1$ MPa. Color indicates of the amount of displacement for each particle during $\Delta t = 1$ ms. Maximum value of the color map: (a) 0.057 mm, (b) 0.797 mm, (c) 0.079 mm, (d) 0.536 mm.

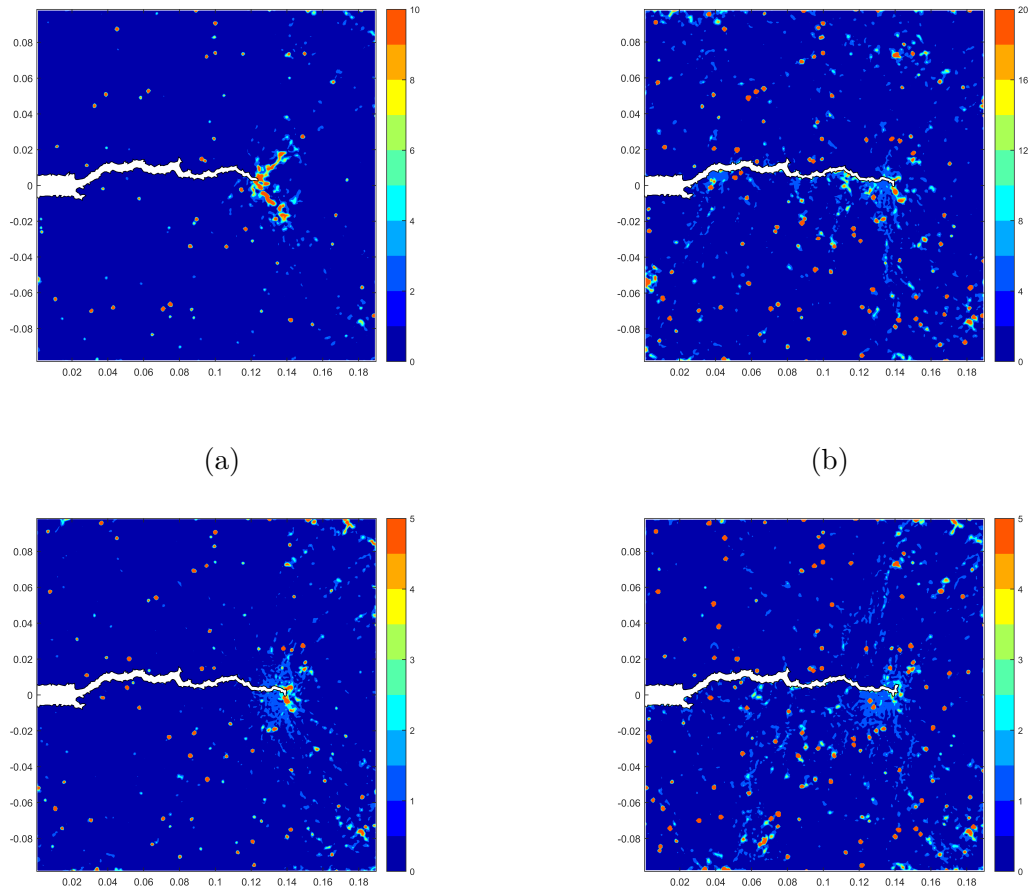

(a) (b)

(c) (d)

Figure 122: Particle rotational velocity for case II with $\sigma_{xx} = 1.5$ MPa, $\sigma_{yy} = 1$ MPa, value of the color map indicates magnitude of rotational velocity in rad/s.

7.5 Conclusions

Fluid injection into an unconsolidated medium under an isotropic or anisotropic stress field is modeled numerically using the DEM code *PFC2D*®. The fluid-grain interface is modeled with the simplification that fluid leakoff is negligible and the fluid can penetrate in between grains if the gap size between two neighboring grains exceed a critical value δ_c, which is taken as $\delta_c/\bar{r} = 0.1$ to simulate the fluid of relatively low viscosity. The numerical analysis is carried out in three types of two-dimensional DEM domains: a rectangular assembly with a center hole, a center slot or a side slot.

The numerical results show that initiation of a fracture near a circular borehole is likely

affected by both the stress anisotropy and the local variation in the contact forces. In the isotropic case, three fractures initiate and are almost equally spaced along the circumference. In the anisotropic case, the fracture initiates near the locations of the least compressive stress.

In the tests with a center or side slot, the fracture initiates at the corners due to stress concentration. After the fractures initiate, they start to align themselves with the direction of the major principal stress. The fracture path shows an oscillating zig-zag pattern which reflects the alternating preference in propagation direction. Boundary of the fractures formed under greater stress contrast are relatively straight and smooth while those formed under smaller stress contrast have more side branches and irregularities.

The propagation process can be described as the alternation of the two stages: propagation of a new segment followed by a decrease in the injection pressure and the fracture width; and steady increase in injection pressure and gradual expanding of the width. Overall, the older segments are wider than the younger segments.

Evidence from the displacement field of particles suggest a process zone exists near the fracture tip. The process zone is manifested as two lobes that are inclined with respect to the fracture plane, which suggests a shear failure mode.

CHAPTER VIII

CONCLUSIONS AND FUTURE WORK

8.1 Conclusions

The objective of this work is to investigate the near-wellbore processes to address the challenges in drilling and completion in naturally fractured or weakly consolidated formations. Both theoretical and numerical analyses are performed in this work.

- Theoretical analysis of the transient drilling mud loss behaviors from a wellbore into a natural fracture is performed. The formulations are based on a radial geometry model and a constant height model, assuming the wellbore axis is either nearly perpendicular or parallel to the natural fracture. A piecewise rheological model incorporating a yield stress and power laws for both the low shear rate and high shear rate is employed. The fracture could be initially closed or has a small opening. The problem formulated is solved numerically using an explicit moving mesh algorithm. Effects of the fluid rheology, in particular, the high shear rate rheology, and the leakoff coefficient on the drilling mud loss behaviors are investigated. The results suggest that the high shear rate rheology is critical to control lost circulation since it takes effect at early time. The overbalance pressure and the yield stress of the fluid determines the ultimate invasion length and volume of the drilling mud at late time. The leakoff coefficient has negligible effect on the ultimate invasion length. But the ultimate mud invasion length is reached earlier, if the leakoff coefficient is smaller. Numerical scheme outlined in this work provides a robust tool that allows not only systematic investigation of the effects of the formation and the fluid characteristics on the drilling mud loss, but also assessment for the improvement in the fluid design to control lost circulation.

- A theoretical solution is derived to study the worst case scenario of mud invasion into an arbitrarily oriented isolated fracture from an inclined wellbore. The fracture is assumed to has a constant width, bounded by rigid walls. The ultimate invasion

profile when the mud eventually stops flowing is solved based on limit equilibrium conditions. Effects of the fluid yield stress, the overbalance pressure, the fracture inclination angle and the wellbore trace on the fracture upon the mud loss behaviors are analyzed. Excellent agreement is achieved between our analytical solution and published experimental data in back calculating the fluid yield stress based on the ultimate invasion radius. The theoretical model can be used to give the lower bound of the fracture permeability based on the mud loss data from the field.

- Fluid injection into an unconsolidated or weakly consolidated medium is modeled numerically using the DEM code *PFC2D*®. The injection process is modeled with the simplification that fluid leakoff is negligible and the fluid can penetrate in between grains if the gap size between two neighboring grains exceeds a critical value δ_c. Such a simplification can be made analogous to considering the effect of surface tension or viscosity. The numerical results suggest that the critical gap size plays an important role in determining the failure mechanism. If the critical gap size δ_c is relatively small, the fluid-grain displacement process has three stages: borehole expansion, initiation of localized features and extension of finger-like features; given a large δ_c, borehole expansion is dominant and the localized features are notch-like. Evidences from the trajectories of localized features as well as particle rotational velocity suggest both opening and shear modes of initiation and growth mechanisms are plausible. What this means is that from the point of view of theoretical modeling at the continuum scale, a growth criterion needs to be able to capture both the opening and shear growth mechanisms. The confining stress, the initial borehole size, the injection rate, the particle friction angle of the particles and the cohesion of the particles also affect the growth modes. Wide and tortuous fingers are obtained at high confining stresses. At low confining stress, relatively thin and straight fingers are obtained with a small δ_c, and notch-like localized features are observed at large δ_c. With an increasing injection rate, the fractures tend to align radially and the number of the main fractures increases. At a small injection rate, the fingers grow in an alternating manner, only one fracture is propagating at a given time; at a large injection rate, multiple small

fingers are initiated but only a number of them are able to extend outward. Shear bands are easier to develop in formations with a lower friction angle. With a higher friction angle, the resistance to the sliding is greater, the medium tends to fail in an opening mode. With a relatively large cohesion, shear failure is less favored and the medium tends to fail in tension.

- Numerical results on the breakdown of the cavity are then compared with those from the bifurcation analysis for the cohesionless case as well as elasto-plasticity solutions for the cohesive case. For cohesionless formations, the breakdown pressure for the case with $\delta_c/\bar{r} = 0.5$ agrees with the cavity pressure corresponding to the onset of bifurcation. For the cohesive formations, the breakdown pressure for the case with $\delta_c/\bar{r} = 0.5$ falls within the range of tensile failure solution and the elastic-perfectly plastic solution. It is also noted that as δ_c increases, the breakdown pressure gradually approaches the elastic-perfectly plastic solution. Parametric study is performed to analyze the effects of the critical gap size, the borehole size, and the confining stress upon the ratio of breakdown pressure ΔP_{max} and confining stress σ_o. Overall, a greater δ_c, a smaller initial borehole and a lower confining stress lead to a greater ratio $\Delta P_{max}/\sigma_o$.

- Stress anisotropy not only governs the location of initiation but also guides the direction of propagation. The injection test in a rectangular domain with a center hole suggests that the initiation of fracture is likely affected by both the stress anisotropy and the local variation of the contact forces. For the isotropic case, three fractures are initiated and almost equally spaced, while in the anisotropic case, the fracture initiates near the locations of minimum compressive stress. After the fractures initiate, they start to align themselves with the direction of the major principal stress. The fractures in the cohesionless medium, in particular, those formed under a smaller stress contrast, are very irregular. Evidences from the displacement field of particles suggest a process zone exists near the fracture tip. The process zone is manifested as two lobes that are inclined at an angle with respect to the fracture plane, an indication

of shear failure. The shear deformation is localized near the tip as well as along the side of the fracture, which indicates the alternating propagation process: extension in the fracture length and expansion in the fracture width.

The theoretical models developed for predicting the mud loss can be applied directly in the field practices not only for drilling, but also for grouting in jointed rock mass. The DEM analysis of the injection process allowed us to gain valuable insights into the fluid-grain displacement process in nearly unconsolidated media and could serve as guides for future development of fracture growth criteria at the continuum scale.

8.2 Recommendations for Future Work

Based on the results from this work, we suggest the following future work.

- Compare the theoretical prediction on the maximum mud loss volume for an arbitrary oriented fracture with experiments and generalize the model for grouting in jointed rock mass when the fracture has a large aperture and a high inclination angle.
- Development of yield stress measurement through squeeze flow in between two parallel plates for grouts.
- Extend the breakdown pressure analysis for the fluid injection problem and compare the theoretical solutions with those from the injection experiments in the literature.
- Develop continuum scale fracture growth criteria for fluid injection in a nearly unconsolidated medium.

APPENDIX A

LIST OF INJECTION TESTS INTO A HOLLOW CYLINDER

Test Name	$\delta_c/\bar{r}$	σ_o (MPa)	$D_{\text{out}}/D_{\text{in}}$	Q $\left(\text{m}^2/\text{s}\right)$	ϕ_b (°)	$\bar{F}_n,\ \bar{F}_s$ (N)
0.1_0.5_20_0.1_30	0.1	0.5	20	0.1	30	0
0.3_0.5_20_0.1_30	0.3	0.5	20	0.1	30	0
0.5_0.5_20_0.1_30	0.5	0.5	20	0.1	30	0
0.1_1_20_0.1_30	0.1	1	20	0.1	30	0
0.3_1_20_0.1_30	0.3	1	20	0.1	30	0
0.5_1_20_0.1_30	0.5	1	20	0.1	30	0
0.1_5_20_0.1_30	0.1	5	20	0.1	30	0
0.3_5_20_0.1_30	0.3	5	20	0.1	30	0
0.5_5_20_0.1_30	0.5	5	20	0.1	30	0
0.3_0.5_10_0.1_30	0.3	0.5	10	0.1	30	0
0.3_1_10_0.1_30	0.3	1	10	0.1	30	0
0.3_5_10_0.1_30	0.3	5	10	0.1	30	0
0.3_0.5_5_0.1_30	0.3	0.5	5	0.1	30	0
0.3_1_5_0.1_30	0.3	1	5	0.1	30	0
0.3_5_5_0.1_30	0.3	5	5	0.1	30	0
0.1_0.5_5_1_30	0.1	0.5	5	1	30	0
0.1_0.5_5_10_30	0.1	0.5	5	10	30	0
0.1_0.5_5_50_30	0.1	0.5	5	50	30	0
0.1_1_5_1_30	0.1	1	5	1	30	0
0.1_1_5_10_30	0.1	1	5	10	30	0
0.1_1_5_50_30	0.1	1	5	50	30	0

Test Name	$\delta_c/\bar{r}$	σ_o (MPa)	$D_{\text{out}}/D_{\text{in}}$	Q $\left(\text{m}^2/\text{s}\right)$	ϕ_b (°)	$\bar{F}_n,\ \bar{F}_s$ (N)
0.1_5_5_1_30	0.1	5	5	1	30	0
0.1_5_5_10_30	0.1	5	5	10	30	0
0.1_5_5_50_30	0.1	5	5	50	30	0
0.1_1_20_0.1_15	0.1	1	20	0.1	15	0
0.3_1_20_0.1_15	0.3	1	20	0.1	15	0
0.5_1_20_0.1_15	0.5	1	20	0.1	15	0
0.1_1_20_0.1_45	0.1	1	20	0.1	45	0
0.3_1_20_0.1_45	0.3	1	20	0.1	45	0
0.5_1_20_0.1_45	0.5	1	20	0.1	45	0
0.1_1_10_0.1_30_c100	0.1	1	10	0.1	30	100
0.3_1_10_0.1_30_c100	0.3	1	10	0.1	30	100
0.5_1_10_0.1_30_c100	0.5	1	10	0.1	30	100
0.1_1_10_0.1_30_c500	0.1	1	10	0.1	30	500
0.3_1_10_0.1_30_c500	0.3	1	10	0.1	30	500
0.5_1_10_0.1_30_c500	0.5	1	10	0.1	30	500
0.1_1_10_0.1_30_c1000	0.1	1	10	0.1	30	1000
0.3_1_10_0.1_30_c1000	0.3	1	10	0.1	30	1000
0.5_1_10_0.1_30_c1000	0.5	1	10	0.1	30	1000

REFERENCES

[1] Abe, H., Keer, L., and Mura, T., "Growth rate of a penny-shaped crack in hydraulic fracturing of rocks, 2," *Journal of Geophysical Research*, vol. 81, no. 35, pp. 6292–6298, 1976.

[2] Alsiny, A., Vardoulakis, I., and Drescher, A., "Deformation localization in cavity inflation experiments on dry sand," *Géotechnique*, vol. 42, no. 3, pp. 395–410, 1992.

[3] Au, S. A., Soga, K., and Yeung, A. T., "A new laboratory apparatus for grout injection studies," 2005.

[4] Banerjee, P., "Hydraulic fracturing technology: Technology evaluation report and application analysis report," tech. rep., PRC Environmental Management, Inc., Rolling Meadows, IL (United States), 1993.

[5] Barenblatt, G. I., "The mathematical theory of equilibrium cracks in brittle fracture," *Advances in applied mechanics*, vol. 7, pp. 55–129, 1962.

[6] Bažant, Z. P. and Oh, B. H., "Crack band theory for fracture of concrete," *Matériaux et construction*, vol. 16, no. 3, pp. 155–177, 1983.

[7] Beda, G. and Carugo, C., "Use of mud microloss analysis while drilling to improve the formation evaluation in fractured reservoir," in *SPE Annual Technical Conference and Exhibition*, Society of Petroleum Engineers, 2001.

[8] Bishop, R., Hill, R., and Mott, N., "The theory of indentation and hardness tests," *Proceedings of the Physical Society*, vol. 57, no. 3, p. 147, 1945.

[9] Bjerrum, L., Nash, J., Kennard, R., and Gibson, R., "Hydraulic fracturing in field permeability testing," *Geotechnique*, vol. 22, no. 2, pp. 319–332, 1972.

[10] Bohloli, B. and De Pater, C., "Experimental study on hydraulic fracturing of soft rocks: Influence of fluid rheology and confining stress," *Journal of Petroleum Science and Engineering*, vol. 53, no. 1, pp. 1–12, 2006.

[11] Bruno, M., Dorfmann, A., Lao, K., and Honeger, C., "Coupled particle and fluid flow modeling of fracture and slurry injection in weakly consolidated granular media," in *DC Rocks 2001, The 38th US Symposium on Rock Mechanics (USRMS)*, American Rock Mechanics Association, 2001.

[12] Carter, J., Booker, J. y., and Yeung, S., "Cavity expansion in cohesive frictional soils," *Geotechnique*, vol. 36, no. 3, pp. 349–358, 1986.

[13] Carter, R., "Derivation of the general equation for estimating the extent of the fractured area," *Drilling and Production Practice*, pp. 261–269, 1957.

[14] Chadwick, P., "The quasi-static expansion of a spherical cavity in metals and ideal soils," *The Quarterly Journal of Mechanics and Applied Mathematics*, vol. 12, no. 1, pp. 52–71, 1959.

[15] Chang, H., *Hydraulic fracturing in particulate materials*. PhD thesis, Georgia Institute of Technology, 2004.

[16] Chin, L. and Montgomery, C., "A numerical model for simulating solid waste injection in soft rock reservoirs," in *SPE Annual Technical Conference and Exhibition*, Society of Petroleum Engineers, 2004.

[17] Cook, B., Lee, M., DiGiovanni, A., Bronowski, D., Perkins, E., and Williams, J., "Discrete element modeling applied to laboratory simulation of near-wellbore mechanics," *International Journal of Geomechanics*, vol. 4, no. 1, pp. 19–27, 2004.

[18] Coussot, P. and Boyer, S., "Determination of yield stress fluid behaviour from inclined plane test," *Rheologica Acta*, vol. 34, no. 6, pp. 534–543, 1995.

[19] Coussot, P., Nguyen, Q. D., Huynh, H., and Bonn, D., "Avalanche behavior in yield stress fluids," *Physical Review Letters*, vol. 88, no. 17, p. 175501, 2002.

[20] de Pater, C., Bohloli, B., Pruiksma, J., and Bezuijen, A., "Experimental study of hydraulic fracturing in sand," *Proc. Soil/Rock America*, 2003.

[21] de Pater, C. J., Dong, Y., and Bohloli, B., "Experimental study of hydraulic fracturing in sand as a function of stress and fluid rheology," in *SPE Hydraulic Fracturing Technology Conference*, Society of Petroleum Engineers, 2007.

[22] Detournay, E., Cheng, A.-D., and McLennan, J., "A poroelastic PKN hydraulic fracture model based on an explicit moving mesh algorithm," *Journal of Energy Resources Technology*, vol. 112, no. 4, pp. 224–230, 1990.

[23] Dong, Y. and De Pater, C., "Observation and modeling of the hydraulic fracture tip in sand," in *The 42nd US Rock Mechanics Symposium (USRMS)*, American Rock Mechanics Association, 2008.

[24] Dong, Y., *Hydraulic Fracture Containment in Sand*. PhD thesis, TU Delft, Delft University of Technology, 2010.

[25] Drummond, J. M., "An appraisal of fracture porosity," *Bulletin of Canadian Petroleum Geology*, vol. 12, no. 2, pp. 226–245, 1964.

[26] Dugdale, D. S., "Yielding of steel sheets containing slits," *Journal of the Mechanics and Physics of Solids*, vol. 8, no. 2, pp. 100–104, 1960.

[27] Dyke, C., Wu, B., and Milton-Tayler, D., "Advances in characterising natural fracture permeability from mud log data," in *Paper SPE 25022 presented at the 1992 European Petroleum Conference, Cannes, France, November 16-18*, 1992.

[28] Ehrlich, R. and Weinberg, B., "An exact method for characterization of grain shape," *Journal of Sedimentary Research*, vol. 40, no. 1, 1970.

[29] Elwood, D. E., *Hydraulic fracture experiments in a frictional material and approximations for maximum allowable mud pressure*. PhD thesis, Queenś University, 2008.

[30] Fang, H.-Y., Mikroudis, G., and Pamukcu, S., "Fracture behavior of compacted fine-grained soils," in *Fracture Mechanics: Perspectives and Directions (Twentieth Symposium)*, ASTM International, 1989.

[31] Gafar, K., Soga, K., Bezuijen, A., Sanders, M., and Van Tol, A., "Fracturing of sand in compensation grouting," in *Geotechnical Aspects of Underground Construction in Soft Ground: Proceedings of the 6th International Symposium (Is-Shanghai), Shanghai, China*, pp. 281–286, 2008.

[32] Geertsma, J. and De Klerk, F., "A rapid method of predicting width and extent of hydraulically induced fractures," *Journal of Petroleum Technology*, vol. 21, no. 12, pp. 1–571, 1969.

[33] Geertsma, J. and Haafkens, R., "A comparison of the theories for predicting width and extent of vertical hydraulically induced fractures," *Journal of Energy Resources Technology*, vol. 101, no. 1, pp. 8–19, 1979.

[34] Germanovich, L., Hurt, R., and Huang, H., "Hydraulic fracturing in saturated cohesionless materials," in *AGU Fall Meeting Abstracts*, vol. 1, p. 0492, 2007.

[35] Golovin, E., Jasarevic, H., Chudnovsky, A., Dudley, J., and Wong, G., "Observation and characterization of hydraulic fracture in cohesionless sand," in *44th US Rock Mechanics Symposium and 5th US-Canada Rock Mechanics Symposium*, American Rock Mechanics Association, 2010.

[36] Gwaba, D., *Fluid-assisted fracturing in geological materials*. PhD thesis, Georgia Institute of Technology, 2016.

[37] Hainey, B. and Troncoso, J., "Frac-pack: an innovative stimulation and sand control technique," in *SPE Formation Damage Control Symposium*, Society of Petroleum Engineers, 1992.

[38] Hanson, J. A., Hardin, B. O., and Mahboub, K., "Fracture toughness of compacted cohesive soils using ring test," *Journal of Geotechnical Engineering*, vol. 120, no. 5, pp. 872–891, 1994.

[39] Herzhaft, B., Ragouilliaux, A., and Coussot, P., "How to unify low-shear-rate rheology and gel properties of drilling muds: A transient rheological and structural model for complex wells applications," in *IADC/SPE Drilling Conference*, 2006.

[40] Hocking, G., "Soil hydraulic fracturing," *Water Well Journal*, vol. 50, no. 5, pp. 70–72, 1996.

[41] Hocking, G. and Wells, S. L., "Groundwater performance monitoring of an iron permeable reactive barrier," in *Proceedings of the Third International Conference on Remediation of Chlorinated and Recalcitrant Compounds (CD), Monterey, CA*, vol. 20, p. 23, 2002.

[42] Huang, H. and Detournay, E., "Cylindrical cavity expansion from a finite radius," in *GeoShanghai 2010 International Conference*, 2010.

[43] Huang, H., Zhang, F., Callahan, P., and Ayoub, J., "Granular fingering in fluid injection into dense granular media in a Hele-Shaw cell," *Physical Review Letters*, vol. 108, no. 25, p. 258001, 2012.

[44] Huang, J., Griffiths, D., and Wong, S.-W., "Characterizing natural-fracture permeability from mud-loss data," *SPE Journal*, vol. 16, no. 1, pp. 111–114, 2011.

[45] Hurt, R. S., *Toughness-dominated hydraulic fractures in cohesionless particulate materials*. PhD thesis, Georgia Institute of Technology, 2012.

[46] Itasca Consulting Group, Inc, Minneapolis, Minnesota, *PFC User Manual*, 2015.

[47] Ito, T., Igarashi, A., and Yamamoto, K., "Laboratory test of hydraulic fracturing in unconsolidated deformable rocks," in *Proc. of the 4th Biot Conf. on Poromech*, pp. 8–10, 2009.

[48] Ito, T., Yamamoto, K., and Nagakubo, S., "Effect of anisotropic confining stresses on hydraulically-induced fracture propagation from perforated cased-hole in unconsolidated sands," in *45th US Rock Mechanics/Geomechanics Symposium*, American Rock Mechanics Association, 2011.

[49] Ito, T., Igarashi, A., Suzuki, K., Nagakubo, S., Matsuzawa, M., and Yamamoto, K., "Laboratory study of hydraulic fracturing behavior in unconsolidated sands for methane hydrate production," in *Offshore Technology Conference*, Offshore Technology Conference, 2008.

[50] Jasarevic, H., Golovin, E., Chudnovsky, A., Dudley, J., and Wong, G., "Observation and modeling of hydraulic fracture initiation in cohesionless sand," in *44th US Rock Mechanics Symposium and 5th US-Canada Rock Mechanics Symposium*, American Rock Mechanics Association, 2010.

[51] Jaworski, G., Duncan, J., and Seed, H., "Laboratory study of hydraulic fracturing," *Journal of the Geotechnical Engineering Division, ASCE*, vol. 107, 1981.

[52] Ji, L., Settari, A., and Sullivan, R. B., "A novel hydraulic fracturing model fully coupled with geomechanics and reservoir simulation," *SPE Journal*, vol. 14, no. 03, pp. 423–430, 2009.

[53] Jones, J. and Soler, D., "Fracture stimulation of shallow, unconsolidated Kern River sands," in *SPE International Thermal Operations and Heavy Oil Symposium*, pp. 167–175, 1999.

[54] Khodaverdian, M., Sorop, T., Van den Hoek, P., Sathyamoorthy, S., and Okoh, E., "Injectivity and fracturing in unconsolidated sand reservoirs: Waterflooding case study, offshore Nigeria," in *44th US Rock Mechanics Symposium and 5th US-Canada Rock Mechanics Symposium*, American Rock Mechanics Association, 2010.

[55] Khodaverdian, M. and McElfresh, P., "Hydraulic fracturing stimulation in poorly consolidated sand: Mechanisms and consequences," in *SPE Annual Technical Conference and Exhibition*, Society of Petroleum Engineers, 2000.

[56] Khodaverdian, M. F., Sorop, T., Postif, S. J., and Van den Hoek, P. J., "Polymer flooding in unconsolidated-sand formations: Fracturing and geomechanical considerations," *SPE Production & Operations*, vol. 25, no. 02, pp. 211–222, 2010.

[57] Khristianovic, S. and Zheltov, Y., "Formation of vertical fractures by means of highly viscous fluids," in *Proceedings of the 4th world petroleum congress, Rome*, 1955.

[58] Kim, D.-H., Motoyuki, S., and Takatoshi, I., "Dynamic monitoring of fracture extension in unconsolidated sand specimen by GPR," in *Ground Penetrating Radar (GPR), 2010 13th International Conference on*, pp. 1–6, IEEE, 2010.

[59] Ladanyi, B., "Expansion of a cavity in a saturated clay medium," *Journal of the Soil Mechanics and Foundations Division, ASCE*, vol. 89, pp. 127–161, 1963.

[60] Lavrov, A., "Newtonian fluid flow from an arbitrarily-oriented fracture into a single sink," *Acta Mechanica*, vol. 186, no. 1-4, pp. 55–74, 2006.

[61] Lavrov, A. and Tronvoll, J., "Mud loss into a single fracture during drilling of petroleum wells: Modeling approach," in *Development and Application of Discontinuous Modelling for Rock Engineering: Proceedings of the 6th International Conference ICADD-6, Trondheim, Norway, October 5-8*, 2003.

[62] Lavrov, A. and Tronvoll, J., "Modeling mud loss in fractured formations," in *Abu Dhabi International Conference and Exhibition*, Society of Petroleum Engineers, 2004.

[63] Lavrov, A. and Tronvoll, J., "Mechanics of borehole ballooning in naturally-fractured formations," in *SPE Middle East Oil and Gas Show and Conference*, Society of Petroleum Engineers, 2005.

[64] Lietard, O., Kirvelis, R., and Guillot, D., "The radial flow model of mud loss into natural fractures: Improvements and field application," in *Unsolicited Paper SPE 88661 received by the SPE office in Richardson, Texas, on April 17*, 2004.

[65] Lietard, O., Unwin, T., Guillot, D., and Hodder, M., "Fracture width logging while drilling and drilling mud/loss-circulation-material selection guidelines in naturally fractured reservoirs (includes associated papers 75283 75284 81590 and 81591)," *SPE Drilling & Completion*, vol. 14, no. 03, pp. 168–177, 1999.

[66] Lo, K. and Kaniaru, K., "Hydraulic fracture in earth and rock-fill dams," *Canadian Geotechnical Journal*, vol. 27, no. 4, pp. 496–506, 1990.

[67] Lullo, G., James, C., and Julio, G., "A fresh look at stimulating unconsolidated sands with proppant-laden fluids," in *SPE Annual Technical Conference and Exhibition*, 2004.

[68] MacMinn, C. W., Dufresne, E. R., and Wettlaufer, J. S., "Fluid-driven deformation of a soft granular material," *Physical Review X*, vol. 5, no. 1, p. 011020, 2015.

[69] Majidi, R., Miska, S., Thompson, L. G., Yu, M., and Zhang, J., "Quantitative analysis of mud losses in naturally fractured reservoirs: The effect of rheology," *SPE Drilling & Completion*, vol. 25, no. 04, pp. 509–517, 2010.

[70] Majidi, R., Miska, S. Z., Ahmed, R., Yu, M., and Thompson, L. G., "Radial flow of yield-power-law fluids: Numerical analysis, experimental study and the application for drilling fluid losses in fractured formations," *Journal of Petroleum Science and Engineering*, vol. 70, no. 3, pp. 334–343, 2010.

[71] Majidi, R., Miska, S. Z., Yu, M., and Thompson, L. G., "Fracture ballooning in naturally fractured formations: Mechanism and controlling factors," in *SPE Annual Technical Conference and Exhibition*, Society of Petroleum Engineers, 2008.

[72] Majidi, R., Miska, S. Z., Yu, M., Thompson, L. G., and Zhang, J., "Modeling of drilling fluid losses in naturally fractured formations," in *SPE Annual Technical Conference and Exhibition*, Society of Petroleum Engineers, 2008.

[73] Mitchell, J. K. and Soga, K., "Fundamentals of soil behavior," 2005.

[74] Møller, P. C., Mewis, J., and Bonn, D., "Yield stress and thixotropy: on the difficulty of measuring yield stresses in practice," *Soft Mtter*, vol. 2, no. 4, pp. 274–283, 2006.

[75] Mori, A. and Tamura, M., "Hydrofracturing pressure of cohesive soils," *Soils and Foundations*, vol. 27, no. 1, pp. 14–22, 1987.

[76] Murdoch, L. C., "Hydraulic fracturing of soil during laboratory experiments part 2. propagation," *Geotechnique*, vol. 43, no. 2, pp. 267–276, 1993.

[77] Murdoch, L. C., "Hydraulic fracturing of soil during laboratory experiments part 3. theoretical analysis," *Geotechnique*, vol. 43, no. 2, pp. 277–287, 1993.

[78] Murdoch, L., "Hydraulic fracturing of soil during laboratory experiments. part 1. methods and observations," *Geotechnique*, vol. 43, no. 2, pp. 255–265, 1993.

[79] Nolte, K. G. and Smith, M. B., "Interpretation of fracturing pressures," *Journal of Petroleum Technology*, vol. 33, no. 09, pp. 1–767, 1981.

[80] Nordgren, R., "Propagation of a vertical hydraulic fracture," *Society of Petroleum Engineers Journal*, vol. 12, no. 04, pp. 306–314, 1972.

[81] Ozdemirtas, M., Babadagli, T., and Kuru, E., "Effects of fractal fracture surface roughness on borehole ballooning," *Vadose Zone Journal*, vol. 8, no. 1, pp. 250–257, 2009.

[82] Panah, A. K. and Yanagisawa, E., "Laboratory studies on hydraulic fracturing criteria in soil," *Soils and Foundations*, vol. 29, no. 4, pp. 14–22, 1989.

[83] Papanastasiou, P., "The influence of plasticity in hydraulic fracturing," *International Journal of Fracture*, vol. 84, no. 1, pp. 61–79, 1997.

[84] Perkins, T. and Kern, L., "Widths of hydraulic fractures," *Journal of Petroleum Technology*, vol. 13, no. 09, pp. 937–949, 1961.

[85] Potyondy, D., *PFC3D Pressure Boundary Conditions*. PFC Development Technical Memorandum. ICG7233-L.

[86] Ragouilliaux, A., Herzhaft, B., Bertrand, F., and Coussot, P., "Flow instability and shear localization in a drilling mud," *Rheologica acta*, vol. 46, no. 2, pp. 261–271, 2006.

[87] Reed, A. and Dusseault, M., "Hydraulic fracturing of soil as an analogue to rock behaviour," *International Journal of Rock Mechanics and Mining Sciences*, vol. 34, no. 3, pp. 255–e1, 1997.

[88] Rege, N. V., *Computational modeling of granular materials*. PhD thesis, Massachusetts Institute of Technology, 1996.

[89] Saada, A., Chudnovsky, A., and Kennedy, M., "A fracture mechanics study of stiff clays," in *Proceedings of the 11th International Conference in Soil Mechanics and Foundations*, vol. 2, pp. 637–640, 1985.

[90] Sanfillippo, F., Brignoli, M., Santarelli, F., and Bezzola, C., "Characterization of conductive fractures while drilling," in *European Formation Damage Conference*, 1997.

[91] Shin, H. and Santamarina, J. C., "Fluid-driven fractures in uncemented sediments: Underlying particle-level processes," *Earth and Planetary Science Letters*, vol. 299, no. 1, pp. 180–189, 2010.

[92] Soga, K., Au, S., Jafari, M., and Bolton, M., "Laboratory investigation of multiple grout injections into clay," *Geotechnique*, vol. 54, no. 2, pp. 81–90, 2004.

[93] Soga, K., Gafar, K., Ng, M., and Au, S., "Macro and micro behaviour of soil fracturing," *Geomechanics and Geotechnics of Particulate Media, Taylor and Francis*, pp. 421–427, 2006.

[94] Staheli, K., Christopher, G., and Wetter, L., "Effectiveness of hydrofracture prediction for HDD design," *North American Society for Trenchless Technology (NASTT), Chicago, IL*, 2010.

[95] Taghipoor, S., Nouri, A., and Chan, D., "Numerical modelling of hydraulic fracturing in cohesionless sand: Validation against laboratory experiments," *Journal of Canadian Petroleum Technology*, 2015.

[96] Timoshenko, S., Timoshenko, S., and Goodier, J., *Theory of Elasticity*. McGraw-Hill book Company, 1970.

[97] Vallejo, L. E., "Shear stresses and the hydraulic fracturing of earth dam soils.," *Soils and Foundations*, vol. 33, no. 3, pp. 14–27, 1993.

[98] Van den Hoek, P., "New 3d model for optimised design of hydraulic fractures and simulation of drill-cutting reinjection," in *Offshore Europe*, Society of Petroleum Engineers, 1993.

[99] Vardoulakis, I., "Theoretical and experimental bounds for shear-band bifurcation strain in biaxial tests on dry sand," *Res Mechanica*, vol. 23, pp. 239–259, 1988.

[100] Verga, F., Carugo, C., Chelini, V., Maglione, R., and De Bacco, G., "Detection and characterization of fractures in naturally fractured reservoirs," in *SPE Annual Technical Conference*, 2000.

[101] Wedman, M. L., Lynch, K. W., and Spearman, J. W., "Hydraulic fracturing for sand control in unconsolidated heavy-oil reservoirs," in *SPE Western Regional Meeting*, Society of Petroleum Engineers, 1999.

[102] Wu, R., *Some fundamental mechanisms of hydraulic fracturing*. PhD thesis, Georgia Institute of Technology, 2006.

[103] Xu, B., Yuan, Y., and Wong, R., "Modeling of the hydraulic fractures in unconsolidated oil sands reservoir," in *44th US Rock Mechanics Symposium and 5th US-Canada Rock Mechanics Symposium*, American Rock Mechanics Association, 2010.

[104] Yanagisawa, E. and Ali, K. P., "Two dimensional study of hydraulic fracturing criteria in cohesive soils," *Soils and Foundations*, vol. 34, no. 1, pp. 1–9, 1994.

[105] Yu, H., "Expansion of a thick cylinder of soils," *Computers and Geotechnics*, vol. 14, no. 1, pp. 21–41, 1992.

[106] Zhang, F. and Huang, H., "Coupled DEM-CFD modeling of fluid injection into granular media," in *45th US Rock Mechanics/Geomechanics Symposium*, American Rock Mechanics Association, 2011.

[107] Zhang, F., *Pattern formation in fluid injection into dense granular media*. PhD thesis, Georgia Institute of Technology, 2012.

[108] Zhang, F., Damjanac, B., and Huang, H., "Coupled discrete element modeling of fluid injection into dense granular media," *Journal of Geophysical Research: Solid Earth*, vol. 118, no. 6, pp. 2703–2722, 2013.

[109] Zhou, Z., Yu, A., and Choi, S.-K., "Numerical simulation of the liquid-induced erosion in a weakly bonded sand assembly," *Powder Technology*, vol. 211, no. 2, pp. 237–249, 2011.

[110] Zimmerman, R. W. and Bodvarsson, G. S., "Hydraulic conductivity of rock fractures," *Transport in Porous Media*, vol. 23, no. 1, pp. 1–30, 1996.